



Durham E-Theses

Models of high energy $\rho\rho, \rho\rho$ scattering

Carter, M.K.

How to cite:

Carter, M.K. (1987) *Models of high energy $\rho\rho, \rho\rho$ scattering*, Durham theses, Durham University.
Available at Durham E-Theses Online: <http://etheses.dur.ac.uk/6718/>

Use policy

The full-text may be used and/or reproduced, and given to third parties in any format or medium, without prior permission or charge, for personal research or study, educational, or not-for-profit purposes provided that:

- a full bibliographic reference is made to the original source
- a [link](#) is made to the metadata record in Durham E-Theses
- the full-text is not changed in any way

The full-text must not be sold in any format or medium without the formal permission of the copyright holders.

Please consult the [full Durham E-Theses policy](#) for further details.

Models of High Energy $pp, \bar{p}p$ Scattering

M.K. Carter
Graduate Society

A thesis submitted to the Faculty of Science for the degree of
Doctor of Philosophy in the University of Durham.

The copyright of this thesis rests with the author.
No quotation from it should be published without
his prior written consent and information derived
from it should be acknowledged.

Department of Physics.

October, 1987.



07 FEB 1988

ABSTRACT

A phenomenological description is sought of the dynamics operating in high energy elastic hadron-hadron scattering. The predictions of a simple Pomeron and weak cut model of high energy elastic scattering are compared with the new and surprising $\bar{p}p$ data from the ISR and $S\bar{p}pS$ Collider. The model, which gives a complete account of all the lower energy data, is incompatible with the unexpected energy dependence of the differential cross-section shown by the Collider data. Modifications within the original framework of the model are examined but found inadequate and it is concluded that new contributions are necessary. Two avenues are explored as likely candidates for the correct approach.

The first approach considered is the possible existence of a small odd charge conjugation term with constant or increasing contribution to the cross-section. Two existing models of such an "Odderon" effect are studied which give good agreement with the new data but neither of which are entirely satisfactory. A reggeized Odderon contribution, analagous to these models, is examined and limitations are placed on its effect.

The second possibility considered as a description of the additional contributions to the model are the correction terms necessary to prevent the violation of unitarity and the breaking of asymptotic bounds. An eikonalization model, in which s -channel unitarity is explicitly satisfied, is reviewed but several theoretical problems emerge due to the nature of the basic exchange and the model gives a relatively poor description of the data. A similar model in which the Born term is described by a Pomeron with the appropriate Regge phase is developed. This clears up some of the theoretical problems but is found to exaggerate the problems encountered in fitting the data and it is concluded that such an eikonal description is unlikely to work. A simple model of the unitarity corrections which gives a better chance of reproducing the data is proposed. The results of the phenomenology of the asymptotic and perturbative Reggeon field theory approaches to elastic scattering are briefly reviewed.

ACKNOWLEDGEMENTS

I would like to thank my supervisor Dr Peter Collins for his patience and direction during the course of this work.

I am grateful to all the numerous people in the particle theory research group in Durham who provided such a friendly atmosphere to work in and whom it has been my pleasure to know.

I would also like to thank my colleagues at RAL for their generosity in allowing me time and facilities to produce this thesis.

CONTENTS

CHAPTER 1. INTRODUCTION

1.1 Objective	1
1.2 Introduction to Elastic Scattering	2
1.3 Chapter Outlines	6

CHAPTER 2. DATA

2.1 Introduction	8
2.2 Total Cross-section, σ_T	14
2.3 Difference of Total Cross-sections, $\Delta\sigma = \sigma_T(pp) - \sigma_T(\bar{p}p)$	17
2.4 Re/Im, Total Elastic Cross-section and Forward Slope Parameter	18
2.5 Elastic Differential Cross-section Data	20
2.6 The Effective Trajectory	26

CHAPTER 3. THEORY DISCUSSION

3.1 Unitarity, Analyticity and Crossing	37
3.2 Partial-wave Amplitudes and Impact Parameter Space	39
3.3 Asymptotic Bounds on the Scattering Amplitude	44
3.4 Regge Poles	46
3.5 Regge Poles and Perturbation Theory	51
3.6 Regge Cuts	52

CHAPTER 4. POLE AND WEAK CUT MODEL

4.1 Introduction	56
4.2 Total Cross-section	61
4.3 Prediction of Re/Im	72
4.4 Fits to the Differential Cross-section	74
4.5 Bent Trajectory Parametrization	86
4.6 Strong Cut Parametrization	93
4.7 Core Term Parametrization	98
4.8 Low Energy Fits to $\frac{d\sigma}{dt}$	101
4.9 Conclusions, the Unitarity Limit and High Energy Extrapolations	107

CHAPTER 5. ODDERON MODELS

5.1 Introduction	112
5.2 The Donnachie-Landshoff Model	113
5.3 The Maximal Odderon Model (GLN model)	132
5.4 Reggeized Odderon Contribution	148

CHAPTER 6. IMPACT PICTURE MODEL

6.1	Introduction	155
6.2	Details of the Computation	159
6.3	High Energy Behaviour of the Profile Function, $A(s, b)$	159
6.4	High Energy Behaviour of σ_T and the Froissart Bound	163
6.5	High Energy Behaviour of Re/Im	167
6.6	High Energy Behaviour of $\frac{d\sigma}{dt}$	168
6.7	The Reggeon Contribution	172
6.8	$\frac{d\sigma}{dt}$ with Reggeon Contribution Included	175
6.9	Conclusions	178

CHAPTER 7. REGGE-EIKONAL MODEL

7.1	Introduction	180
7.2	Fitting $\frac{d\sigma}{dt}$ and σ_T	183
7.3	Fitting the $\frac{d\sigma}{dt}$ data in the dip region and beyond	189
7.4	Eikonalized Reggeon Contribution	199
7.5	Conclusions	203

CHAPTER 8. REGGEON FIELD THEORY PHENOMENOLOGY

8.1	Introduction	205
8.2	Behaviour of σ_T	208
8.3	The Differential Cross-section	212

CHAPTER 9. UNITARIZATION MODEL

9.1	Introduction	215
9.2	A Simple Model	215
9.3	An Extension of the Simple Model	219

CHAPTER 10. GENERAL DISCUSSION AND SUMMARY

10.1	Summary of Results	226
10.2	Comparison of High Energy Predictions	230
10.3	Future Prospects	231
10.4	Conclusions	233

APPENDIX A	235
------------	-----------	-----

APPENDIX B	237
------------	-----------	-----

APPENDIX C	240
------------	-----------	-----

REFERENCES	242
------------	-----------	-----

Introduction.

1.1. Objective.

The vast increase in the energies produced in particle accelerators in recent years has brought much new physics into the laboratory. Most of the phenomenological interest in the last decade has centred on the increase in transverse momentum that the higher energies allow. More so because of the non-abelian nature of QCD and the asymptotic freedom and infra-red confinement that this implies. Along with the high p_T physics the new machines have also provided a wealth of new data on high energy soft hadronic scattering. Recent work in the area of soft physics has been directed at understanding the longitudinal momentum distributions in the fragmentation region in terms of the parton model; diffraction disassociation; heavy flavour production; understanding the dynamics of elastic scattering at high energies and the Pomeron in terms of QCD.

Since the models describing soft physics at high energies are mostly applicable only at energies much greater than the hadronic mass scale, s_0 , so that $\log \frac{s}{s_0}$ is large, new higher energy data is a crucial test of their validity and also necessitates some reappraisal of the data at lower energies. In the following we examine how well existing models of elastic scattering confront the high energy data from the $S\bar{p}pS$ Collider and CERN ISR and seek ways in which they can be improved. We also study their predictions at the higher energies likely to be attained in new accelerators over the next decade.

Current theory falls a long way short of having any real understanding of diffractive scattering in terms of a fundamental theory. On the other hand a phenomenological description in terms of Regge poles (and cuts) has had great success in tying together and predicting the huge amount of data on diffractive hadron-hadron scattering. The major outstanding problems in the Regge theory approach to strong interactions are the fundamental nature of the Pomeron and the role played by Regge cuts. The best place to try to understand these problems is at high energies where the effects of other Regge trajectories and different helicity amplitudes are small and first we need an accurate phenomenological description of how the Pomeron behaves. This requires more understanding of how the Regge cut terms behave and how the Pomeron



is compatible with unitarity; and whether an odd charge conjugation contribution survives at high energy and its possible effect. A better theoretical appreciation of the Pomeron and of Regge cuts would have implications for the whole range of processes that Regge theory describes.

The problem presented by the high energy $\bar{p}p$ data from the ISR and the $S\bar{p}pS$ Collider is the significant difference in shape in the dip region at both energies compared with the ISR pp data and the surprisingly large energy dependence between the ISR and the Collider. In the next decade new machines should provide data at much higher energies, up to $\sqrt{s} = 40$ TeV, so that the predictions of the various models are relevant and experimentally testable.

1.2. Introduction to Elastic Scattering.

The high energy behaviours of the quantities $\sigma_T(s)$, $\rho(s)$ and $B(s)$ have received much attention. Most of the analyses of hadron-hadron elastic scattering are directed towards pp and $\bar{p}p$ scattering since these are the most accurately measured processes. The total cross-sections for various hadron-proton collisions are shown in figure 1.1 . In all cases the antiparticle-proton cross-section is substantially greater than the particle-proton cross-section and the difference falls with increasing energy. The particle-proton cross-sections are relatively independent of energy showing only a slight minimum for $\sqrt{s} \approx 10$ GeV (apart from the K^+p cross-section which increases monotonically). The cross-sections are of order 10's of millibarns giving a hadronic radius of approximately one fermi.

Originally it appeared that the total cross-sections were approaching constant values at high energy, in which case the Pomeranchuk theorem implied that crossed channel total cross-sections should become asymptotically equal as the data seem to imply (provided that there is no odd charge conjugation contribution with real part growing as $\log^2 s$). The behaviour of the cross-section differences : $\bar{p}p - pp$, $\pi^-p - \pi^+p$, $K^-p - K^+p$, all show a very clean $\approx s^{-\frac{1}{2}}$ energy dependence and are attributed to odd signature Regge exchanges. Regge theory predicts that the high energy behaviour of the direct-channel amplitudes are governed by the cross-channel resonances through an $s^{\alpha(t)}$ behaviour for their energy dependence.

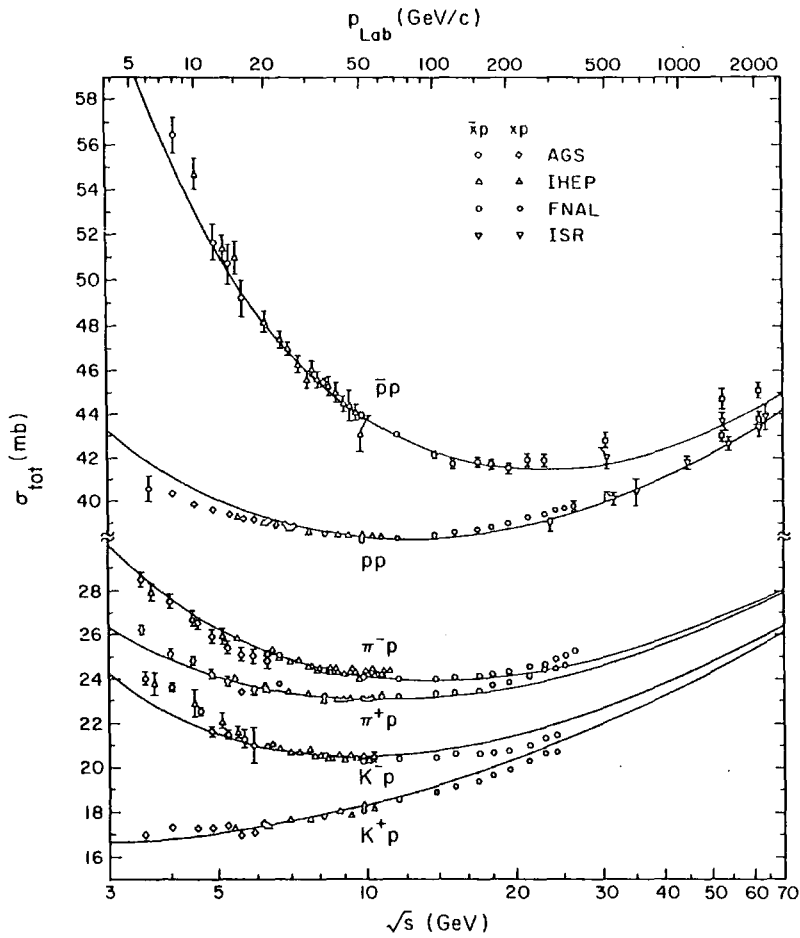


FIG.1.1 Total cross-sections for hadron-proton scattering (figure is taken from Carboni (1985), curves are due to Lipkin (1975)).

In the crossed-channel $\alpha(t)$ corresponds to the spins of a set of resonances lying on the same Regge trajectory when $t = M_R^2$ corresponds to the resonance mass. Experimentally it is found that the Regge trajectories are linear, which can naively be thought of as arising from the constant energy density along a tube-like region between two quarks. The Chew-Frautschi plot of spin against resonance mass squared for the leading meson Regge trajectories is shown in figure 1.2 .

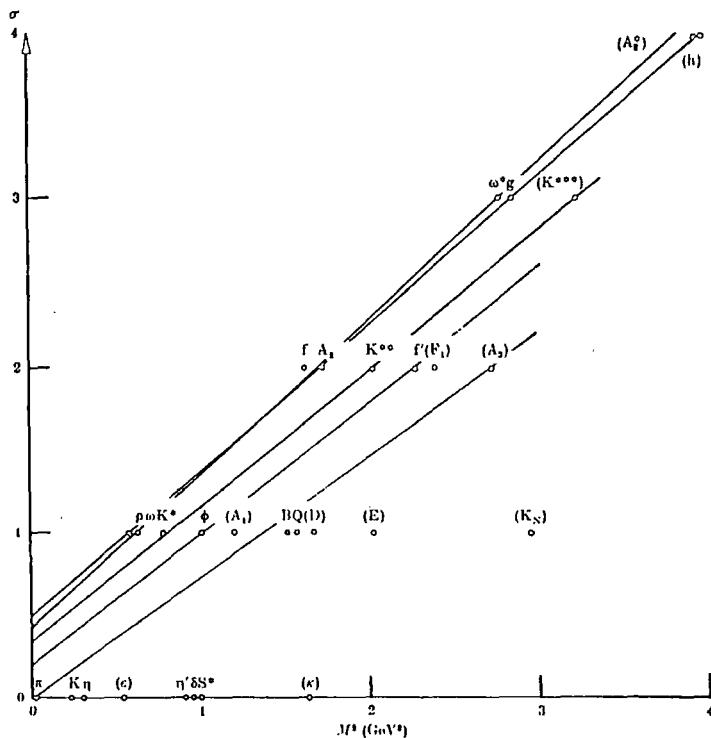


FIG.1.2 Chew-Frautschi plot for leading meson resonances (figure is taken from Collins (1977)).

The constant component of the cross-section is due to diffractive processes which do not involve the exchange of constituent quarks between the colliding hadrons. This was described by the Pomeron trajectory, with intercept at one and even signature to give the constant, asymptotically equal cross-sections in the s - and u -channel processes and the predominantly imaginary amplitudes. Unlike conventional trajectories no established particle states lie on this trajectory and it is higher and flatter than known meson Regge trajectories. The true nature of the Pomeron trajectory is still unclear. The small contribution of the non-diffractive Regge exchanges to π^+p , K^+p , pp in comparison with those to π^-p , K^-p , $\bar{p}p$ correlates with the observation that the former processes are exotic in the direct channel and that the t -channel Regge exchanges which govern the asymptotic s -channel behaviour are “dual” to the s -channel resonances. This implies exchange degenerate trajectories and residues which, as the Chew-Frautschi plot in figure 1.2 shows, is obeyed very well by the leading trajectories. The small departure of the pp , K^+p and π^+p cross-sections from a constant value does however imply some breaking of exchange degeneracy.

The ratios of the total cross-sections in figure 1.1 obey the additive quark model predictions reasonably accurately and therefore imply that the Pomeron couples to single quarks. The f -dominated Pomeron idea further supports this, and analogous to

vector meson dominance, describes the coupling of the Pomeron to quarks through the f mesons, which have the same quantum numbers as the Pomeron. Another important property of Regge poles is the factorizability of their couplings as a product of the couplings at each vertex, which gives Regge theory great predictive power through SU(3) of flavour.

The predictions of dispersion relations and the later confirmation by direct measurements of σ_T at the ISR and the $S\bar{p}pS$ Collider and from cosmic ray data showed that the constant behaviour of σ_T does not continue at higher energies and the total cross-section rises with an approximate $\log^2 s$ dependence for $\sqrt{s} \geq 15$ GeV, which is as fast as allowed by asymptotic theorems. In terms of a Regge pole model for the Pomeron an increasing cross-section corresponds to a trajectory above one. Since this gives a cross-section growing faster than $\log^2 s$ it will eventually violate the asymptotic bound, but by this time Pomeron cut effects should be important and restore the $\log^2 s$ behaviour.

Since Pomeron exchange is thought not to involve the interchange of quarks it is naturally attributed to gluon exchange. The basic diagram for colourless gluon exchange is the 2 gluon box diagram shown in figure 1.3(a), which gives an is contribution to the amplitude as required for the Pomeron. However, *a priori*, higher order exchanges will swamp this behaviour and there is not much reason for supposing this simple diagram has any relevance except that it produces the right answer so well. A field theory model for how the higher order effects may sum to give the Pomeron trajectory represents the Pomeron by the sum of gluon ladder diagrams like figure 1.3(b). The Pomeron cut effects result from multiple scattering of Pomerons from different constituents of the hadrons as in figure 1.3(c). The Pomeron conserves helicity in the s -channel and at high energies the effect of different spin amplitudes are small and can be neglected.

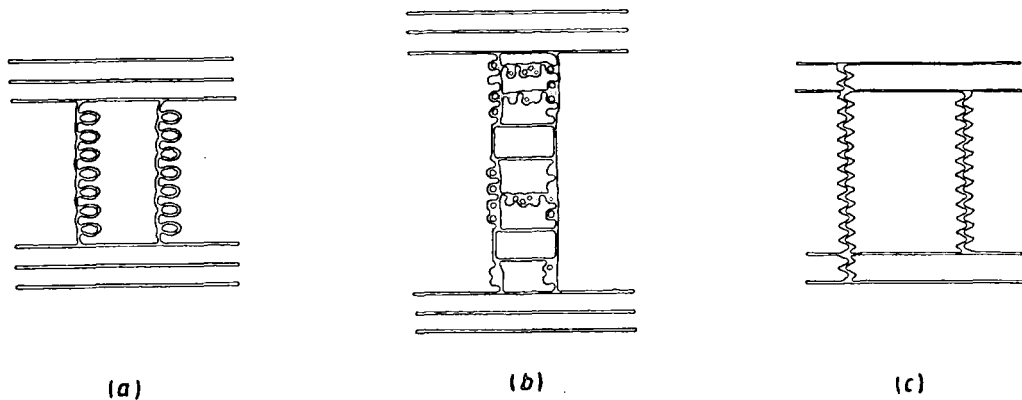


FIG.1.3 (a) Basic two gluon exchange diagram representing Pomeron exchange. (b) Gluon ladder diagram reggeizing basic exchange to give Pomeron trajectory. (c) Two Pomeron exchange giving a Pomeron cut.

One of the major reasons for supposing the Pomeron may be described by a Regge pole is the characteristic shrinkage of the forward elastic differential cross-section. Since all the hadron-hadron scattering processes show a similar t -dependence and shrinkage with energy this implies that the Pomeron couples universally to hadrons and is flavour independent. At larger $|t|$ the data show dip/bump structure reminiscent of that in optical diffraction and similar in shape to the first order Bessel function resulting from scattering from a black disk.

At low energies the large $|t|$ behaviour of the differential cross-section can be predicted from perturbative QCD. The dimensional counting rules relate $\frac{d\sigma}{dt}$ in the region $s, t \rightarrow \infty$ ($\frac{s}{t}$ fixed) to the scale invariant qq scattering sub-process and the tail of the hadron form factor. These give

$$s^2 \frac{d\sigma}{dt} \sim f\left(\frac{t}{s}\right) s^{-2n_s} \quad (1.2.1)$$

where n_s is the number of spectator quarks.

1.3. Chapter Outlines.

In chapter 2 we review the available high energy data on pp and $\bar{p}p$ scattering for the experimental observables σ_T , $\Delta\sigma$, ρ , σ_{el} , B and $\frac{d\sigma}{dt}$ and perform a calculation of the effective trajectory.

In chapter 3 we summarise the relevant parts of Regge theory and field theory used in the other chapters.

In chapter 4 we examine the predictions of the Pomeron and weak cut model and compare them with the new data from the ISR and the Collider. We adjust the parameter values used to obtain the best fit within the framework of the original model and then try out various modifications to improve the description of the data.

The behaviour of an odd charge conjugation contribution is explored in chapter 5 using the models of Donnachie and Landshoff, and Gauron, Leader and Nicolescu and a reggeized version of these examined.

In chapters 6, 7 and 9 we look at ways of ensuring that the amplitude does not exceed s -channel unitarity limits and violate asymptotic bounds. Chapter 8 reviews the results from Reggeon field theory which is thought to satisfy both s - and t -channel unitarity.

The computing work in the following has been performed on the RAL IBM 3081, NUMAC and a microvax at RAL. Where we have quoted computation times this refers to the IBM machine.

Data

2.1. Introduction

The major accelerators from which the high energy ($\sqrt{s} > 4$ GeV) total and elastic cross-sections have been obtained are all synchrotron machines and are detailed in table 2.1. The first five accelerators in the table are fixed target machines where the primary beam from the synchrotron is incident onto a target and produces a secondary beam for scattering experiments made up of π , K , p , \bar{p} , μ and e which is then projected onto a liquid Hydrogen target away from the synchrotron. The CERN ISR and $S\bar{p}pS$ Collider are colliding beam machines and the collisions take place inside the synchrotron in areas around the machine where the two beams intersect. Because of the momentum conservation constraints the centre of mass energy in colliding beam machines is much greater than that in fixed target machines but at the cost of a much lower luminosity and diversity of types of particle beams that can be used. The ISR was developed first as a pp collider and then adapted for use as a $\bar{p}p$ collider also. The $S\bar{p}pS$ Collider uses the 400 GeV SPS machine to contain a counter rotating beam of antiprotons along with the proton beam and collides the two beams at various points around the ring. Of the others, only the Tevatron (fixed target) and Tevatron I ($\bar{p}p$ collider) are in operation and so far these have not yet produced any data on total or elastic cross-sections except at lower energies. The Tevatron is an upgrade of the existing 500 GeV proton synchrotron at Fermilab. It uses superconducting magnets instead of conventional magnets and gives a $\sqrt{s} = 1$ Tev beam which is used both as a fixed target machine and as a $\sqrt{s} = 2$ Tev $\bar{p}p$ collider (Tevatron I).

There are three other hadron-hadron machines planned at higher energies in the near future. The UNK is a Russian machine currently being built at Serpukhov and due for completion in 1993. The facilities available will be a superconducting magnet ring producing 3 Tev protons allowing both fixed target experiments and 400 GeV on 3 Tev pp colliding beam experiments with a 400 GeV conventional magnet storage ring and eventually including an antiproton beam in the main ring giving a 3 Tev on 3 Tev $\bar{p}p$ collider. The Large Hadron Collider (LHC) proposal is still under discussion and involves building a pp collider within the LEP tunnel giving an 8 Tev on 8 Tev collider.

The SSC project has now been given the green light and will consist of a 20 Tev on 20 Tev proton-proton collider which should be completed around 1996.

Accelerator	Beam	Energy	Luminosity ($cm^{-2}s^{-1}$)	Circumference	Year
CERN PS	p	28 GeV	$\sim 10^{38}$	600 m	1959
BNL AGS	p	33 GeV	$\sim 10^{38}$	800 m	1960
Serpukhov IHEP	p	76 GeV	$\sim 10^{38}$	1500 m	1967
CERN SPS	p	450 GeV	$\sim 10^{38}$	7 km	1976
FNAL	p	200/500 GeV	$\sim 10^{38}$	6 km	1972
CERN ISR	pp	31.4 + 31.4 GeV	$10^{31} - 10^{32}$	940 m	1971
	$\bar{p}p$		$\sim 10^{28}$		1981
<i>S$\bar{p}p$S</i> Collider	$\bar{p}p$	273+273 GeV (450+450)	$> 10^{30}$	7 km	1981
Tevatron	p	1 Tev	$\sim 10^{38}$	6 km	1983
Tevatron I	$\bar{p}p$	1 + 1 Tev	$\geq 10^{30}$	6 km	1985
UNK	p	3 Tev		20 km	≥ 1993
	pp	400 + 3000 GeV	10^{32}		
	$\bar{p}p$	3 + 3 Tev			
LHC	pp	8 + 8 Tev	$10^{33} - 10^{34}$	27 km	≥ 1995
SSC	pp	20 + 20 Tev	10^{33}	84 km	≥ 1996

TABLE 2.1. Hadron-Hadron Colliders.

In fixed target experiments a typical set-up would consist of directing the secondary beam into a liquid Hydrogen or Deuterium target. The beam particles would be detected with a beam hodoscope and identified with differential Čerenkov counters, the scattered particles detected with a counter hodoscope and MWPC. These measure the angle of ingoing and outgoing particles and then elastic scattering events can be selected by coplanarity and kinematic angle requirements. Comparison of the count rates with the target full and empty and the dimensions of the hydrogen target gives the cross-sections directly. An alternative experimental technique is to replace the Hydrogen target by a Hydrogen bubble chamber and observe the number of elastic and inelastic events giving a measurement of σ_T and $\frac{d\sigma}{dt}$.

The most direct way to determine σ_T in a fixed target experiment is to measure the fraction of the beam transmitted through the target without interaction which gives σ_T through :

$$\text{Transmission ratio} = B_i e^{-\sigma_i \rho \frac{LN}{M}} \quad (2.1.1)$$

where ρ is the density of liquid Hydrogen, L is the length of the Hydrogen column, N is Avogadro's number and M is the atomic weight of Hydrogen. B_i is the fraction of the beam transmitted with the target empty. The subscript i refers to the fact that what is actually measured is the number of particles detected by a transmission counter i , which subtends a finite solid angle Ω_i at the target. The calculated cross-section σ_i is then underestimated since particles which suffer only small deflections are also detected, so that

$$\sigma_i = \sigma_T - \int_0^{\Omega_i} \frac{d\sigma}{d\Omega} d\Omega \quad (2.1.2)$$

In practice σ_i is measured for various Ω_i and σ_T obtained by extrapolating down to $\Omega = 0$. This is the so called good geometry transmission method. The extrapolation is not straightforward because the Coulomb scattering cross-section must be subtracted and Coulomb/Nuclear interference taken into account. This method typically gives errors of $\sim 0.3\%$ and has been used by Galbraith (1965), Foley (1967), Denisov (1973) and Carroll (1976/79) amongst others.

The colliding beam machines required different techniques to measure σ_T and $\frac{d\sigma}{dt}$ since it is not possible to interrupt the beam. Detectors were developed, called Roman pots, which were placed inside movable sections of the vacuum chamber and could be inserted into the beam pipe and get very close to the beam. At the ISR these were positioned 90 m down the beam pipe from the interaction region and could get as close as 9 mm from the beam so that they could detect particles scattered at an angle of only 1 mrad.

Measurement of the differential cross-section involves the measurement of the number of particles, $\frac{dN}{dt} \Delta t$, scattered into a bin of width Δt over some time period and a measurement of the integrated luminosity, L , over that period. The cross-section is then given by

$$\frac{d\sigma}{dt} = \frac{1}{L} \frac{dN}{dt} \quad (2.1.3)$$

The integrated luminosity was determined at the ISR by measuring the number of counts recorded over the period by a given detector and calibrating the detector using the Van der Meer method, a technique which involves sweeping the two beams through each other whilst measuring the count rate in the detector. With some later improvements this technique gave luminosity measurements accurate to 0.3%.

A number of methods were employed to measure σ_T at the ISR. The two basic ones were performed by the Pisa-Stony Brook (PSB) group and the CERN-Rome (CR) group. Both made use of the luminosity determined by the Van der Meer method. The PSB collaboration measured the total interaction rate and so required efficient coverage of the complete solid angle around the zone of interaction (Amendolia 1973). Making the beam pipe elliptic in cross-section reduced the holes in the detector for the incoming and outgoing beams and the remaining losses at small angles of elastically and quasi-elastically scattered particles were estimated. The total cross-section was then obtained from

$$\sigma_T = \frac{1}{L} R_{Total} \quad (2.1.4)$$

Where R_{Total} is the total number of elastic and inelastic events recorded over the period. The CR method found σ_T by measuring small $|t|$ elastic scattering and determining the optical point by extrapolating to $t = 0$ (Amaldi 1973b). The optical theorem then gives σ_T from :

$$\left. \frac{d\sigma}{dt} \right|_{t=0} = \frac{(1 + \rho^2)\sigma_T^2}{16\pi} \quad (2.1.5)$$

The ratio of the real to imaginary parts of the amplitude, ρ , can be determined from Coulomb/nuclear interference.

For very low momentum transfers, $|t| < 0.001 \text{ GeV}^2$, the cross-section is dominated by Coulomb scattering giving a differential cross-section behaving like :

$$\frac{d\sigma^C}{dt} = 4\pi\alpha^2 \frac{G^4(t)}{t^2} \quad (2.1.6)$$

Where α is the fine structure constant and $G(t)$ is the proton electromagnetic form factor which is well parametrized empirically by

$$G(t) = \frac{1}{(1 + \frac{|t|}{0.71})^2} \quad (2.1.7)$$

For larger $|t| > 0.01 \text{ GeV}^2$, the cross-section is dominated by diffractive nuclear scattering and can be parametrized at small $|t|$ by :

$$\frac{d\sigma^N}{dt} = \frac{(1 + \rho^2)}{16\pi} \sigma_T^2 e^{B_0 t} \quad (2.1.8)$$

In the intermediate region, $0.001 < |t| < 0.01 \text{ GeV}^2$, the cross-section is dominated by the coherent superposition of the coulomb and nuclear amplitudes and this gives rise to an interference term. Thus we have :

$$\frac{d\sigma}{dt} = \frac{d\sigma^C}{dt} + \frac{d\sigma^N}{dt} - \frac{\alpha\sigma_T}{|t|}(\rho + \delta)G^2(t)e^{\frac{B_0 t}{2}} \quad (2.1.9)$$

Where δ can be calculated (see for example Block and Cahn (1985)) and is given by $\delta = \alpha(\log \frac{0.08}{|t|} - 0.577)$. It can be seen that at small $|t|$ the Coulomb term has a $\frac{1}{t^2}$ dependence, the interference term a $\frac{1}{t}$ dependence and the nuclear term is approximately independent of $|t|$ for small $|t|$. This allows the contributions of the three terms to be separated and provided the data penetrates into the Coulomb interference region ρ , B_0 and σ_T can be found by fitting the data using (2.1.9). The Coulomb/Nuclear interference subtracts from the pp nuclear amplitude (for $\rho > 0$) and adds to the $\bar{p}p$ amplitude. Since $\frac{d\sigma}{dt}$ is obtained from $\frac{1}{L} \frac{dN}{dt}$ the cross-section calculated this way depends on the luminosity through $\sigma_T \sim \frac{1}{\sqrt{L}}$. The different luminosity dependences of the PSB and CR methods provides an independent check on the luminosity calibration. More recent measurements of $\sigma_T(pp)$ and $\sigma_T(\bar{p}p)$ using the PSB and CR methods have been performed by the CERN-Naples-Pisa-Stony Brook collaboration (Carboni 1985) and the Louvain-Northwestern collaboration (Amos 1985) respectively.

The energy dependence of the position of the region of Coulomb/nuclear interference is produced by the energy dependence of the nuclear term. Through the ISR energy range the interference region occurs for $|t| \approx 0.0017 \text{ GeV}^2$ corresponding to an angle of $\approx 2 \text{ mrad}$ which can be easily obtained using the Roman pot detectors described above. In fact these detectors can penetrate well into the region where Coulomb scattering dominates and since the cross-section for Coulomb scattering is known (2.1.6) the data can be normalized relative to this. This provides another independent measurement of luminosity and has been used in the past by the CR group (Amaldi 1973a) in preference to other methods of measuring luminosity.

By measuring the cross-sections using the CR and PSB methods simultaneously at the same intersection region it is possible to eliminate the dependence of σ_T on the

calibrated luminosity. Combining equations (2.1.3), (2.1.4) and (2.1.9) gives

$$\sigma_T = \frac{16\pi}{R_{Tot}(1 + \rho^2)} \left. \frac{dN_{el}}{dt} \right|_{t=0} \quad (2.1.10)$$

This method was used by a collaboration of the PSB and CR groups to give another luminosity independent measurement of σ_T (Amaldi 1978) using the Split Field Magnet Detector. With this it was not possible to detect particles at small enough angles to probe the Coulomb interference region and determine ρ and so ρ was obtained from previous measurements of the CR group.

At the $S\bar{p}pS$ Collider the luminosity can only be determined to 10% accuracy giving a 5% error in σ_T with the CR method so that a luminosity independent method of measuring σ_T is preferable. At $\sqrt{s} = 546$ GeV the Coulomb interference region occurs for $|t| \approx 0.001$ GeV² which corresponds to an angle of $\theta = 0.12$ mrad to be compared with the $\theta_{min} = 0.65$ mrad so far obtained. At this angle Coulomb interference has only a small effect and therefore ρ must be calculated by extrapolation from lower energy data (Bozzo 1984). The $S\bar{p}pS$ Collider has also run at an increased energy of 310 GeV/c per beam (1984) and in pulsed mode where the beam is accelerated between energies of 100 and 450 GeV/c allowing measurements at $\sqrt{s} = 200$ and 900 GeV (1985).

At the forthcoming higher energy colliders the small angle problem will be even worse. At the SSC, for instance, with $\sqrt{s} = 40$ TeV the Coulomb interference region occurs for $|t| = 0.0004$ GeV² giving $\theta = 1$ μ rad which will require new experimental techniques to attain though this is not beyond the bounds of possibility (Foley 1985).

Some data at these TeV energies are already available from another source : that of cosmic ray air showers. These yield data for the total inelastic proton-air cross-sections, $\sigma_{abs}(p - Air)$, at energies up to $\sqrt{s} \sim 10^5$ GeV. Using Glauber scattering theory this allows a determination of the pp total inelastic cross-section, $\sigma_{inel}(pp)$ to be made provided the forward slope of the amplitude can be estimated. This then gives σ_T assuming a model for the ratio $R = \frac{\sigma_{el}}{\sigma_T}$. The calculated values of σ_T have large errors and are model dependent. There is some disagreement in the literature as to the correct result of the calculation (Kopeliovich 1986).

In the following sections we briefly review the currently available experimental data on elastic and total cross-section measurements.

2.2. Total Cross-section, σ_T

In figure 2.1 we show the data for $\sigma_T(pp)$ and $\sigma_T(\bar{p}p)$ from $\sqrt{s} > 2$ GeV up to the highest laboratory energy measured at $\sqrt{s} = 900$ GeV. Above threshold, at $\sqrt{s} = 1.76$ GeV, $\sigma_T(pp)$ falls sharply to a minimum and then rises rapidly again to a maximum at $\sqrt{s} = 2.3$ GeV where $\sigma_T(pp) = 47.6$ mb. Beyond this the cross-section drops steeply until $\sqrt{s} = 3$ GeV and then flattens off, falling slowly until a minimum at $\sqrt{s} \approx 10$ GeV followed by a slow rise thereafter up to $\sqrt{s} = 63$ GeV which is the highest energy the pp cross-section has been measured at in the laboratory. Through the whole of the region $3 \leq \sqrt{s} \leq 63$ GeV the cross-section lies within the band 41 ± 3 mb.

The $\bar{p}p$ cross-section lies approximately 50% above the pp data at low energy. It does not have the same structure as in pp but drops rapidly and smoothly to a minimum at $\sqrt{s} \approx 20$ GeV (though it shows some sign of resonance structure for $p_{lab} < 2$ GeV/c). Through the ISR energy range $\sigma_T(\bar{p}p)$ rises slowly and gets steadily closer to $\sigma_T(pp)$. The $\bar{p}p$ total cross-section data from the $S\bar{p}pS$ Collider at $\sqrt{s} = 546$ and 900 GeV show this rise continuing.

We are only concerned with the data for the energy region $\sqrt{s} \geq 4$ GeV where threshold effects are expected to be small and below which the Regge parametrization is complicated by daughters and lower lying trajectories. In our fits we use the sub-set of the available data shown in Table 2.2.

Energy \sqrt{s} GeV	ScaleError mb	Author	Year	Accelerator	Technique
pp					
4 → 7	±0.02	Foley	1967	BNL AGS	Transmission method
7 → 26	±0.02	Carroll	1976/79	FNAL	Transmission method
23 → 63	±0.25	Amos	1985	ISR	Compilation
$\bar{p}p$					
4 → 6		Galbraith	1965	BNL AGS	Transmission method
8 → 23	±0.02	Carroll	1976/79	FNAL	method
30 → 63	±0.25	Amos	1985	ISR	CR method
30 → 63	±0.25	Carboni	1985	ISR	PSB method
546	±0.6	Bozzo	1984	Collider	Luminosity Independent
900	±1.8	Rushbrooke	1985	Collider	Measures σ_{inel}

TABLE 2.2. Sources for total cross-section data.

The Amos (1985) paper updates the summary of pp scattering results at the ISR given in Amaldi (1980) and gives a new best value for $\sigma_T(pp)$ at ISR energies obtained by averaging the results of the three different methods used at the ISR to measure σ_T . The measurement of $\sigma_T(\bar{p}p)$ at the Collider uses the result of a dispersion relation fit to determine $\rho(s, t = 0)$ at $\sqrt{s} = 546$ GeV (assumes $\rho = 0.15$) and obtains σ_T from the luminosity independent measurement of $\sigma_T(1 + \rho^2)$. Though the effect of ρ is small this can produce a slight difference in models where ρ is different from its predicted value (due to an asymptotic odd charge conjugation contribution for example). The datum at $\sqrt{s} = 900$ GeV is calculated from a measurement of the ratio of $\sigma_{inel}(\sqrt{s} = 200$ GeV) to $\sigma_{inel}(\sqrt{s} = 900$ GeV) and so to extract σ_T they have to obtain $R = \frac{\sigma_{inel}}{\sigma_T}$ at $\sqrt{s} = 200$ and 900 GeV and $\sigma_{inel}(\sqrt{s} = 200$ GeV) by extrapolation from previous measurements.

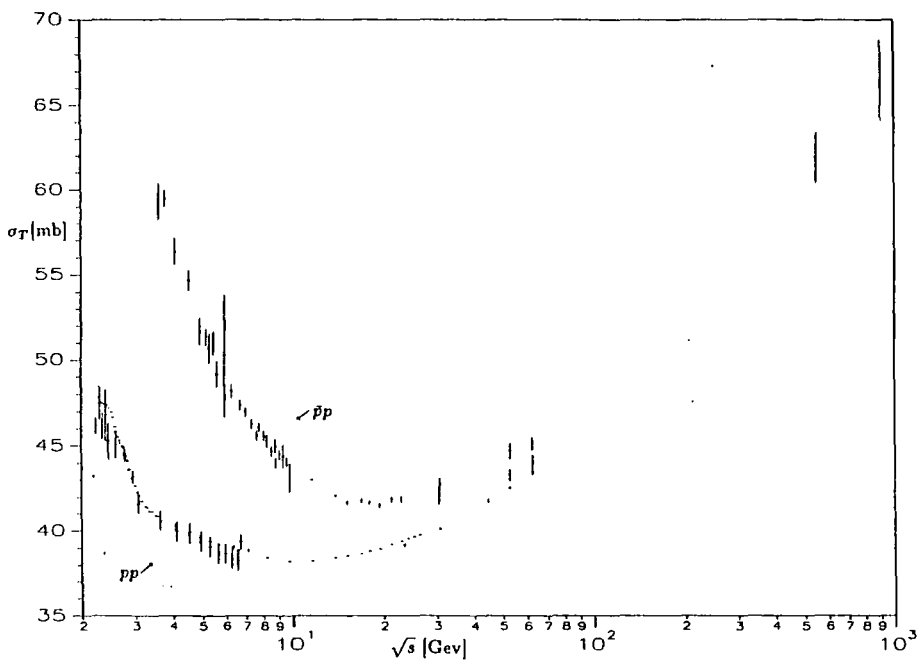


FIG. 2.1 $\bar{p}p$ and pp total cross-sections.

We have not included in our fits the data at very high energies obtained from the analysis of cosmic ray protons since as described above they have large uncertainties and model dependencies. We do, however, use them as a useful comparison to the prediction of the models at energies where no data is currently available. Figure 2.2 shows the cosmic ray data from the Akeno experiment (Hara 1983), the Fly's eye experiment (Baltrusaitis 1984) and the results produced by Linsley (1985) from experiments at Haverah Park, Yakutsk and Dugway. Included for comparison are the recalculated total cross-sections from Kopeliovich (1986).

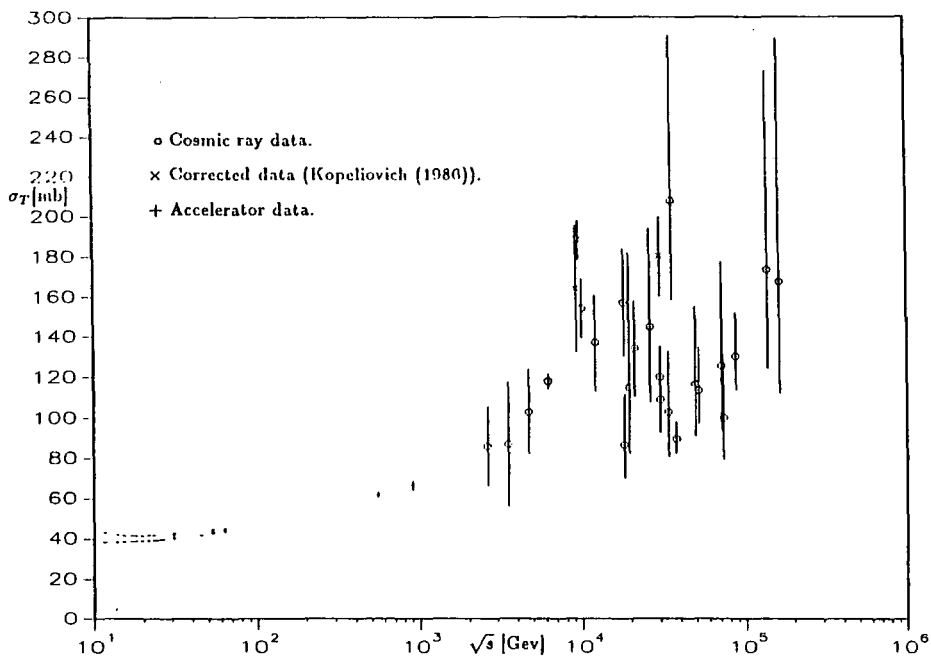


FIG. 2.2 Cosmic ray data on pp total cross-section

2.3. Difference of Total cross-sections, $\Delta\sigma = \sigma_T(\bar{p}p) - \sigma_T(pp)$

When $\sigma_T(pp)$ and $\sigma_T(\bar{p}p)$ have both been measured a value for $\Delta\sigma$ is obtained with better errors than the individual measurements combined because some of the systematic errors cancel. The data for $\Delta\sigma$ detailed in Table 2.3 is plotted in figure 2.3 on log/log axes and the resulting approximate straight line shows that the $\bar{p}p, pp$ difference is decreasing with a simple power law behaviour $\Delta\sigma \sim s^{-\beta}$ with $\beta \approx \frac{1}{2}$.

Energy \sqrt{s} GeV	Author	Year	Accelerator	Technique
3.6 → 6	Galbraith	1965	BNL AGS	Transmission method
3.8 → 10	Denisov	1973	Serpukhov	Transmission method
8 → 23	Carroll	1976/79	FNAL	Transmission method
31 → 63	Amos	1985	ISR	CR method
31 → 63	Carboni	1985	ISR	PSB method
53	Ambrosio	1982	ISR	CR and PSB methods

TABLE 2.3. Data sources for difference of $\bar{p}p$ and pp total cross-sections.

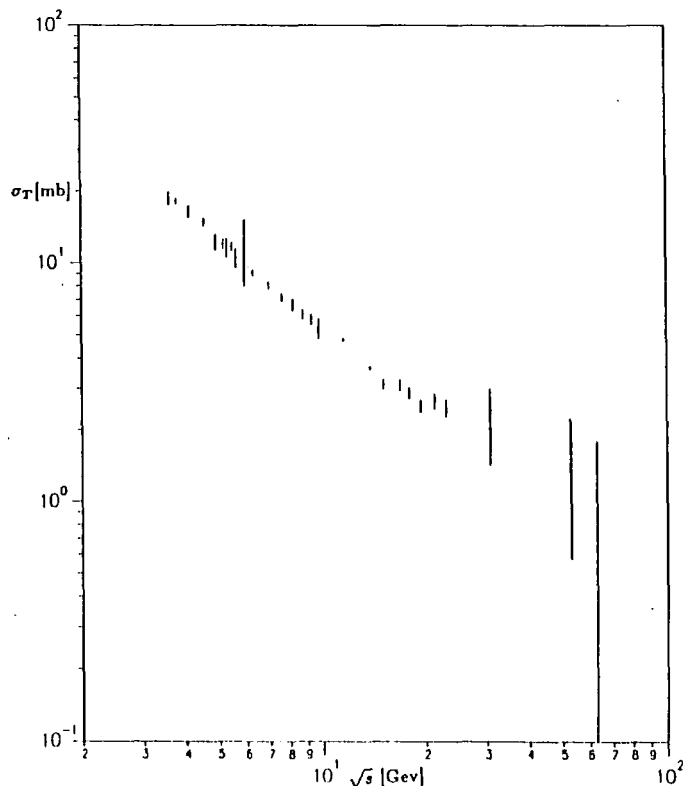


FIG. 2.3 Difference of $\bar{p}p$ and pp total cross-sections.

2.4. Re/Im, total elastic cross-section and forward slope parameter.

We do not use the data for ρ , σ_{el} and B in our fits but compare them to the predictions of the models. The data for $\sqrt{s} > 4$ GeV are shown in figures 2.4, 2.5 and 2.6.

$\rho(pp)$ increases uniformly from a value of -0.38 at $\sqrt{s} = 4$ GeV through to a small positive value at $\sqrt{s} = 63$ GeV, the highest energy at which it has so far been measured. The zero crossing point occurs at $\sqrt{s} \approx 22$ GeV. Below $\sqrt{s} = 3$ GeV $\rho(pp)$ increases sharply and has a value of $+0.25$ at $\sqrt{s} = 2$ GeV.

The data for $\rho(\bar{p}p)$ are a lot poorer and show a slow increase from a value of approximately zero for $\sqrt{s} = 15$ GeV to $+0.12$ at $\sqrt{s} = 63$ GeV. Over this energy range the data are not much different from $\rho(pp)$ and the difference seems to shrink with increasing energy. At lower energies the data are fairly well scattered and have relatively large errors but indicate a value around zero which is substantially different from $\rho(pp)$ at this energy. A value for $\rho(\bar{p}p)$ at $\sqrt{s} = 546$ GeV of 0.240 ± 0.024 has recently been measured (Bernard (1987)).

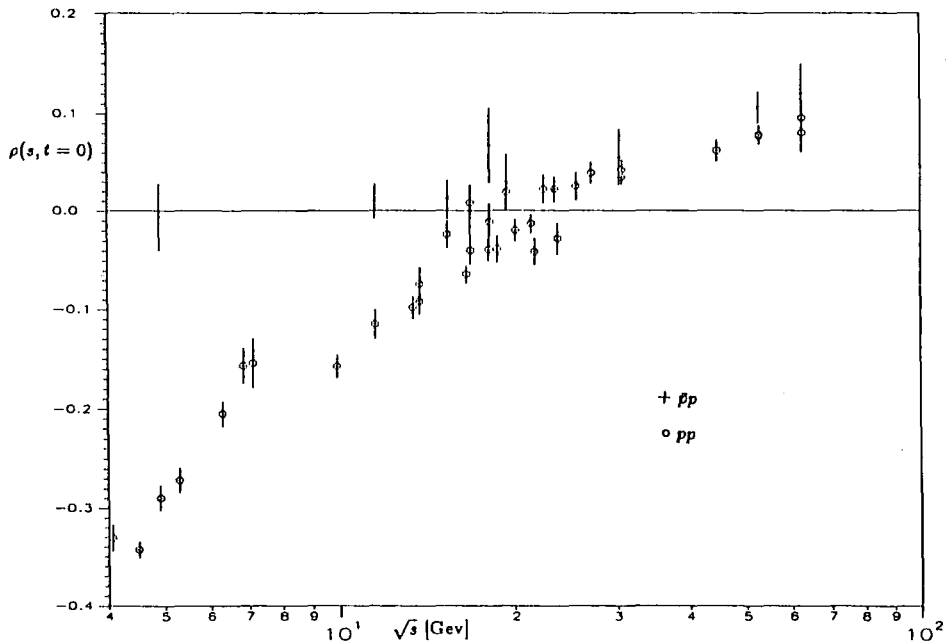


FIG. 2.4 Re/Im data for pp , and $\bar{p}p$.

The integrated elastic cross-section, σ_{el} , is shown in figure 2.5 and can be seen to decrease steeply in both pp and $\bar{p}p$, levelling off for $\sqrt{s} \geq 10$ GeV where $\sigma_{el}(pp)$ and

$\sigma_{el}(\bar{p}p)$ are indistinguishable and $\sigma_{el} \approx 7$ mb. Up to $\sqrt{s} = 63$ GeV it shows only a slight increase with energy, but the measurement of $\sigma_{el}(\bar{p}p)$ at the Collider shows that the elastic cross-section has almost doubled between the ISR and the Collider energies.

The ratio $R = \frac{\sigma_{el}}{\sigma_T}$ is approximately constant over ISR energies and similar for both pp and $\bar{p}p$. In fact at ISR energies we have

$$\frac{\sigma_{el}}{\sigma_T} = 0.170 \pm 0.004 \quad (2.1.11)$$

throughout the energy range for both pp and $\bar{p}p$, whilst at $\sqrt{s} = 546$ GeV

$$\frac{\sigma_{el}}{\sigma_T} = 0.215 \pm 0.005 \quad (2.1.12)$$

So the ratio $\frac{\sigma_{el}}{\sigma_T}$ increases quite markedly between the ISR and the Collider, a fact that has serious implications for any models in which asymptotia should already have been reached.

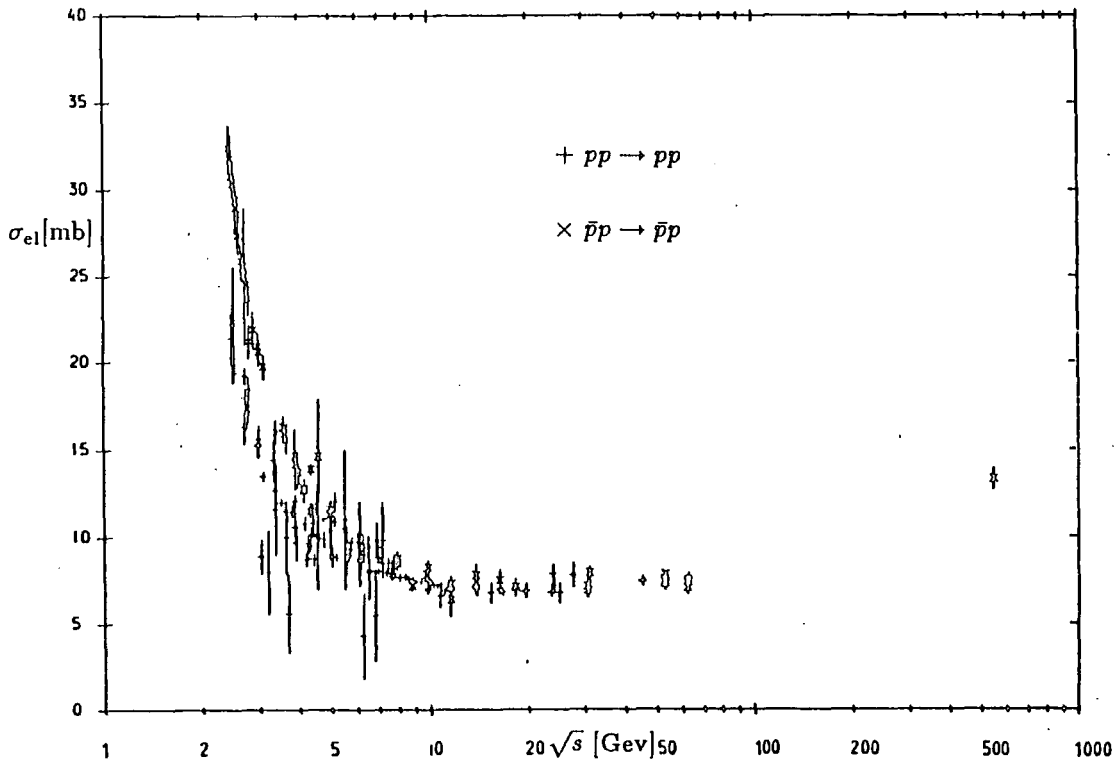


FIG. 2.5 Elastic Total Cross-section data for both pp and $\bar{p}p$.

Figure 2.6 shows a compilation of the data available on the forward slope of the pp and $\bar{p}p$ differential cross-sections defined by :

$$B \equiv \left. \frac{d}{dt} \log \frac{d\sigma}{dt} \right|_{t=0} \quad (2.1.13)$$

It can be seen that for $\sqrt{s} > 5$ GeV the $B_{\bar{p}p}$ increases approximately linearly with increasing $\log s$. At low energy $B_{\bar{p}p}$ is more or less constant with energy and larger than B_{pp} , but approaches B_{pp} as the energy increases. The value of $B_{\bar{p}p}$ measured at the Collider seems consistent with the linear increase in B_{pp} .

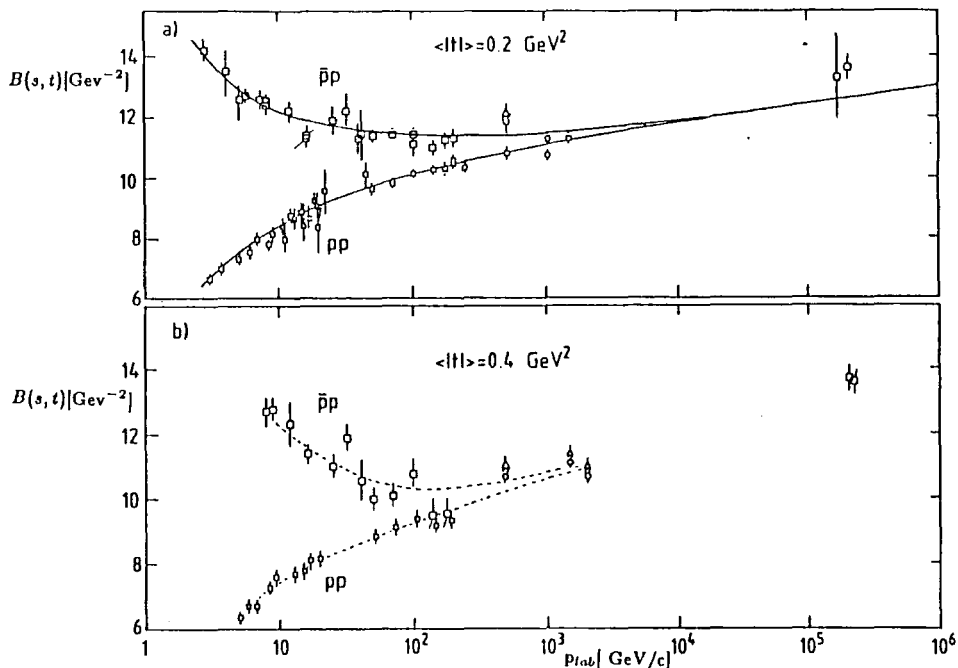


FIG. 2.6 Forward Elastic Slope parameter for pp and $\bar{p}p$.

2.5. Elastic differential Cross-section data.

The pp elastic differential cross-section as a function of t has been exceptionally well measured for a wide range of energies and $|t|$ values; up to the highest ISR energy of $\sqrt{s} = 63$ GeV and out as far as $|t| = 18$ GeV². Figure 2.7 shows a compilation of the pp scattering data for $\sqrt{s} \geq 3$ GeV and $|t| \leq 5$ GeV². At small $|t|$ the differential cross-section drops off exponentially with increasing $|t|$, $\frac{d\sigma}{dt} \sim e^{Bt}$, where $B = 7 \rightarrow 13$ GeV⁻² as the energy increases from $\sqrt{s} = 3 \rightarrow 63$ GeV (see figure 2.6) and produces the “shrinkage” of the forward peak seen clearly in figure 2.7. At ISR energies the small $|t|$ data show an abrupt change of exponential slope, $\Delta B \approx 1.6$ GeV², which occurs around $|t| = 0.2$ GeV². This effect, termed the Carrigan break, can be seen at lower energies for $p_{lab} = 50 \rightarrow 175$ GeV/c (Ayres 1977) and is also present in the $\bar{p}p$ data at $\sqrt{s} = 546$ GeV. For $|t| = 0.2 \rightarrow 0.85$ GeV² the data do not differ from a simple exponential t -dependence (Breakstone 1984).

At larger $|t|$, $\frac{d\sigma}{dt}(pp)$ again has a simple exponential $|t|$ dependence but with a much reduced slope, $B \approx 1.5 \text{ GeV}^{-2}$. As the energy increases the magnitude of $\frac{d\sigma}{dt}$ at large $|t|$ falls dramatically until $p_{lab} \approx 50 \text{ GeV}/c$ and thereafter shows a marked energy independence up to $\sqrt{s} = 63 \text{ GeV}$. At very low energies, $p_{lab} \leq 5 \text{ GeV}/c$, the small $|t|$ and large $|t|$ regions map smoothly together but as the energy increases a slight shoulder appears in the intermediate region around $|t| = 1.5 \text{ GeV}^2$. This gradually develops into a dip between $p_{lab} = 100$ and $150 \text{ GeV}/c$ which continues to get deeper until it reaches a minimum depth at $\sqrt{s} = 31 \text{ GeV}$ and then fills in slowly up to $\sqrt{s} = 63 \text{ GeV}$. The behaviour of the dip for $p_{lab} \geq 50 \text{ GeV}/c$ can be seen in figure 2.8 where the data are decaded for clarity. For $p_{lab} \geq 200 \text{ GeV}/c$ the dip position shows a small but quantifiable movement towards $t = 0$.

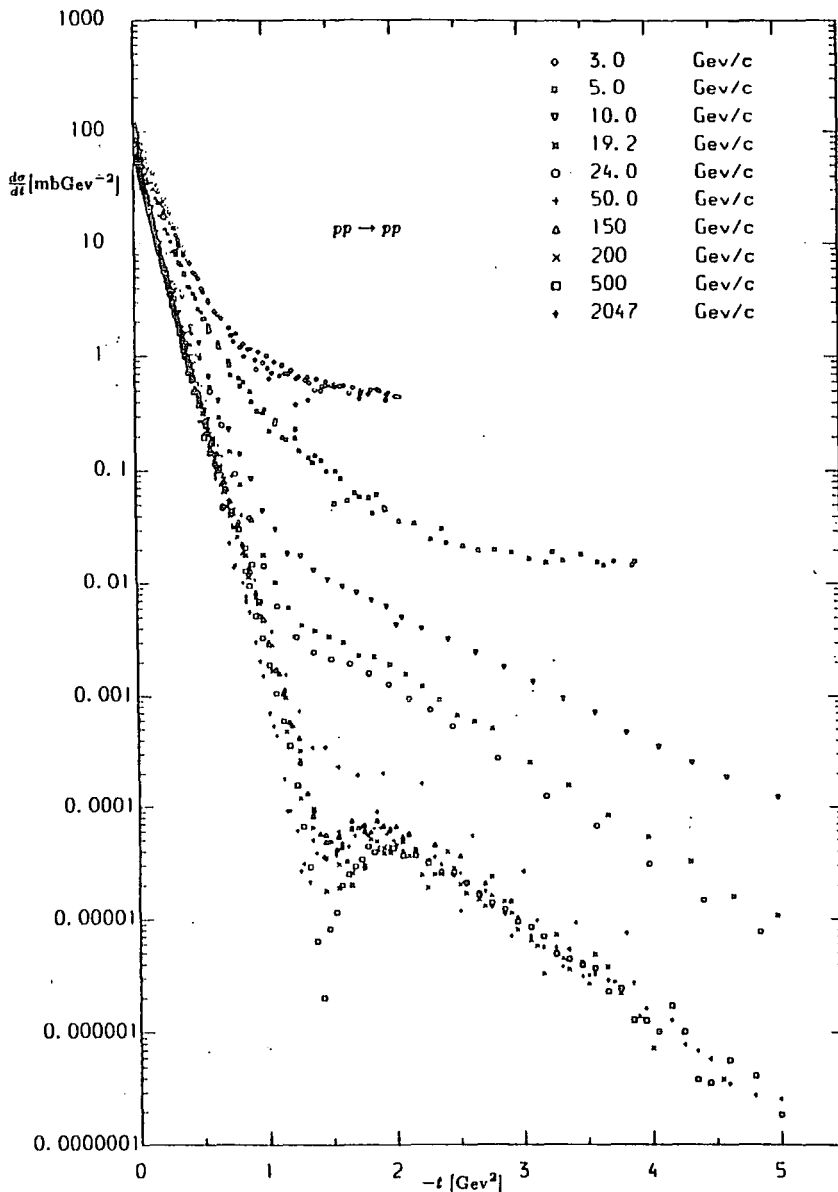


FIG. 2.7 Overlaid $\frac{d\sigma}{dt}(pp)$ data at selected incident momenta for $p_{lab} \geq 3 \text{ GeV}/c$.

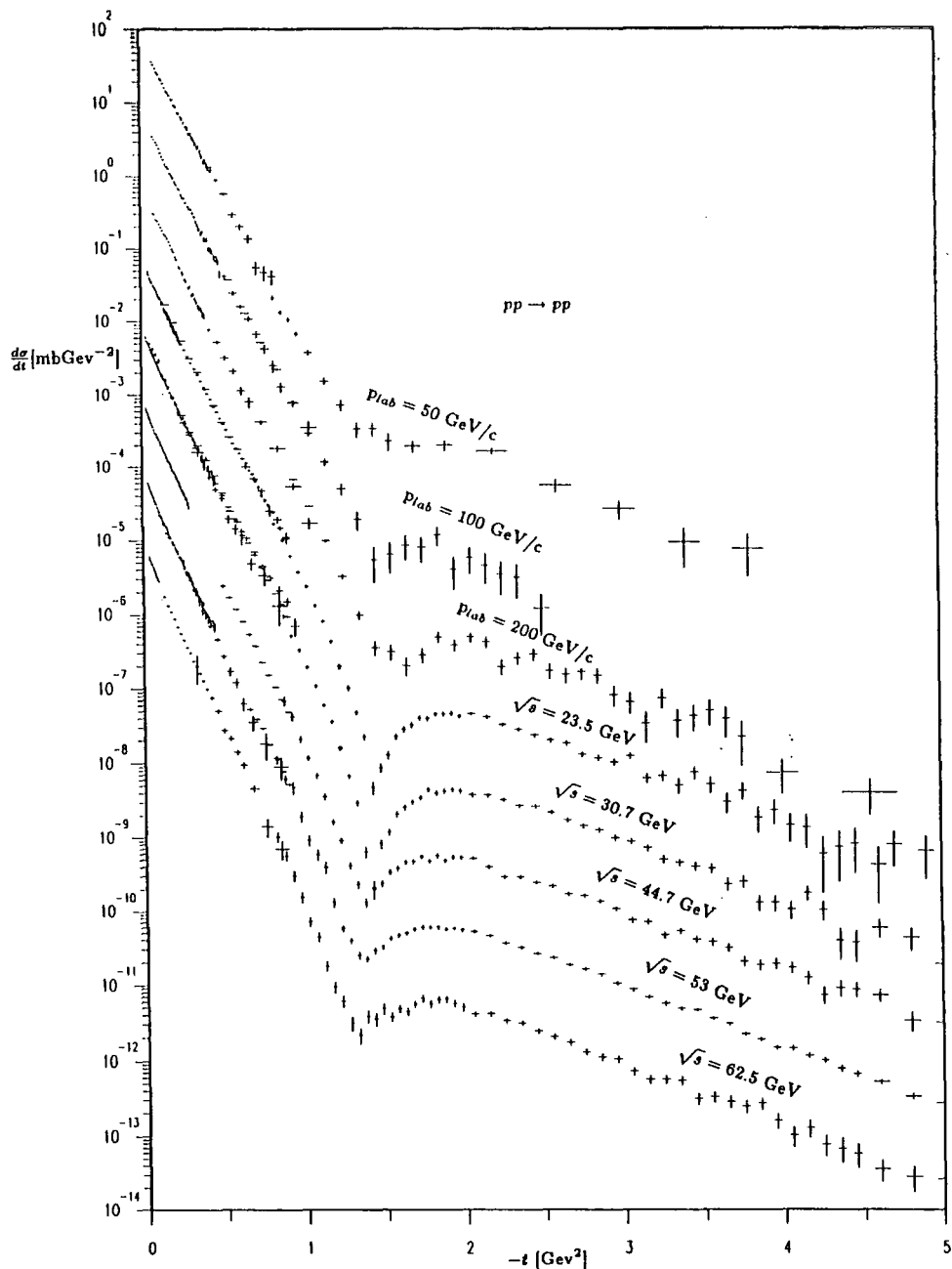


FIG. 2.8 Decaded $\frac{d\sigma}{dt}(pp)$ data at selected incident momenta for $p_{lab} \geq 50$ GeV/c.

The $\bar{p}p$ elastic differential cross-section is not as accurately or as comprehensively measured as in pp scattering, nevertheless very good data exist over a large energy range and there is data available at a much higher energy (from the $S\bar{p}pS$ Collider). Figure 2.9 shows a comparison of the pp and $\bar{p}p$ differential cross-sections for $p_{lab} \geq 5$ GeV/c up to $\sqrt{s} = 53$ GeV, which is the highest energy at which both have been measured. For small $|t|$ the $\bar{p}p$ differential cross-section shows a simple exponential t -dependence with a slight break in slope at $|t| = 0.2$ GeV² as in pp . At low energies $B_{\bar{p}p}$ is greater than B_{pp} so that there is a cross-over point at small $|t| \approx 0.19$ GeV² beyond which $\frac{d\sigma}{dt}(\bar{p}p) < \frac{d\sigma}{dt}(pp)$. This is most obvious in the $pp/\bar{p}p$ data of Ambats (1974) for $p_{lab} = 3 \rightarrow 6$ GeV/c. In the FNAL small $|t|$ data for $p_{lab} = 50 \rightarrow 175$ GeV/c (Ayres 1977) the difference $\Delta B = B_{\bar{p}p} - B_{pp}$ is much smaller but is still clearly present

in the data with $\Delta B \approx 2 \pm 0.4 \text{ GeV}^{-2}$. By ISR energies the pp and $\bar{p}p$ slopes are approximately equal though there is some evidence for a small systematic difference of $\Delta B \approx 0.3 \pm 0.2 \text{ GeV}^{-2}$ (Breakstone 1984).

The low energy $\frac{d\sigma}{dt}(\bar{p}p)$ data show more structure than in pp scattering. There is a dip at $p_{lab} = 5 \text{ GeV}/c$ for $|t| \approx 0.6 \text{ GeV}^2$ followed by a second maximum and then a shoulder at $|t| \approx 2 \text{ GeV}^2$. As the energy increases the first dip fills in. By $p_{lab} = 30 \text{ GeV}/c$ the position of the dip is marked only by a slight shoulder and by $p_{lab} = 50 \text{ GeV}/c$ it has disappeared entirely. The shoulder at $|t| = 2 \text{ GeV}^2$ on the other hand appears to deepen into a shallow dip at $p_{lab} = 10 \text{ GeV}/c$ and by $p_{lab} = 30 \text{ GeV}/c$ gives a distinct dip which is still present at $p_{lab} = 50$ and $100 \text{ GeV}/c$ (Asa'd 1984, Rubinstein 1984). Beyond $p_{lab} = 50 \text{ GeV}/c$ measurements of $\frac{d\sigma}{dt}(\bar{p}p)$ for $|t| > 1 \text{ GeV}^2$ are fairly sparse because of the problem of measuring a small cross-section with machines of relatively low luminosity. The pp and $\bar{p}p$ data at $p_{lab} = 100$ and $200 \text{ GeV}/c$ have been measured at FNAL but the data are not sufficiently accurate to show any statistically significant differences between pp and $\bar{p}p$ (Rubinstein 1984). At the ISR, for $\sqrt{s} = 53 \text{ GeV}$, fairly accurate measurements of $\frac{d\sigma}{dt}(\bar{p}p)$ have been made (Breakstone 1985, Erhan 1984) and can be compared with the very accurate $\frac{d\sigma}{dt}(pp)$ data. This comparison is shown in figure 2.10(a) and indicates that there is a shoulder in $\bar{p}p$ for $|t| = 1.4 \text{ GeV}^2$ rather than the dip seen in pp (In the figure the $\bar{p}p$ data do not include the 1.3 normalization factor required for pp in the same experiment). However, because of the low statistics of the $\bar{p}p$ data it is by no means a certain conclusion that the difference exists. The bin size in the $\bar{p}p$ data is twice as large as in the more accurate pp data which results in the entire dip region being spanned by just three points, only one of which differs significantly from the pp data. In the same experiment low statistics pp data were also taken which agreed reasonably well with the previous pp data. A more meaningful $pp/\bar{p}p$ comparison can be made between the two sets of data taken in the same experiment and this is shown in figure 2.10(b). Taking into account the uncertainties in the relative normalizations it is not clear that there is a $pp/\bar{p}p$ difference at this high energy.

A further indication that $\frac{d\sigma}{dt}(\bar{p}p)$ may be different from $\frac{d\sigma}{dt}(pp)$ at high energies comes from the $S\bar{p}pS$ Collider data at $\sqrt{s} = 546$ and 630 GeV^2 which is shown in figure 2.11 compared with the pp data at $\sqrt{s} = 53 \text{ GeV}^2$. At $\sqrt{s} = 546 \text{ GeV}$ there is a definite shoulder in $\bar{p}p$ starting at $|t| = 0.8 \text{ GeV}^2$ which is confirmed by the data at

the slightly higher energy, $\sqrt{s} = 630 \text{ GeV}^2$. The higher energy data go out to larger $|t|$ (since the angular acceptance of the detector was fixed) and seem to show the cross-section approaching the large $|t|$ ISR data though at $|t| = 2 \text{ GeV}^2$ there is still a factor of 2 or 3 between them.

We shall now concentrate on the high energy data for $p_{lab} \geq 200 \text{ GeV}/c$ from FNAL, ISR, SPS and $S\bar{p}pS$ Collider and calculate the effective trajectory over this energy range.

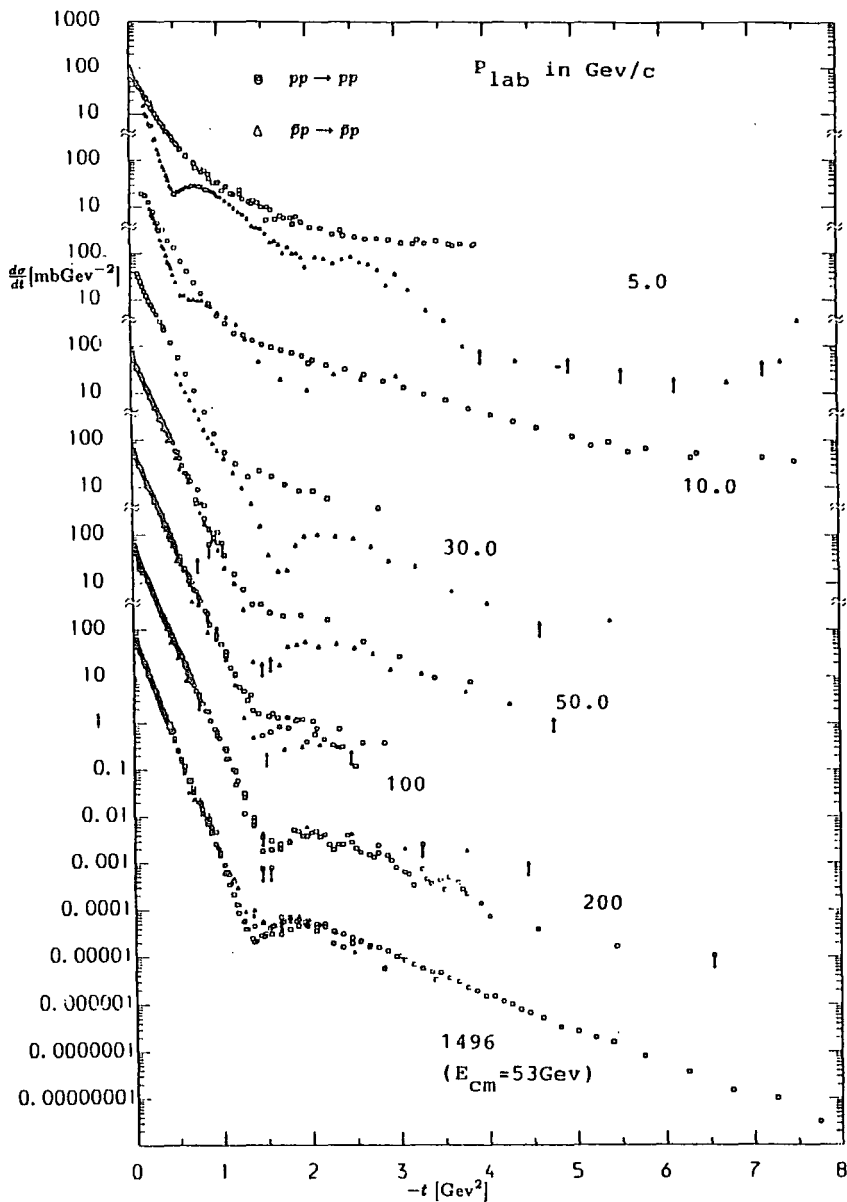


FIG. 2.9 Comparison of pp and $\bar{p}p$ differential cross-sections at selected incident momenta for $p_{lab} \geq 5 \text{ GeV}/c$.

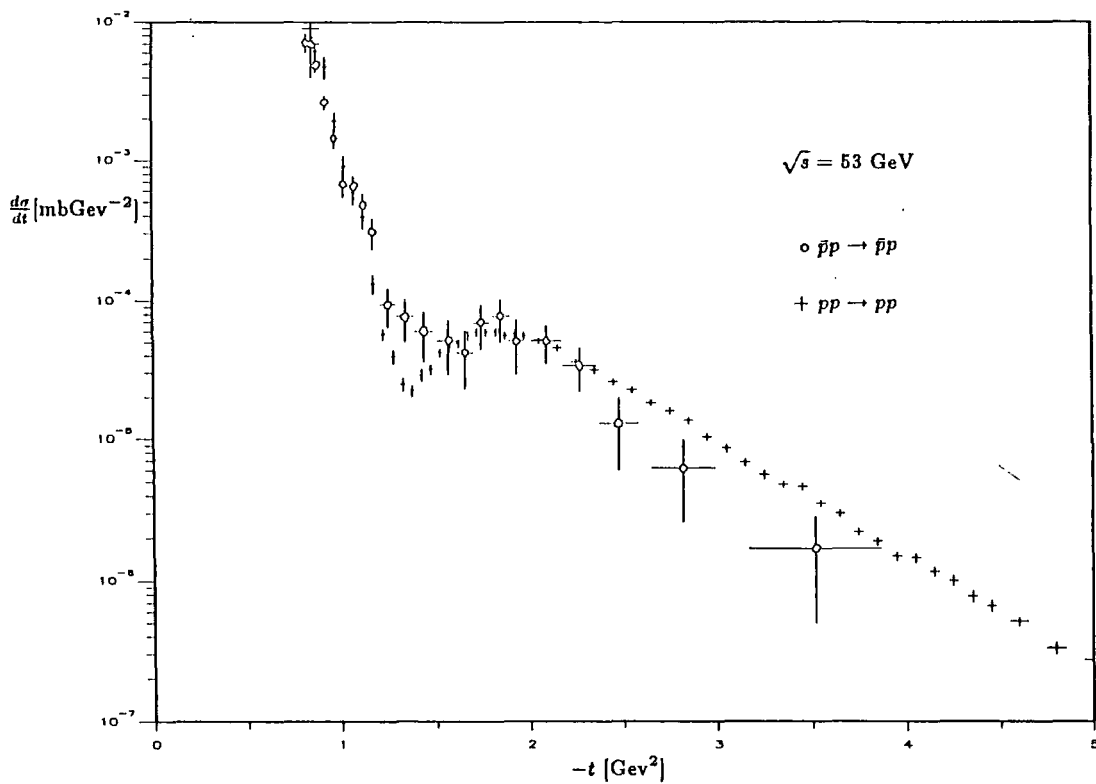


FIG. 2.10(a) Comparison of $\frac{d\sigma}{dt}(\bar{p}p)$ with $\frac{d\sigma}{dt}(pp)$ at $\sqrt{s} = 53 \text{ GeV}$ (Breakstone (1985), Nagy (1979)).

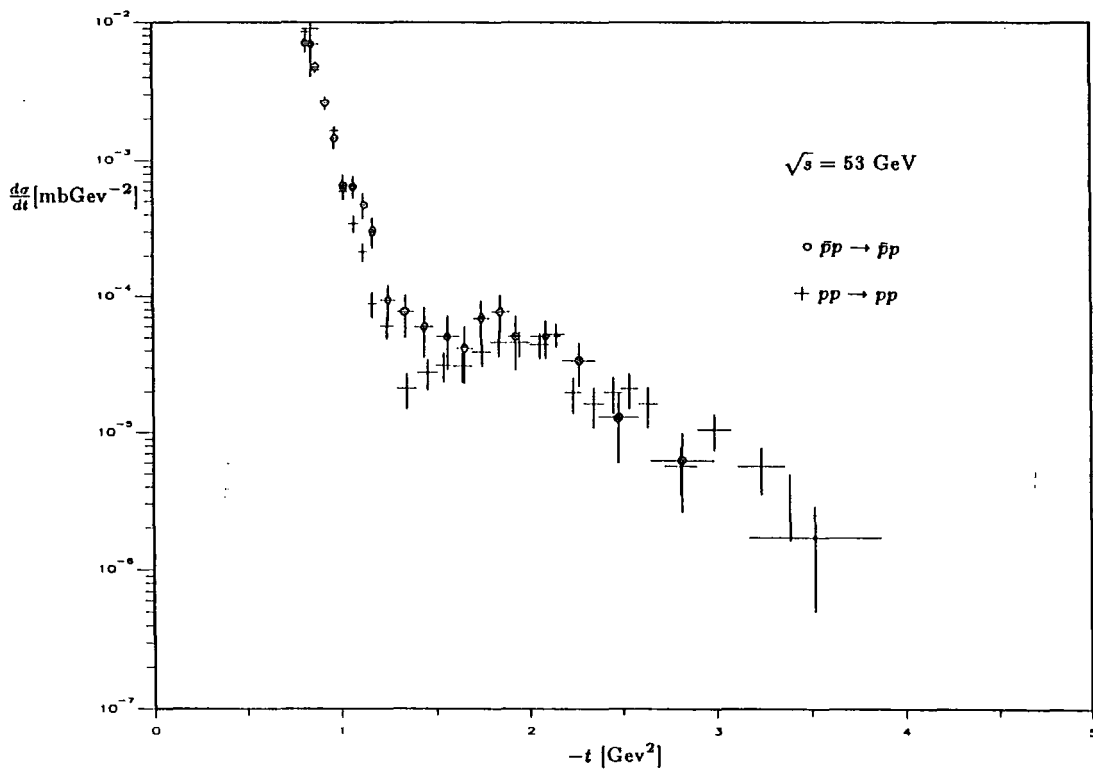


FIG. 2.10(b) Comparison of $\frac{d\sigma}{dt}(\bar{p}p)$ and $\frac{d\sigma}{dt}(pp)$ at $\sqrt{s} = 53 \text{ GeV}$ (Breakstone 1985).

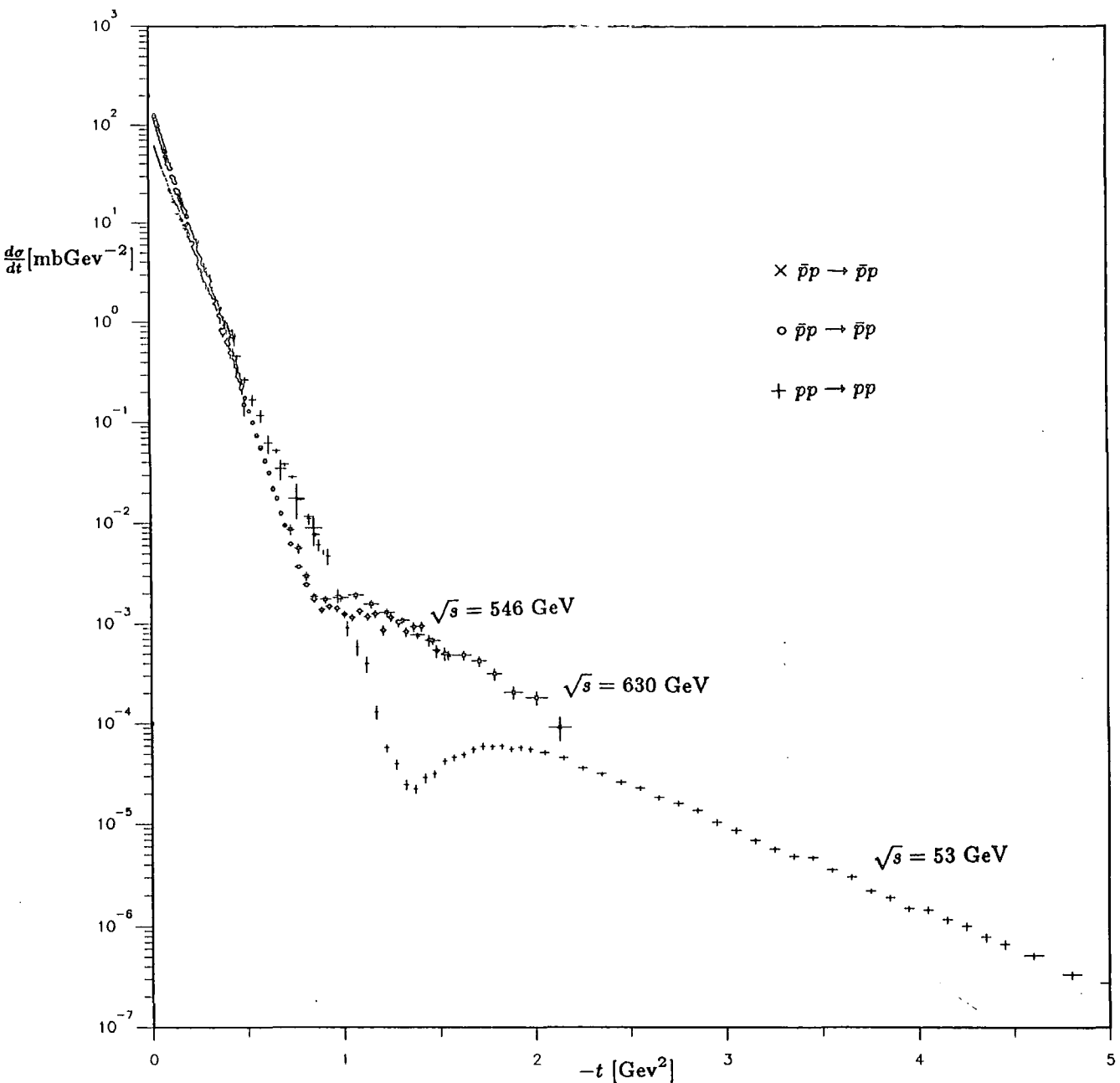


FIG. 2.11 Comparison of $\frac{d\sigma}{dt}(\bar{p}p)$ data at $\sqrt{s} = 546$ GeV (Bozzo (1984)) and at $\sqrt{s} = 630$ GeV (Bernard (1986)) with $\frac{d\sigma}{dt}(pp)$ at $\sqrt{s} = 53$ GeV (Nagy (1979)).

2.6. The Effective Trajectory.

The shrinkage observed in figure 2.7 at small $|t|$ is a characteristic feature of Regge poles and suggests that a useful quantity to extract from the data would be the effective trajectory, $\alpha_{\text{eff}}(t)$, defined by :

$$\frac{d\sigma}{dt}(s, t) \equiv F(t) \left(\frac{s}{s_0} \right)^{2\alpha_{\text{eff}}(t)-2} \quad (2.6.1)$$

If a single Regge pole, R , dominates the amplitude then $\alpha_{\text{eff}}(t) = \alpha_R(t)$. From (2.6.1) we have

$$\log \frac{d\sigma}{dt} = (2\alpha_{\text{eff}}(t) - 2) \log s + \log \frac{F(t)}{(2\alpha_{\text{eff}}(t) - 2)s_0} \quad (2.6.2)$$

Therefore the slope of $\log \frac{d\sigma}{dt}$ vs $\log s$ for a given process at fixed t gives $\alpha_{\text{eff}}(t)$. The computer program we use to calculate α_{eff} is taken from Harrison, Irving and Martin (1973). Each data set consists of a number of points at different t -values at a given energy and is fitted with a parametrization of the form (2.6.3) using the method of least squares.

$$\frac{d\sigma}{dt} = Ae^{Bt+Ct^2+\dots} \quad (2.6.3)$$

This allows a value of $\frac{d\sigma}{dt}$, with the appropriate errors, to be calculated from each data set at any given value of t . The effective trajectory can then be calculated by a least squares fit to the interpolated data using (2.6.2) and the result at different t -values fitted to a linear form giving the intercept and slope of the trajectory. Extrapolation of (2.6.3) to values outside the t -range of the data set is only valid in the immediate neighbourhood of the data and errors in the extrapolation will increase rapidly outside this range. Extrapolated values from either side of the Carrigan break or from either side of the dip at $|t| = 1.4 \text{ GeV}^2$ would be meaningless. For this reason we broke the determination of $\alpha_{\text{eff}}(t)$ up into values within overlapping t -regions and only included data which extended into these regions in the calculation.

For $p_{\text{lab}} \geq 200 \text{ GeV}/c$ there is a large amount of pp and $\bar{p}p$ data available. This is summarized in table 2.4 below. We only use the data outside the Coulomb/nuclear interference region $|t| > 0.01 \text{ GeV}^2$.

Author	Type	\sqrt{s}	$ t _{\min}$	$ t _{\max}$	Scale error	Accelerator	Year
Fidecaro	pp	19.4	0.613	3.9		SPS	1981
Rubinstein	pp	19.4	0.95	10.3	15%	FNAL	1984
	$\bar{p}p$		0.95	4.45	35%		
Faessler	pp	19.5	5.0	11.9	15%	FNAL	1980
		27.4	5.5	14.2			
Amos	pp	23.5	0.00037	0.0102	1%	ISR	1985
		30.6	0.00050	0.0176			
		52.8	0.00107	0.0555			
		62.3	0.00543	0.0512			
	$\bar{p}p$	30.4	0.00067	0.0156	2.5%	ISR	1985
		52.8	0.00097	0.0387			
		62.3	0.00632	0.0382			
Baksay	pp	44.9	0.022	0.052	1.5%	ISR	1978
		52.8	0.031	0.072			
		62.5	0.037	0.099			
Barbiellini	pp	21.5	0.042	0.238	Unnormalized	ISR	1972
		30.8	0.016	0.456			
		44.9	0.054	0.289			
		53.0	0.076	0.448			
Albrow	pp	23.4	0.15	1.05	15%	ISR	1976
		26.9	0.15	0.55			
		30.6	0.25	0.95			
		32.4	0.20	0.35			
		35.2	0.20	0.75			
		38.3	0.20	0.70			

TABLE 2.4 Differential cross-section data for pp and $\bar{p}p$ for $p_{lab} \geq 200$ GeV/c and $|t| \geq 0.01$ GeV/c.

Author	Type	\sqrt{s}	$ t _{\min}$	$ t _{\max}$	Scale error	Accelerator	Year
Breakstone	pp	31	0.05	0.85	10%	ISR	1984
		53	0.11	0.85			
		62	0.13	0.85			
	$\bar{p}p$	31	0.05	0.85	10%	ISR	1984
		53	0.11	0.85			
		62	0.13	0.85			
Böhm	pp	23.5	0.15	1.40	Unnormalized	ISR	1974
		30.7	0.26	2.45			
		44.9	0.50	4.60			
		53.0	0.66	5.30			
Kwak	pp	23.5	0.03	3.5	5%	ISR	1975
		62.0	0.21	3.5			
Nagy	pp	23.5	0.825	5.75	5%	ISR	1979
		30.5	0.875	5.75			
		44.6	0.875	7.25			
		52.8	0.825	9.75			
		62.1	0.825	6.25			
Breakstone	pp	53	0.623	3.390	20%	ISR	1985
	$\bar{p}p$	53	0.523	3.520	30%		
Erhan	pp	53	0.65	2.05	10%	ISR	1985
	$\bar{p}p$	53	0.65	1.95			
Bozzo	$\bar{p}p$	546	0.0325	0.3175	5%	$S\bar{p}pS$	1984
			0.215	0.495	8%		
			0.46	1.53	10%		
Bernard	$\bar{p}p$	630	0.7	2.2	15%	$S\bar{p}pS$	1986

TABLE 2.4 Continued from overleaf.

The above table does not represent a complete list of the available data in this energy range but is fairly comprehensive. For a more complete list see Carter, Collins and Whalley (1985). Accurate normalization of the data is only possible at small $|t|$. A review of the $\frac{d\sigma}{dt}(pp)$ data at the ISR was given in Amaldi (1978) and Landolt-Bornstein (1980) where a consistent set of data was obtained by requiring contiguous data sets join together smoothly and adjusting the normalization factors within the scale errors of the data. For the most part this involves scaling factors which differ from unity by $\leq 1\%$ and are not significant. The only sizeable deviation from the normalized data was at $\sqrt{s} = 23.5$ GeV where a 7.5% increase in normalization was required for the Nagy (1979) data set which has a scale error of 5%. In the Amaldi compilation the ISR data were normalized to the optical points, which were determined using equation (2.1.5) from the average of the total cross-section measurements at each energy and from the measured values of ρ . A value for the forward slope, $B(s)$, was obtained by interpolation from the experimental data and was used to describe the differential cross-section over the Coulomb interference region $|t| < 0.01$ GeV². Using this procedure a normalization factor was calculated for the unnormalized data sets of Barbiellini (1972) and Böhm (1974). For the most part we use the relative normalizations of Amaldi in the following fits. However, for $\sqrt{s} = 23.5$ GeV, the total cross-sections found at the ISR are consistently lower than the values obtained at similar energies at FNAL (Carroll et al 1979) by about 0.7 mb. For this reason we determine the optical points from a fit to the total cross-section for $\sqrt{s} \geq 10$ GeV (see §4.2). This produces a 3% increase in the normalization factor at $\sqrt{s} = 23.5$ GeV and an insignificant difference at other energies ($< 1\%$). This gives an overall 11% normalization correction to the Nagy data at $\sqrt{s} = 23.5$ GeV. The latest measurement of σ_T at the ISR for $\sqrt{s} = 23.5$ GeV from Amos (1985) is in agreement with the FNAL data. The earlier data from the same experiment presented in Kwak (1974), which extends down to small $|t|$ at $\sqrt{s} = 23.5$ GeV, requires a 30% correction to bring it in line with the current normalization. The pp and $\bar{p}p$ data from Breakstone (1984) are consistent with the current normalization. Figure 2.12 shows the resulting data set at ISR and Collider energies for $|t| \leq 1$ GeV².

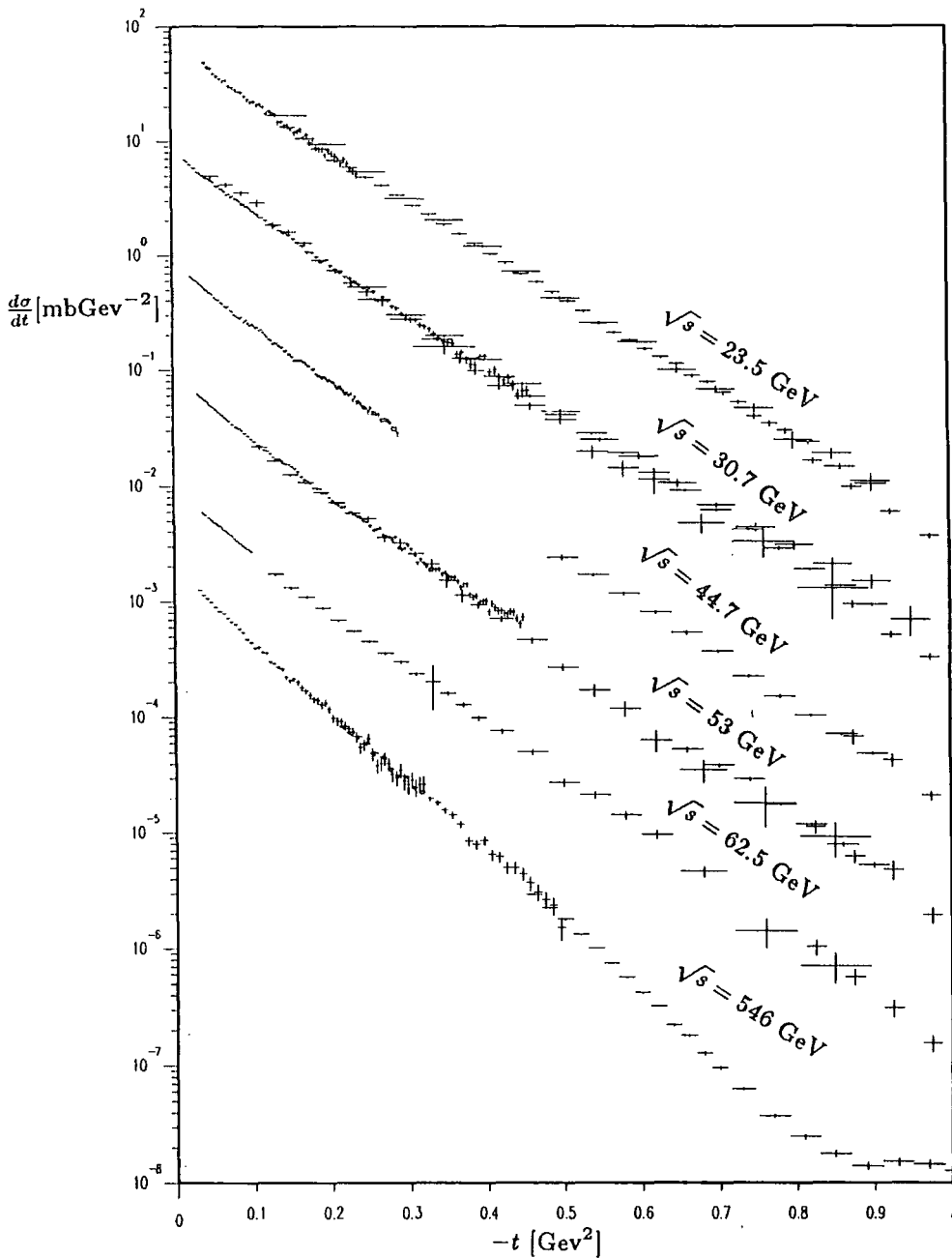


FIG. 2.12 Small $|t|$ $\frac{d\sigma}{dt}$ data for $\sqrt{s} = 23 \rightarrow 546$ GeV.

In the forward direction, we determined $\alpha_{\text{eff}}(t)$ separately in the three regions : $0 \leq |t| \leq 0.2$, $0.2 \leq |t| \leq 0.6$ and $0.5 \leq |t| \leq 1.3$ GeV^2 , using in each range the data from table 2.4 . The results were not sensitive to the degree of the polynomial in t used in the exponential in (2.6.3). Figure 2.13 shows the interpolated values of $\frac{d\sigma}{dt}$ for the various data sets plotted against $\log \sqrt{s}$ at selected values of t (using a polynomial fit of degree 2). Equation (2.6.2) implies these points should lie on straight lines and within fairly large errors the data are consistent with this. The straight lines shown in the figure correspond to the calculated values of α_{eff} . In the region beyond $|t| = 0.8$ GeV^2 the Collider data are extrapolated and so take no account of the shoulder that appears in the data. The long lever arm the $S\bar{p}pS$ Collider data provide is clearly very important in the calculation of α_{eff} , though it is consistent with the lower energy data. The values

of $\alpha_{\text{eff}}(t)$ obtained at different values of t are plotted in figure 2.14 . The determination of α_{eff} with no Collider data gives results showing the same general trend but followed less accurately. The dotted lines correspond to $\alpha_P(0) = 1.095$, $\alpha'_P = 0.2$ (normal) and 0.3 GeV^{-2} (bold).

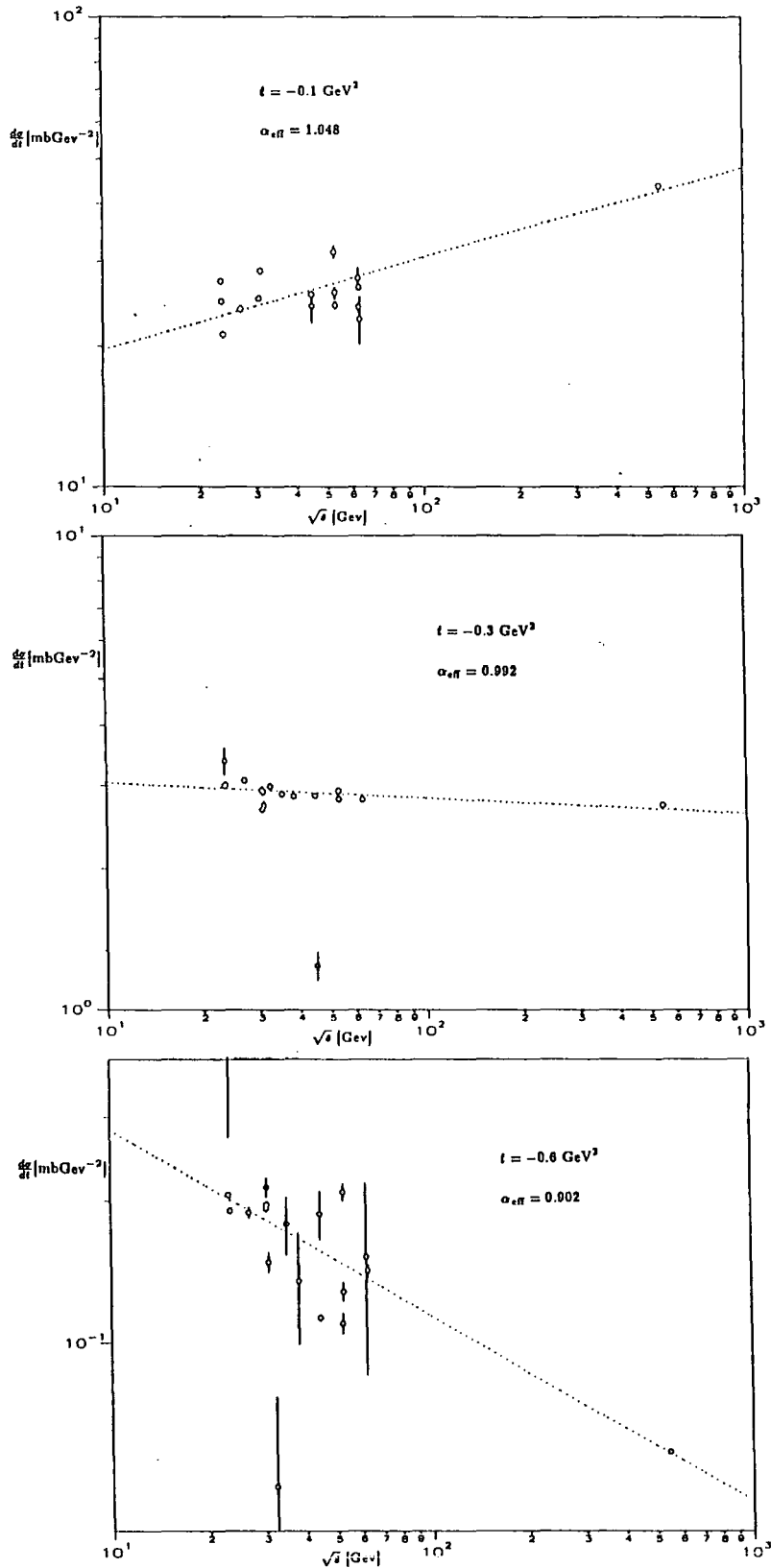


FIG. 2.13 Interpolated values of $\frac{d\sigma}{dt}$ for data from table 2.4 at $|t| = 0.1, 0.3$ and 0.6 GeV^2 .

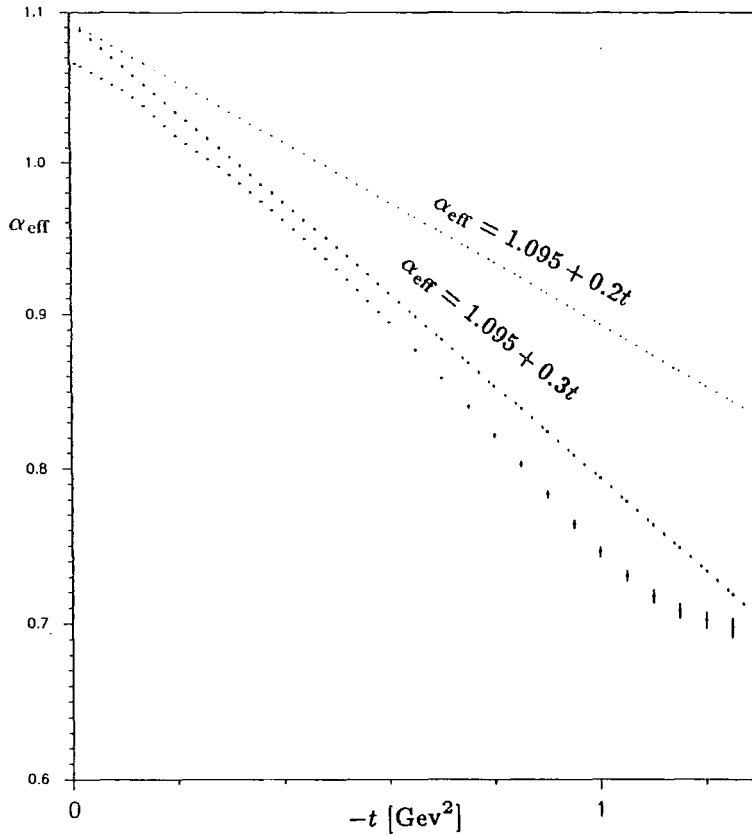


FIG. 2.14 α_{eff} obtained by fitting small $|t|$ data.

It can be seen that the data indicate a linear effective trajectory out to $|t| \approx 1.3 \text{ GeV}^2$ with slope approximately $\alpha'_p = 0.3 \text{ GeV}^2$. The effective trajectories found in the three regions were :

$$\begin{aligned}
 \alpha_{\text{eff}}(t) &= (1.071 \pm 0.001) + (0.25 \pm 0.01)t & \text{for } 0.0 \leq |t| \leq 0.2 \text{ GeV}^2 \\
 \alpha_{\text{eff}}(t) &= (1.084 \pm 0.002) + (0.309 \pm 0.004)t & \text{for } 0.2 \leq |t| \leq 0.6 \text{ GeV}^2 \\
 \alpha_{\text{eff}}(t) &= (1.11 \pm 0.01) + (0.35 \pm 0.02)t & \text{for } 0.5 \leq |t| \leq 1.3 \text{ GeV}^2
 \end{aligned} \tag{2.6.4}$$

Combined, these give

$$\alpha_{\text{eff}}(t) = (1.083 \pm 0.002) + (0.319 \pm 0.004)t \tag{2.6.5}$$

The trajectory obtained combining all the data sets at each energy into one data set and using their original normalizations was

$$\alpha_{\text{eff}}(t) = (1.076 \pm 0.001) + (0.297 \pm 0.002)t \quad \text{for } 0.0 \leq |t| \leq 1.3 \text{ GeV}^2 \tag{2.6.6}$$

We also repeated the calculation using only the data for $\sqrt{s} \geq 53 \text{ GeV}$ and obtained the trajectories

$$\begin{aligned}
 \alpha_{\text{eff}}(t) &= (1.074 \pm 0.002) + (0.21 \pm 0.01)t & \text{for } 0.0 \leq |t| \leq 0.2 \text{ GeV}^2 \\
 \alpha_{\text{eff}}(t) &= (1.095 \pm 0.002) + (0.365 \pm 0.004)t & \text{for } 0.2 \leq |t| \leq 0.6 \text{ GeV}^2
 \end{aligned} \tag{2.6.7}$$

The agreement of these values provides a check on the consistency of the data and indicates that the same mechanism is responsible for the shrinkage through the ISR and from the ISR to the Collider. The effective trajectory crosses $\alpha_{\text{eff}} = 1$ for $|t| = 0.27 \text{ GeV}^2$ at which point the differential cross-section is energy independent.

The calculation of α_{eff} for large $|t|$ beyond the dip region is hampered by the lack of large $|t|$ data at the Collider energy and by the larger statistical errors and normalization uncertainties in the data. The effect we are trying to measure is also smaller than in the forward diffraction peak.

The main source of large $|t|$ data is from Nagy (1979) taken at the ISR for energies $\sqrt{s} = 23.5 \rightarrow 62.5 \text{ GeV}^2$. There also exists large $|t|$ data from FNAL at $p_{\text{lab}} = 200$ and $400 \text{ GeV}/c$ (Faissler (1980) and Rubinstein (1984)) and from the SPS at $p_{\text{lab}} = 200 \text{ GeV}/c$ (Fidecaro (1981)). Using this lower energy data is complicated by the uncertainty in the point at which the high energy behaviour sets in. Figure 2.15 shows the energy dependence at fixed $|t| \approx 2 \text{ GeV}^2$ of $\frac{d\sigma}{dt}$ against $\log \sqrt{s}$ extending down to low energies. The result of fitting the high energy part of this with a straight line depends on where the low energy cut off is applied. We use the data for $p_{\text{lab}} \geq 200 \text{ GeV}/c$ for $|t| \geq 2 \text{ GeV}^2$.

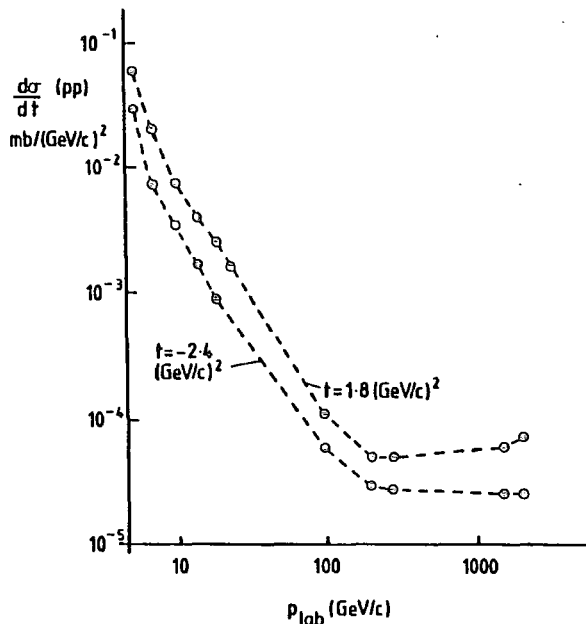


FIG. 2.15 Interpolated values of $\frac{d\sigma}{dt}$ for data extending down to low energies at $|t| = 1.8$ and 2.4 GeV^2 (figure taken from Collins and Kearney (1984)).

Fitting this data with the form (2.6.3) we find that a double exponential only gives a significant improvement in the χ^2 of the fit for the data where a relatively large t -range is spanned (Nagy ($\sqrt{s} = 53$ GeV) and Faissler data). The Fidecaro (1980) data do not extend out to very large $|t|$ and the Rubinstein (1984) data are relatively inaccurate compared with the ISR data. The calculated values of $\frac{d\sigma}{dt}$ at large $|t|$ for these data sets do not agree very well with the ISR data and are omitted. The behaviour of the $\sqrt{s} = 31$ GeV² ISR data for $|t| \geq 4$ GeV² also seems inconsistent with the rest of the ISR data and is omitted.

The resulting values for α_{eff} are shown in fig.2.16 . The trajectory calculated at large $|t|$ was

$$\alpha_{\text{eff}}(t) = (1.17 \pm 0.03) + (0.075 \pm 0.01)t \quad \text{for } 2.0 \leq |t| \leq 6.0 \text{ GeV}^2 \quad (2.6.8)$$

The energy independent point where $\alpha_{\text{eff}} = 1$ occurs for $|t| \approx 2.2$ GeV².

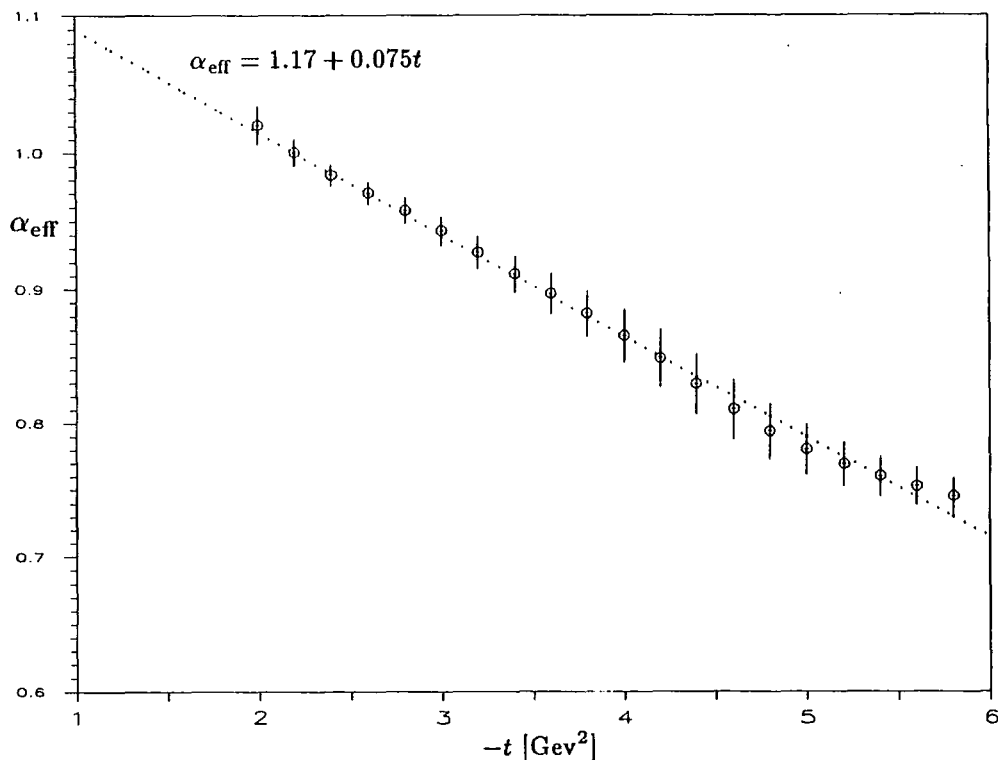


FIG. 2.16 α_{eff} obtained by fitting large $|t|$ data.

A similar study of just the ISR data given in Nagy (1979) found no indication of energy dependence in the large $|t|$ data. The discrepancy appears to be caused by the use of more recent FNAL data (Faissler 1980); the normalization correction applied to the $\sqrt{s} = 23.5$ GeV ISR data; the omission of the data at $\sqrt{s} = 31$ GeV (causes quite a significant change); the use of a quadratic form in the exponential and a slightly different t -range used in the fits. The calculated value of $\alpha_{\text{eff}}(t)$ is our "best estimate" of the energy dependence but the ISR data alone are compatible with no energy dependence. Figure 2.17 is a comparison of the data at $\sqrt{s} = 23$ and 53 GeV and the FNAL data at $p_{\text{lab}} = 200$ and 400 GeV/c and shows the energy dependence. The α_{eff} 's calculated should perhaps be conservatively taken as indicating an upper limit on the energy dependence and thus on α' .

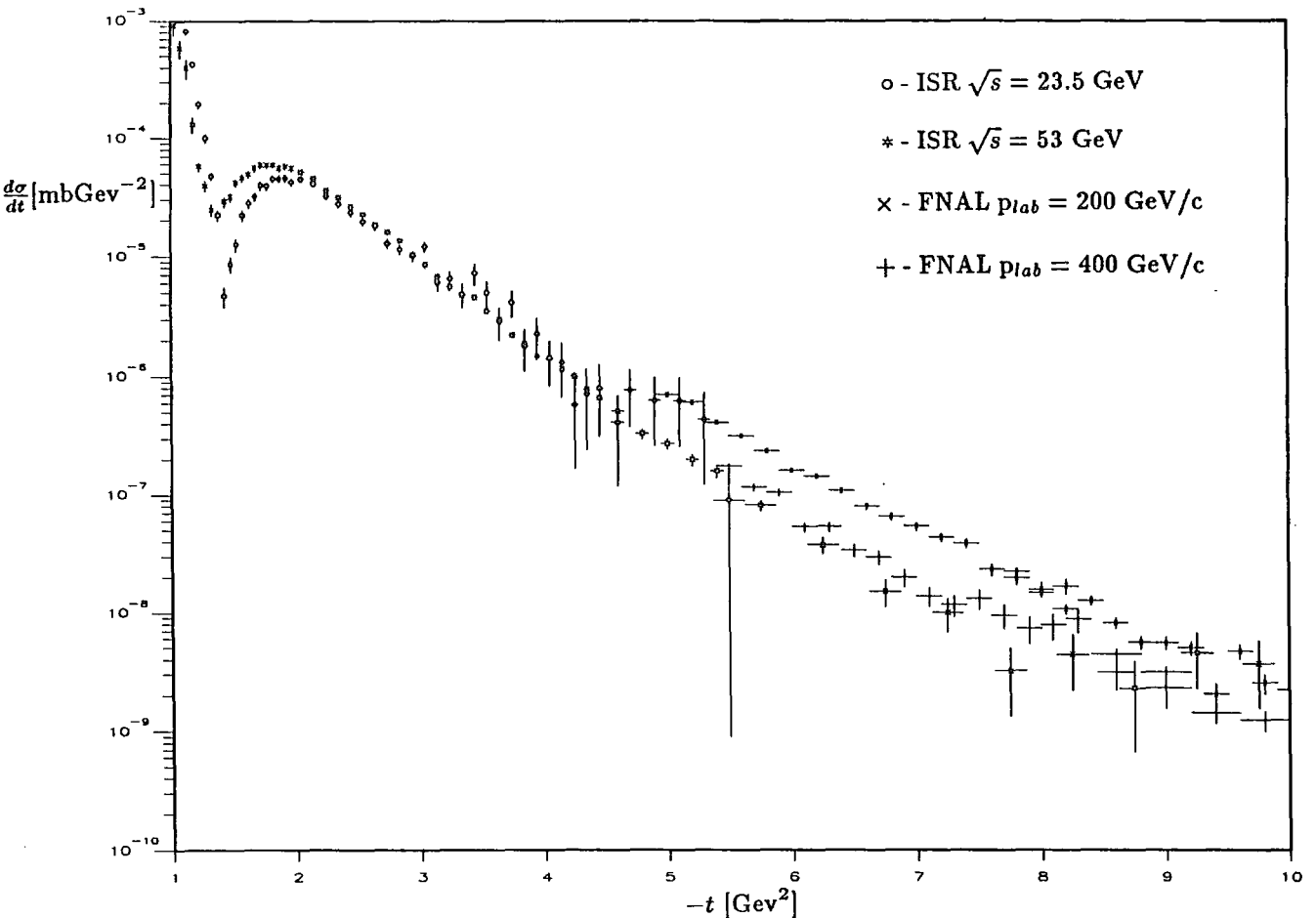


FIG. 2.17 Comparison of large $|t|$ data at $\sqrt{s} = 23.5$ and 53 GeV and $p_{\text{lab}} = 200$ and 400 GeV/c.

Theoretical Discussion

3.1. Unitarity, Analyticity and Crossing.

The S-matrix elements, S_{if} , represent the transition probability amplitude from an initial state, i , to a final state, f . The probability of transition is given by

$$\begin{aligned} w_{if} &= |S_{if}|^2 = \langle f|S|i \rangle^* \langle f|S|i \rangle \\ &= \langle i|S^\dagger|f \rangle \langle f|S|i \rangle \end{aligned} \quad (3.1.1)$$

Unitarity is the requirement that the sum of the probabilities over all final states must be unity :

$$\sum_f w_{if} = \langle i|S^\dagger S|i \rangle = 1 \quad (3.1.2)$$

and so the S-matrix is unitary : $S^\dagger S = S S^\dagger = 1$.

The two-particle scattering amplitude, A , is obtained from S through

$$\langle p'_1, p'_2 | S | p_1, p_2 \rangle = \langle p'_1, p'_2 | p_1, p_2 \rangle + i(2\pi)^4 \delta^4(p_1 + p_2 - p'_1 - p'_2) \langle p'_1, p'_2 | A | p_1, p_2 \rangle \quad (3.1.3)$$

For spinless particles Lorentz invariance implies that the scattering amplitude depends on the external particle momenta only through their invariant scalar products which for $2 \rightarrow 2$ can be written in terms of the Mandelstam invariants s , t and u where $s + t + u = 4m^2$ for equal mass scattering.

$$A(s, t, u) = \langle p'_1, p'_2 | A | p_1, p_2 \rangle \quad (3.1.4)$$

One of the basic postulates of S-matrix theory is that the scattering amplitudes are analytic functions of the Lorentz invariant quantities and the physical amplitudes are obtained as real-boundary values of these functions. The only singularities of the amplitude on the physical sheet are the elementary particle poles and the threshold branch cuts demanded by unitarity.

The unitarity equation (3.1.2) gives non-linear equations for the scattering amplitude, $A(s, t)$. Below the inelastic threshold in the s -channel this yields

$$A - A^\dagger = \frac{i\sqrt{\frac{s}{4} - m^2}}{(4\pi)^2 \sqrt{s}} \int d\Omega A A^\dagger \quad (3.1.5)$$

At each new threshold a new term contributes to the r.h.s of (3.1.5) giving rise to the threshold singularities in $A - A^\dagger$ (the discontinuities across which are given by Cutkosky's formula). For energies outside of the physical region, below the elastic threshold, it can be shown that

$$A - A^\dagger = 0 \quad (3.1.6)$$

The physical amplitudes are obtained as real boundary values from above the real axis. This prescription is equivalent to the $+i\epsilon$ prescription in perturbation theory and stems from causality. Thus

$$\text{Physical} \quad A(s, \dots) = \lim_{\epsilon \rightarrow 0} A(s + i\epsilon, \dots) \quad (3.1.7)$$

Using the analyticity postulate we can expand the scattering amplitude as a Laurent series in s so that

$$A_{fi} = \lim_{s \rightarrow \text{real}^+} \sum_r a_r s^r \quad (3.1.8)$$

and for the reverse transition

$$A_{if} = \lim_{s \rightarrow \text{real}^+} \sum_r b_r s^r \quad (3.1.9)$$

Then we have

$$A_{fi}^\dagger = (A_{if})^* = \lim_{s \rightarrow \text{real}^-} \sum_r b_r^* s^r \quad (3.1.10)$$

so that A and A^\dagger are opposite boundary values of analytic functions. The condition (3.1.6) implies $a_r = b_r^*$ and thus that A and A^\dagger are opposite boundary values of the same analytic function. Equation (3.1.5) therefore represents the discontinuity across the threshold branch cut. If the symmetry condition $A_{fi} = A_{if}$ holds, which follows just from Lorentz invariance for the elastic scattering of spinless particles and from PT invariance for inelastic $2 \rightarrow 2$ amplitudes, then (3.1.6) implies that $a_r = a_r^*$ and therefore $A(s, t) = A^*(s^*, t)$ so that $A(s, t)$ is a real analytic function and the discontinuity across the branch cut gives the imaginary part of the scattering amplitude.

Analytic continuation allows amplitudes involving antiparticles to be related to those for the corresponding particles by "crossing". This follows provided an analytic continuation exists which connects the physical regions of the two processes. This can be shown to exist in quantum field theory and in S-matrix theory (with certain other analyticity assumptions).

Using Cauchy's integral formula (A.3) a dispersion relation in s can be written for the scattering amplitude (provided $\lim_{s \rightarrow \infty} |A(s, t)| \rightarrow |s|^{-\epsilon}$ where $\epsilon > 0$) giving

$$A(s, t) = \frac{g_s(t)}{m^2 - s} + \frac{g_u(t)}{m^2 - u} + \frac{1}{\pi} \int_{s_T}^{\infty} \frac{D_s(s', t)}{s' - s} ds' + \frac{1}{\pi} \int_{u_T}^{\infty} \frac{D_u(u', t)}{u' - u} du' \quad (3.1.11)$$

where D_s and D_u are the discontinuities across the s - and u -channel branch cuts and the first two terms represent the contributions of the stable physical particles in the s - and u -channels. In general $\lim_{s \rightarrow \infty} |A(s, t)| \rightarrow |s|^{N-\epsilon}$ and N subtractions will be needed to obtain a similar result to the above. The point of this dispersion relation is that it embodies the (s -plane) analyticity assumptions we have made about the scattering amplitude.

The optical theorem is a particular case of the unitarity relation for identical initial and final states. In this case the sum over all possible intermediate states just gives the total cross-section and the discontinuity across the branch cut gives the imaginary part of the elastic scattering amplitude. It then follows from the unitarity equation that :

$$\sigma_T = \frac{1}{2q_{s12}\sqrt{s}} \text{Im} A_{\text{el}}(s, t = 0) \quad (3.1.12)$$

where $2q_{s12} = \sqrt{s - 4m^2}$ for equal mass scattering.

3.2. Partial-wave Amplitudes and Impact Parameter Space.

A useful decomposition of the scattering amplitude is obtained by defining partial-wave amplitudes. Since angular momentum is a conserved quantity, scattering of states with different angular momenta can be treated independently and satisfy independent unitarity equations which take a very simple form. The s -channel centre-of-mass partial-wave amplitudes for spinless particles are defined by

$$A_l(s) \equiv \frac{1}{16\pi} \frac{1}{2} \int_{-1}^1 dz_s P_l(z_s) A(s, t) \quad l = 0, 1, 2, \dots \quad (3.2.1)$$

and the inverse transformation by

$$A(s, t) = 16\pi \sum_{l=0}^{\infty} (2l+1) A_l(s) P_l(z_s) \quad (3.2.2)$$

where $z_s = \cos \theta_s = 1 + \frac{2t}{s-4m^2}$ and θ_s is the s -channel centre-of-mass scattering angle.

Substituting this into the two-particle unitarity equation gives

$$A_l^{if}(s_+) - A_l^{if}(s_-) = \frac{4iq_{sn}}{\sqrt{s}} A_l^{in}(s_+) A_l^{nf}(s_-) + \dots \quad (3.2.3)$$

which for elastic scattering, where the initial and final states are the same, yields

$$\begin{aligned} \text{Im } A_l^{\text{el}}(s) &= \frac{2q_{s12}}{\sqrt{s}} |A_l^{\text{el}}(s)|^2 + \sum_{n \neq i} \frac{2q_{sn}}{\sqrt{s}} A_l^{\text{in}}(s_+) A_l^{\text{ni}}(s_-) \\ &+ 3 \text{ body channels etc.} \end{aligned} \quad (3.2.4)$$

The first term on the r.h.s corresponds to elastic scattering, the second is the sum over inelastic two particle intermediate states, further terms give the contributions of n-particle intermediate states. Since $2q_{s12} = \sqrt{s - 4m^2} \rightarrow \sqrt{s}$ for large s and all the terms on the r.h.s are positive the above equation implies that

$$0 \leq |A_l^{\text{el}}|^2 \leq \text{Im } \{A_l^{\text{el}}\} \leq 1 \quad (3.2.5)$$

which just represents the condition that the probability of elastic scattering cannot exceed unity and that no scattering process can be purely inelastic, elastic scattering is always present as the 'shadow' of inelastic processes.

The elastic partial-wave amplitudes are often parametrized as in (3.2.6) below, explicitly satisfying the above unitarity condition.

$$A_l^{\text{el}} = \frac{\eta_l e^{2i\delta_l} - 1}{2i \left(\frac{2q_{s12}}{\sqrt{s}} \right)} \quad (3.2.6)$$

where η_l is the inelasticity factor and δ_l is the real phase shift. For unitarity to be satisfied $0 \leq \eta_l \leq 1$.

In terms of the partial wave amplitudes the optical theorem (3.1.12) gives

$$\sigma_T(s) = \frac{8\pi}{q_{s12}\sqrt{s}} \sum_l (2l+1) \text{Im } \{A_l^{\text{el}}(s)\} = \frac{2\pi}{q_{s12}^2} \sum_l (2l+1) [1 - \eta_l \cos 2\delta_l] \quad (3.2.7)$$

and integrating over all angles we find

$$\sigma_{\text{el}}(s) = \frac{16\pi}{s} \sum_l (2l+1) |A_l^{\text{el}}(s)|^2 = \frac{\pi}{q_{s12}^2} \sum_l (2l+1) [1 + \eta_l^2 - 2\eta_l \cos 2\delta_l] \quad (3.2.8)$$

and therefore

$$\sigma_{\text{inel}}(s) = \sigma_T - \sigma_{\text{el}} = \frac{\pi}{q_{s12}^2} \sum_l (2l+1) [1 - \eta_l^2] \quad (3.2.9)$$

so that the contribution of any individual partial wave to the total cross-section decreases with increasing energy and, if σ_T does not fall, more and more partial waves must contribute as the energy increases.

For purely elastic scattering $\eta_l = 1$ so that $\sigma_T^l = \sigma_{el}^l$ whilst for maximum absorption $\eta_l = 0$ and $\sigma_{el}^l = \sigma_{inel}^l = \frac{1}{2}\sigma_T^l$. At an elastic resonance $A_l(s) \rightarrow i$ and $\delta_l = (2n+1)\frac{\pi}{2}$ so all of the partial wave is elastically scattered. In the "black disk limit" all partial waves suffer maximum absorption up to some maximum, $l_{\max} \leq Rq_{s12}$, where R is the particle radius, and so $\sigma_{el} = \sigma_{inel} = \frac{1}{2}\sigma_T = \pi R^2$.

For high energies and small angles ($s \gg |t|$), where a large number of partial waves contribute, we can simplify things further by replacing the summations over partial-wave amplitudes by integrals in impact parameter (b) space. This proceeds through the classical relation $l = q_s b - \frac{1}{2}$ and for large l

$$P_l(z_s) \simeq J_0\left((2l+1)\sin\frac{\theta_s}{2}\right) \quad , \quad \sum_l \rightarrow \int dl \rightarrow \int q_s db$$

and writing

$$A_l(s) \rightarrow A(s, b) \quad , \quad \sin\frac{\theta}{2} \simeq \frac{\theta}{2} \simeq \left(\frac{-t}{q_s^2}\right)^{\frac{1}{2}}$$

we get

$$A(s, t) = 8\pi s \int_0^\infty b db J_0(b\sqrt{-t}) A(s, b) \quad (3.2.10)$$

while the inverse transformation corresponding to (3.2.1) is

$$A(s, b) = \frac{1}{16\pi s} \int_{-\infty}^0 dt J_0(b\sqrt{-t}) A(s, t) \quad (3.2.11)$$

This is just the 2-dimensional Fourier transform of the scattering amplitude in impact parameter space with the azimuthal angle integrated out. Conservation of angular momentum is replaced by constancy of the impact parameter for scattering at high energy and small angle. Note that the above equation holds exactly for the S-wave so that $A(s, b)|_{b=0} = A_l(s)|_{l=0}$.

In terms of the elastic profile function, $A(s, b)$, the unitarity condition on the elastic partial-waves (3.2.5) becomes

$$0 \leq |A(s, b)|^2 \leq \text{Im} A(s, b) \leq 1 \quad (3.2.12)$$

and analagous to (3.2.6) we define the eikonal phase, $\chi(s, b)$, and eikonal series by

$$A(s, b) = \frac{e^{i\chi(s, b)} - 1}{2i} = \frac{1}{2i} \sum_{n=1}^{\infty} \frac{(i\chi(s, b))^n}{n!} \quad (3.2.13)$$

so that $\chi(s, b) \leftrightarrow 2\delta_l(s)$ for large s and $\chi(s, b)$ is complex with positive imaginary part.

The equations (3.2.7),(3.2.8) and (3.2.9) translate to

$$\sigma_T(s) = 8\pi \int_0^{\infty} b db \operatorname{Im} A(s, b) \quad (3.2.14)$$

$$\sigma_{el}(s) = 8\pi \int_0^{\infty} b db |A(s, b)|^2 \quad (3.2.15)$$

$$\sigma_{inel}(s) = 8\pi \int_0^{\infty} b db G_{inel}(s, b) \quad (3.2.16)$$

where we have defined the inelastic profile function, $G_{inel}(s, b)$, by

$$G_{inel}(s, b) \equiv \operatorname{Im} A(s, b) - |A(s, b)|^2 \quad (3.2.17)$$

and by analogy with optics we also define the ‘‘opacity’’, $\Omega(s, b)$, by

$$\Omega(s, b) \equiv -i\chi(s, b) \quad (3.2.18)$$

so that

$$G_{inel}(s, b) = 1 - e^{-2\operatorname{Re} \Omega(s, b)} \quad (3.2.19)$$

Re-writing equation (3.2.13) as in (3.2.6) and defining the absorbtion factor, $\eta(s, b) \equiv e^{-\operatorname{Re} \Omega(s, b)}$, we get

$$A(s, b) = \frac{\eta(s, b)e^{2i\delta(s, b)} - 1}{2i} \quad (3.2.20)$$

where $2\delta(s, b) = \operatorname{Re} \chi(s, b)$ and therefore

$$\operatorname{Re} A(s, b) = \frac{\eta}{2} \sin 2\delta \quad , \quad \operatorname{Im} A(s, b) = \frac{1}{2}(1 - \eta \cos 2\delta) \quad (3.2.21)$$

The unitarity condition (3.2.12) then corresponds to $A(s, b)$ lying within the ‘‘unitarity circle’’ centred on $\operatorname{Im} A(s, b) = \frac{1}{2}$ with radius $\frac{1}{2}$ (see fig.3.1). In terms of the absorbtion factor the inelastic profile function is given by

$$G_{inel}(s, b) = 1 - \eta^2(s, b) \quad (3.2.22)$$

As the energy increases, more and more inelastic channels become available so that at high energy $\eta \rightarrow 0$ corresponding to maximum absorption and giving the black disk limit, $A(s, b) \rightarrow \frac{i}{2}$. Since we are far away from the resonance region we expect elastic scattering to be purely diffractive (no resonance scattering), so that it is produced only as the shadow of $G_{\text{inel}}(s, b)$, and therefore

$$\text{Im } A(s, b) = \frac{1}{2}(1 - \eta(s, b)) \quad (3.2.23)$$

i.e it has the minimum value compatible with a given amount of absorption. This puts a stronger limit on $\text{Im } A(s, b)$ than (3.2.12) which we call the diffractive limit :

$$\text{Im } A(s, b) \leq \frac{1}{2} \quad (3.2.24)$$

This limit corresponds to the $\text{Re } \Omega \rightarrow \infty$ and the particle becoming infinitely black and totally absorbing. However, the dispersion relation (3.1.11) implies that a cross-section which changes with energy must have a finite real part. In QCD this can be thought of as the difference between the basic exchange given by two gluon amplitude which is energy independent and pure imaginary and the sum of the ladder diagrams (see §3.5) which is energy dependent and gives the real part of the amplitude.

Let $\rho(s, b)$ be the ratio of the real to the imaginary part of the profile function $A(s, b)$.

$$\rho(s, b) \equiv \frac{\text{Re}}{\text{Im}} A(s, b) \quad (3.2.25)$$

The energy dependence of σ_T implies a finite value for $\rho(s, b)$. This gives the constraint

$$\text{Im } A(s, b) \leq \frac{1}{2(1 + \rho^2(s, b))} \quad (3.2.26)$$

rather than (3.2.24). For fixed $\rho(s, b)$ the maximum allowed value of $\text{Im } A(s, b)$ corresponds to minimum η . This is shown in fig.3.1 . Since the energy dependence of the forward peak changes only slowly with t then

$$\rho(s, b)|_{b=0} \simeq \rho(s, t)|_{t=0} \quad (3.2.27)$$

This fixes the maximum value allowed for $\text{Im } A(s, b)$ and since $\rho(s, t = 0)$ is small this is not much different from (3.2.24).

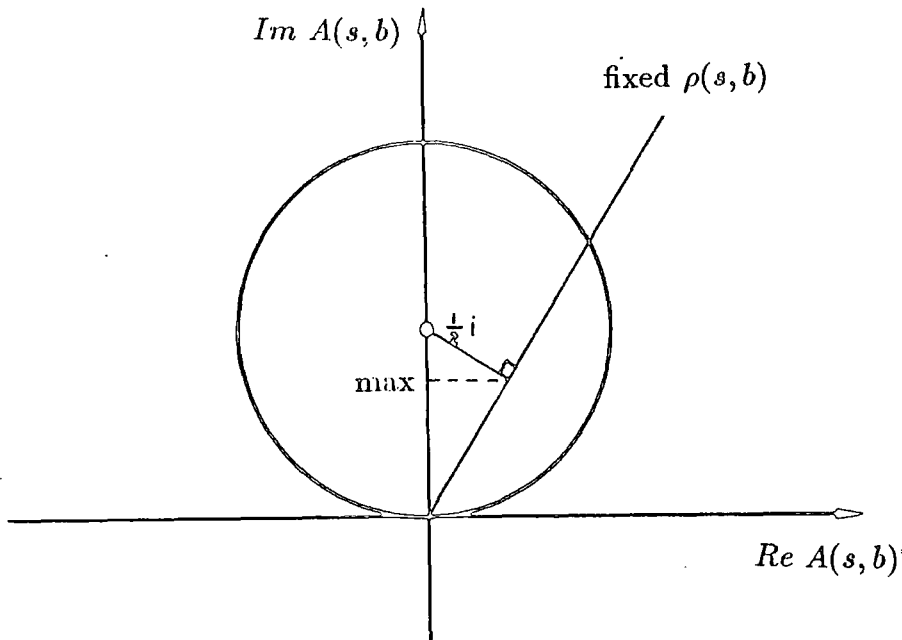


FIG.3.1 Maximum value of $Im A(s, b)$ allowed in diffractive limit for fixed $\rho(s, b)$.

The above discussion clearly does not correctly represent an amplitude with an odd charge conjugation contribution increasing with energy at a similar rate to the even C part, in which case $Re A(s, b)$ does not tend asymptotically to zero. The amplitude should still however satisfy the constraint (3.2.24). Impact space analyses of the high energy pp and $\bar{p}p$ differential cross-section data have been given in Amaldi (1980) and Fearnley (1985) respectively. The nearly exponential t -dependence of the forward peak gives $Im A(s, b)$ a Gaussian shape as a function of b . The large $|t|$ structure in $\frac{d\sigma}{dt}$ beyond the dip region produces a decrease in $Im A(s, b)$ at small b , slightly flattening the profile function, whilst the slope variation at small $|t|$ (Carrigan break) produces an increase above the Gaussian for $b \geq 2 \text{ GeV}^{-2}$. The values of $Im A(s, b = 0)$ quoted for $\bar{p}p$ at $\sqrt{s} = 53 \text{ GeV}$ and $\sqrt{s} = 546 \text{ GeV}$ are (0.353 ± 0.002) and (0.425 ± 0.002) respectively with the nucleon mean square radius increasing from $(0.953 \pm 0.005 \text{ fm})$ to $(1.061 \pm 0.003 \text{ fm})$. The increase of $G_{inel}(s, b)$ over these energies is greatest at large $b \approx 1 \text{ fm}$ showing the peripheral nature of the scattering that produces the rising cross-section. This *peripherality* is a consequence of the unitarity limit. Thus the profile function represents a grey disk which gets blacker and larger with increasing energy.

3.3. Asymptotic Bounds on the Scattering Amplitude.

Using unitarity and the analyticity of the scattering amplitude useful bounds can be put upon the asymptotic energy dependence and t -dependence of the total and elastic cross-sections. Since t only enters the partial wave series (3.2.2) through z_s in the

Legendre functions $P_l(z_s)$ the series must diverge if it is continued into the t -channel physical region to the nearest t -channel singularity. The nearest t -channel singularity in pp scattering turns out to be the two pion threshold, $t_0 = (2m_\pi)^2$ (the π pole does not occur in the spin amplitude relevant at high energy because it has negative parity). If we assume that the amplitude is analytic for $t < t_0$ and is polynomial bounded in s so that $A(s, t) < Cs^N$, which is true in quantum field theory (and $N \leq 2$ follows from unitarity), then following Block and Cahn (1985) and applying this to equation (3.2.11) at $t = t_0 > 0$ and using (A.7) gives

$$A(s, t_0) = 8\pi s \int_0^\infty b db I_0(b\sqrt{t_0}) A(s, b) < Cs^N \quad (3.3.1)$$

where I_0 is the modified Bessel function and C is an unknown constant. Since I_0 is an increasing function of its argument the maximum value of $8\pi s \int_0^\infty b db I_0(b\sqrt{t}) \text{Im} A(s, b)$ for $0 \leq t < t_0$ subject to the above constraint is obtained for saturation of the imaginary part of the low impact parameter profile function i.e for $A(s, b) = \begin{cases} i & b \leq b_c \\ 0 & b > b_c \end{cases}$.

Substituting this into (3.3.1) and using (A.8) we find

$$\begin{aligned} 8\pi s \int_0^\infty b db I_0(b\sqrt{t}) \text{Im} A(s, b) &= 8\pi s \int_0^{b_c} b db I_0(b\sqrt{t}) \\ &= 8\pi s \frac{b_c}{\sqrt{t}} I_1(b_c\sqrt{t}) \end{aligned} \quad (3.3.2)$$

At $t = t_0$ this gives

$$\frac{8\pi b_c}{\sqrt{t_0}} I_1(b_c\sqrt{t_0}) < Cs^{N-1} \quad (3.3.3)$$

so that for high energy where b_c is large

$$b_c \simeq \frac{1}{\sqrt{t_0}} \left[(N-1) \log \frac{s}{s_0} - \frac{1}{2} \log \left\{ (N-1) \log \frac{s}{s_0} \right\} + \dots \right] \quad (3.3.4)$$

and thus for $0 \leq t < t_0$ we have

$$\max \{ \text{Im} A(s, t) \} = 4\pi s b_c^2 \left[\frac{2I_1(b_c\sqrt{t})}{b_c\sqrt{t}} \right] \quad (3.3.5)$$

At $t = 0$ using (A.12) and (3.2.14) this gives

$$\sigma_T^{\max} = \frac{4\pi}{t_0} \left[(N-1)^2 \log^2 \frac{s}{s_0} - (N-1) \log \left(\frac{s}{s_0} \right) \log \left\{ (N-1) \log \frac{s}{s_0} \right\} + \dots \right] \quad (3.3.6)$$

so for $N = 2$ and $t_0 = 4m_\pi^2$ it follows that

$$\sigma_T \leq \frac{\pi}{m_\pi^2} \log^2 \frac{s}{s_0} \approx 60 \log^2 \frac{s}{s_0} \text{ mb} \quad (3.3.7)$$

This is the Froissart bound which puts a limit on how fast σ_T can grow with energy. The scale factor s_0 in the above equations is unknown because the constant C in (3.3.1) is incalculable but s_0 should be of the order of the hadronic mass scale : $s_0 \approx 1 \text{ GeV}$. The σ_T data at present energies do not show any sign of saturating the Froissart bound. Their energy dependence indicates a coefficient of $\log^2 s$ of about 0.6 mb, a factor of $100\times$ below the corresponding coefficient in the Froissart bound.

If the amplitude satisfies a more stringent limit on its energy dependence at $t = t_0$ than (3.3.1) so that $A(s, t) < Cs^{1+\epsilon}$ with $0 < \epsilon < 1$ then σ_T satisfies the bound with reduced coefficient.

$$\sigma_T \leq \frac{4\pi}{t_0} \epsilon^2 \log^2 \frac{s}{s_0} \quad (3.3.8)$$

For $\epsilon \approx 0.1$ as in Pomeron dominated models and eikonal type models with the Born term giving single Pomeron exchange (see §7) this reduces the coefficient of the bound by a factor of 100. Similarly, if the effective region of analyticity of the amplitude bounded by $t = t_0$ is larger than that given by $t_0 = 4m_\pi^2$ the bound is also improved. The t -dependence of the differential cross-section in hadronic processes indicates that the 2π threshold is not responsible for the effective range of the interaction which corresponds to a singularity at $t_0 \approx 0.7 \text{ GeV}^2$ (as in the proton electromagnetic form factor) giving a factor $\approx 10\times$ reduction in the coefficient.

For $t > 0$ equations (3.3.4) and (3.3.5) give

$$\begin{aligned} \text{Im } A(s, t) &\leq \frac{4\sqrt{2\pi}}{t} \left(\frac{t}{t_0}\right)^{\frac{1}{4}} s \left(\frac{s}{s_0}\right)^{(N-1)\sqrt{\frac{t}{t_0}}} \left[(N-1) \log \frac{s}{s_0} \right]^{\frac{1}{2}(1-\sqrt{\frac{t}{t_0}})} \\ &\sim s^{1+\sqrt{\frac{t}{t_0}}} \text{ for } N = 2 \text{ and } s \gg s_0 \end{aligned} \quad (3.3.9)$$

At $t = 0$ this reproduces (3.3.1) and puts some constraint on the form of the amplitude. For instance a form like $ise^{(b \log^2 s)t}$ is not consistent with (3.3.9).

3.4. Regge Poles.

The partial-wave amplitude given by equation (3.2.1) is also defined for non-integer and complex values of l so that we can consider continuing the amplitude into the complex

angular momentum plane. In order that the continuation be unique it is required that the function both vanishes for $l \rightarrow C \pm i\infty$ and is regular for $l > C$ where C is some real constant. To ensure this for t -channel partial-wave amplitudes we have to decompose the amplitude into parts which are even and odd under the interchange $\cos \theta_t \leftrightarrow -\cos \theta_t$ (i.e $s \leftrightarrow u$) This gives even and odd *signed* amplitudes ($\mathfrak{S} = \pm 1$), which have only right hand cuts in the complex z_t plane, and the corresponding partial-wave decompositions give the physical partial-wave amplitudes for l even and odd respectively, i.e.

$$A_l(t) = \begin{cases} A_l^+(t) & \text{for } l \text{ even} \\ A_l^-(t) & \text{for } l \text{ odd} \end{cases} \quad (3.4.1)$$

Using a Sommerfeld-Watson transformation we can write the partial-wave series for the signed amplitude as an integral in the complex l -plane

$$A^{\mathfrak{S}}(s, t) = -\frac{16\pi}{2i} \oint_{C_1} (2l+1) A_l^{\mathfrak{S}}(t) \frac{P_l(-z_t)}{\sin \pi l} dl \quad (3.4.2)$$

where C_1 is a contour enclosing zero and the positive integers. The analyticity in l of $A_l^{\mathfrak{S}}(t)$ allows the contour C_1 to be expanded to a semi-circle at infinity with its base along the line $Re l = C$. The convergence properties of $A_l^{\mathfrak{S}}(t)$ means the contribution from the semi-circle vanishes leaving only the base contribution. If it is assumed that the signed partial-wave amplitudes have only isolated singularities (poles and branch cuts) for $Re l < C$ then the base line of the contour can be pushed further to the left picking up separate contributions from each of these singularities. The Legendre function $P_l(z)$ decreases most rapidly as a function of z for $l = -\frac{1}{2}$, for which $P_{-\frac{1}{2}}(z) \rightarrow z^{-\frac{1}{2}}$ as $z \rightarrow \infty$. If the base of the contour is displaced to the left as far as the line $Re l = C = -\frac{1}{2}$ then the contribution to the contour integral along this will be asymptotically negligible compared to that of any singularities encountered to the right of the line. These t -channel singularities are the Regge poles and Regge cuts and they determine the asymptotic behaviour of the s -channel amplitude. The base of the contour in the above can in fact be pushed as far to the left as we like using the Mandelstam-Sommerfeld-Watson transformation. The reason for using the integral representation (3.4.2) rather than the partial-wave series (3.2.2) is that whilst the latter diverges at the nearest s -channel singularity the former is valid throughout the complex z -plane provided the partial-wave amplitudes are sufficiently convergent in the l -plane.

In general the position of the singularity will be a function of t and describe a trajectory in the l -plane as t varies, $l = \alpha(t)$. A simple pole, R , with signature, \mathfrak{S} , and residue,

$\beta(t)$, of the form

$$A_l^{\Im}(t) = \frac{\beta(t)}{l - \alpha_R(t)} \quad (3.4.3)$$

substituted into (3.4.2) gives the amplitude

$$A_R^{\Im}(z_t, t) = -16\pi^2(2\alpha_R(t) + 1)\beta(t) \frac{P_{\alpha_R(t)}(-z_t)}{\sin \pi\alpha_R(t)} \quad (3.4.4)$$

The contribution to the physical amplitude is then given by

$$A_R^{\Im}(s, t) = A_R^{\Im}(z_t, t) + \Im A_R^{\Im}(-z_t, t) \quad (3.4.5)$$

and in the s -channel this has the high energy behaviour

$$A_R^{\Im}(s, t) \sim (1 + \Im e^{-i\pi\alpha_R(t)}) s^{\alpha_R(t)} \quad (3.4.6)$$

It follows from the disconnectedness postulate of S-matrix theory that the residue of the pole, $\beta(t)$, factorizes into a product of its couplings to each of the external particle lines, so that $\beta(t) = \gamma_{1,3}(t)\gamma_{2,4}(t)$. As it is written, equation (3.4.4) also has unphysical poles at negative integer values of $\alpha_R(t)$. A convenient expression summarizing the properties of a Regge pole in both the asymptotic s -channel and the resonance region of the t -channel is (from Collins (1982))

$$A(s, t) = \gamma_{1,3}(t)\gamma_{2,4}(t) \frac{e^{-i\pi\alpha(t)} + \Im}{2 \sin \pi\alpha(t)} \frac{1}{\Gamma(\alpha(t) + 1)} \left(\frac{s}{s_0}\right)^{\alpha(t)} \quad (3.4.7)$$

The poles of the Γ function cancels the poles in (3.4.4) for negative integer values of $\alpha(t)$.

It can be shown that the Regge trajectory, $l = \alpha_R(t)$, is a real analytic function of t and contains the right-hand threshold branch cut. So below the t -channel threshold $\alpha_R(t)$ is purely real but for $t > t_T$ it develops an imaginary part. When a Regge pole with even signature occurs at an even value of l , or with odd signature at an odd value of l , then it gives a pole in the physical partial-wave amplitude. If this occurs below the t -channel threshold the pole corresponds to a bound state, above threshold the trajectory has an imaginary part and corresponds to a resonance.

Thus the trajectory, $\alpha_R(t)$, produces both the asymptotic s -channel behaviour and the t -channel poles of the amplitude. As t is varied, for $t > 0$, we expect a trajectory with definite signature to generate a sequence of bound states and resonances corresponding

to observable particles with the same quantum numbers, apart from their spins which differ by two units of angular momentum between successive states. The experimental data on the particle masses and spins (see fig.1.2) indicate that such sequences of particles do occur, and that the trajectories associated with them are linear functions of t ($= \text{mass}^2$) of the form $\alpha_R(t) = \alpha_R(0) + \alpha'_R t$. The experimental data on the appropriate high energy crossed channel elastic differential cross-sections show that the linear behaviour of some meson trajectories continues to negative values of t at least as far as $t \approx -1.5 \text{ GeV}^2$.

The above discussion can be extended to include the scattering of particles with spin. This significantly complicates the formalism because we have to worry about the kinematical singularities and crossing properties of the helicity amplitudes. However, these complications can be taken care of, and essentially the same result holds as for spin-zero scattering (see Collins (1977)). For the s -channel helicity amplitudes it is found that

$$A_{H_s}^R(s, t) \rightarrow - \left(\frac{-t}{s_0} \right)^{\frac{1}{2}m} \frac{e^{-i\pi(\alpha-\nu)} + \Im}{2 \sin \pi(\alpha - \nu)} \beta_{H_s}(t) \left(\frac{s}{s_0} \right)^{\alpha(t)} \quad (3.4.8)$$

in which :

$$H_s \equiv \{\mu_1, \mu_2, \mu_3, \mu_4\} \quad (3.4.9)$$

where the μ 's are the s -channel c-of-m helicities;

$$m \equiv |\mu_1 - \mu_3| + |\mu_2 - \mu_4| \quad (3.4.10)$$

ν is zero or a half corresponding to whether the total angular momentum states are integer or half-integer respectively; and the residue function $\beta_{H_s}(t)$ can be factorized as

$$\beta_{H_s}(t) = \gamma_{\mu_1 \mu_3}(t) \gamma_{\mu_2 \mu_4}(t) \quad (3.4.11)$$

We have found that the asymptotic s -channel behaviour of the amplitude is controlled by the rightmost j -plane singularities in the t -channel partial-wave amplitude. The Froissart bound, derived above in §3.3 using s -channel unitarity, gave $Im A(s, t) \leq \text{constant} \times s \log^2 s$ so that only one subtraction is needed in the dispersion relation (3.1.11) and the partial-wave amplitudes are free of singularities (analytic) for $j > 1$.

We can also use t -channel unitarity to constrain the asymptotic behaviour of the s -channel amplitude through the connection with the t -channel partial-wave singularities. As in eq.(3.2.3), elastic t -channel unitarity gives for the signed partial-wave

amplitudes

$$A_l^{\mathfrak{S}}(t) - A_l^{\mathfrak{S}\dagger}(t) = 2i\rho(t)A_l^{\mathfrak{S}}(t)A_l^{\mathfrak{S}\dagger}(t) \quad (3.4.12)$$

where $\rho(t) = \sqrt{1 - \frac{4m^2}{t}}$. Eliminating the kinematical singularities in $A_l^{\mathfrak{S}}(t)$ by writing, $A_l^{\mathfrak{S}}(t) \rightarrow B_l^{\mathfrak{S}}(t) \times$ kinematical singularities, and using the real analyticity of $B_l^{\mathfrak{S}}(t)$ to write

$$B_l^{\mathfrak{S}\dagger}(t) = B_l^{\mathfrak{S}*}(t) \quad (3.4.13)$$

equation (3.4.12) gives

$$B_l^{\mathfrak{S}}(t) - B_l^{\mathfrak{S}*}(t) = 2i\rho_l(t)B_l^{\mathfrak{S}}(t)B_l^{\mathfrak{S}*}(t) \quad (3.4.14)$$

This equation is valid for the amplitudes $B_l^{\mathfrak{S}}(t)$ continued in l as well as at right-signature integer values and applies in the region $t_{\mathcal{R}} < t < t_{\text{inel}}$ (i.e in the t -channel region above the elastic but below the inelastic threshold). The non-linearity of the equation implies that the partial-wave amplitudes cannot contain any hard singularities at real values of j in the region of t over which it applies. Thus (fixed) poles and hard branch cuts whose positions are independent of t are forbidden since real analyticity of $B_l^{\mathfrak{S}}(t)$ means they occur at real values of j . Moving singularities are allowed because below threshold they can occur at real j but develop an imaginary part above threshold. Soft branch points at real values of j in the elastic t -channel region are also allowed.

The asymptotic s -channel behaviour corresponding to a given j -plane singularity structure can be conveniently found from the asymptotic limit of eq.(3.4.2) which yields a Mellin transform for the amplitude and the imaginary part then has the form

$$\text{Im } A^{\mathfrak{S}}(s, t) \sim \frac{1}{2\pi i} \int_{C-i\infty}^{C+i\infty} A_l^{\mathfrak{S}}(t) s^l dl \quad \text{for } s \rightarrow \infty \quad (3.4.15)$$

As we have already found above, a simple pole in the j -plane gives rise to an asymptotic power behaviour in the s -channel. More generally, a singularity of the form $(j - \alpha)^\nu$ ($\nu \neq 0$), which corresponds to a multiple pole in the j -plane if $\nu =$ negative integer or a hard (soft) branch point if $\nu =$ real and negative (positive), gives the s -channel behaviour :

$$(j - \alpha)^\nu \longleftrightarrow \frac{s^\alpha}{(\log s)^{\nu+1}} \quad (3.4.16)$$

A logarithmic branch point in the j -plane gives :

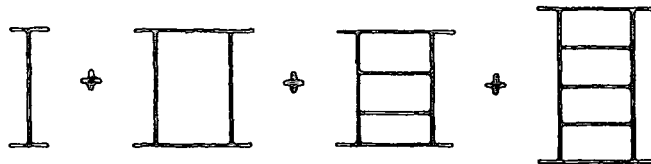
$$(\log(j - \alpha))^\nu \longleftrightarrow \frac{s^\alpha (\log \log s)^{\nu-1}}{\log s} \quad (3.4.17)$$

From eq.(3.4.16) the $s \log^2 s$ asymptotic behaviour of the Froissart bound comes from a j -plane singularity with the form $\frac{1}{(j-1)^3}$ at $t = 0$. If the asymptotic s and t dependence of the s -channel amplitude factorizes, so that $A(s, t) \rightarrow \beta(t)f(s)$, then since this corresponds to $A_j(t) \rightarrow \beta(t)F(j)$, a fixed j -plane singularity, the singularity can only be a soft branch cut and so $A(s, t) \rightarrow \frac{s}{(\log s)^{\nu+1}}$ where $\nu > 0$ and so the total cross-section must decrease at least as fast as $\frac{1}{\log s}$.

3.5. Regge poles and Perturbation Field Theory.

We would like to be able to see how Regge poles arise from a fundamental theory of strong interactions in which hadrons are made of quarks and gluons. However, there are numerous problems preventing the use of QCD in the relevant regions of Regge physics. Not least of these are the ultra-violet confining nature of non-abelian QCD and the infra-red complications produced by a massless vector gluon. A perturbative approach is not really suited to the calculation of Regge pole behaviour since it must involve the study of bound states. The best that can be done is to examine field theories which are more easily calculable but less physically realistic and hope that these give a valid indication of how strong interactions behave.

The simplest field theory we can look at is one involving only scalar mesons with a ϕ^3 interaction. If we consider only planar diagrams then the leading behaviour in the s -channel comes from diagrams with only two particle states in the t -channel, so that it is given by the sum of ladder diagrams shown in figure 3.2 .



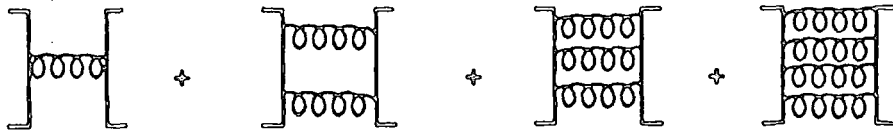
3.2 The planar graphs giving the leading logarithm behaviour in the s -channel.

Each of these graphs has the leading behaviour $s^{-1}(\log s)^{n-1}$ where $n \geq 1$ is the number of rungs in a given ladder and determines the power of $\log s$ that appears. The sum of the ladder graphs has the asymptotic behaviour (see Eden (1967))

$$A(s, t) \sim \frac{g^2}{s} e^{K(t) \log s} \quad (3.5.1)$$

and so has a Regge pole-like behaviour with trajectory $\alpha(t) = -1 + K(t)$. As $|t| \rightarrow \infty$, the (t -channel) Born term with propagator $\sim \frac{1}{s}$ dominates and so $K(t) \rightarrow 0$ and $\alpha(t) \rightarrow -1$. The Born term gives rise to a fixed pole at $l = -1$ in the t -channel partial-wave amplitude which as we saw in §3.4 is forbidden by t -channel unitarity. Iteration in the t -channel restores unitarity and converts the fixed pole into a moving pole and so *Reggeizes* the exchange.

We may then hope that a similar mechanism operates with multiple gluon exchange in which the basic t -channel Born diagram goes like $\sim \frac{t}{s}$. This is illustrated in figure 3.3 .



3.3 The multiple-gluon ladders representing a Regge pole exchange.

The $\frac{1}{s}$ dependence of the Born term again means that the trajectory $\alpha(t) \rightarrow -1$ as $|t| \rightarrow \infty$. The above diagram corresponds to a meson Regge trajectory. A similar set of diagrams may be expected to give Pomeron exchange. In this case the exchange of a single t -channel gluon has the form $\sim \frac{s}{t}$ and so the trajectory asymptotes to one as $|t| \rightarrow \infty$.

The properties of the field theory of massive quantum electrodynamics has also been studied in the hope that it bears some relation to the physics of hadron scattering since it preserves at least the vector nature of the field. The leading high energy behaviour is given by summing ladder diagrams as in ϕ^3 theory, but twisted ladders are included in order to preserve gauge invariance. The sum of these diagrams, called a *tower*, has the asymptotic behaviour

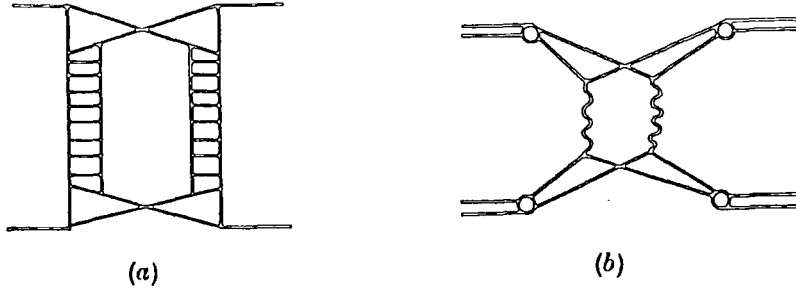
$$A(s, t) \rightarrow \frac{iss^a}{\log^2 s} f(t) \quad (3.5.2)$$

where a is a positive constant and so (3.5.2) violates the Froissart bound.

3.6. Regge Cuts.

The existence of branch cut singularities in the j -plane can be deduced from two particle

t -channel unitarity (for theories with third Mandelstam double spectral functions). Regge cuts can be shown to arise in Feynmann diagrams as a result of the exchange of two or more Reggeons with nested couplings as in figure 3.4(a).



3.4 (a) Mandelstam cross diagram for two Reggeon exchange giving rise to a Regge cut, (b) Physical representation of two Reggeon exchange.

The asymptotic behaviour of the sum of two such Reggeon diagrams summed over all numbers of rungs has the form (see Collins (1977))

$$A(s, t) = \frac{ig^4}{16\pi^2} \int dt_1 \int dt_2 \frac{(N(t, t_1, t_2))^2 \theta(-\lambda)}{(-\lambda(t, t_1, t_2))^{\frac{1}{2}}} s^{\alpha(t_1) + \alpha(t_2) - 1} \quad (3.6.1)$$

where $N(t, t_1, t_2)$ is the Feynmann integral of the cross structure which is present in each of the couplings of the two Reggeons to the external particles and is not in general calculable.

Equation (3.6.1) behaves asymptotically like

$$A(s, t) \sim \frac{s^{\alpha_1(0) + \alpha_2(0) - 1 + \frac{\alpha'_1 \alpha'_2}{\alpha'_1 + \alpha'_2} t}}{(\alpha'_1 + \alpha'_2) \log s} \quad (3.6.2)$$

and so corresponds to a Regge cut with branch point at

$$\alpha_c(t) = \alpha_1(0) + \alpha_2(0) - 1 + \frac{\alpha'_1 \alpha'_2}{\alpha'_1 + \alpha'_2} t \quad (3.6.3)$$

More generally, the exchange of n Reggeons, with trajectories $\alpha_i(t)$, leads to a branch cut with branch point given by

$$\alpha_{c_n}(t) = \max \left\{ \sum_{i=1}^n \alpha_i(t_i) - n + 1 \right\} \quad (3.6.4)$$

subject to the phase space constraint

$$\sum_{i=1}^n \sqrt{-t_i} = \sqrt{-t} \quad (3.6.5)$$

(at least for trajectories which increase with increasing t).

For identical Reggeons this gives a branch point at

$$\alpha_{c_n}(t) = n\alpha\left(\frac{t}{n^2}\right) - n + 1 \quad (3.6.6)$$

which for linear trajectories gives

$$\alpha_{c_n}(t) = n(\alpha_0 - 1) + 1 + \frac{\alpha'}{n}t \quad (3.6.7)$$

Thus for a Pomeron trajectory with intercept one, all the Pomeron cut trajectories intersect at one for $t = 0$. For sufficiently large $-t$, the higher order Reggeon cuts dominate the lower order cuts and the pole since the slope of the cut trajectory gets smaller as n increases.

Physically, it is expected that the Regge cuts will arise from the coherent scattering by separate constituents in the particles as in figure 3.4(b) which can be represented in ϕ^3 theory by figure 3.4(a). Replacing the ladder diagram in (3.6.1) by Reggeon amplitudes gives

$$\begin{aligned} A_{R_1 R_2}(s, t) &= \frac{i}{16\pi^2 |s|} \int_{-\infty}^0 \int_{-\infty}^0 \frac{dt_1 dt_2 \theta_1(-\lambda)}{(-\lambda(t, t_1, t_2))^{\frac{1}{2}}} [N(t, t_1, t_2)]^2 A_{R_1}(s, t_1) A_{R_2}(s, t_2) \quad (3.6.8) \\ &= \frac{i}{16\pi^2 |s|} \int_{-\infty}^0 \int_{-\infty}^0 dt_1 dt_2 \int_0^\infty b db J_0(b\sqrt{-t_1}) J_0(b\sqrt{-t_2}) J_0(b\sqrt{-t}) \\ &\quad \times \frac{\pi}{2} [N(t, t_1, t_2)]^2 A_{R_1}(s, t_1) A_{R_2}(s, t_2) \quad (3.6.9) \end{aligned}$$

A model for calculating the contributions of multiple Reggeon exchanges and their strengths relative to the pole term is given by the eikonal series (3.2.13) which sums the repeated exchange of the Born term in the s -channel in the approximation that none of the exchanges carry much momentum relative to that of the scattered particle. This corresponds to the high energy small angle limit and can be shown to hold in perturbation field theory for the exchange of ladders with nested couplings. For two-particle exchange this corresponds to putting the Gribov vertex $N(t, t_1, t_2) = 1$ in

equation (3.6.9). The series of diagrams summed by this procedure consist of planar as well as non-planar diagrams so that the higher terms in the eikonal series contain parts which contribute to the renormalization of the pole term rather than to Pomeron cuts (as in the AFS cut). Also the series does not take into account the composite nature of the exchanged particle, so that more complicated diagrams are allowed where the exchanged particles interact, and so it does not satisfy t -channel unitarity.

However, one of the features of the eikonal model that makes it useful is that it does explicitly satisfy s -channel unitarity and thus the Froissart bound. Similar models have been proposed for multiple-Pomeron exchange, with an enhancement (suppression) factor, λ , representing the contribution of diffractively produced intermediate states (see Collins *et al* (1974)), so that

$$A(s, b) = \frac{e^{i\lambda\chi(s, b)} - 1}{2i\lambda} \quad (3.6.10)$$

This can be shown to satisfy the Froissart bound but clearly it does not necessarily respect the unitarity condition (3.2.12) (if $\chi \rightarrow i\infty$ then $A(s, b) \rightarrow \frac{i}{2\lambda}$).

Pole and Weak Cut Model

4.1. Introduction

We saw in §1 that the pp and $\bar{p}p$ total cross-sections are well described as the sum of two components: a diffractive part due to the Pomeron which contributes equally to pp and $\bar{p}p$ scattering and increases slowly with energy; and a secondary Regge exchange contribution which falls with energy approximately like $s^{-\frac{1}{2}}$ and contributes mainly to $\sigma_T(\bar{p}p)$ which has non-exotic s -channel quantum numbers. The Chew-Frautschi plot in figure 1.2 shows that the leading meson Regge trajectories which can be exchanged in pp and $\bar{p}p$ scattering are the ρ , A_2 , f and ω trajectories. These have approximately degenerate trajectories with intercept, $\alpha_R(0) \approx \frac{1}{2}$, and slope, $\alpha'_R \approx 0.9 \text{ GeV}^{-2}$, so from (3.4.7) have energy dependence $s^{\alpha_R(0)-1} \simeq s^{-\frac{1}{2}}$.

Experimentally the couplings of the ρ and A_2 Reggeons, which have isospin one, are small in comparison with the f and ω couplings with zero isospin. This is reflected in the near equality of the $\bar{p}p$ and $\bar{p}n$ ($=p\bar{n}$) and the pp and pn total cross-sections. In fact we have

$$\begin{aligned}
 \sigma_T(pp \rightarrow pp) &= P + f - \omega - \rho + A_2 \\
 \sigma_T(\bar{p}p \rightarrow \bar{p}p) &= P + f + \omega + \rho + A_2 \\
 \sigma_T(pn \rightarrow pn) &= P + f - \omega + \rho - A_2 \\
 \sigma_T(\bar{p}n \rightarrow \bar{p}n) &= P + f + \omega - \rho - A_2
 \end{aligned}
 \tag{4.1.1}$$

so that if the ρ and A_2 were exchange degenerate their imaginary parts would cancel in pp and pn scattering and only produce a difference in the $\bar{p}p$ and $\bar{p}n$ total cross-sections. In practice the $pn, \bar{p}n$ cross-sections are determined from deuteron scattering experiments and the Glauber screening corrections introduce too large an uncertainty to accurately determine the ρ and A_2 exchange contribution from the difference between $pn, \bar{p}n$ and $pp, \bar{p}p$ scattering. However, determining the coupling of the ρ to the pp vertex, γ_{pp}^ρ , from $\Delta(\pi p) = \sigma_T(\pi^- p) - \sigma_T(\pi^+ p)$ and using the factorization of Regge residues and ρ universality gives $\gamma_{pp}^\rho = 1.31 \text{ mb}$ (Hendrick et al (1975)), whereas obtaining γ_{Kp}^ω (and γ_{Kp}^ρ) from $\Delta(Kp)$ and using ω universality gives $\gamma_{pp}^\omega = 23.9 \text{ mb}$. So ρ and A_2 trajectory exchanges are only a 5% effect in pp and $\bar{p}p$ scattering and since we are mainly interested in determining the diffractive component of the amplitude

and the ρ , A_2 , f , ω trajectories are at least approximately exchange degenerate we shall neglect the small effects of the ρ and A_2 Reggeon exchanges and effectively include them in the ω and f Reggeon exchange contributions respectively.

The f trajectory has same quantum numbers as the Pomeron and so adds to the imaginary part of the Pomeron contribution. The ω Reggeon has odd charge conjugation and so will contribute to pp and $\bar{p}p$ scattering with opposite sign. Since experimentally $\sigma_T(\bar{p}p) > \sigma_T(pp)$ clearly we need the ω Reggeon to subtract from the imaginary part of the amplitude in pp scattering and to add in $\bar{p}p$ scattering as in (4.1.1). This is as we expect from the basic quark diagrams for Reggeon exchange which in pp and $\bar{p}p$ scattering are (see Collins and Martin (1984))

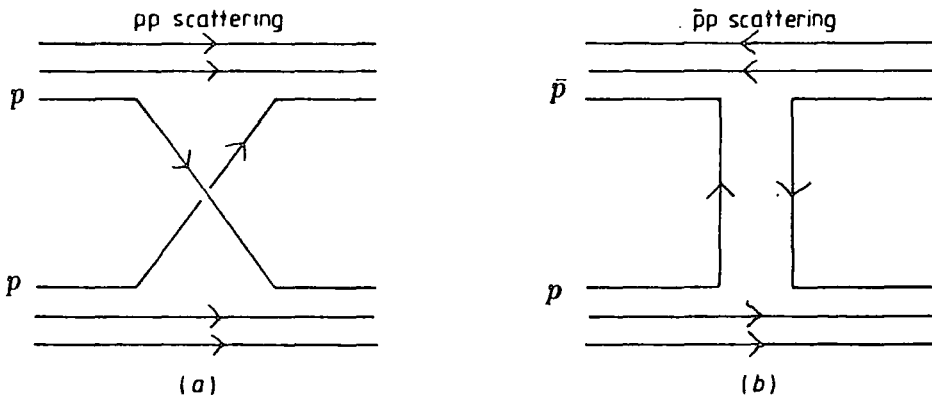


FIG.4.1 Basic quark exchange diagrams for Reggeons in (a) pp and (b) $\bar{p}p$ scattering.

so that Regge exchange in pp scattering gives to a first approximation a purely real contribution to the amplitude and in $\bar{p}p$ a mixture of real and imaginary parts due to the rotating phase i.e f and ω Reggeons are exchange degenerate.

Phenomenologically it has proved successful to also treat the Pomeron as a Regge pole. As we saw in §1, since its contribution to σ_T increases with energy, the intercept, $\alpha_P(0)$, of the Pomeron trajectory must lie above one. In fact we find $\alpha_P(0) \approx 1.095$, and the shrinkage of the small $|t|$ high energy data indicates a trajectory slope, α'_P , of about 0.25 GeV^{-2} . Thus the Pomeron trajectory is markedly different from the meson Regge trajectories and there are no known particles which lie on it. Because of its strange properties and its basic description in terms of two gluon exchange it has been speculated (Collins 1985) that the t -channel resonances lying on the trajectory

may be glueballs. Extrapolation of the Pomeron trajectory gives a mass of about 2 GeV for the lowest state, the 2^{++} glueball. There are candidates in this region but the nature of these states has not yet been confirmed experimentally.

As we saw in figure 2.9, to a good approximation the differential cross-section has a simple exponential t -dependence out to $|t| \approx 1 \text{ GeV}^2$. At ISR energies there is then a dip at $|t| \approx 1.4 \text{ GeV}^2$ and beyond this, for $|t| > 2 \text{ GeV}^2$, there is again a simple exponential t -dependence but with a slope which is about $6\times$ smaller and almost independent of energy. The natural description of the amplitude giving this behaviour is in terms of two imaginary components with opposite sign; one with the steep slope seen at small $|t|$, the other with the shallow slope from large $|t|$, so that for $|t| = 1.4 \text{ GeV}^2$ they interfere and give a dip in the differential cross-section as in figure 4.2.

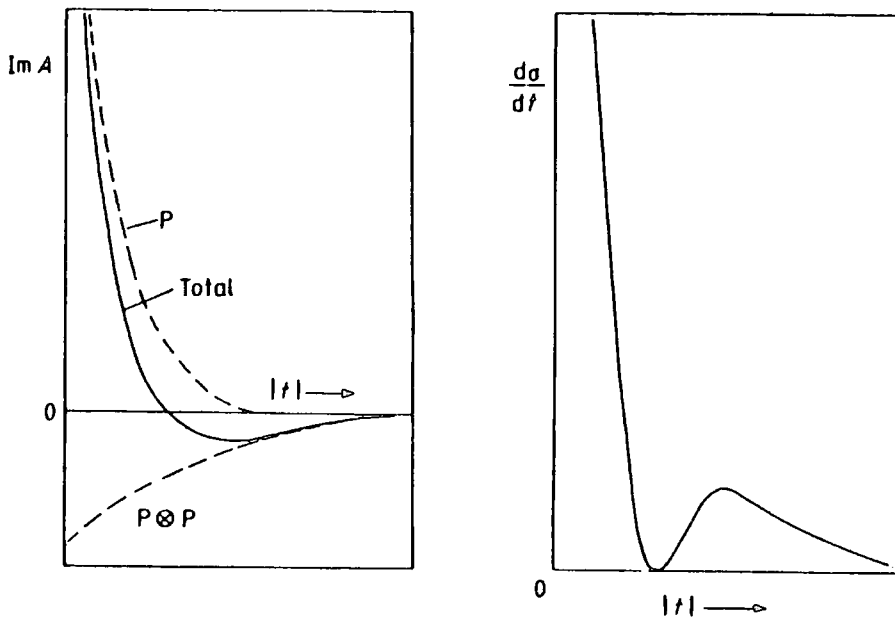


FIG.4.2 Production of a zero in the amplitude by the interference of two exponential contributions (figure from Collins and Martin (1984)).

Since we believe the Pomeron pole dominates the amplitude at $t = 0$ it is easiest to interpret the forward peak as due to the Pomeron with some other contribution giving the large $|t|$ behaviour. We know from §3.6 that the Pomeron cut contribution to the amplitude will have a flatter t -dependence than the pole and will be approximately independent of energy since it has a trajectory with intercept of about one and a slope half that of the pole. For a purely imaginary Pomeron the cut is also purely imaginary but with opposite sign so the cut should have the right phase to produce

the dip observed in $\frac{d\sigma}{dt}$. However, the t -dependence of the cut calculated using (3.6.10) from the eikonal model is only about half as steep as that of the pole and so still much too steep to describe the large $|t|$ data and its magnitude is such that it produces a dip at too small a value of $|t|$. There is some uncertainty though, in the form of the Gribov vertex $N(t, t_1, t_2)$ in (3.6.9), which allows us to change the magnitude and t -dependence of the cut relative to the pole. In the eikonal model, $N(t, t_1, t_2) = 1$, but we can reproduce the right sort of shape for the cut if we instead take

$$(N(t, t_1, t_2))^2 = \lambda e^{b_1 t} \quad (4.1.2)$$

for the Gribov vertex, which just multiplies the cut contribution calculated from (3.6.10) since it is independent of t_1 and t_2 . Then if $b_1 < 0$ this factor reduces the rate at which the cut contribution falls off with $|t|$ in agreement with the large $|t|$ data.

From (3.6.6) the Pomeron cut has trajectory given by

$$\alpha_{2P}(t) = 2\alpha_P\left(\frac{t}{4}\right) - 1 \quad (4.1.3)$$

and so the s -dependences of the cut term, modulo $\log s$ factors, and the pole term, assuming a linear Pomeron trajectory, $\alpha_P(t) = \alpha_P(0) + \alpha'_P t$, are given by

$$A^P \simeq s^{\alpha_P(0) + \alpha'_P t} \quad \text{and} \quad A^{2P} \simeq s^{2\alpha_P(0) - 1 + \frac{\alpha'_P}{2} t} \quad (4.1.4)$$

So that, using, $\frac{d\sigma}{dt} \simeq \frac{|A|^2}{s^2}$, the pole contribution to the differential cross-section has an energy independent point at $|t| = \frac{\epsilon_P}{\alpha'_P}$ (where $\epsilon_P = \alpha_P(0) - 1$) and the cut at $|t| = \frac{4\epsilon_P}{\alpha'_P}$. The shrinkage of $\frac{d\sigma}{dt}$ with energy occurs with these points as fulcrums and the angle turned through depends on the slope of the trajectory. From the ISR and Collider small $|t|$ data in figure 2.11 the energy independent point in the Pomeron contribution, which dominates small $|t|$, occurs for $|t| \approx 0.4 \text{ GeV}^2$ and so that of the cut should occur around $|t| \approx 1.6 \text{ GeV}^2$. In the region where the pole and the cut contributions overlap they cancel destructively and give a dip which moves with energy due to shrinkage as in figure 4.3. The data from ISR in figure 2.8 looks very much like this simple description.

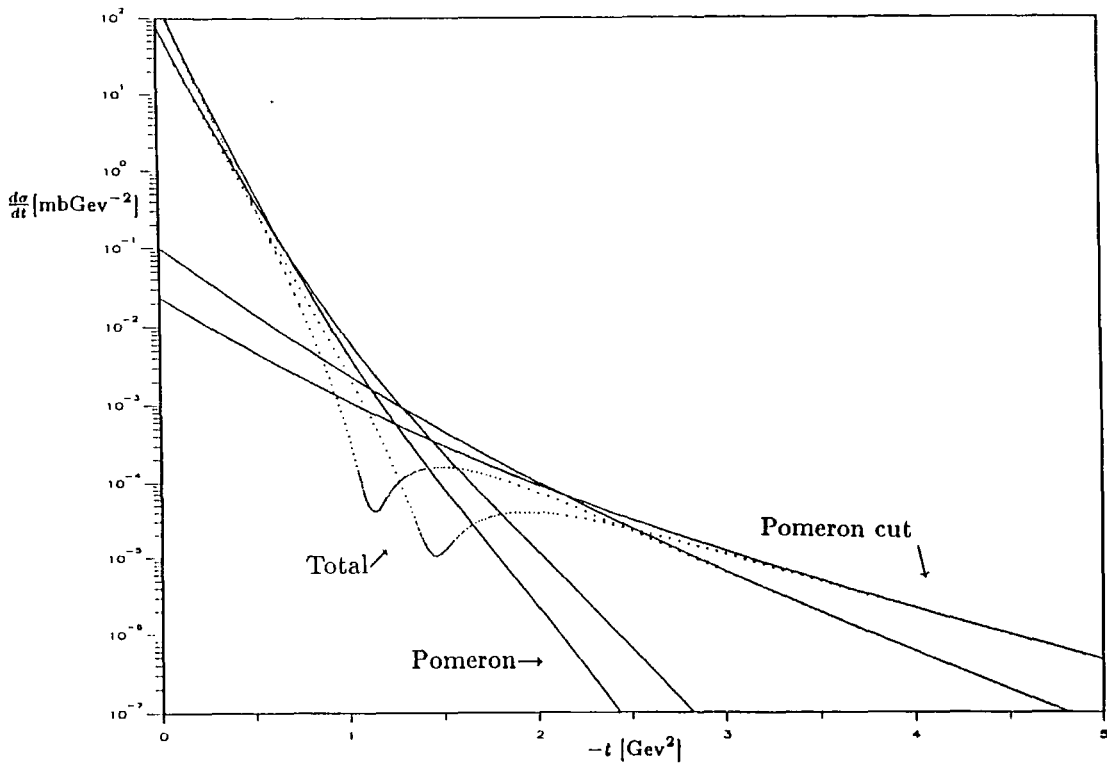


FIG.4.3 Movement of dip position with energy due to shrinkage of the pole and cut.

This “weak cut model” has been used very successfully to fit the ISR and lower energy data (see Collins and Gault (1976)). The finite value of $\frac{d\sigma}{dt}$ in the dip region occurs because of the small real part of the Pomeron pole and its cut due to their Regge phase. The shrinkage of the pole and cut produce movement and a filling in of the dip like that observed in the ISR data. At low energy, the large $|t|$ data require a different sort of energy behaviour from that seen in the ISR data (see §2.6). In Collins and Kearney (1984) this was described by a complicated superposition of $R \otimes P$ cuts and gave a reasonable fit to all the available data. Since then data has become available at very high energy from the collider at $\sqrt{s} = 546$ GeV. Straightforward extrapolation to the collider energy of the model with the parameters described in Collins and Gault (1978) gives the prediction shown in figure 4.4 . The small $|t|$ slope and magnitude at $\sqrt{s} = 546$ GeV is slightly wrong but more importantly the model fails to predict the change in $\frac{d\sigma}{dt}$ from a dip at the ISR to a shoulder at the collider. In this chapter we shall examine how the new data affect the parameter values and whether the model is compatible with the better data at high and low energies. We start by refitting the total cross-section which gives a best value for the Pomeron trajectory intercept. We

then try to fit the high energy differential cross-section data from the ISR and the Collider which fixes the Pomeron trajectory slope and finally extrapolate these fits to low energy and see how well the data can be described by the model.

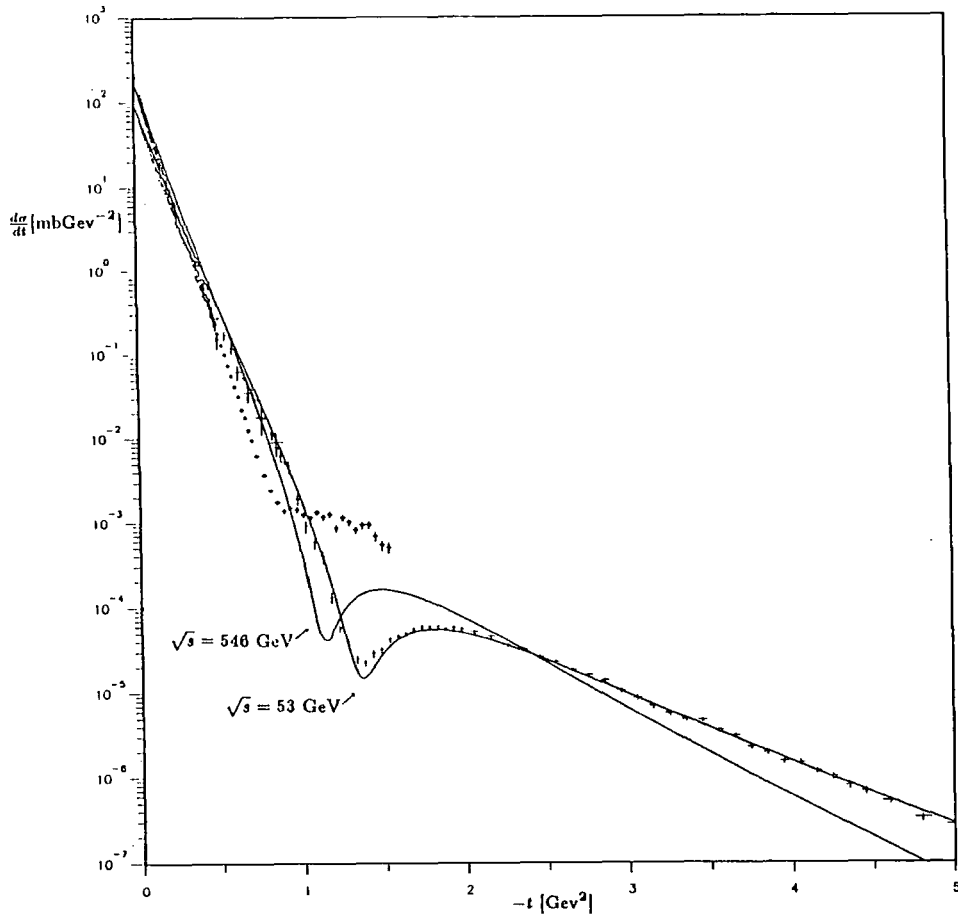


FIG.4.4 Prediction of the model of Collins and Gault (1978) for the differential cross-section at $\sqrt{s} = 53$ GeV (pp) and $\sqrt{s} = 546$ GeV ($\bar{p}p$).

4.2 Total cross-section.

Neglecting for the moment the Pomeron cut contribution to the total cross-section we have using (3.4.7) for the Regge pole amplitudes and the optical theorem :

$$\sigma_T \begin{pmatrix} pp \\ \bar{p}p \end{pmatrix} = \frac{1}{s} \left\{ \beta_P \left(\frac{s}{s_0} \right)^{\alpha_P(0)} + \beta_f \left(\frac{s}{s_0} \right)^{\alpha_f(0)} \mp \beta_\omega \left(\frac{s}{s_0} \right)^{\alpha_\omega(0)} \right\} \quad (4.2.1)$$

In this section we shall use the above expression to determine the value of the Regge parameters at $t = 0$. In the above s_0 is a scale parameter and should be of the order of the hadronic mass scale and so we choose for convenience $s_0 = 1$ GeV². For the above asymptotic behaviour to be applicable we need $s \gg s_0$. At lower energies we

expect other non-leading meson Regge trajectories and daughter trajectories to become significant. In fact the optical theorem (3.1.12) actually gives

$$\sigma_T = \frac{1}{s\sqrt{1 - \frac{4m^2}{s}}} \text{Im } A^{el}(s, t = 0) \quad (4.2.2)$$

which would produce deviations from leading Regge behaviour for $\sqrt{s} < 10 \text{ GeV}^2$ (unitarity implies A^{el} has a square root branch point of the form $\sqrt{1 - \frac{4m^2}{s}}$ at threshold which cancels the above singularity in pp but not $\bar{p}p$). Only by reference to the data can it be determined to how low an energy we can apply (4.2.1) but we expect that it should hold at least for $\sqrt{s} \geq 10 \text{ GeV}$ where s/s_0 is $\geq 10^2$.

As we saw in the previous section, the exchange degeneracy of the f and ω means that the f and ω Reggeon contributions to σ_T interfere destructively in pp scattering and constructively in $\bar{p}p$ scattering so that the pp amplitude is due mainly to the Pomeron. However, $\sigma_T(pp)$ falls with energy for $\sqrt{s} < 10 \text{ GeV}$, see figure 2.1, indicating either that exchange degeneracy does not hold exactly, or that the Pomeron contribution does not behave as a simple Regge pole, as we have supposed, but rises at low energy, or that there are some other contributions to σ_T which are important for $\sqrt{s} < 10 \text{ GeV}$. In both $\sigma_T(pp)$ and $\sigma_T(\bar{p}p)$ the fall of the cross-section with energy at low energies has approximately an $s^{-\frac{1}{2}}$ energy dependence indicating that the fall is most likely due to a breaking of the exchange degeneracy of the f and ω residues.

This simple s^α energy dependence continues down to $\sqrt{s} = 3.6 \text{ GeV}$ in $\Delta\sigma$ and the fall in $\sigma_T(pp)$ seems to have a similar energy dependence down to $\sqrt{s} = 4 \text{ GeV}$ below which there is a much steeper fall off with energy (see figure 2.1). Thus the data indicate that the simple Regge pole picture of (4.2.1) should hold down to $\sqrt{s} = 4 \text{ GeV}$. Below this one requires the inclusion of daughter trajectories in the amplitude (see Collins and Wright (1978)). If it is assumed that the exchange degeneracy of the residues is broken whilst that of the trajectories remains intact (so called weak exchange degeneracy) then, before data at the collider energy were available, a relatively small $\approx 20\%$ breaking of exchange degeneracy in the residues allowed a good fit to all the data on total hadronic cross-sections (as in, for example, Collins and Wright (1978)) so that exchange degeneracy was reasonably well obeyed. However, the collider data show that $\sigma_T(\bar{p}p)$ (and thus the Pomeron contribution to σ_T) increases faster at very high energies than the data at lower energies had previously indicated. From (4.2.1) we see

that the difference between the $\bar{p}p$ and pp total cross-sections is given by

$$\Delta\sigma = 2\beta_\omega \left(\frac{s}{s_0}\right)^{\alpha_\omega(0)-1} \text{ mb} \quad (4.2.3)$$

and depends only on the ω Reggeon which can thus be determined. The data on $\Delta\sigma$, figure 2.3, gives $\alpha_\omega(0) \approx \frac{1}{2}$. Since the f Reggeon has the same quantum numbers as the Pomeron it is not possible to separate their contributions uniquely and the data could be fitted with $\alpha_f(0) = \frac{1}{2}$, degenerate with the ω trajectory, by choosing suitable Pomeron parameters. However, the data at $\sqrt{s} = 546$ GeV give a better indication of the energy dependence of the Pomeron. We wish to see how well the Pomeron and f Reggeon can be determined using this longer lever-arm in energy (but still assuming that they behave as simple Regge poles).

Fixing $\alpha_f(0) = \alpha_\omega(0) = \frac{1}{2}$ in (4.2.1) and fitting $\sigma_T(pp)$ and $\sigma_T(\bar{p}p)$ for $\sqrt{s} \geq 4$ GeV we find

$$\sigma_T = \frac{1}{s} \{23.1s^{1.076} + 81.3s^{\frac{1}{2}} \mp 28.6s^{\frac{1}{2}}\} \text{ mb} \quad (4.2.4)$$

which is shown in figure 4.5 (this is very similar to the σ_T parametrization in Donnachie and Landshoff (1979) which uses $\alpha_R(0) = 0.44$ GeV⁻²). For $\sqrt{s} < 6$ GeV the fit misses the pp data and the overall χ^2 is very high, $\chi^2 = 413$ for 51 points. So the collider data implies that exchange degeneracy of the residues is broken by a factor $\frac{81.3}{28.6} \approx 300\%$ and the poor fit in the above shows we need breaking of exchange degeneracy of the trajectories also.

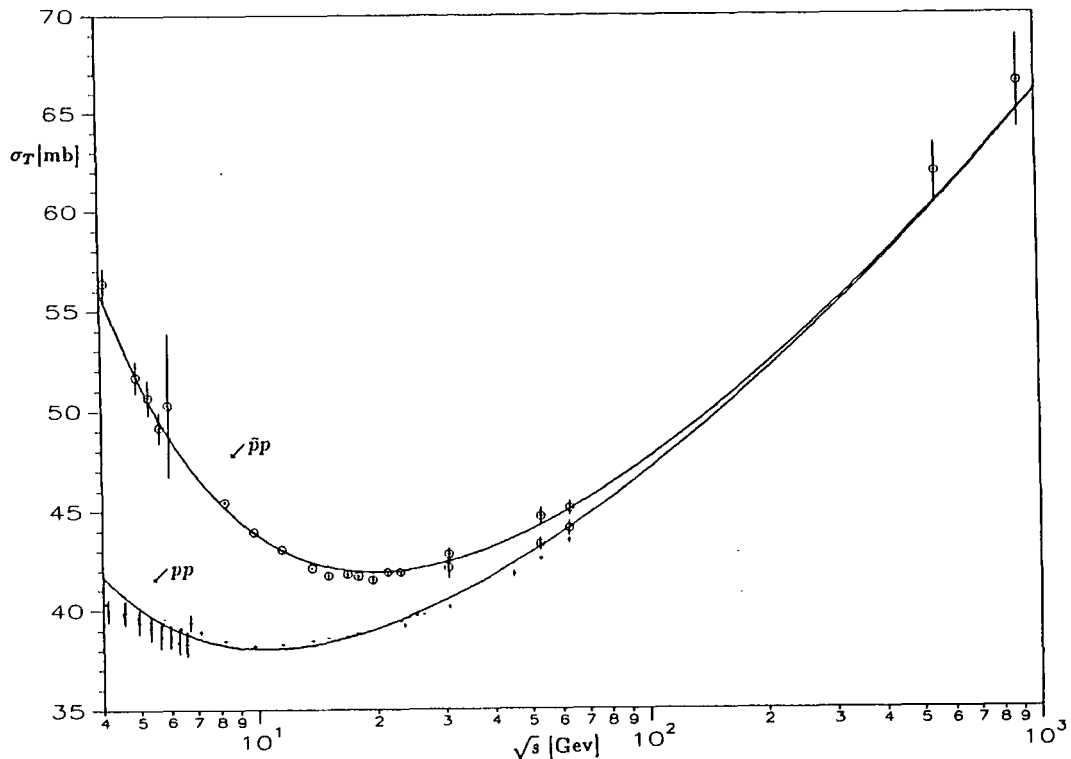


FIG.4.5 Prediction of the $\sigma_T(pp)$ and $\sigma_T(\bar{p}p)$ using exchange degenerate parametrization of eq.(4.2.4).

In our fits to σ_T we have forced the parametrization to go through the collider point by giving it a large weighting but we take the error of the measurement into account by using the data point as a variable parameter in the minimization program MINUIT and allowing it to vary within the experimental error of 61.9 ± 1.5 mb. We incorporate the systematic errors in the different data sets by giving each set a free parameter which adds equally to every point and is allowed to vary within the systematic error. The data from Carroll *et al* (1976/79) (see §2.2) are held fixed to normalize the surrounding data sets. A weight of $\times 3$ was attached to the ISR data. These extra parameters make it harder for MINUIT to find the minimum so we verify the results by repeating the fits with different initial parameter values and checking they converge to the same minimum. Typically we found that varying five parameters needed 800 calls to find the minimum and took about one CPU second on the IBM 3081.

We determine the trajectories from the data on $\sigma_T(pp)$ and $\sigma_T(\bar{p}p)$ but it should be born in mind that they are constrained by the particle masses in the Chew-Frautschi plots. The particles thought to lie on the f Reggeon trajectory are the $f_2(1270)$, $f_4(2030)$ and possibly the $f_6(2510)$ and on the ω trajectory the $\omega(783)$ and $\omega_3(1670)$

(formerly the f , h and r mesons and the ω and ω^* mesons). From the *Review of particle properties 1986* we have

Particle	$I^G(J^{PC})$	Mass (Gev)	Full Width (Gev)
$\omega(783)$	$0^-(1^{--})$	0.7826 ± 0.0002	0.0098 ± 0.0003
$\omega_3(1670)$	$0^-(3^{--})$	1.668 ± 0.005	0.166 ± 0.015
$f_2(1270)$	$0^+(2^{++})$	1.274 ± 0.005	0.176 ± 0.020
$f_4(2030)$	$0^+(4^{++})$	2.026 ± 0.012	0.200 ± 0.013
$f_6(2510)^\dagger$	$0^+(6^{++})$	2.510 ± 0.030	0.240 ± 0.060
† Not an established resonance.			

TABLE 4.1. Properties of particles on the f and ω trajectories.

The errors on the masses of the particles are much smaller than their full widths and using the mass errors the trajectories are well determined. The data does not support this precise continuation of the trajectories through the particle masses, for instance the f_6 does not lie exactly on the trajectory through the f_2 and f_4 . However, because in this t -region we are above the t -channel threshold, $t = 4m_\pi^2$, the trajectories are no longer purely real and at values of t corresponding to resonances they have an imaginary part given by

$$Im \alpha_R(m^2) = m \Gamma Re \alpha'_R(m^2) \quad (4.2.5)$$

where m and Γ are the mass and width of the resonance respectively. To account for the uncertainty in how to continue the trajectories for $t > 0$ we use the widths of the resonances as errors on the masses used to determine the trajectories rather than the experimental errors to which the masses are known. Figure 4.6 shows the Chew-Frautschi plots for the two trajectories.

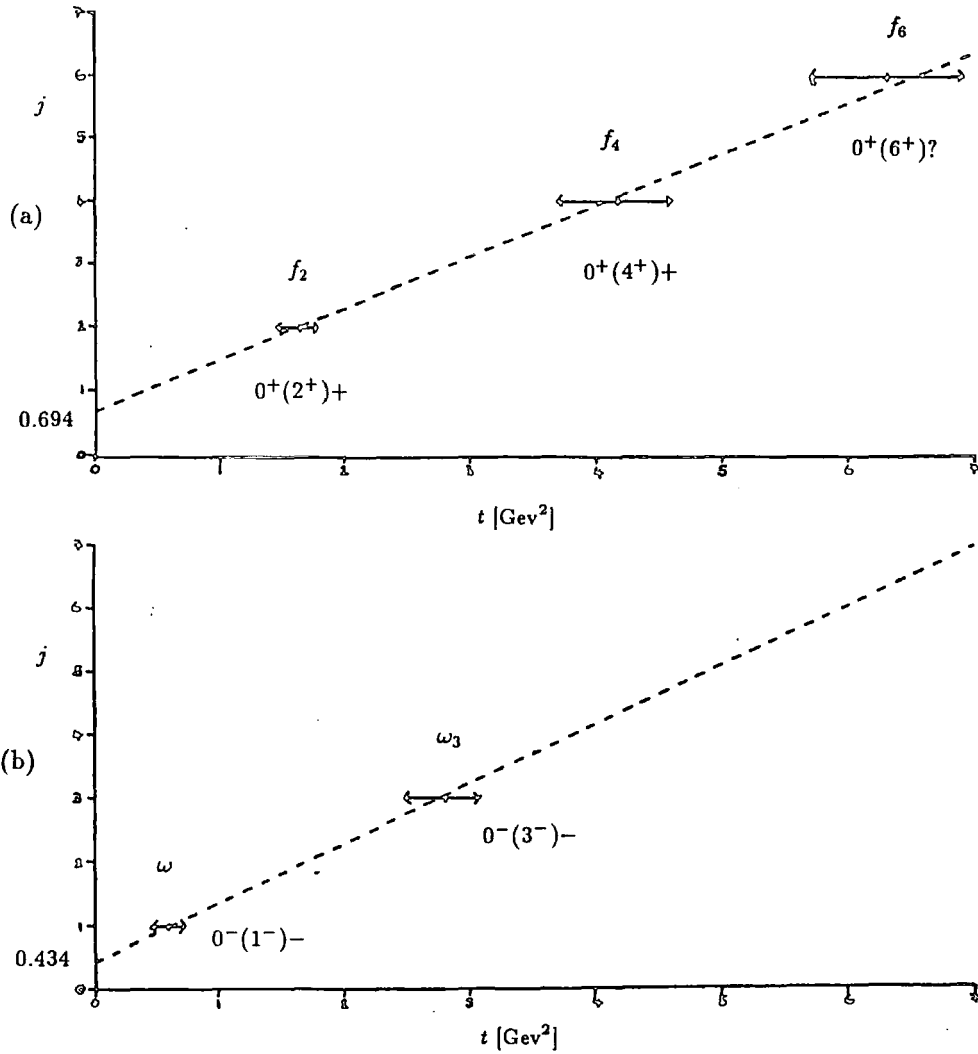


FIG.4.6 Chew-Frautschi plots for the (a) f and (b) ω Regge trajectories.

Using a simple least squares calculation for the trajectories we obtain

	(a) Using Full Width	(b) Using Mass errors
$\alpha_\omega(0)$	0.435 ± 0.128	0.435 ± 0.008
α'_ω	0.922 ± 0.118	0.922 ± 0.007
$\alpha_f(0)$	0.623 ± 0.337	0.669 ± 0.037
α'_f	0.842 ± 0.102	0.819 ± 0.014

TABLE 4.2. Trajectory intercepts and slopes from particle masses.

Column (a) in table 4.2 contains the values obtained using the the full widths and column (b) using the errors on the particle masses.

The ω intercept can also be determined from the $\Delta\sigma$ data using (4.2.3). We performed

a fit to the data on $\Delta\sigma$ for $\sqrt{s} > 3.6$ GeV from §2.3) and found a best fit for

$$\beta_\omega = 41.6 \text{ mb} , \alpha_\omega(0) = 0.412 \quad (4.2.6)$$

which gave $\frac{\chi^2}{\nu} = \frac{40}{32}$ and agrees with the value obtained from the masses of the ω and ω_3 in table 4.2 . This is shown in figure 4.7 . For $\sqrt{s} < 3$ GeV some other contribution to the odd part of the amplitude is needed with steeper energy dependence than ω Reggeon exchange as can be seen from the $\sigma_T(pp)$ data in fig.2.1 .

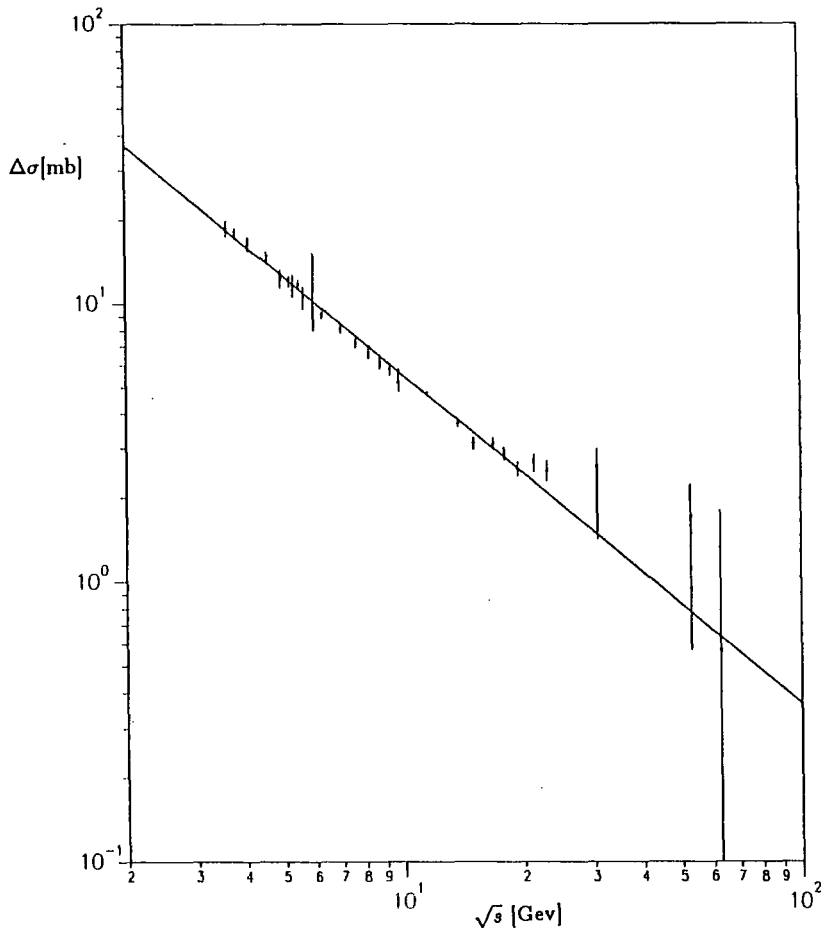


FIG.4.7 Result of a fit to $\Delta\sigma$ using (4.2.3) and (4.2.6).

The small contribution of the ρ Reggeon to $\Delta\sigma$ should have been included if we were trying to obtain the ω intercept as accurately as possible and we could also have included the data for $t < 0$ on $K_L^0 p \rightarrow K_S^0 p$ which is due mainly to the ω Reggeon, though universality implies that the ω residue is $3\times$ smaller than in pp scattering whilst the ρ contribution is the same so that the effect of the ρ is more significant. These are taken into account in Aronson 1983 where it is found $\alpha_\omega(0) = 0.44 \pm 0.01$ consistent with the above. However, we are interested only in fixing the odd charge conjugation part of the amplitude and so shall use (4.2.6).

With the ω parameters : $\beta_\omega, \alpha_\omega(0)$, fixed we determined the parameters of the Pomeron and f Reggeon : $\beta_P, \alpha_P(0), \beta_f, \alpha_f(0)$, in (4.2.1) by fitting the $\sigma_T(pp)$ and $\sigma_T(\bar{p}p)$ data for $\sqrt{s} > 4$ GeV as described above. We obtain a best fit for the parametrization

$$\sigma_T = \frac{1}{s} \{18.8s^{(1.094)} + 66.6s^{(0.629)} \mp 41.55s^{(0.412)}\} \text{ mb} \quad (4.2.7)$$

This is shown below in figure 4.8 . We find the collider data requires a larger value for $\alpha_P(0)$ than before *e.g.* Collins and Gault (1978) used $\alpha_P(0) = 1.067$. It is also slightly larger than that found in Donnachie and Landshoff (1979) where $\alpha_P(0) = 1.08$ because we have allowed different intercepts for the f and ω trajectories and therefore obtain a better fit to the data. The f trajectory intercept, $\alpha_f(0) = 0.629$, is in agreement with that from the particle masses in table 4.2 .

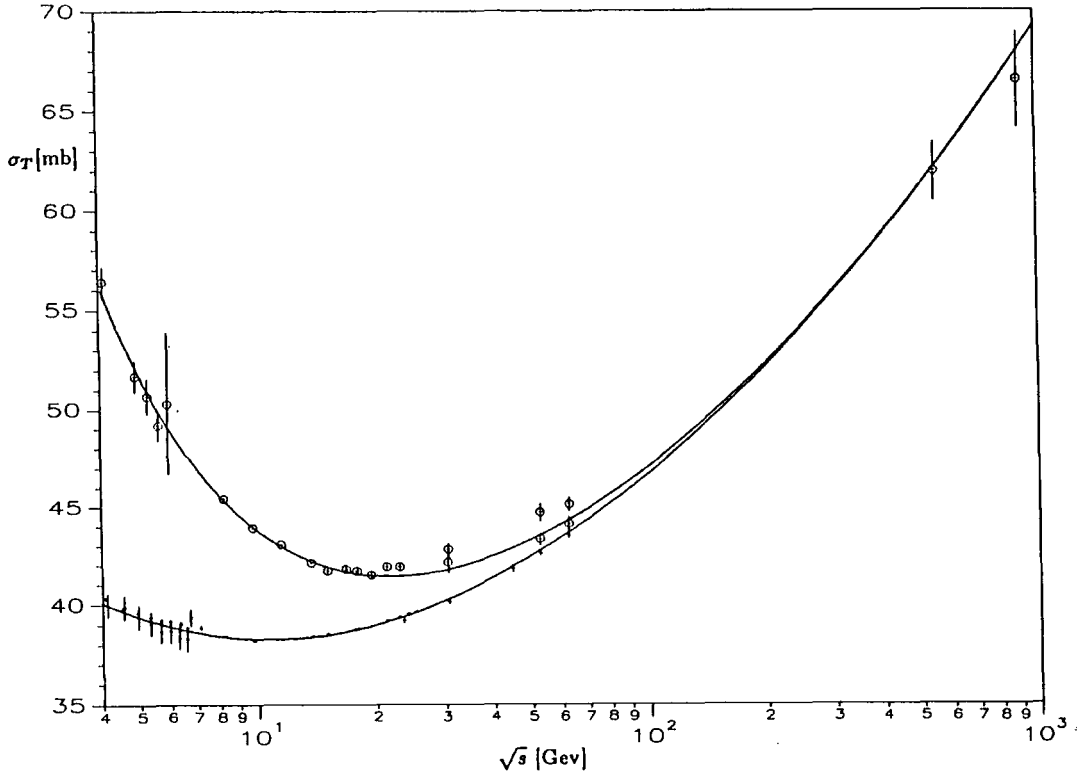


FIG.4.8 Result of a fit to $\sigma_T(pp)$ and $\sigma_T(\bar{p}p)$ using (4.2.7).

In order to determine the possible range of $\alpha_P(0)$ we have fitted the $\sigma_T(pp)$ and $\sigma_T(\bar{p}p)$ for $\sqrt{s} \geq 10$ GeV with different values of $\alpha_P(0)$ and varied $\beta_P, \beta_f, \alpha_f(0)$, with β_ω and $\alpha_\omega(0)$ fixed as above. For large values of $\alpha_P(0)$, $\alpha_f(0)$ also gets large and, if somewhat arbitrarily, we regard $\alpha_f(0) = 0.75$ as the largest value we are prepared to tolerate, this fixes $\alpha_P(0) \leq 1.12$ (though as we saw above $\alpha_f(0)$ is not really much

restricted by the particle masses). It is only the requirement that the f trajectory should not be too different from the other meson Regge trajectories that places an upper limit on $\alpha_f(0)$. Using only the cross-section data for $\sqrt{s} \geq 10$ GeV we find the best fit for $\alpha_p(0) = 1.091$ but $\alpha_p(0)$ is not well determined and values within the range $1.08 \leq \alpha_p(0) \leq 1.11$ give reasonable fits to σ_T consistent with the f intercept from the particle masses (note that the best fit does not correspond to lowest χ^2 in table 4.3 because of the weighting we have used).

We repeated these fits using the data for $\sqrt{s} \geq 4$ GeV with similar results which are shown in figure 4.9 for selected values of $\alpha_p(0)$ compared with the $\sigma_T(pp)$ data. The best fit occurs for $\alpha_p(0) = 1.089$ but $\alpha_p(0) = 1.090 \pm 0.005$ does almost as well. Figure 4.9 shows that only for $\alpha_p(0) > 1.10$ do the fits differ significantly (note ISR data have a 0.25 mb systematic error). The fact that we get about the same values for the parameters whether or not we include the low energy data lends support to the idea that our parametrization of the amplitude is valid down to $\sqrt{s} = 4$ GeV. Table 4.3 shows the parameter values obtained using the data for both $\sqrt{s} \geq 10$ GeV and $\sqrt{s} \geq 4$ GeV.

	(a) $\sqrt{s} \geq 10$ GeV ($\nu = 16$ points)					(b) $\sqrt{s} \geq 4$ GeV ($\nu = 51$ points)				
$\alpha_P(0)$	β_P	β_f	$\alpha_f(0)$	$\sigma_T(546)$	χ^2	β_P	β_f	$\alpha_f(0)$	$\sigma_T(546)$	χ^2
1.070	24.90	355.7	0.19	60.2	152.7					
1.080	21.96	91.07	0.47	60.4	16.6	21.91	77.65	0.539	60.3	96.4
1.085	20.72	74.66	0.57	60.9	10.4	20.66	71.41	0.584	60.7	50.0
1.089						19.81	70.14	0.602	61.6	49.8
1.090	19.66	69.52	0.61	61.6	9.5	19.68	69.91	0.604	61.7	48.3
1.095	18.63	65.76	0.63	62.3	9.1	18.73	68.76	0.623	62.6	52.0
1.100	17.64	63.86	0.66	63.1	8.6	17.76	67.12	0.643	63.4	63.3
1.105						16.60	63.92	0.675	63.4	122.
1.110	15.41	53.46	0.73	63.4	11.1	15.50	61.70	0.700	63.4	207.
1.115						14.46	60.05	0.723	63.5	312.
1.120	13.31	49.12	0.78	63.4	19.4	13.47	57.99	0.745	63.5	488.
1.130	11.44	46.84	0.81	63.4	29.6	11.66	55.95	0.778	63.4	555.

TABLE 4.3. Results of fits to $\sigma_T(pp)$ data for $\sqrt{s} \geq 10$ GeV and $\sqrt{s} \geq 4$ GeV at various fixed values of $\alpha_P(0)$. The value of σ_T given is at $\sqrt{s} = 546$ GeV.

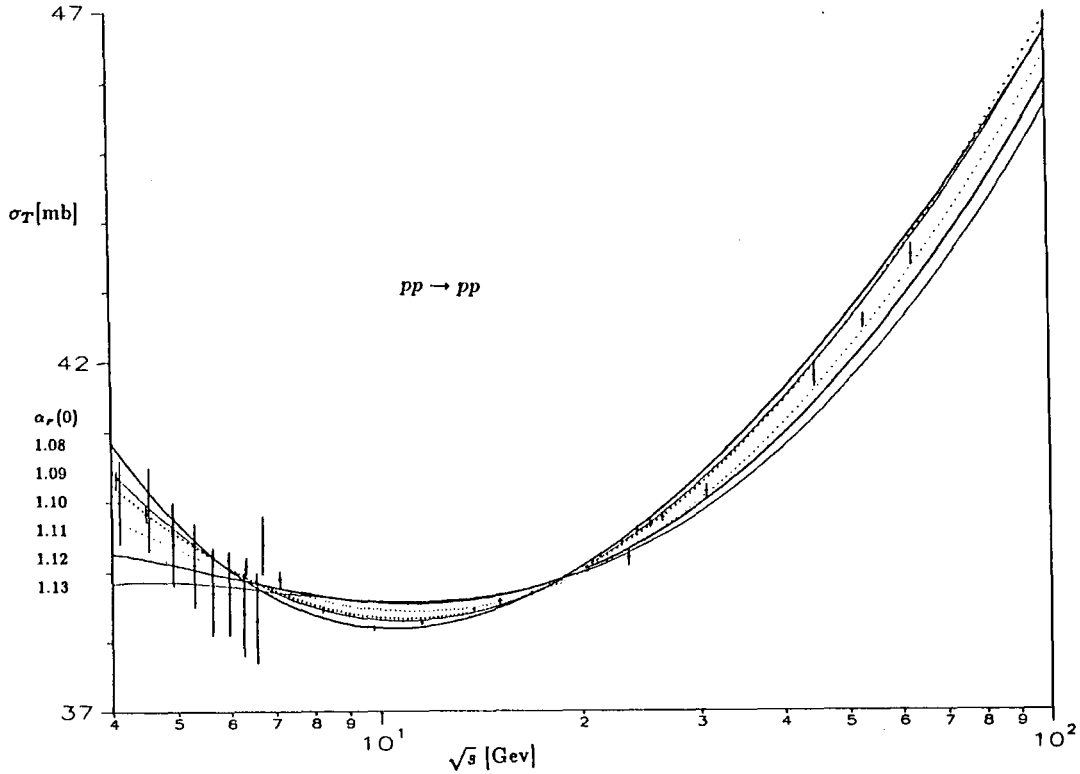


FIG.4.9 Resulting fit to σ_T using data for $\sqrt{s} \geq 4$ GeV for $\alpha_P(0)$ fixed at : 1.08, 1.09, 1.10, 1.11, 1.12, 1.13 .

Figure 4.10 shows the different contributions of the terms in (4.2.7) to σ_T . It can be seen that the f Reggeon contribution is much larger than that of the ω Reggeon and at $\sqrt{s} = 4$ GeV it is as large as the Pomeron contribution but falls rapidly with energy. The Pomeron contribution shows quite a steep rise with energy. The Pomeron cut contribution shown is that calculated from fit (4a) in §4.4 and gives a contribution of approximately one millibarn at the Collider energy. Including the Pomeron cut contribution (4.1.4) in the parametrization of σ_T will produce a small change in the parameter values. Since the cut contribution interferes destructively with the Pomeron pole and its magnitude increases with energy we expect that the cut will increase the value of $\alpha_P(0)$ (see §4.7).

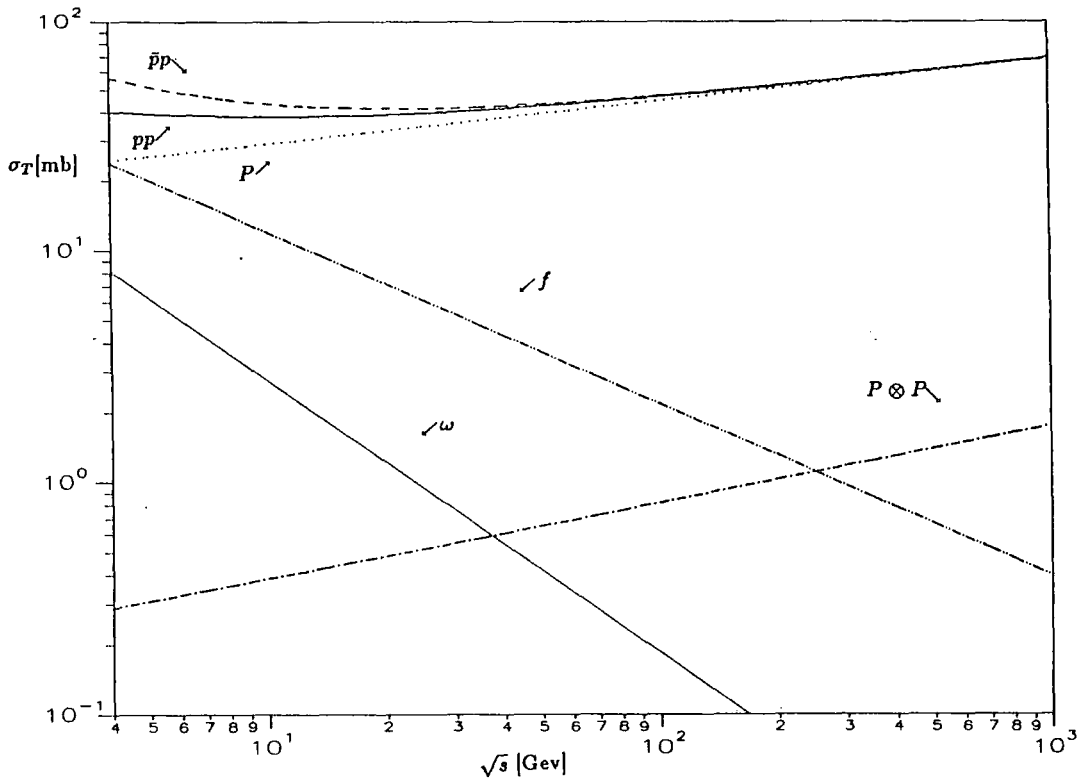


FIG.4.10 Contributions to σ_T in (4.2.7).

4.3 Prediction of Re/Im.

The data for ρ have been described in §2.4. Since we have fitted $\sigma_T(pp)$ and $\sigma_T(\bar{p}p)$, which determines the imaginary part of the amplitude for both positive and negative, the real part should be given by the dispersion relation (3.1.11) (with one subtraction provided $\Delta\sigma \rightarrow s^{-\delta}$ for $s \rightarrow \infty$ where $\delta > 0$). Thus to the extent that we can neglect the low energy behaviour of σ_T , which is not fitted by (4.2.1), ρ is completely dependent on σ_T (if subtraction constant negligible) and does not have to be fitted separately (see Amaldi (1977)). The value of ρ predicted by the Regge phases of (4.2.7) is shown in figure 4.11 as a function of \sqrt{s} for pp and $\bar{p}p$ scattering. It can be seen that for $\sqrt{s} \leq 10$ GeV the prediction falls about 20% below the data. Also shown in figure 4.12 are the predictions for $\alpha_P(0) = 1.08 \rightarrow 1.13$ from the fits in table 4.3. As the value of $\alpha_P(0)$ increases the agreement with the low energy data for ρ improves and we find a good agreement with ρ for $\alpha_P(0) \geq 1.12$, but from table 4.3 this is too high a value of $\alpha_P(0)$ to give an acceptable fit to σ_T . Thus it does not seem to be as good to assume that the real part of the amplitude is entirely due to $P + f + \omega$ down to $\sqrt{s} = 4$ GeV as it is for the imaginary part. At low energy one cannot neglect the low energy behaviour of σ_T in the calculation of the real part of the amplitude from dispersion relations and the full dispersion relation should be used. In Regge terms this means that other trajectories should be included in the calculation of the real part

and that all the pole amplitude cuts should start at $s = 4m_p^2$ not at $s = 0$.

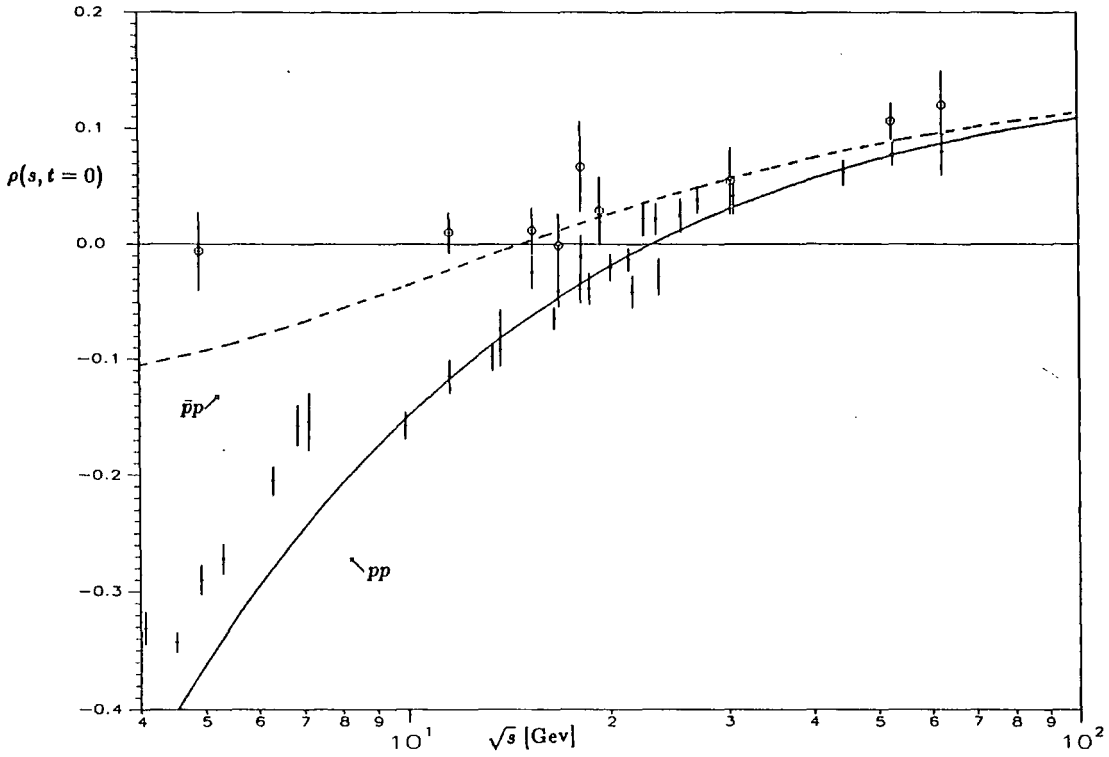


FIG.4.11 Prediction of ρ using (4.2.7) compared with $\rho(pp)$.

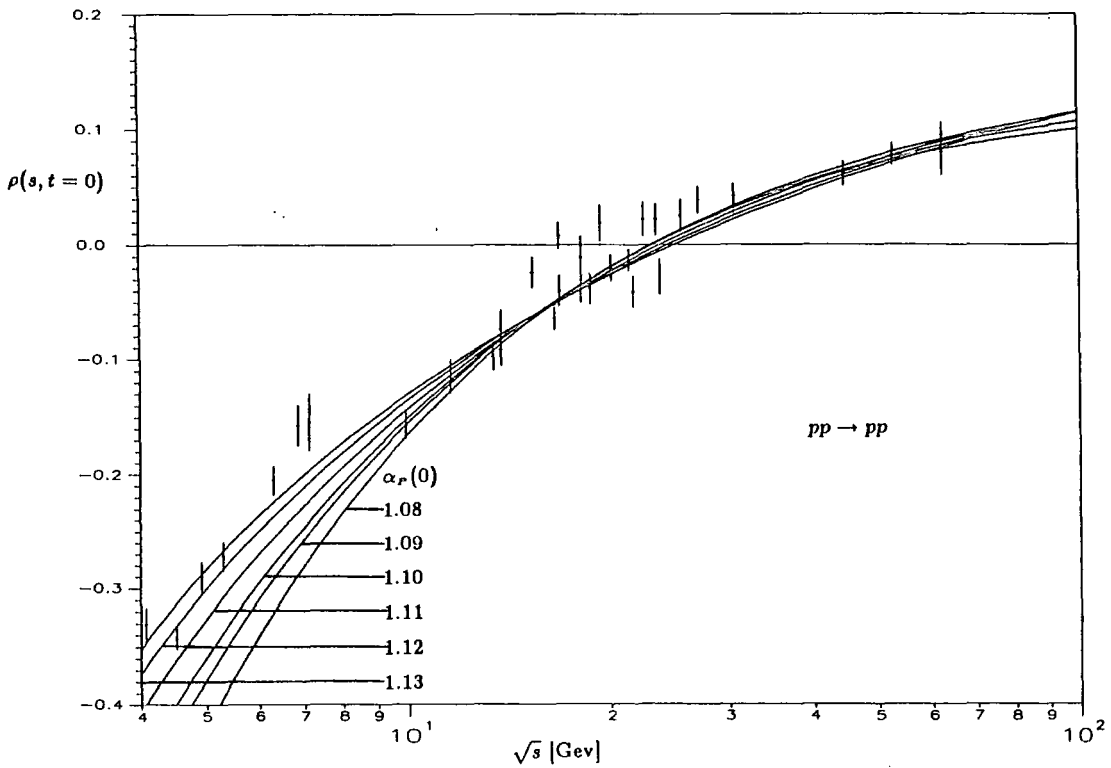


FIG.4.12 Prediction of ρ using fits (b) from table 4.3 compared with $\rho(pp)$.

4.4 Fits to the Differential Cross-section

Following Collins and Gault (1974a) we have used a double exponential form for the residue of the Pomeron pole in order to describe the break in the forward slope apparent in the data at $|t| \approx 0.2 \text{ GeV}^2$ (see figure 2.12). From (3.4.7) this gives for the even-signatured Pomeron amplitude

$$A^P(s, t) = -G_P \left(e^{-i\frac{\pi}{2}} \frac{s}{s_0} \right)^{\alpha_P(0)} e^{c_P t} [(1-x) + x e^{a_1 t}] \quad (4.4.1)$$

where $c_P = a_P + \alpha'_P \left(\ln \frac{s}{s_0} - i\frac{\pi}{2} \right)$. We define x and a_1 to be positive and put $s_0 = 1 \text{ GeV}^2$.

Substituting this into equation (3.6.1) for the cut amplitude and using the form

$$(N(t, t_1, t_2))^2 = \lambda e^{b_1 t} \quad (4.4.2)$$

for the Gribov vertex we find for the Pomeron cut amplitude (using equations A.4 and A.5)

$$\begin{aligned} A^{2P}(s, t) = & + \frac{G_P^2}{32\pi} \left(e^{-i\frac{\pi}{2}} \frac{s}{s_0} \right)^{2\alpha_P(0)-1} \lambda e^{b_1 t} \left[\frac{(1-x)^2}{c_P} \exp \left\{ \frac{1}{2} c_P t \right\} \right. \\ & + \frac{4x(1-x)}{(a_1 + 2c_P)} \exp \left\{ \frac{c_P(a_1 + c_P)}{(a_1 + 2c_P)} t \right\} \\ & \left. + \frac{x^2}{(a_1 + c_P)} \exp \left\{ \frac{1}{2}(a_1 + c_P)t \right\} \right] \end{aligned} \quad (4.4.3)$$

This represents a hard branch cut in the complex angular momentum plane of the form, $\log(j - \alpha_{2P})$, with rightmost branchpoint occurring at $\alpha_{2P}(t) = 2\alpha_P\left(\frac{t}{4}\right) - 1$ as in (3.6.6). Using (4.1.4) for the Pomeron trajectory, $\alpha_P(t)$, the cut trajectory is given by

$$\alpha_{2P}(t) = 2\alpha_P(0) - 1 + \frac{\alpha'_P}{2} t \quad (4.4.4)$$

so that it has half the slope of the pole. The $\frac{1}{c_P}$ factors in the denominators of the terms in (4.4.3) are complex and so at non-asymptotic energies the phase of the cut term is not just given by its trajectory. For $\ln s \gg \frac{\alpha_P}{\alpha'_P}$ these effects are negligible and (4.4.3) has the simple energy behaviour $A^{2P} \sim \frac{1}{\ln s} (e^{-i\frac{\pi}{2}} s)^{\alpha_{2P}(t)}$. At ISR energies $\ln s \approx 8$ and $\frac{\alpha_P}{\alpha'_P} \approx 10 \rightarrow 60$, so that it is not a good approximation that the $\ln s$ term dominates at current energies.

The f and ω Reggeons with even and odd signatures respectively are given by

$$\begin{aligned}
 A^f(s, t) &= -G_f \left(e^{-i\frac{\pi}{2}} \frac{s}{s_0} \right)^{\alpha_f(0)} e^{c_f t} \\
 A^\omega(s, t) &= \mp i G_\omega \left(e^{-i\frac{\pi}{2}} \frac{s}{s_0} \right)^{\alpha_\omega(0)} e^{c_\omega t} \left(1 + \frac{t}{t_0} \right) \quad \text{for } \begin{array}{l} pp \\ \bar{p}p \end{array}
 \end{aligned}
 \tag{4.4.5}$$

where $c_R = a_R + \alpha'_R \left(\ln \frac{s}{s_0} - i\frac{\pi}{2} \right)$. The $\left(1 + \frac{t}{t_0} \right)$ factor is introduced into the residue of the ω Reggeon in order to account for the cross-over zero effect which occurs in pp and $\bar{p}p$ scattering (see Collins, Gault and Martin (1974a)). This is just used as a convenient way of reproducing the effect seen in the data. It is known from polarization measurements that the zero only occurs in the imaginary part of the amplitude at this point and not in the real part and also it is not seen in some other processes connected by factorization like $\pi^\pm p \rightarrow \rho^\pm p$ suggesting that cuts are also present but since the amplitude is predominantly imaginary the real part is negligible and this parametrization will do (it also gives some evidence that the cuts are pole dominated).

The amplitudes defined above are dimensionless and σ_T and $\frac{d\sigma}{dt}$ are given by (A.1) and (A.2). Comparing with (4.2.1) this gives

$$\begin{aligned}
 \beta_P &= \frac{1}{0.3893} G_P \sin \frac{\pi}{2} \alpha_P(0) \\
 \beta_f &= \frac{1}{0.3893} G_f \sin \frac{\pi}{2} \alpha_f(0) \\
 \beta_\omega &= \frac{1}{0.3893} G_\omega \cos \frac{\pi}{2} \alpha_\omega(0)
 \end{aligned}
 \tag{4.4.6}$$

so that G_P , G_f , G_ω , $\alpha_P(0)$, $\alpha_f(0)$ and $\alpha_\omega(0)$ are all determined by (4.2.7). The Reggeon slope parameters are fixed by the Chew-Frautschi mass plots above and we take the values of α'_f and α'_ω from table 4.2(a). The high energy differential cross-section should not be very sensitive to the Reggeon parameters and so for a first approximation we fix the values for a_f , a_ω and t_0 in (4.4.5) at those obtained in Collins and Gault (1978).

Thus the only free parameters left are those that give the t -dependence of the Pomeron pole and cut and the magnitude of the cut relative to the pole namely: α'_P , x , a_1 , a_P , λ and b_1 . At large $|t|$ the Pomeron cut should dominate the amplitude because of its flat t -dependence even at quite low energies, but should not be too important at sufficiently small $|t|$. From the fit of Collins and Gault (1978), at $\sqrt{s} = 53$ GeV the cut gives a 3% correction to the differential cross-section at $|t| = 0$ and 17% at

$|t| = 0.4 \text{ GeV}^2$, rising to 5% and 26% respectively at $\sqrt{s} = 546 \text{ GeV}$, so the fit to even very small $|t|$ will be affected by the cut. However, as a first approximation we determine the Pomeron parameters α'_p , x , a_1 and a_p by fitting only the data for $|t| \leq 0.4 \text{ GeV}^2$. The contribution of the Reggeons in (4.2.7) has about a 20% effect on $\frac{d\sigma}{dt}$ at $t = 0$ and $\sqrt{s} = 53 \text{ GeV}$ and so cannot be neglected but the the Reggeon parameters have been reasonably well tied down so they do not much effect our determination of the Pomeron contribution. We fit only the high energy data for $\sqrt{s} \geq 53 \text{ GeV}$ in order to minimize the effect of the Reggeons. Fitting the data for $|t| \leq 0.4 \text{ GeV}^2$ at $\sqrt{s} = 53 \text{ GeV}$ and $\sqrt{s} = 546 \text{ GeV}$ from §2.5 with no cut contribution included in the parametrization and adjusting the weighting of the data to obtain the best fit, we find the data requires $\alpha'_p \approx 0.25 \rightarrow 0.32 \text{ GeV}^{-2}$. The lowest value of α'_p which can be tolerated by the data is about $\alpha'_p = 0.2 \text{ GeV}^{-2}$, the best fit obtained for $\alpha_p(0) = 0.31$. The resulting fit using $\alpha_p(0) = 0.31$ is shown in figure 4.12(a) and the effect of omitting the Reggeon contributions on the fit is shown in figure 4.12(b). Though the Reggeons are a small effect their effect on $\frac{d\sigma}{dt}$ is not negligible. We also used two dipole form factor parametrizations for the Pomeron residue taken from Donnachie and Landshoff (1979) eq.(4.4.7) and Collins and Wright (1978) eq.(4.4.8) and fitted them to the same data to compare with the double exponential parametrization we used in (4.4.1). The dipole fits gave a significantly better χ^2 compared with the double exponential parametrization and there was no significant difference between the results obtained with the different dipole forms (the χ^2 obtained depends on the weights attached to the data sets and only provides a relative measure of the quality of the fits).

$$F_1(t) = \frac{4m_p^2 - 2.79t}{4m_p^2 - t} \frac{1}{\left(1 - \frac{t}{0.71}\right)^2} \quad (4.4.7)$$

$$F_1(t) = \frac{1}{\left(1 - \frac{t}{m_p^2}\right)} \frac{1}{\left(1 - \frac{t}{0.9}\right)} \quad (4.4.8)$$

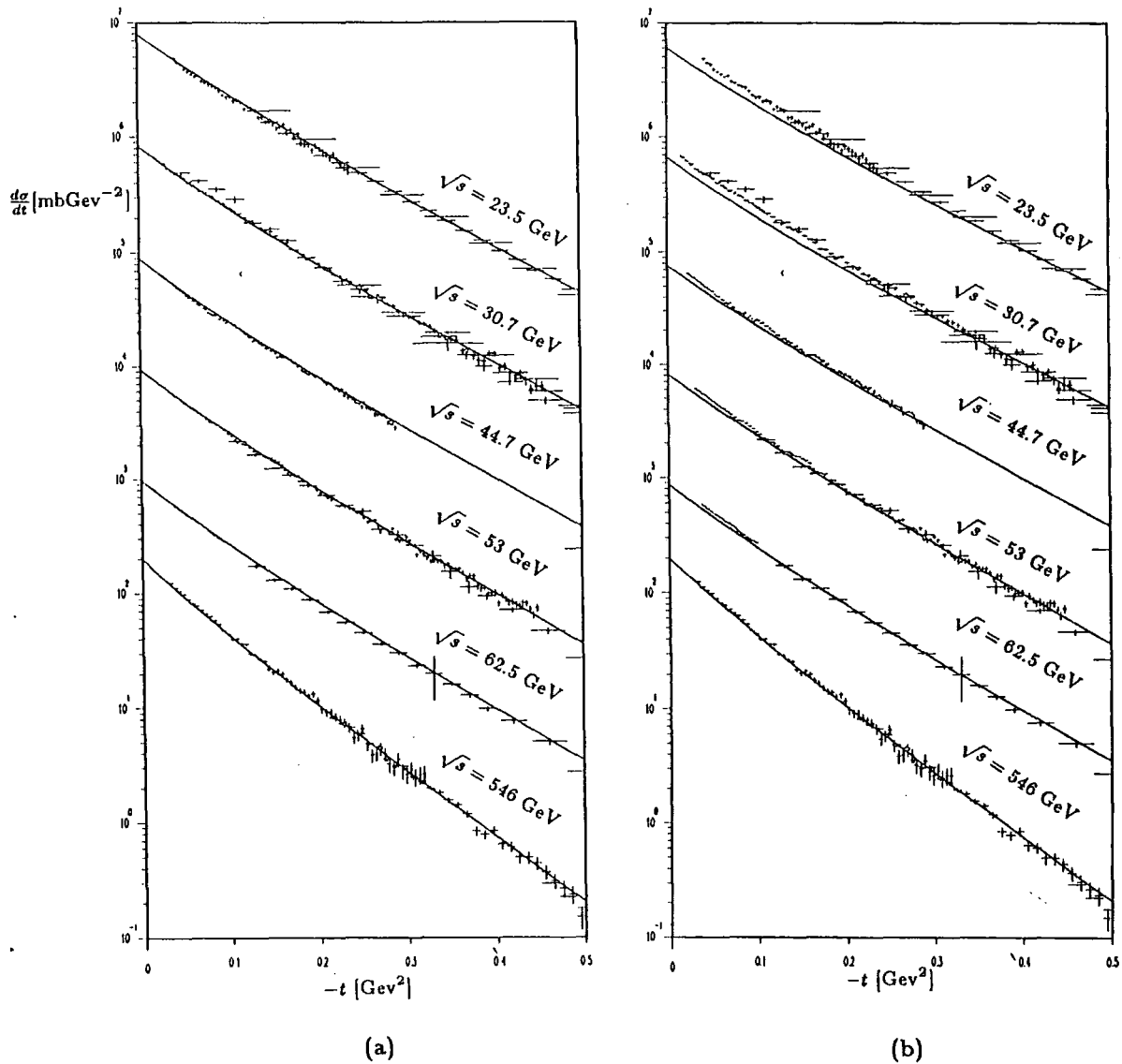


FIG.4.12 (a) Resulting small $|t| \frac{d\sigma}{dt}$ from above fit at various energies, (b) effect of omitting Reggeon contribution in above fit.

In the above fits we used the normalizations for the data discussed in §2.6, those of Breakstone, Battiston and Bozzo were allowed to vary within their scale errors. The program typically took 20 cpu secs and 600 calls to find the minimum whilst varying 6 parameters.

We now try to include the cut contribution and to fit out to larger $|t|$ at the ISR by alternately fitting the small $|t|$ data for $|t| \leq 0.8 \text{ GeV}^2$ and $\sqrt{s} \geq 53 \text{ GeV}$ and then adjusting the cut parameters λ and b_1 to fit the large $|t|$ data for $|t| > 1 \text{ GeV}^2$ at

$\sqrt{s} = 23.5$ and 52.8 GeV from Nagy (1979). This does give a very good fit to the forward peak with $\alpha'_p = 0.31$ GeV $^{-2}$ but for the ISR data right of the dip region we find the model predicts too much energy dependence and the fit gives too high a value compared with the large $|t|$ data at $\sqrt{s} = 23.5$ GeV and too low a value compared with that at $\sqrt{s} = 53$ GeV. This is shown in figure 4.13. The model also gives a dip rather than the shoulder seen in the data at the Collider.

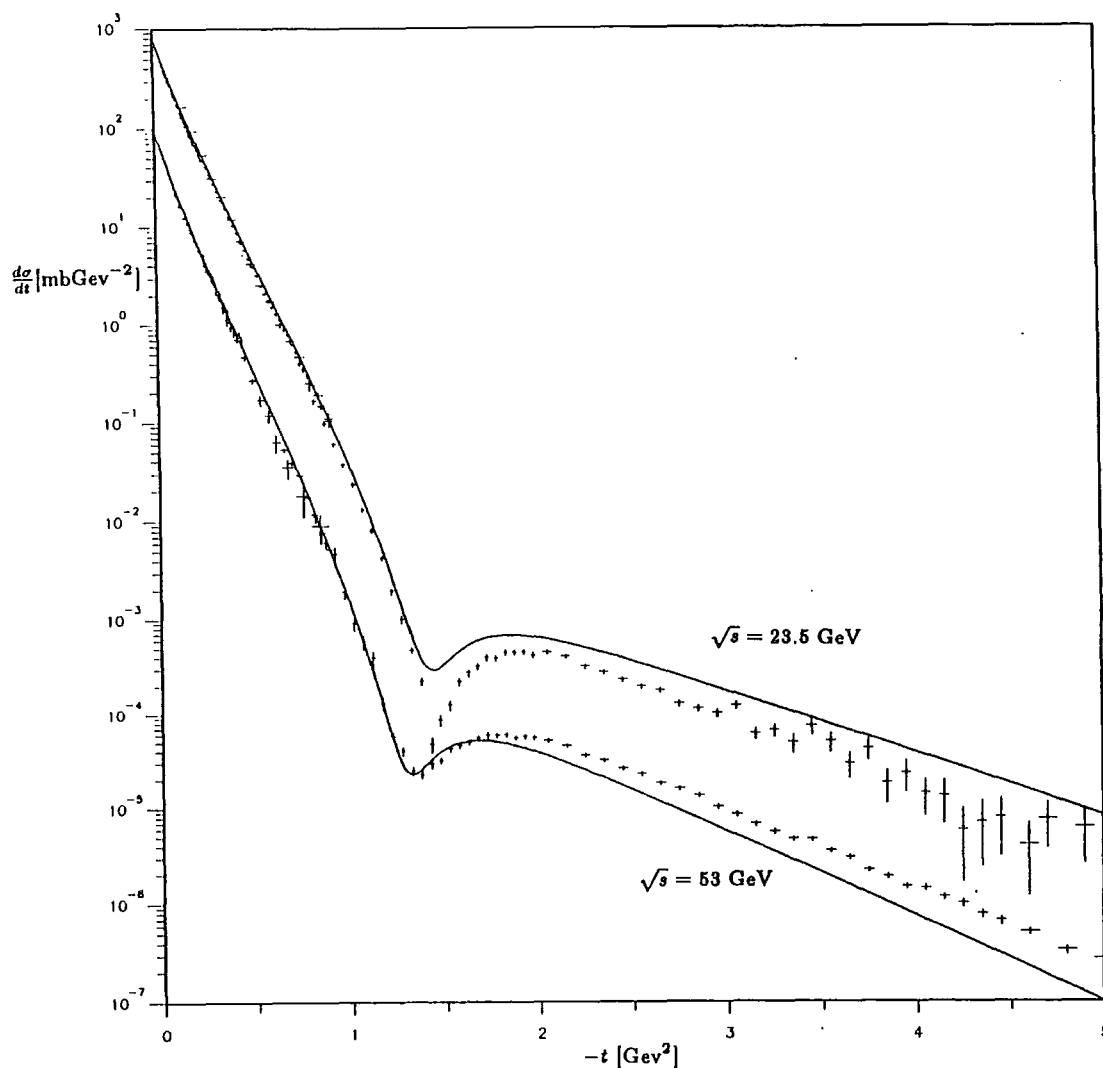


FIG.4.13 Fit to large $|t|$ data at $\sqrt{s} = 23.5$ and 53 GeV using $\alpha'_p = 0.31$ GeV $^{-2}$.

The large $|t|$ problem is caused by the high value of α'_p which determines the energy dependence of the Pomeron cut as well as the pole. The discrepancy can be clearly seen

from a plot of the cut trajectories at large $|t|$ calculated from the effective trajectory at small $|t|$ according to (3.6.6), compared with the effective trajectory at large $|t|$. This shown in figure 4.14 for 2-, 3-, 4-Pomeron cuts. The 2-Pomeron cut calculation is significantly different from effective trajectory for $|t| \geq 2 \text{ GeV}^2$. In fact the data agree much better with $\alpha'_{cut} = \frac{\alpha'_P}{3}$ corresponding to a three Pomeron cut. In view of this we tried fits in which the large $|t|$ data was described by a 3-Pomeron cut with a 2-Pomeron cut cancelling the Pomeron in the dip region. However, the phases of the three terms do not allow a fit with the correct shape in the dip region.

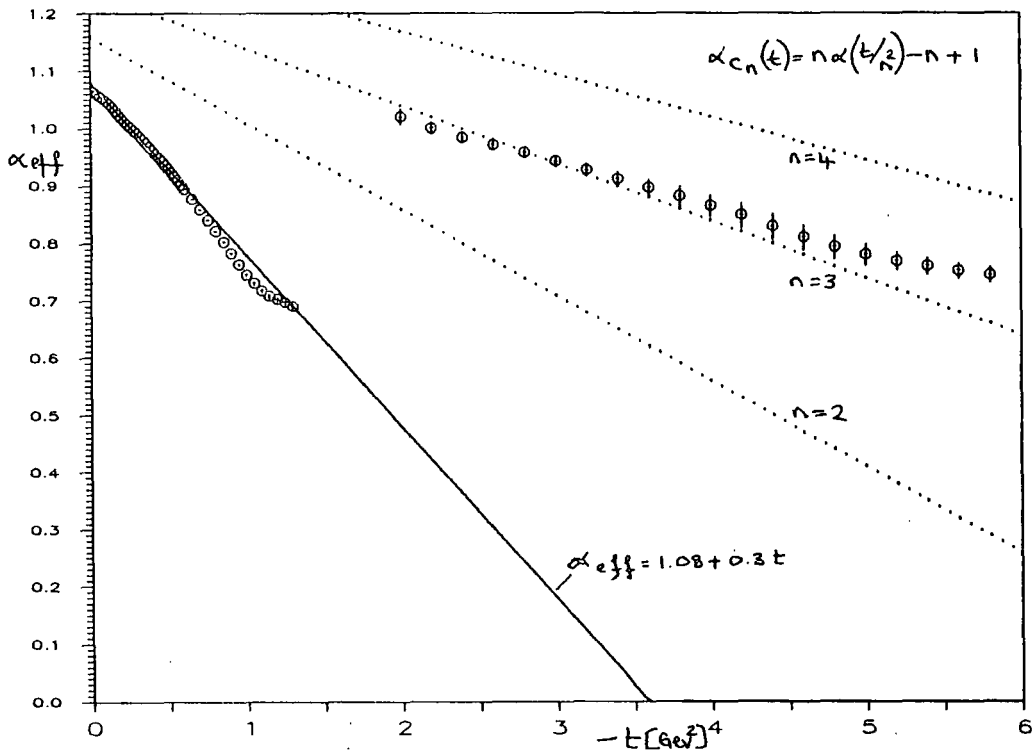


FIG.4.14 Multiple-Pomeron cut trajectories compared with large $|t|$ effective trajectory.

The problem of the energy dependence at large $|t|$ is therefore inherent in the simple version of the pole and weak cut model. The amplitude is dominated at small $|t|$ by the Pomeron pole and at large $|t|$ by the Pomeron cut with trajectories given by (4.1.3) having slopes α'_P and $\frac{\alpha'_P}{2}$ respectively. However, the effective trajectory calculation in §2.6 gives the trajectory slopes at small and large $|t|$ as $\alpha'_{eff} \approx 0.3$ and 0.07 GeV^{-2} respectively and so is incompatible with (4.1.3) (though the intercepts of the effective trajectories do more or less agree with their predicted values). We shall try to find the best fit possible in spite of this problem.

We have fitted the whole t -range simultaneously using the data at $\sqrt{s} = 23.5, 52.8$ and 546 GeV and the large $|t|$ data from Faissler at $\sqrt{s} = 19.5$ and 27.4 GeV (see Table 2.4). We find a best fit for $\alpha'_P = 0.15 \text{ GeV}^{-2}$ shown in fig.4.15 . The energy dependence at large $|t|$ and the dip at $\sqrt{s} = 53$ GeV are about right. The dip moves slowly inwards and is filled in as the energy is increased through the ISR region, which is in agreement with the ISR data though this does show the dip deepest at $\sqrt{s} = 30.7$ GeV rather than at $\sqrt{s} = 23.5$ GeV² and the dip produced by the fit is not quite deep enough at these two lowest ISR energies. The small $|t|$ fit is now not so good because of the low value of α'_P and the fit to the collider data for $|t| > 0.8 \text{ GeV}^2$ is not improved and still gives a dip, much below the data, rather than a shoulder. The parameter values obtained in this fit are given in table 4.6 and are referred to as fit(4a). A graph showing the individual contributions of the Pomeron and its cut is shown in figure 4.16 .

$\alpha_P(0)$	1.094	$\alpha_f(0)$	0.629	$\alpha_\omega(0)$	0.412
α'_P	0.145	α'_f	0.805	α'_ω	0.922
β_P	18.8	β_f	66.6	β_ω	41.6
a_P	2.452	a_f	1.35	a_ω	1.03
a_1	4.09	x	0.753	λ	0.107
b_1	-1.08	b_2	0.0	t_0	0.19

TABLE 4.4. Fit (4a) parameter values.

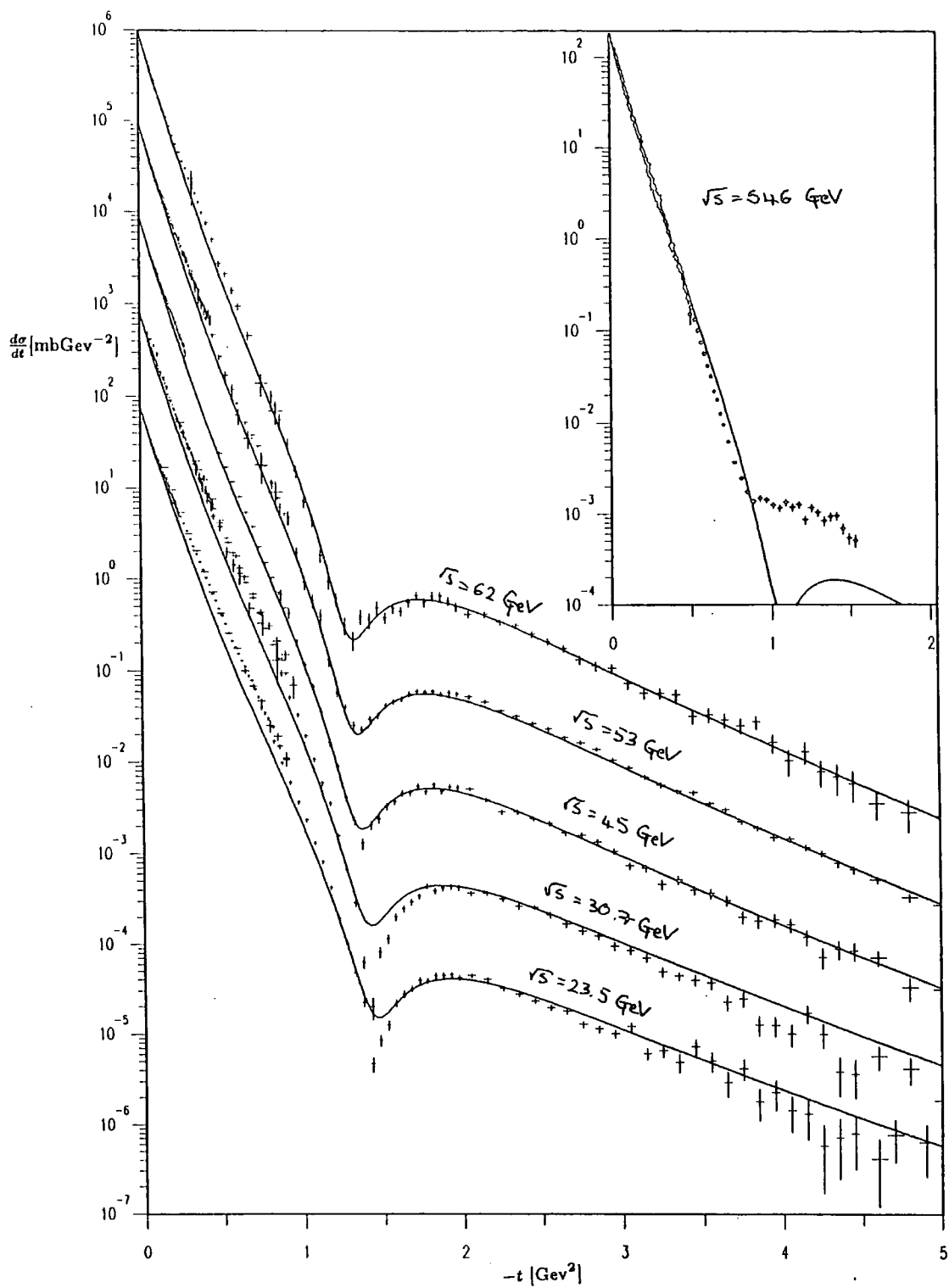


FIG.4.15 Fit (4a) compared with data at $\sqrt{s} = 23.5 \rightarrow 546 \text{ GeV}$.

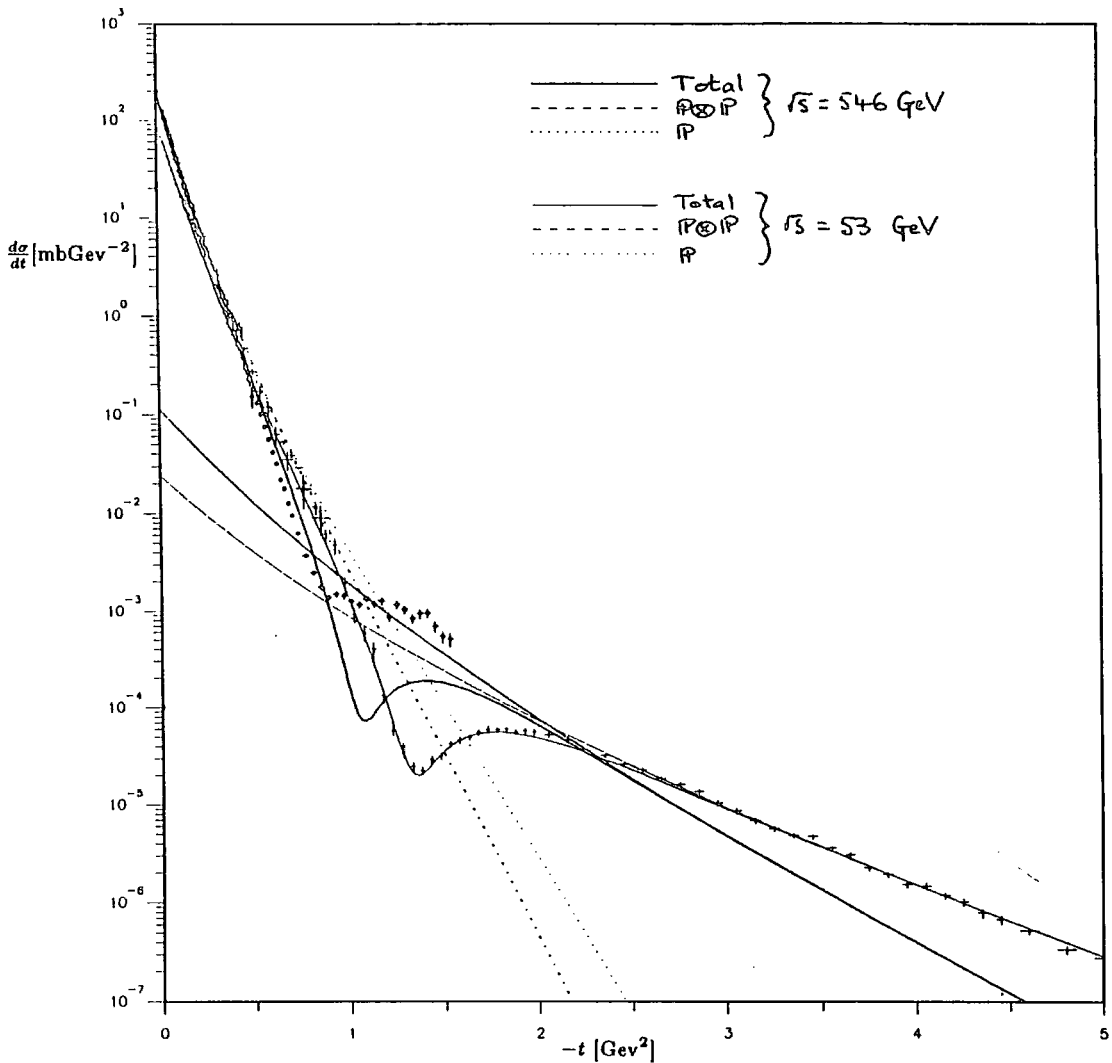


FIG.4.16 Individual contributions of Pomeron and Pomeron cut to $\frac{d\sigma}{dt}$ at $\sqrt{s} = 53$ and 546 GeV.

The deepness of the dip given by destructive interference of the pole and the cut depends upon how nearly out of phase the two contributions are and upon their t -dependences in the dip region. Both of these affect how large a real part is left at the point where the imaginary parts of the pole and cut cancel. To the extent that the phase of the cut is determined wholly by its trajectory the relative phase of the pole and cut depends only upon the difference between their trajectories. The closer the two trajectories are the more exact the cancellation of the two terms and the deeper is the dip. The complex denominators in (4.4.3) have a roughly t -independent affect

upon the phase of the cut and change only slowly with energy due to the $\ln s$ term. The phase and the energy dependence of the denominators are affected by including a more complex structure in the Gribov vertex i.e $[N(t, t_1, t_2)]^2 = \lambda e^{b_1 t + b_2(t_1 + t_2)}$. However, we were not able to obtain any significant improvement using this extra freedom.

The difference between the pole and cut trajectories increases with increasing $|t|$ at a rate determined by α'_p . Their difference at $t = 0$ is determined by $\alpha_p(0)$. So we should get a deeper dip for small α'_p and $\alpha_p(0)$. Note that this also means that the cancellation of the pole and cut will tend to be better if it occurs at smaller $|t|$ and so we expect to have problems getting a shoulder at $|t| = 0.8 \text{ GeV}^2$ at collider energies but a dip at $|t| = 1.4 \text{ GeV}^2$ as occurs in the ISR data.

Below, we plot the real and imaginary parts of the amplitude at $\sqrt{s} = 53 \text{ GeV}$ for above fit (4a). We have omitted the Reggeon contributions for the sake of clarity.

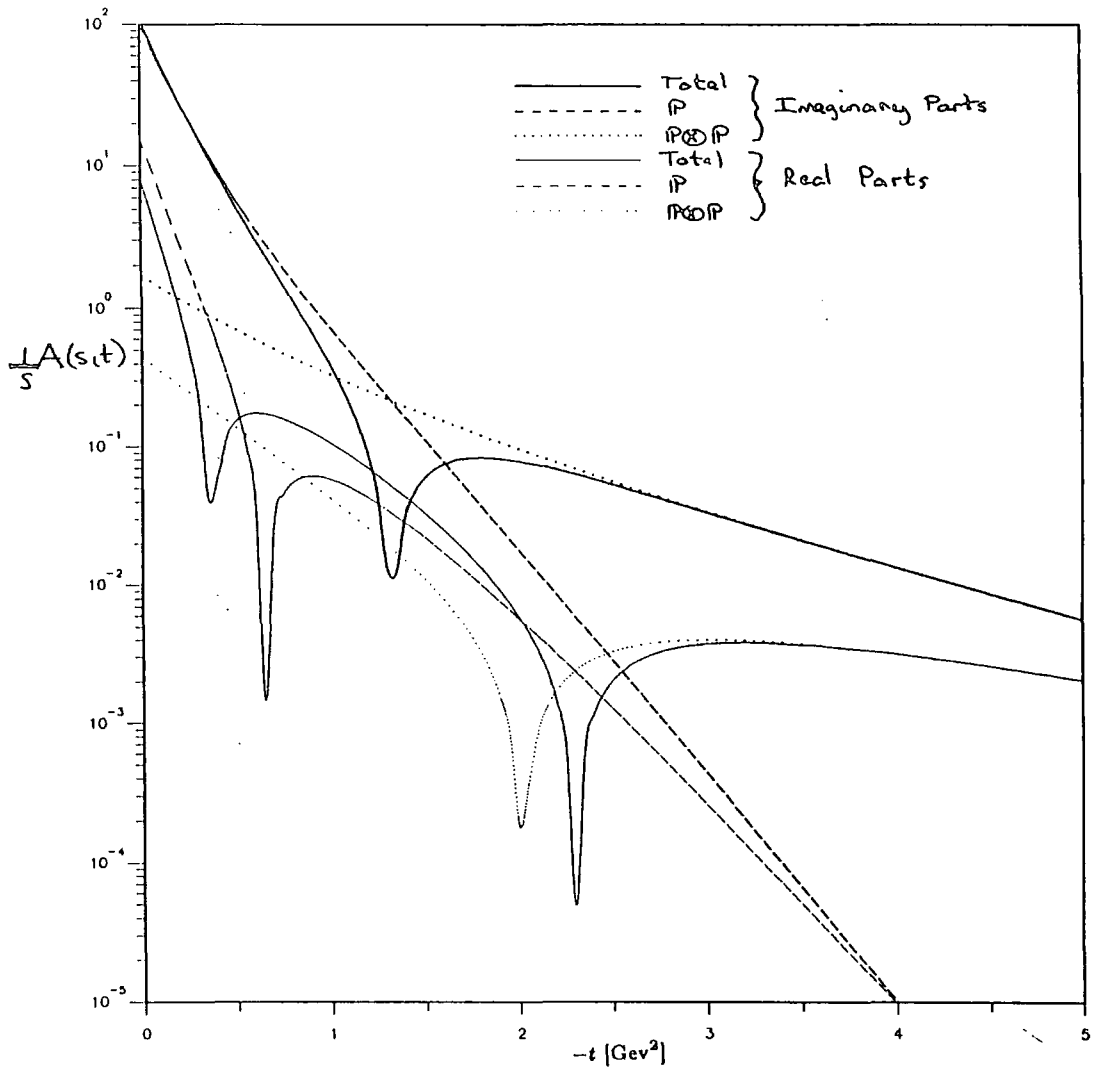


FIG.4.17 Real and Imaginary parts of the contributions to the amplitude in fit(4a) at $\sqrt{s} = 53$ GeV.

In figure 4.18 we vary the phase of the cut term at $\sqrt{s} = 546$ GeV in the above fit, keeping everything else fixed, and plot the results for different phases *i.e* we plot $P + e^{i\pi\phi} P \otimes P$ for different values of ϕ . It can be seen that to get a shoulder at the Collider with this cut the pole and the cut need to be more in phase by 0.1π and the shoulder produced lies a factor $5\times$ below the data. Constructive interference between the pole and the cut would produce the wrong shape for the shoulder.

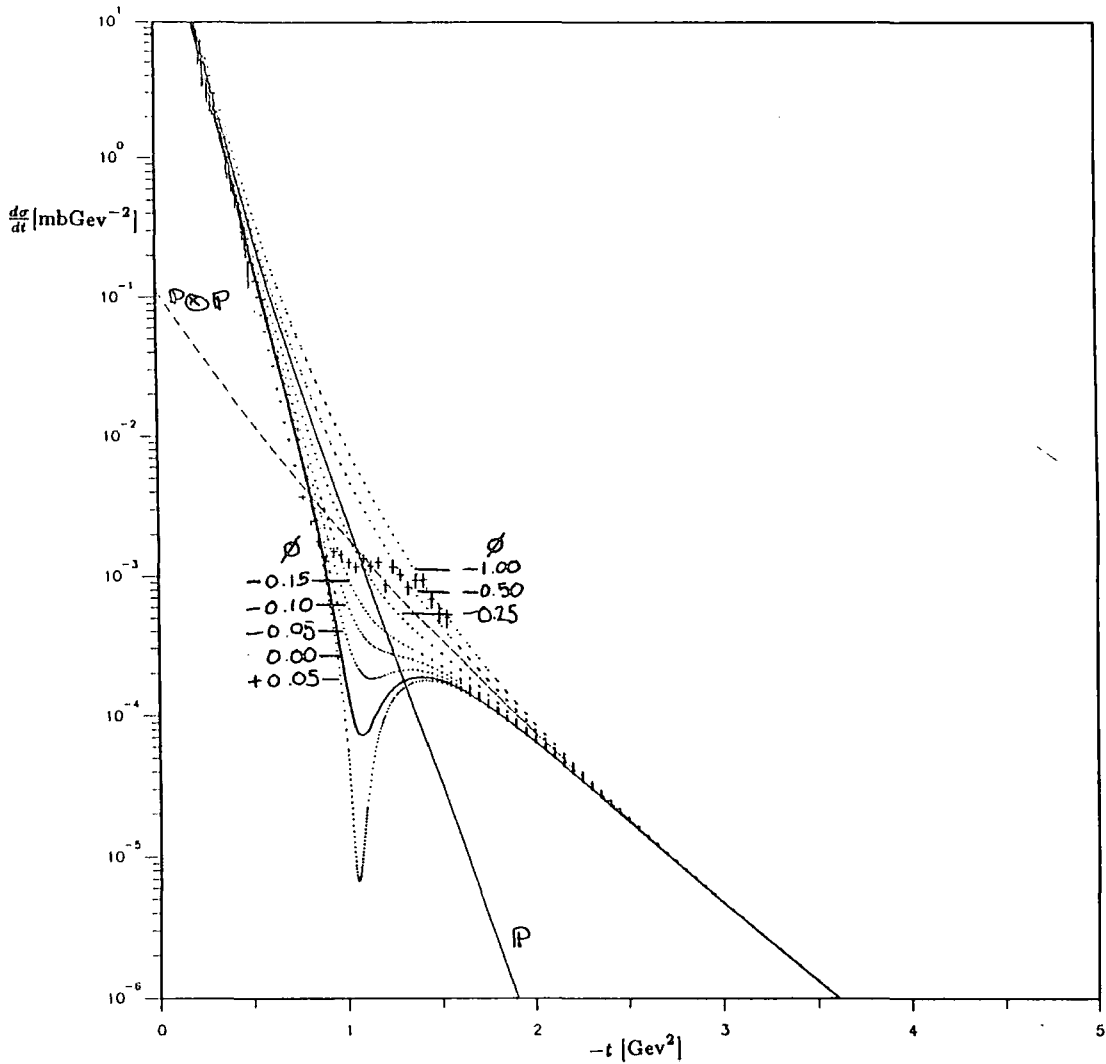


FIG.4.18 $\frac{d\sigma}{dt}(P + e^{i\pi\phi}P \otimes P)$ plotted for different ϕ in fit(4a) at $\sqrt{s} = 546$ GeV.

So the simple version of this model has four drawbacks:

- the energy independence of the large $|t|$ data at ISR energies and below is not consistent with the Pomeron cut generated from a Pomeron pole with trajectory slope $\alpha'_p \approx 0.3 \text{ GeV}^{-2}$ which the small $|t|$ data seems to need,
- the magnitude of the cut is too small to give the shoulder at the Collider even if the phase were right,
- the relative phases of the pole and cut do not change sufficiently between $\sqrt{s} = 53 \text{ GeV}$, $|t| = 1.4 \text{ GeV}^2$ and $\sqrt{s} = 546 \text{ GeV}$, $|t| = 0.8 \text{ GeV}^2$ to produce a dip in $\frac{d\sigma}{dt}$ at the first value of t and a shoulder at the other,
- the destructive interference between the pole and the cut does not produce a deep enough dip at $\sqrt{s} = 23.5 \text{ GeV}^2$.

4.5 Bent Trajectory Parametrization.

One way in which we can attempt to clear up some of the above problems is to allow some deviation of the Pomeron trajectory from a purely linear form. In this section we shall explore whether this idea can improve matters.

The t -dependence of the meson Regge trajectories appears to be linear, at least for $t \geq -1.5 \text{ GeV}^2$ (see Collins (1977)). However, Regge cuts also seem to be important so the effective trajectories do not necessarily reflect just the energy dependence of the Regge poles. As we saw in §3.5, in perturbation theory the large $|t|$ behaviour of the Regge trajectory is governed by the Born diagram which $\sim \frac{t}{s}$ for large s , $-t$ and so $\alpha_R(t) \rightarrow -1$ as $t \rightarrow -\infty$. This behaviour gives agreement with the CIM dimensional counting rules of Brodsky *et al* (1973) which give :

$$\frac{d\sigma}{dt} \sim \frac{1}{s^2} f\left(\frac{t}{s}\right) t^{-2n_s} \quad (4.5.1)$$

where $f\left(\frac{t}{s}\right) \rightarrow \frac{t^2}{s^2}$ for $s, -t \rightarrow \infty$, $\frac{t}{s}$ fixed and n_s is the number of spectator quarks. This works quite well in hadron-hadron scattering at low energy and $|t| \geq 2.4 \text{ GeV}^2$.

A model which gives a satisfactory account of the low energy data was proposed by Collins and Kearney (1984). In this the Regge poles and their daughters dominate at large $|t|$ as well as at small $|t|$ because of the bending of their trajectories, with Regge cuts only being important for $1 \leq |t| \leq 3 \text{ GeV}^2$. The linearity of the Pomeron trajectory is even more open to question since it has no particles which lie on it and it already has quite different properties from the meson Regge trajectories *i.e* the string tension associated with the Pomeron trajectory, $T = \frac{1}{2\pi\alpha_P}$, is about $4\times$ larger than in the meson Regge trajectories. The effective trajectory calculation in §2.6 supports a linear Pomeron trajectory for $|t| \leq 1 \text{ GeV}^2$ but as noted above this depends on the amount of pole-cut interference.

By analogy with the above argument for the large $|t|$ behaviour of meson Regge trajectories, the Pomeron trajectory should end up at $\alpha_P(t) = 1$ since the basic gluon diagram has an $\sim \frac{s}{t}$ behaviour. Similarly the Pomeron cut trajectory should also tend to $\alpha_{2P}(t) \rightarrow 1$ as $|t| \rightarrow \infty$ in accord with (3.6.6) but since it has more factors of α_s than the pole (see fig.3.5), where $\alpha_s \rightarrow 0$ for large $|t|$, it is expected to be negligible

compared to the pole term at large enough $|t|$. At the ISR energies however, there is no evidence that anything except the Pomeron cut is needed to describe large $|t|$.

It seems plausible therefore, that bending the Pomeron trajectory might clear up the phase and energy dependence problems noted at the end of §4.3. Bending the Pomeron trajectory so that it asymptotes to $\alpha_P(t) = 1$ will allow the energy dependence of the cut at large $|t|$ to be disassociated somewhat from that of the pole at small $|t|$ (since the pole trajectory for $t > \tilde{t}$ only affects the cut trajectory for $t > \frac{\tilde{t}}{4}$). It brings the pole and cut trajectories closer together in the dip region than if the trajectories were linear so that the real and imaginary parts cancel more exactly and give a deeper dip. It also allows their trajectories to be closer at $|t| = 1.4 \text{ GeV}^2$ than at $|t| = 0.8 \text{ GeV}^2$ and thus produce less of a dip at the latter.

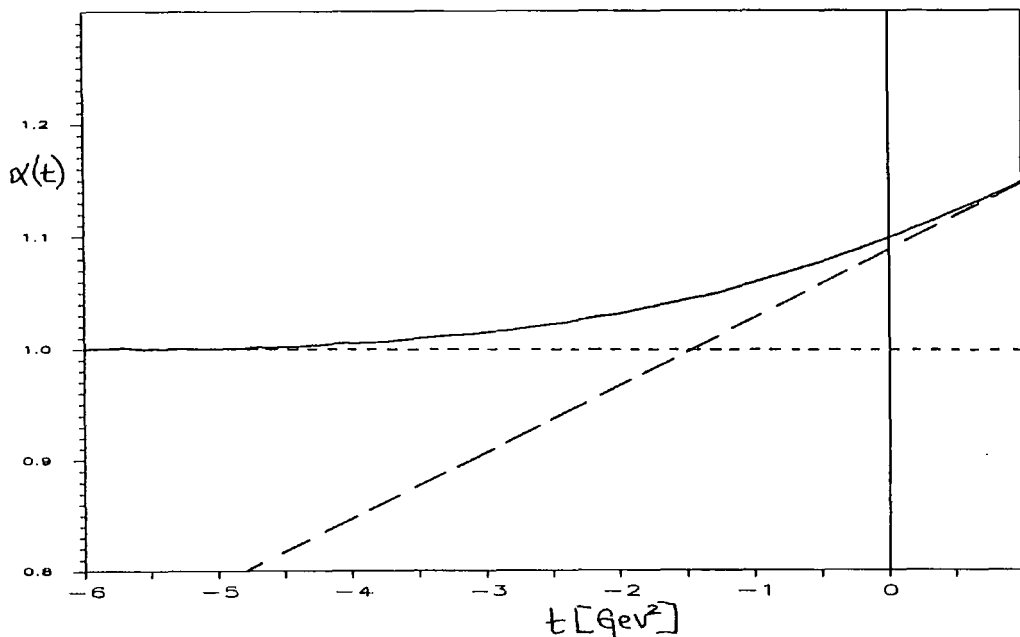


FIG.4.19 Bent Pomeron trajectory asymptoting to one from above.

We first examined whether these ideas can be made to work with a Pomeron trajectory which asymptotes to one from above as shown in fig.4.19. However, even taking into account the tendency of the pole-cut interference to produce some of the observed shrinkage at small $|t|$ we found that the above trajectory was incompatible with the energy independence of the data for $|t| \approx 0.3 \text{ GeV}^2$ which implies that the dominant trajectory passes through one at small $|t|$ (as shown by the α_{eff} plot in fig.2.13). If the trajectory is to pass through one at small $|t|$ and asymptote to one at large $|t|$ then it

must bend back up again as in figure 4.20 .

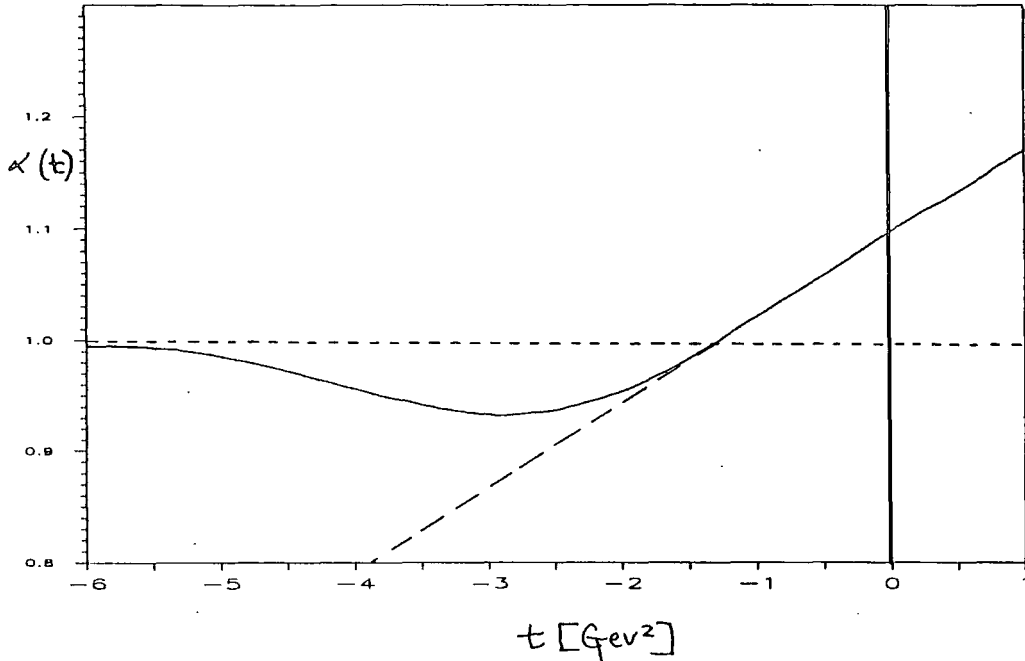


FIG.4.20 Bent Pomeron trajectory asymptoting to one from below.

There are theoretical problems with this behaviour since trajectory functions should be Herglotz and have all derivatives positive for $t < t_T$. However, the behaviour of the Pomeron trajectory is complicated by its collision with all the multi-Pomeron cut trajectories at $t = 0$ and it is not obvious that this restriction necessarily applies. The fits are also not much affected by the trajectories bending upwards at large $|t|$ and the results are unchanged if the Pomeron trajectory asymptotes to zero or some negative value rather than bending back up.

We parametrize a trajectory with the form shown in figure 4.20 by

$$\begin{aligned} \alpha_P(t) &= 1 + x + |x| + (x - |x|) \frac{u^2 v}{(v|x| + u^2)(|x| + v)} \\ &= \begin{cases} 1 + 2x & \text{if } x \geq 0; \\ 1 + \frac{2xu^2v}{(-vx + u^2)(-x + v)} & \text{otherwise.} \end{cases} \end{aligned} \quad (4.5.2)$$

where $x = \frac{1}{2}(\alpha_P(0) - 1 + \alpha'_P t)$ and u and v are free parameters. This function has the properties that (i) it passes through one at $x = 0$; (ii) its first derivative is continuous at $x = 0$ and (iii) it tends to one as $x \rightarrow -\infty$. The minimum value of the function occurs at $x = -u$ and the width of the minimum is determined by v . It is not possible to calculate the cut amplitude analytically using (3.6.9) so we use its leading behaviour

given by

$$A_{2P}(s, t) = \frac{\lambda G_P^2}{32\pi} e^{b_1 + \frac{a_P}{2} t} \frac{(e^{-i\frac{\pi}{2}} s)^{\alpha_{2P}(t)}}{a_P + \alpha'_P (\log s - \frac{i\pi}{2})} \quad (4.5.3)$$

in which $\alpha_{2P}(t)$ is calculated from (3.6.6) and is given by

$$\alpha_{2P}(t) = 1 + y + |y| + (y - |y|) \frac{u^2 v}{(v \frac{|y|}{2} + u^2)(\frac{|y|}{2} + v)} \quad (4.5.4)$$

where $y = \alpha_P(0) - 1 + \frac{\alpha'_P t}{4}$.

With this parametrization we varied the parameters : a_P , α'_P , x , a_1 , λ , b_1 , u and v ; and fitted the data at $\sqrt{s} = 23.5, 53$ and 546 GeV as above. We obtained the fit (4b) shown in figure 4.22 . The parameter values are given in table 4.5 . As expected, with this parametrization we were able to get a deeper dip at the ISR and more of a shoulder at the Collider. However, the dip shape at the higher ISR energies does not agree very well with the data and the shoulder produced at the Collider energy is still a factor $10\times$ below the data. This fit has $\alpha'_P = 0.18 \text{ GeV}^{-2}$ which is not much larger than found previously and would give a reasonable energy dependence at large $|t|$ even without bending the trajectory. The pole and cut trajectories produced by this are shown in figure 4.21 .

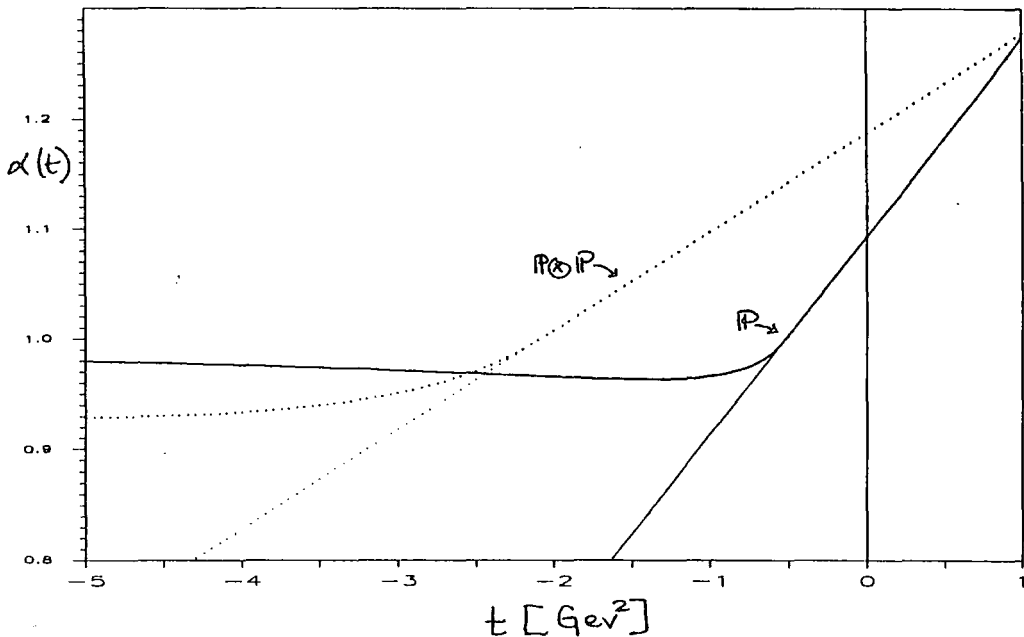


FIG.4.21 Bent Pomeron pole and cut trajectories from fit (4b).

As stated above, the cut trajectory does not bend back up appreciably over the t -range of the data. Effectively the cut trajectory is independent of t for $|t| \geq 3 \text{ GeV}^2$ and a linear function of t with slope $\frac{\alpha'_P}{2}$ for $|t| \leq 2 \text{ GeV}^2$. The t -dependence of the cut amplitude for $|t| \geq 2 \text{ GeV}^2$ is fixed by the data which gives $A_{2P}(s, t) \sim e^{1.2t}$, so the change in the cut trajectory for $|t| \approx 3 \text{ GeV}^2$ produces a small $|t|$ increase in the t -dependence of the cut amplitude (*i.e.* $A_{2P}(s, t) \sim e^{1.2t + \frac{\alpha'_P}{2} \log st}$ at small $|t|$, where $\frac{\alpha'_P}{2} \log s \approx 0.8 \text{ GeV}^{-2}$). So the bent trajectory affects the t -dependence of the cut amplitude. A larger cut increases the amount of shrinkage produced by the pole-cut interference so that $\alpha'_P = 0.18 \text{ GeV}^{-2}$ is large enough to produce the effective shrinkage seen in the data. This is why the fits do not reproduce the larger value for α'_P found in α_{eff} . It is also this affect (rather than the change in phase) which produces a shoulder instead of a dip at the Collider energy. The contributions of the pole and cut to the amplitude at $\sqrt{s} = 53$ and 546 GeV are shown in figure 4.23 .

In the same way, the bending of the Pomeron trajectory affects the t -dependence of the Pomeron and at large enough t the Pomeron again gives the dominant contribution to the amplitude. The main effect then of bending the trajectory is to change the t -dependence of the cut (although the change in phase does produce a deeper dip at ISR energies). This effect can be reproduced more simply by changing the structure of the Gribov vertex $N(t, t_1, t_2)$ in equation (3.6.9).

α'_P	0.180	a_1	3.43	λ	0.143	u	0.0773
a_P	2.80	x	0.515	b_1	-0.501	v	0.0437

TABLE 4.5. Fit (4b) parameter values.

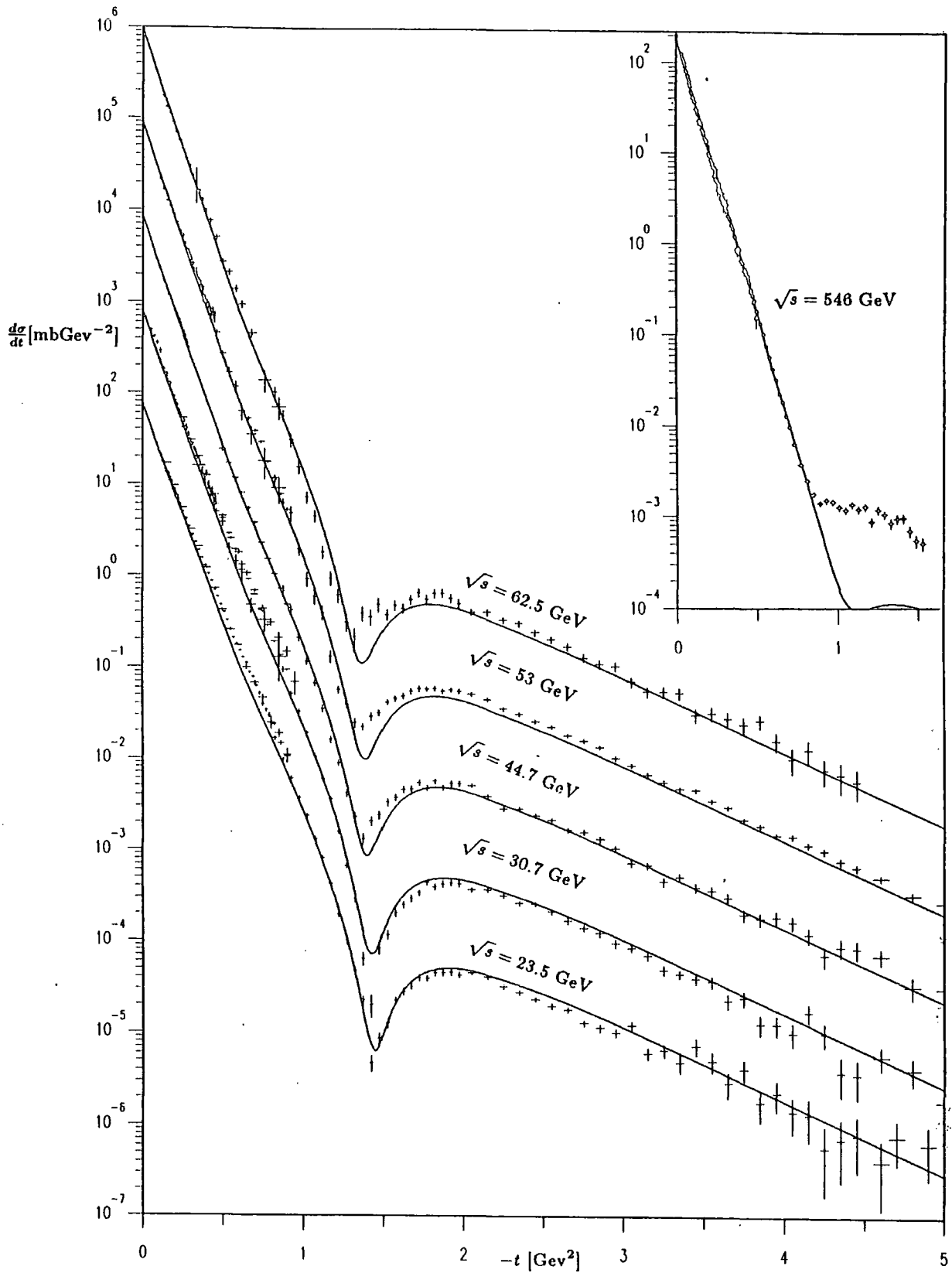


FIG.4.22 Fit using bent trajectory parametrization (4b).

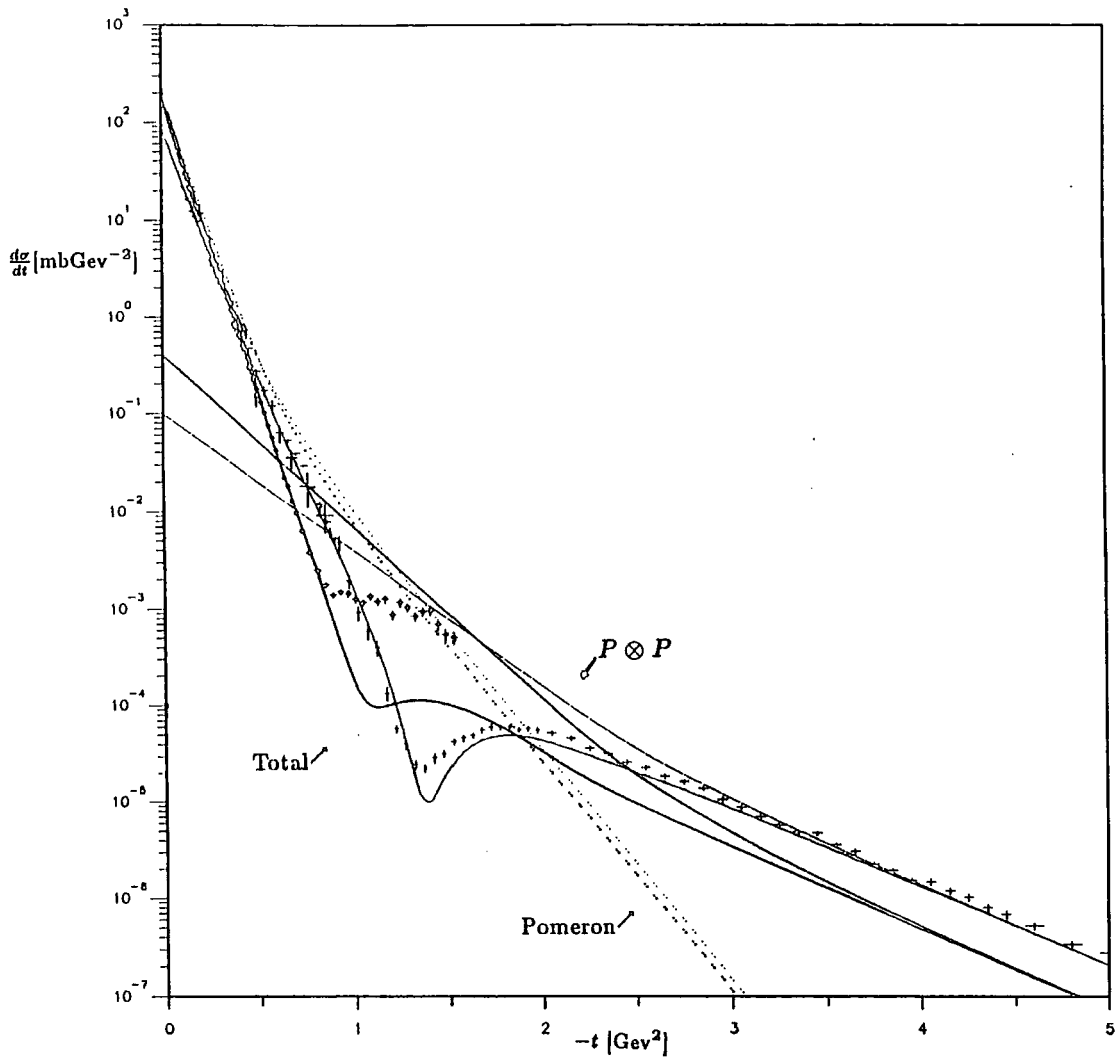


FIG.4.23 Pole and cut contributions to the amplitude using (4b).

4.6. Strong Cut Parametrization.

As we have seen above, by making the Pomeron cut term larger at small $|t|$, the effective shrinkage at small $|t|$ is increased so that the α_{eff} seen at large $|t|$ is more compatible with that expected from the Pomeron pole. We have also found that to reproduce the shoulder, the magnitude of the cut term needs to be bigger and its t -dependence needs to be steeper. This has led us to try increasing the magnitude of the cut in the shoulder region by either giving it more energy dependence or by making the energy-independent part of the amplitude larger at small $|t|$.

To give the cut more energy dependence at $|t| \approx 0.8 \text{ GeV}^2$ the cut trajectory has to be increased in this region (*i.e* increase $\alpha_P(0)$ or decrease α'_P) but this is constrained by σ_T and the large $|t|$ data. With the parametrization used in §4.4 we forced a fit to the Collider shoulder by weighting the data appropriately, while also trying to fit the ISR data. The best fit is shown in figure 4.24 . Though this fits the data at $\sqrt{s} = 546 \text{ GeV}$ very well, it gives a very poor account of the ISR data in the dip region and beyond. There is not sufficient freedom in the t -dependence of the cut, using the above parametrization, to cope with the required difference in its magnitude at the ISR and the Collider.

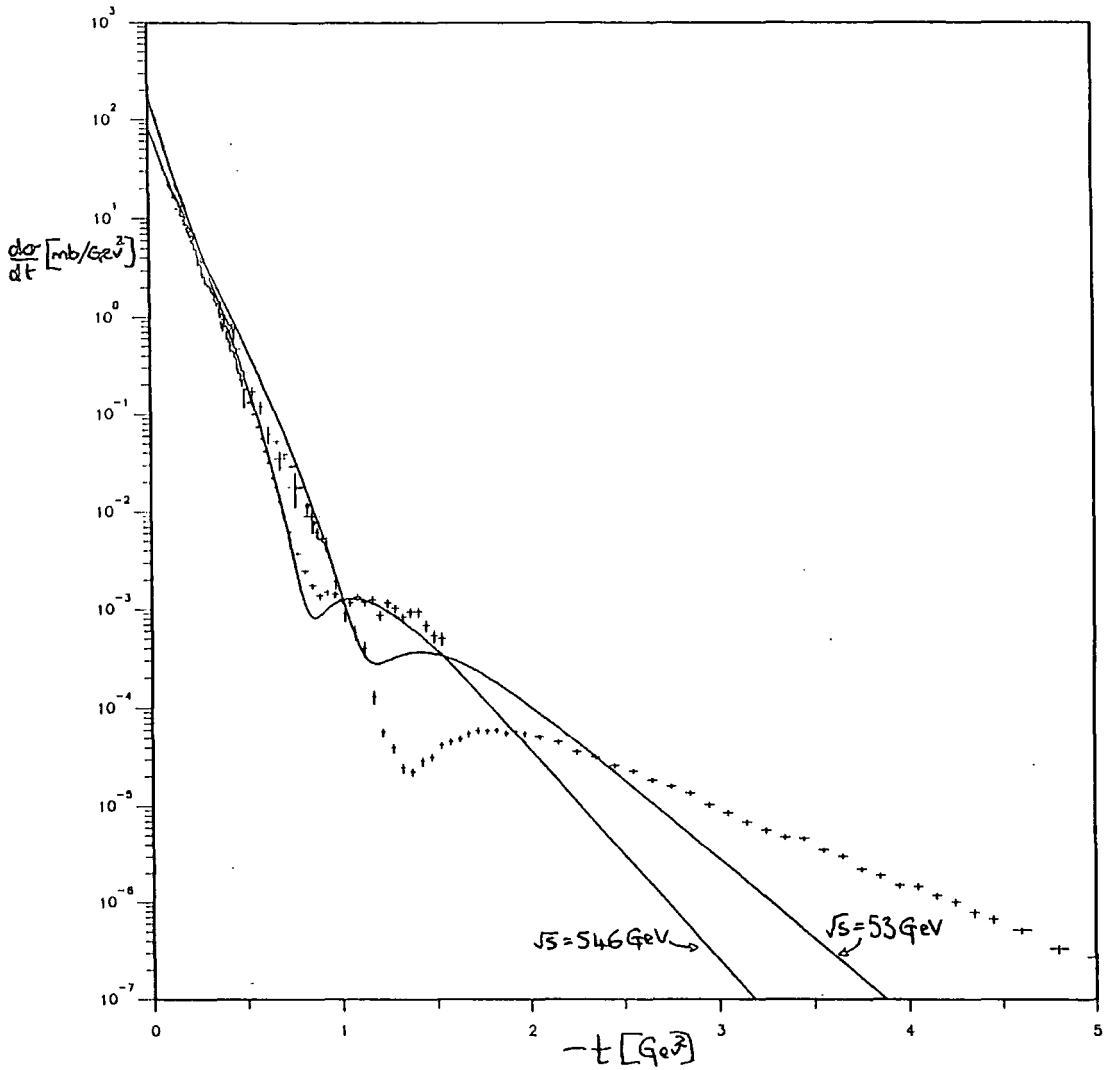


FIG.4.24 Fit to $\sqrt{s} = 546$ GeV using parametrization of §4.4 compared with data at $\sqrt{s} = 53$ and 546 GeV.

In order to get something which can produce a cut of the right magnitude at $|t| = 0.8 \text{ GeV}^2$ but still fit the ISR data for $|t| \geq 2 \text{ GeV}^2$, which is entirely due to the cut in this model, more t -dependence is needed in the Gribov vertex. We therefore replace (4.4.2) by

$$(N(t, t_1, t_2))^2 = \lambda e^{b_1 t} (1 - y + y e^{b_2 t}) \quad (4.6.1)$$

and for convenience adapt (4.5.3) slightly to give

$$A_{2P}(s, t) = \frac{\lambda G_P^2}{32\pi} (N(t))^2 \frac{|C_P|}{C_P} e^{\frac{\alpha_P}{2} t} (e^{-i\frac{\pi}{2} s})^{\alpha_{2P}(t)} \quad (4.6.2)$$

Using this to fit the data at $\sqrt{s} = 23.5, 53$ and 546 GeV we obtain a reasonable fit to both the dip at $\sqrt{s} = 53$ GeV and the shoulder at $\sqrt{s} = 546$ GeV. We find $\alpha'_p = 0.08 \text{ GeV}^{-2}$ so that most of the shrinkage at small $|t|$ (corresponding to $\alpha_{\text{eff}} = 0.3 \text{ GeV}^{-2}$) comes from the interference of the pole and the cut. This parametrization produces a marked increase in the magnitude of the cut at $t = 0$ and so it is no longer true that its effect on σ_T and the optical point is insignificant. Hence in the above, for each iteration of the fit, we have had to refit σ_T with the cut contribution included and so find slightly different values for the parameters : $\alpha_p(0), G_p, \alpha_f(0), G_f$; from the previous fits. However, the energy dependence is now such that we do not get a good fit to the dip and large $|t|$ data at $\sqrt{s} = 23.5$ GeV. The fit (4c) is shown below in figure 4.25 and the pole and cut contributions in figure 4.26 . Comparing figures 4.16 and 4.26 shows how having a larger cut with smaller α'_p and bigger $\alpha_p(0)$ produces the rise in cross-section between the Collider and the ISR.

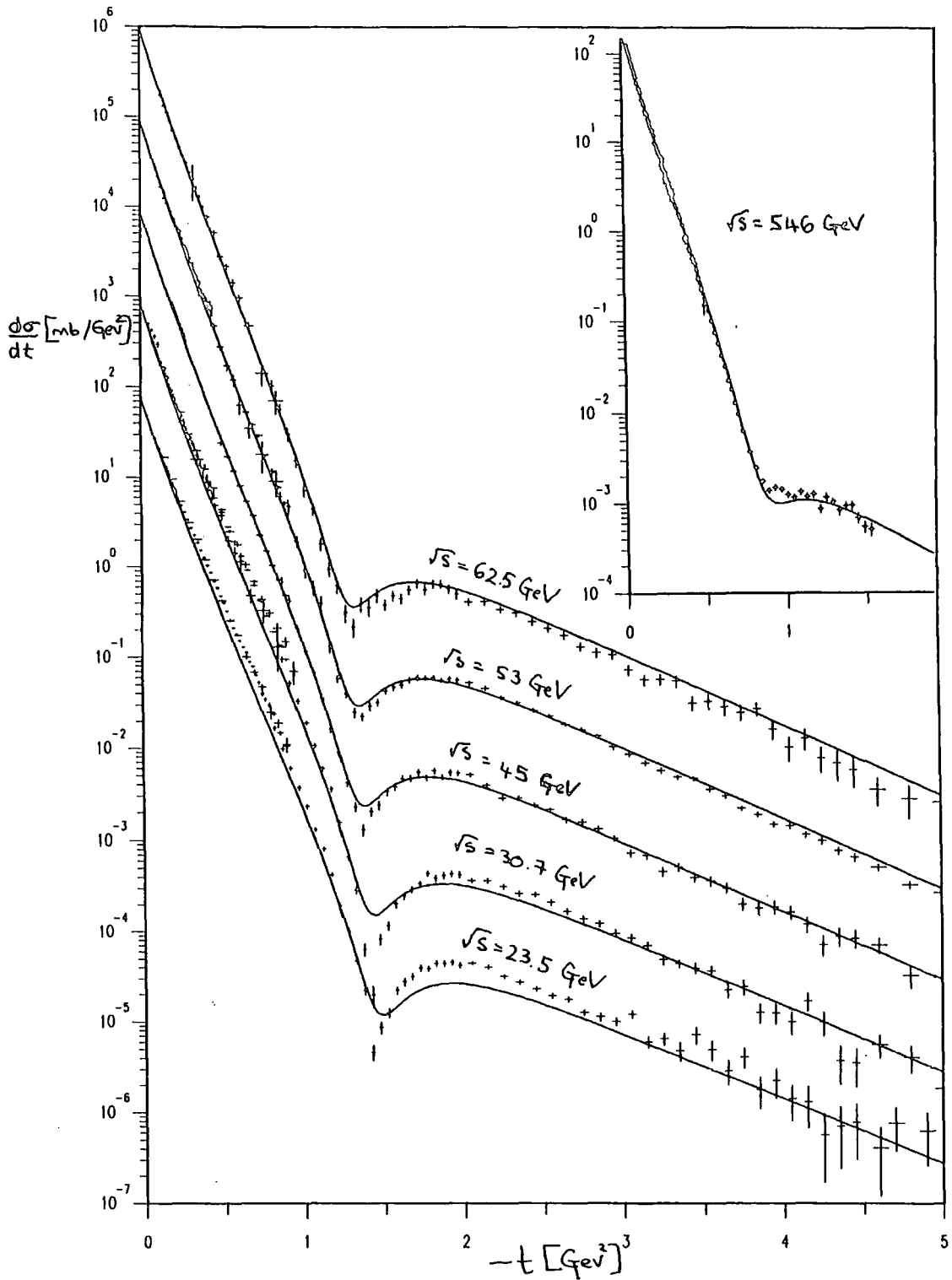


FIG.4.25 Fit (4c) using parametrization of (4.6.2) and §4.4 compared with data for $\sqrt{s} = 23.5 \rightarrow 546 \text{ GeV}$.

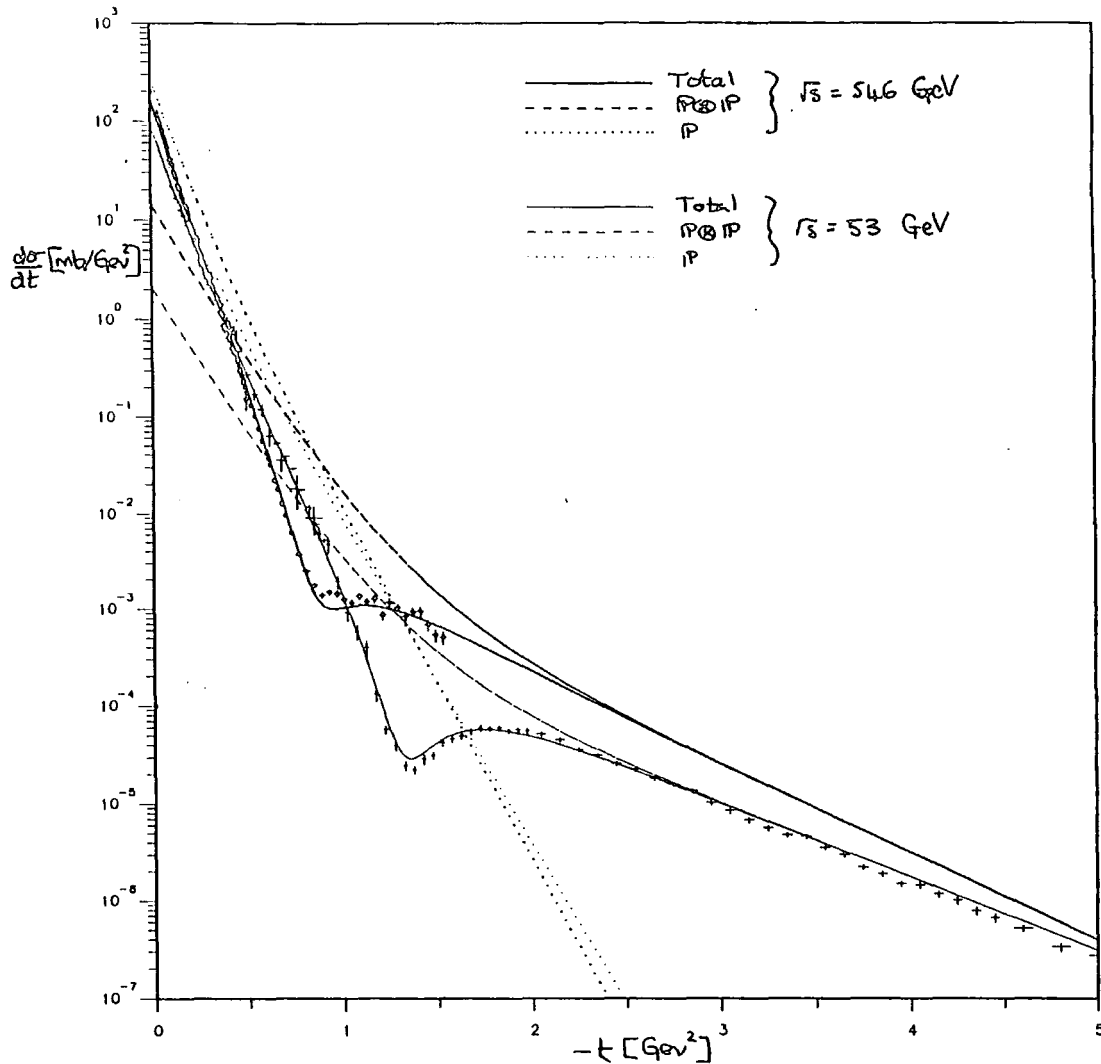


FIG.4.26 Pole and cut contributions of fit (4c) at $\sqrt{s} = 53$ and 546 GeV.

$\alpha_P(0)$	1.103	$\alpha_f(0)$	0.610	α'_P	0.0714	a_P	3.24	a_1	3.26	x	0.609
β_P	19.7	β_f	70.7	λ	0.121	b_1	0.594	b_2	2.653	y	0.969

TABLE 4.6. Fit (4c) parameter values.

The low value of α'_P means the pole amplitude is more or less energy independent in the dip region and pushes the energy independent point in the cut amplitude out to larger $|t|$ so that in the dip region the energy dependence of the cut is close to its value at $t = 0$ which $\sim s^{2\alpha_P(0)}$ and this produces too much energy dependence to agree with the ISR data. A higher value of α'_P (*i.e.* $= 0.14 \text{ GeV}^{-2}$ as found in §2.6 for cut) makes the Pomeron cut effectively energy independent in the dip region but now the shrinkage of the pole and the t -dependence of the cut combine to give too much dip

movement.

Thus it is impossible to get the energy dependence right in the dip region between the ISR and the Collider without getting the energy dependence over the ISR energy range wrong. Perhaps some contribution could be added which fixes the fit to the low energy ISR data but vanishes at the higher energies, but the parametrization is already a very unnatural description of the data. We conclude that if this model gives the correct description of the ISR data then something else must be responsible for the shoulder at the Collider.

4.7. Core term Parametrization.

The problem of the different energy dependences needed at small and large $|t|$ lead us to try to better fix the Pomeron parameters by using an arbitrary parametric form for the large $|t|$ contribution, neglecting for the moment the question of its origin. We replaced the cut amplitude used in (4.4.3) by a term with the energy dependence found by α_{eff} in §2.6 and an arbitrary phase and t -dependence. This was parametrized by

$$A_C(s, t) = \lambda \frac{G_P^2}{32\pi} e^{i\pi\phi} e^{b_1 t} (1 - y + y e^{b_2 t}) (e^{-i\frac{\pi}{2} s})^{\alpha_C(t)} \quad (4.7.1)$$

where $\alpha_C(t) = \alpha_{\text{eff}}(t) = 1.16 + 0.07t$.

With this, and the parameters (4.2.7) for the Pomeron and Reggeons, we have refitted the ISR and Collider data (no shoulder region data) and obtain a very good fit to the small $|t|$ data with $\alpha'_p = 0.28 \text{ GeV}^{-2}$ and $\phi = 0.24$. The agreement with the large $|t|$ data is reasonably good but the energy dependence of the shape and position of the dip does not correspond very well to the data. The non-zero value of ϕ in (4.7.1) means that the core term does not have the correct Regge phase and its real part cancels with the real part of the Pomeron pole in the dip region in contrast to the Pomeron cut of (4.4.3).

This still has the same problem as fit (4a) and cannot reproduce the Collider shoulder, so that an extra contribution is necessary. We add a term (4.7.2) which only appears at the Collider energy and produces the shoulder. Keeping the parameter values found in the above fit and allowing the extra term to vary gives an excellent description of the Collider shoulder. The parameter values (fit (4d)) are given in table 4.7 and the fit displayed in figure 4.27 .

α'_P	0.278	x	0.457	λ	0.0081	y	0.933
a_P	2.25	a_1	4.56	b_1	0.0105	b_2	0.487
β_{ex}	1.34	c_{ex}	1.43	φ_{ex}	1.90		

TABLE 4.7. Fit (4d) parameter values.

The freedom given by this extra term should allow a better parameterization to be found with different Pomeron parameters. So we also re-fitted the ISR and Collider data using this term, the core term in (4.7.1) and the Pomeron of (4.4.1). The best fit was found using $\alpha'_P = 0.225 \text{ GeV}^{-2}$.

$$A_{ex}(s, t) = \begin{cases} \beta_{ex} s e^{i\varphi_{ex}\pi} e^{c_{ex}t} & \text{for } \sqrt{s} = 546 \text{ GeV} \\ 0 & \text{for } \sqrt{s} < 546 \text{ GeV} \end{cases} \quad (4.7.2)$$

Thus the effect of the term giving the Collider shoulder produces quite a large variation in the shrinkage attributed to the pole and so α'_P is not necessarily as great as α_{eff} would indicate and perhaps closer to that needed to generate the energy dependence of the large $|t|$ ISR data.

We repeated the above exercise for the parametrization of §4.4. Adding the term (4.7.2) to fit (4a) allows a good description of the Collider shoulder. Refitting all the data including the extra term gives a slight improvement on (4a) at the ISR and a good fit to the Collider shoulder. This uses $\alpha'_P = 0.117 \text{ GeV}^{-2}$.

The extra term added to fit the Collider shoulder is not very well determined. To get some estimate of the contribution of this term to the total cross-section we can look at these four different versions of fits to the Collider shoulder. Assuming the phase of the extra term has no t -dependence these give at $\sqrt{s} = 546 \text{ GeV}$

	Fit (4a)	Refitted (4a)	Fit (4d)	Refitted (4d)
$\sigma_T(\text{cut/core})$	-1.44 mb	-1.20 mb	-0.49 mb	-0.50 mb
$\sigma_T(\text{extra term})$	-0.53 mb	-3.35 mb	-0.17 mb	-0.73 mb

TABLE 4.8. Contribution of cut and the term of (4.7.2) to σ_T at $\sqrt{s} = 546 \text{ GeV}$.

so the combined contribution to σ_T is about $1 \rightarrow 5$ mb. As we saw in figure 4.18, we need destructive interference with the Pomeron to give a shoulder of the right shape at the Collider so the contribution to σ_T is negative. Including this effect in the fit to σ_T makes little difference to the parameter values obtained and justifies neglecting the contribution in (4.2.1). For example including the 1.5 mb effect of the cut in fit (4a) we find a best fit for : $\alpha_P(0) = 1.094$, $\beta_P = 19.2$, $\alpha_f(0) = 0.616$, $\beta_f = 70.2$ mb, which are similar to the values obtained in (4.2.7).

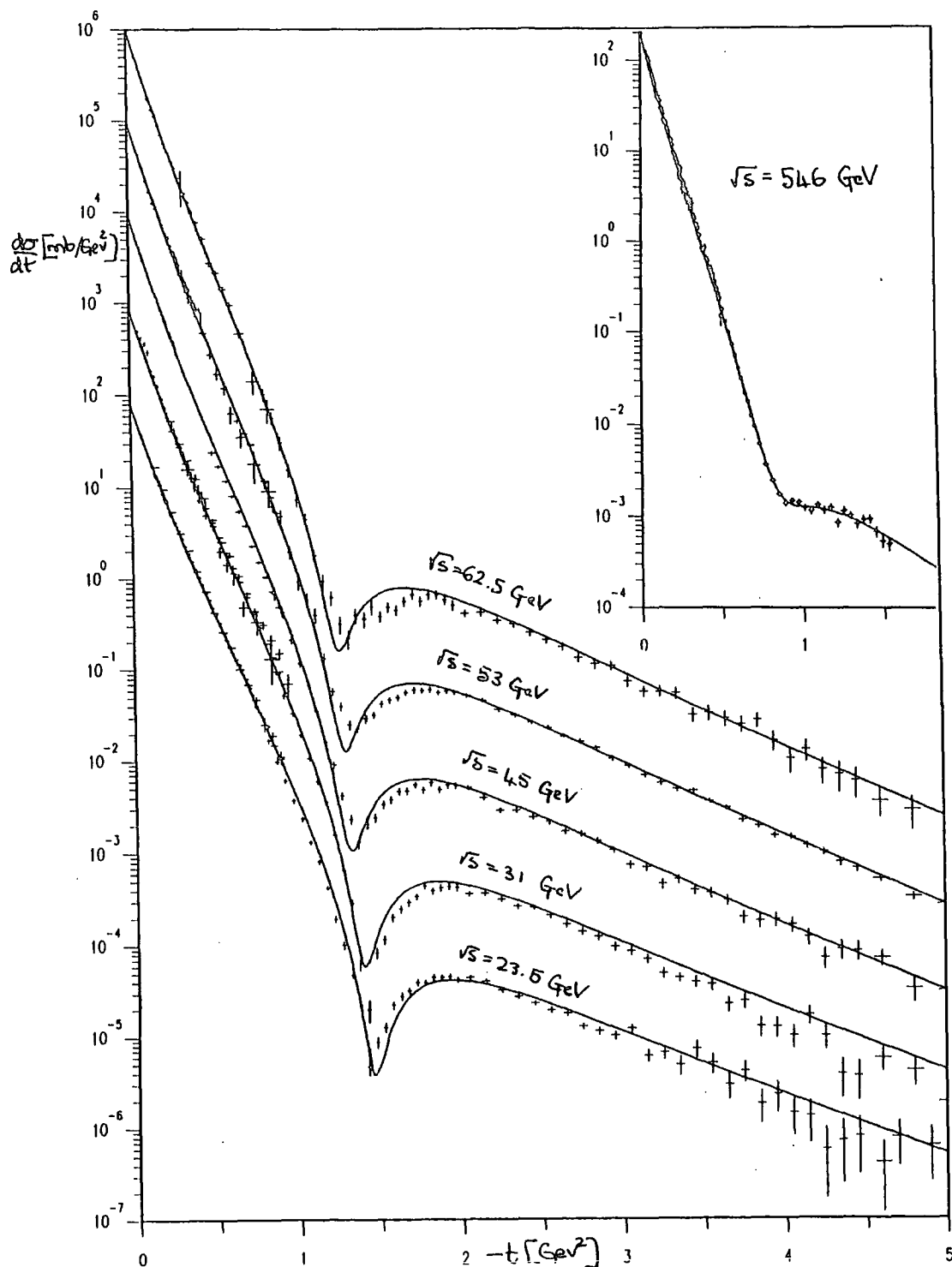


FIG.4.27 Fit obtained using parametrization (4d) of table 4.7 .

4.8. Low Energy Fits to $\frac{d\sigma}{dt}$.

We saw in §2.5 that for $p_{lab} \leq 30$ GeV/c the large $|t|$ data in both pp and $\bar{p}p$ have a quite different energy dependence from the data at higher energies. This indicates that different dynamics give the dominant large $|t|$ contribution in the two energy regimes. The same dynamics that are responsible for the ISR data appear to dominate the amplitude down to $p_{lab} = 50$ GeV/c. The only remnant of the low energy effects above this energy is the difference between $\frac{d\sigma}{dt}(pp)$ and $\frac{d\sigma}{dt}(\bar{p}p)$ in the dip region where the cross-section is small. It is an important check on the consistency of a model which purports to describe the dynamics operating at the ISR and Collider energies that it also gives a reasonable description of the data for $p_{lab} \geq 50$ GeV/c. A parametrization of the data for $p_{lab} \leq 30$ GeV/c and of the $pp/\bar{p}p$ difference for $p_{lab} \geq 50$ GeV/c is also needed to determine what low energy effects are still present at higher energies. In previous versions of this model the low energy data at large $|t|$ have been described by an effective pole (Collins and Gault (1976)) and a detailed superposition of Reggeon-Pomeron cuts incorporating polarization data (Collins and Kearney (1984)). We have adopted the former approach of trying to find a simple parametrization of the low energy effects.

Extrapolating the differential cross-section for fit (4d) from §4.7 down to low energies we find good agreement with the small $|t| \leq 1$ GeV² data for $p_{lab} \geq 20$ GeV/c, but the agreement with the data at $p_{lab} = 5$ and 10 GeV/c, where the cross-over zero is prominent, is very poor. To improve the low energy, small $|t|$ parametrization we have fine tuned the parameters a_f and a_ω in (4.4.5) by fitting the pp and $\bar{p}p$ data for $|t| \leq 0.6$ GeV² and $p_{lab} = 5 \rightarrow 30$ GeV/c. This does not affect the fit at higher energies. The parameter values found are given in table 4.9 and the small $|t|$ prediction of the model is shown in figure 4.28. The energy dependence of the cross-over zero effect is not properly accounted for by the shrinkage of the ω pole. In particular the parametrization does not reproduce very well the small $|t|$ difference between pp and $\bar{p}p$ for $p_{lab} = 50 \rightarrow 200$ GeV/c present in the data from Ayres (1977) and Akerlof (1976). If the difference seen in the small $|t|$ data at higher energies (Breakstone (1984) see §2.5) is a real effect it certainly cannot be accounted for by just the ω Reggeon, since this would then give too large a difference at lower energies. As noted above the cross-over zero cannot be simply due to a change of sign in the ω residue and is probably caused by the presence of cuts, giving a more complicated energy dependence. For



$p_{lab} \approx 5 \text{ GeV}/c$ the Reggeons are comparable in magnitude to the Pomeron and for a detailed fit to the data it would be necessary to include other effects such as more complicated Reggeon residues, other Reggeon contributions and spin effects.

a_f	2.73	a_ω	1.61
-------	------	------------	------

Table 4.9 Re-fitted Reggeon parameters for fit (4d).

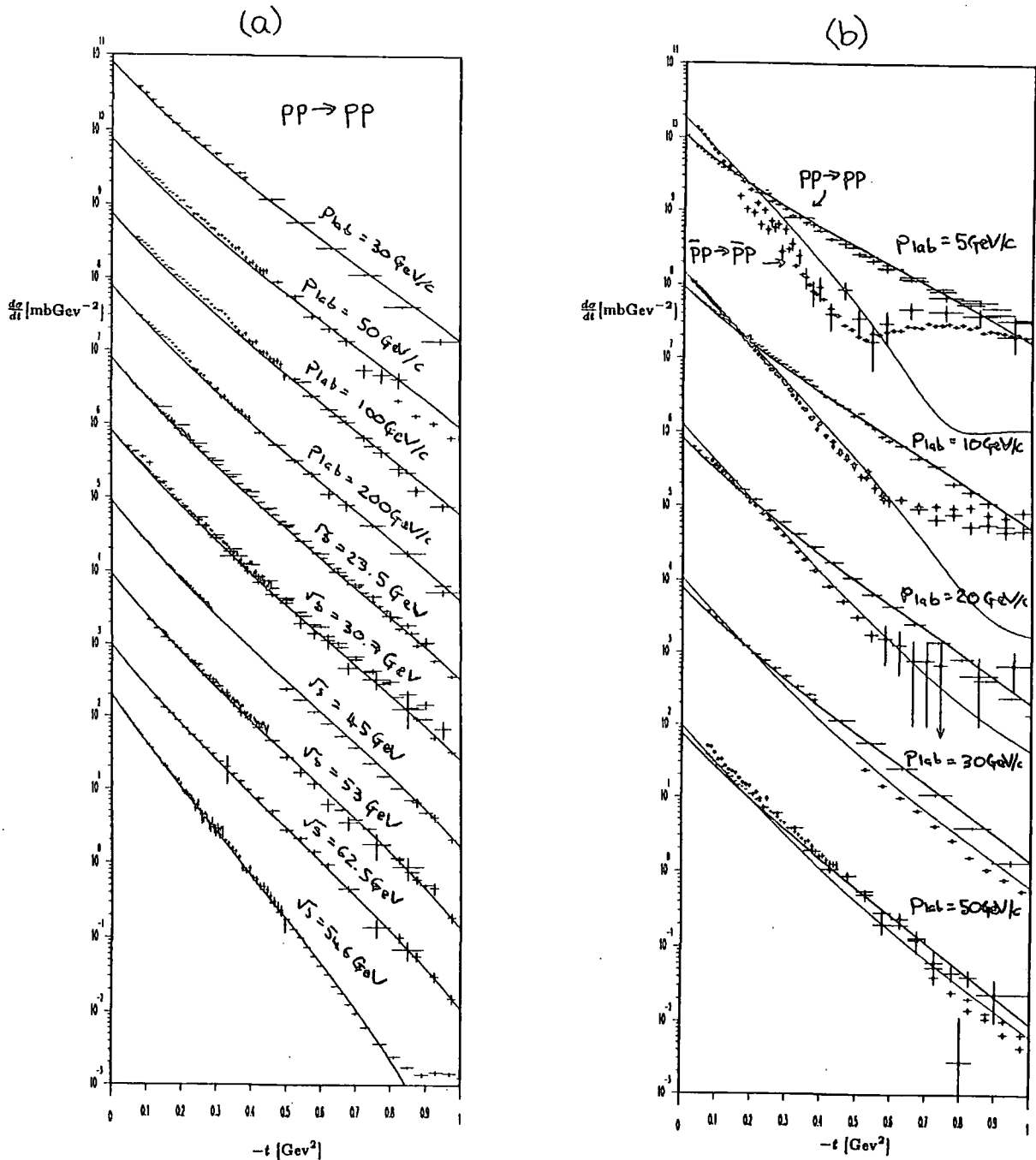


FIG.4.28 Small $|t|$ prediction of (a) $\frac{d\sigma}{dt}(pp)$ for $p_{lab} \geq 30 \text{ GeV}/c$, (b) $\frac{d\sigma}{dt}(pp)$ and $\frac{d\sigma}{dt}(\bar{p}p)$ for $p_{lab} = 5 \rightarrow 50 \text{ GeV}/c$.

In the dip region and at larger $|t|$ the prediction only agrees with the pp data for $p_{lab} \geq 200$ GeV/c. The agreement with the $\bar{p}p$ data is reasonable for $p_{lab} \geq 50$ GeV/c but the odd charge conjugation contribution due to the ω Reggeon is too small to produce a significant difference between pp and $\bar{p}p$. For $p_{lab} = 5, 10$ GeV/c the predicted cross-section is a factor of $100\times$ below the data for $|t| \geq 1$ GeV/c.

To fit the pp data for $|t| \geq 1$ GeV² and $p_{lab} \leq 30$ GeV/c we add a term with the form

$$A_x(s, t) = \beta_x s e^{i\pi\phi_x} \left(e^{-i\frac{\pi}{2}s} \right)^{\alpha_x(t)} e^{b_x t} \quad (4.8.1)$$

where $\alpha_x(t) = \alpha_x(0) + \alpha'_x t$. Using (4.8.1) with $\alpha'_x = 0$ we obtained a reasonable parametrization of the large $|t|$ data for $\alpha_x(0) = -0.43$. At higher energies where the extra term (4.8.1) is comparable to the Pomeron cut in magnitude the relative phases are such that the dip in the $P + P \otimes P$ cross-section is deepened, in contradiction with the pp data. However, we noted above that fit (4d) has the wrong sign for the real part of the amplitude in the dip region. Using fit (4a) instead, which gives a poor fit to the small $|t|$ data, we find that the dip structure of $\frac{d\sigma}{dt}(pp)$ is well reproduced for $p_{lab} = 5 \rightarrow 200$ GeV/c. This is shown in figure 4.29 with parameters given in table 4.10. At the lowest ISR energy, $\sqrt{s} = 23.5$ GeV, the extra term gives a small but significant contribution and increases $\frac{d\sigma}{dt}$ slightly in the dip region and large $|t|$. This raises the possibility that the low energy effects are not negligible in determining the dip shape and the large $|t|$ energy dependence at ISR energies, as we have assumed above.

We attempted to describe the low energy $\bar{p}p$ data by adding another term similar to (4.8.1) but with odd charge conjugation but were unable to obtain a suitable parametrization of the data at $p_{lab} = 5$ and 10 GeV/c. The $\bar{p}p$ data at higher energies is well described by the original parametrization with no extra terms so we obtain a reasonable description of the pp and $\bar{p}p$ data if we assume that the extra terms cancels in $\bar{p}p$ but add in pp . The result of this is shown in figure 4.30.

It is tempting to think of the extra contribution as due to Reggeon-Pomeron cuts, which should have a flatter t -dependence than the Reggeons and shrink much less with energy. The value of α_{eff} for the low energy data for $|t| \geq 1$ GeV², $\alpha_{\text{eff}} \approx 0 \rightarrow -0.5$, is too high for a conventional Reggeon trajectory. The trajectory agrees much better

with that expected from Reggeon-Pomeron cuts. From (3.6.3) these have trajectories given by

$$\begin{aligned}\alpha_{RP}(t) &\simeq \alpha_R(0) + \frac{\alpha'_R \alpha'_P}{\alpha'_R + \alpha'_P} t \\ &\approx 0.5 + 0.2t\end{aligned}\tag{4.8.2}$$

The t -dependence of the low energy, large $|t|$ data is also similar to that of the Pomeron cut at ISR energies. We tried fits in which we replaced the term (4.8.1) by Reggeon-Pomeron cut generated by (3.6.9) from the f and ω Reggeons of (4.4.5) giving the form

$$A_{RP}(s, t) = \frac{\lambda_{RP} x_R G_R G_P}{16\pi s} (e^{-i\frac{\pi}{2}} s)^{\alpha_{RP}(0)} e^{b_{RP} t} \frac{e^{\frac{c_R c_P}{c_R + c_P} t}}{c_R + c_P}\tag{4.8.3}$$

where $x_R = \frac{1}{-i}$ for $R = f$. We found that although the energy dependences of the terms calculated using (4.8.3) were about what was needed they did not give the correct phase to properly reproduce the dip structure for $p_{lab} = 50 \rightarrow 280$ GeV/c.

β_x	314	b_x	0.758	$\alpha_x(0)$	-0.43	ϕ_x	1.19
-----------	-----	-------	-------	---------------	-------	----------	------

Table 4.10 Parameter values used in (4.8.1).

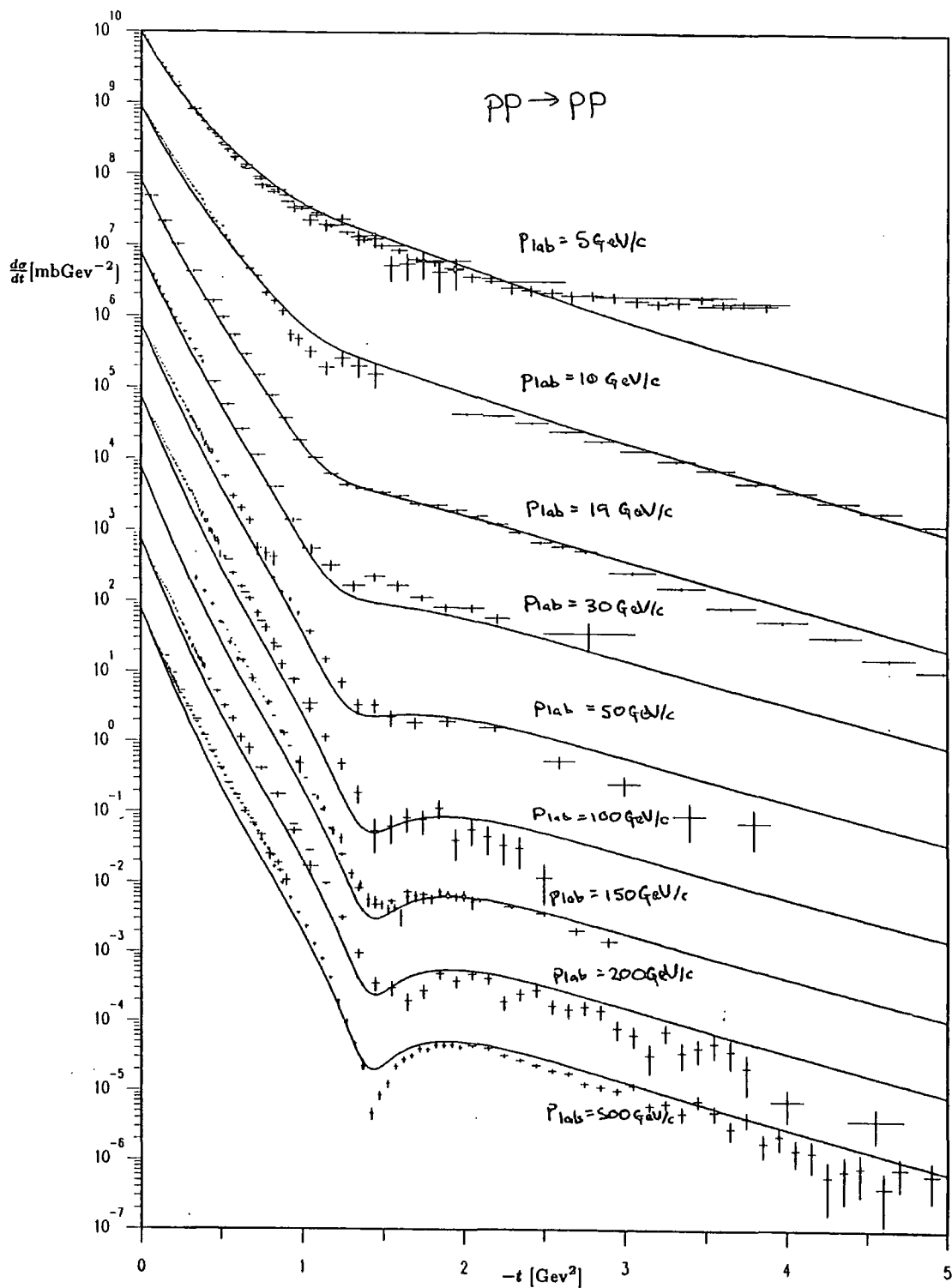


FIG.4.29 $\frac{d\sigma}{dt}$ using (4.8.1) with fit (4a) for $p_{\text{lab}} = 5 \rightarrow 280 \text{ GeV}/c$.

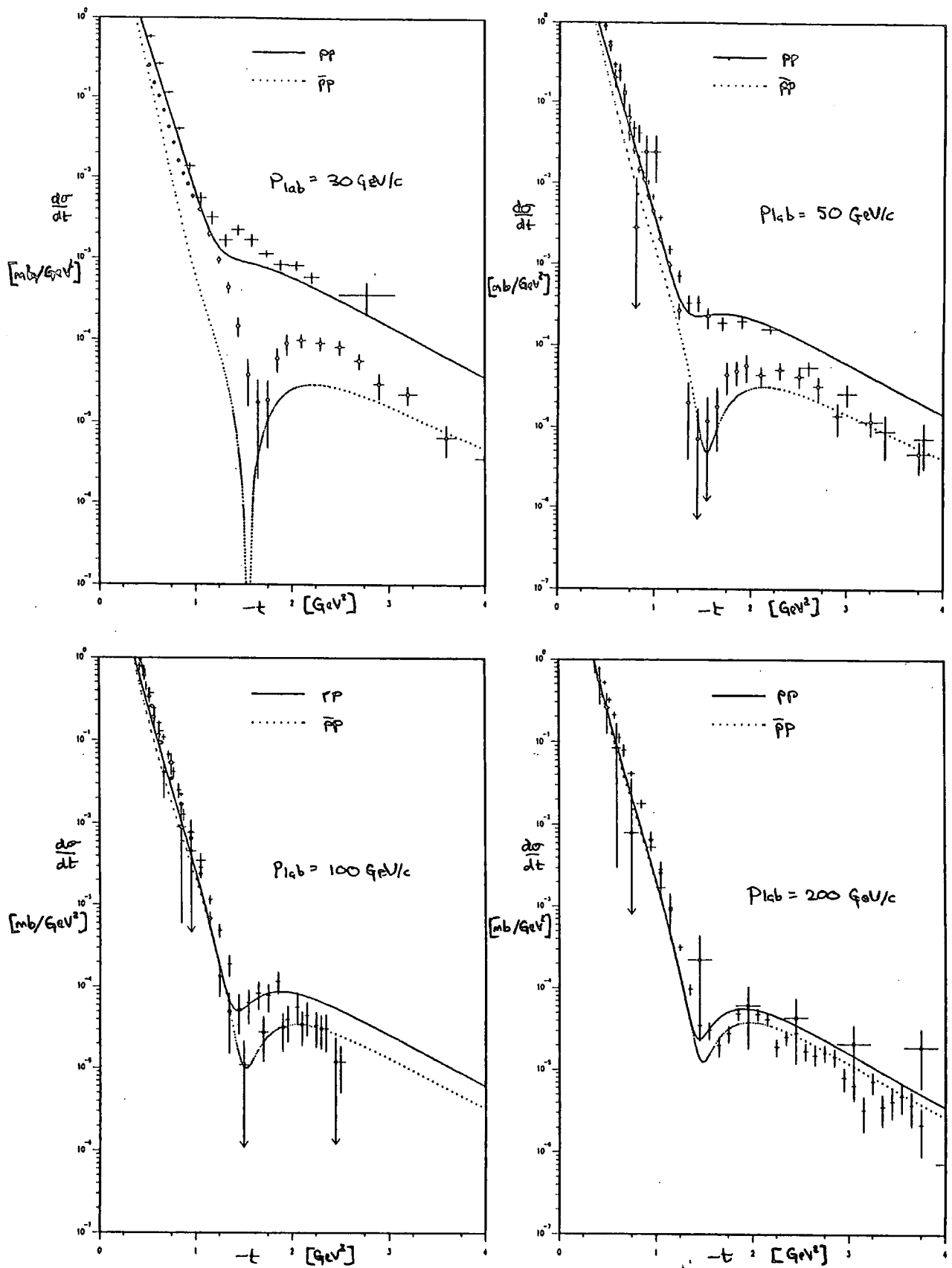


FIG.4.30 The differential cross-sections for pp and $\bar{p}p$ at $p_{\text{lab}} = 30, 50, 100$ and $200 \text{ GeV}/c$ using above description.

4.9. Conclusions, the Unitarity Limit and High Energy Extrapolations.

We have found above that the energy dependence of the Pomeron cut at large $|t|$ is not compatible with the energy dependence of the Pomeron at small $|t|$. The phase of the Pomeron determined by the energy dependence at small $|t|$ does not reproduce the sharp dip in the ISR data by interference between the Pomeron and the Pomeron cut. The energy independence of the large $|t|$ data at the ISR is incompatible with the growth of the cross-section in the dip region between the ISR and the Collider if the same dynamics are responsible for both. Thus the simple version of the model is incapable of answering any of the questions posed by the Collider data.

We have examined some possible refinements of the model to test if they can improve the agreement with the data. Incorporating a bent Pomeron trajectory to bring the Pomeron and cut more out of phase allows some improvement due to both the phase effect and the effect on the t -dependence of the Pomeron cut, though in practice it was difficult to get a reasonable description of the evolution of the dip through the ISR and the parametrization was unable to produce a shoulder at $\sqrt{s} = 546$ GeV of the correct magnitude. Allowing extra t -dependence in the simple cut parametrization was able to reproduce a shoulder at the Collider and a dip at the ISR but could not then reproduce the energy independence of the ISR data.

Extrapolating the fits to low energies we found that a reasonable description of the data could be found for $p_{lab} \geq 50$ GeV/c. This indicated that there was still a small low energy effect present at the lowest of the ISR energies. This could account for the large $|t|$ shrinkage found in §2.6 so that the cut off, $p_{lab} = 200$ GeV/c, applied in figure 2.13 is possibly too low.

We concluded that in this model some extra contribution is needed to describe the Collider data and examined the effects on the Pomeron parameters of including an arbitrary parametrization of the extra term.

The predictions of the model at high energy using fit (4a) are shown in figures 4.31-34. The high energy behaviour of σ_T is displayed in figure 4.31 for \sqrt{s} up to 10^8 GeV and is consistent with the cosmic ray data. The contributions to σ_T of the Pomeron and cut are also included in the figure. The cut has very little effect at these energies.

The Froissart bound (3.3.7) is eventually violated by the Pomeron contribution. In fit (4a) this occurs for $\sqrt{s} \approx 10^{25}$ GeV, too high an energy to attach much significance to. The reduced bound given by (3.3.8) is violated for $\sqrt{s} \approx 10^{10}$ GeV. The energy dependence of the cut means that eventually it will dominate the amplitude but this does not occur until $\sqrt{s} \approx 10^{13}$ GeV. Figure 4.32 shows the high energy behaviour of ρ . For $\sqrt{s} \geq 1$ TeV the Pomeron contribution dominates the amplitude resulting in a constant value for the ratio Re/Im given by

$$\rho = \tan \frac{\pi}{2}(\alpha_P(0) - 1) \simeq \frac{\pi}{2}(\alpha_P(0) - 1) = \frac{\pi}{2}0.094 = 0.148 \quad (4.9.1)$$

The ratio, $R = \sigma_{el}/\sigma_T$, exceeds the diffractive limit value of one half for $\sqrt{s} \geq 200$ TeV and continues growing as $\frac{s^{\epsilon}}{\log s}$ neglecting the fact that unitarity is violated by a Pomeron with intercept greater than unity. The elastic profile function, $A(s, b)$, for the full amplitude of fit (4a) is shown in figure 4.33 at various energies. It violates the diffractive limit (3.2.24) for $\sqrt{s} \approx 1.8$ TeV and the unitarity limit (3.2.12) for $\sqrt{s} \approx 300$ TeV. A simple parametrization of the elastic scattering amplitude by the Pomeron pole

$$A^P(s, t) = -G_P(e^{-i\frac{\pi}{2}}s)^{\alpha_P(0)}e^{c_P t} \quad \text{where} \quad c_P = a_P + \alpha'_P \left(\log s - \frac{i\pi}{2} \right) \quad (4.9.2)$$

gives for the profile function

$$A^P(s, b) = i \frac{G_P(e^{-i\frac{\pi}{2}}s)^{\alpha_P(0)-1}}{16\pi} \frac{e^{-\frac{b^2}{4c_P}}}{c_P} \quad (4.9.3)$$

so that as the energy increases this increases without bound and violates the unitarity constraint.

To the extent that c_P is real in the above, the ratio $\rho'(s, b) = \text{Re/Im } A(s, b)$, is just $\rho'(s, b) = \rho(s, t) \simeq \frac{\pi}{2}(\alpha_P(0) - 1)$. An Argand plot of the elastic profile function as a function of energy at fixed b is therefore linear with slope $1/\rho$. This is shown in figure 4.34 for both the Pomeron contribution alone and with the cut contribution included. The Pomeron alone violates the diffractive limit for $\sqrt{s} \approx 900$ GeV. We shall consider the effects of restoring unitarity in chapters §6 → 9.

The dependence on $\alpha_P(0)$ of the energy, \sqrt{s} , at which the Pomeron violates the diffractive limit is explored in table 4.11 using the fits obtained for various values of $\alpha_P(0)$ in table 4.3(a). Increasing $\alpha_P(0)$ means β_P must decrease to fit σ_T at the Collider

so $\sqrt{\tilde{s}}$ is fairly independent of $\alpha_P(0)$ and given by $\sqrt{\tilde{s}} \approx 1$ Tev. Also given in table 4.11 are the predicted cross-sections at $\sqrt{s} = 2$ and 40 Tev for the various values of $\alpha_P(0)$. These give a range of about 10 mb and 30 mb respectively at the two energies for viable fits to σ_T .

$\alpha_P(0)$	$\sqrt{\tilde{s}}$ GeV	$\sigma_T(2 \text{ Tev})$	$\sigma_T(40 \text{ Tev})$
1.07	2500	72.2	110
1.08	1700	74.1	120
1.085	1400	75.5	126
1.09	1100	77.4	132
1.095	1000	78.8	139
1.10	850	81.0	147
1.11	840	82.9	159
1.12	900	84.2	170
1.13	1000	85.2	181

TABLE 4.11 Predicted energies at which diffractive limit is exceeded for fits of table 4.3(a) and total cross-sections at $\sqrt{s} = 2$ and 40 Tev.

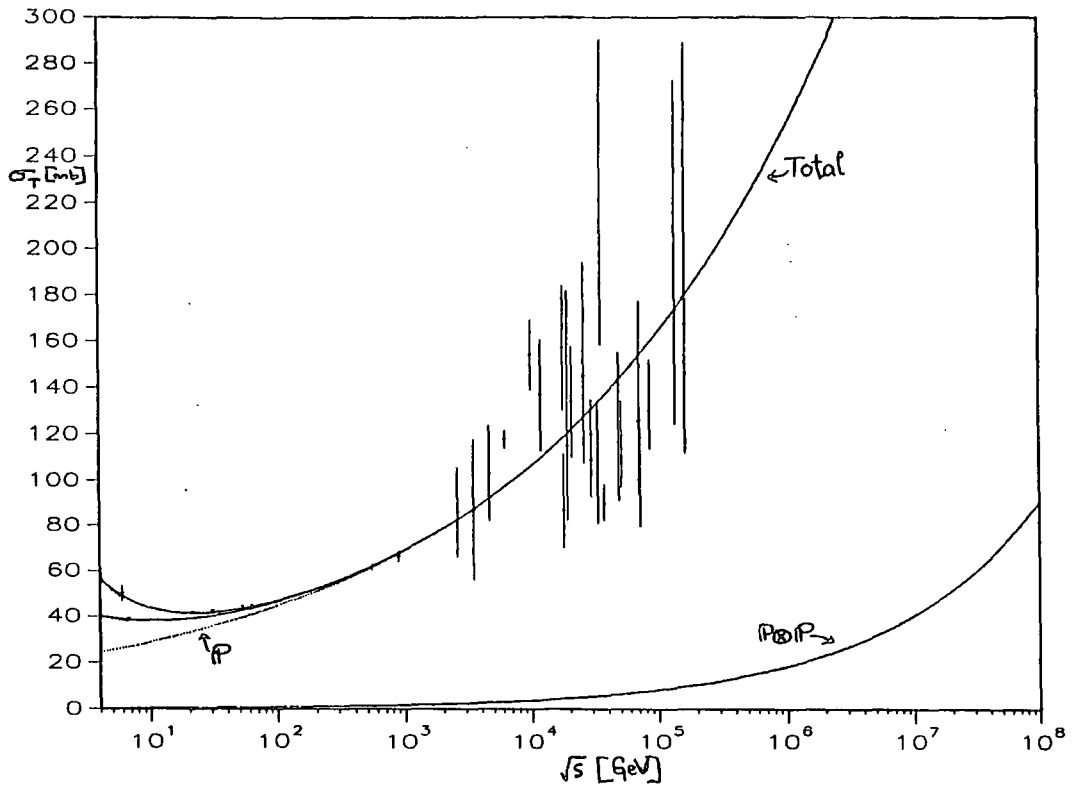


FIG.4.31 High energy behaviour of σ_T for pp and $\bar{p}p$ using fit (4a) (Pomeron and Pomeron cut contributions also shown).

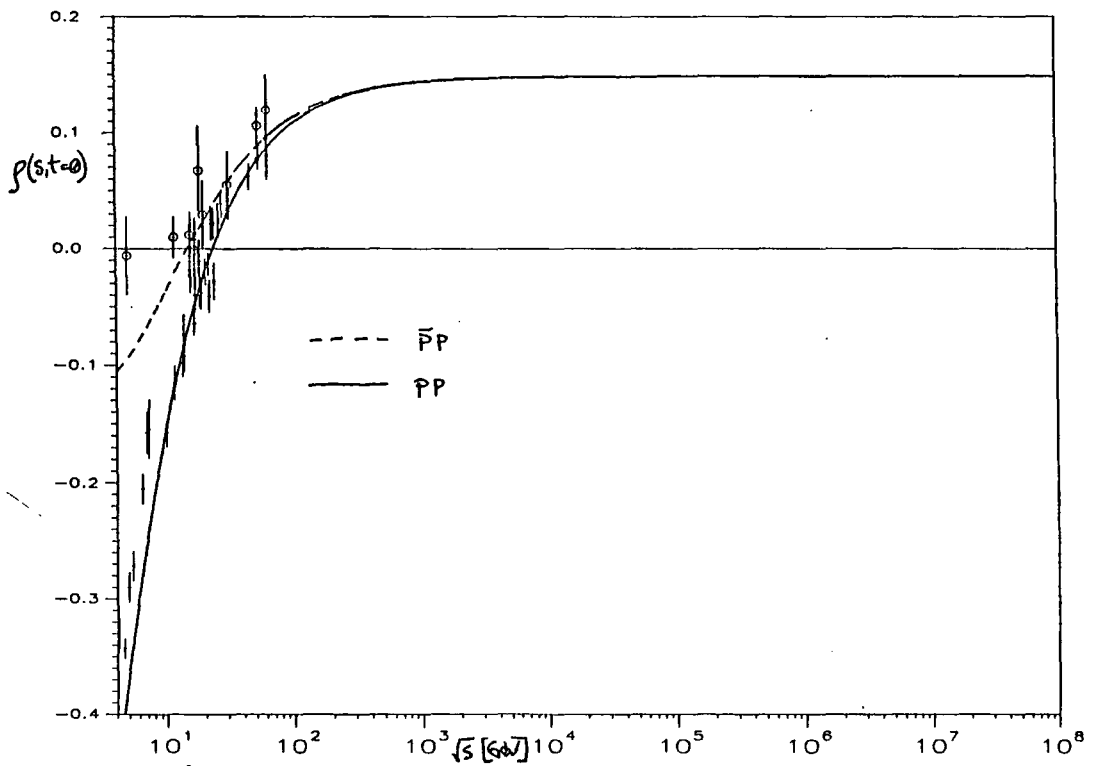


FIG.4.32 High energy behaviour of ρ for pp and $\bar{p}p$ using fit (4a).

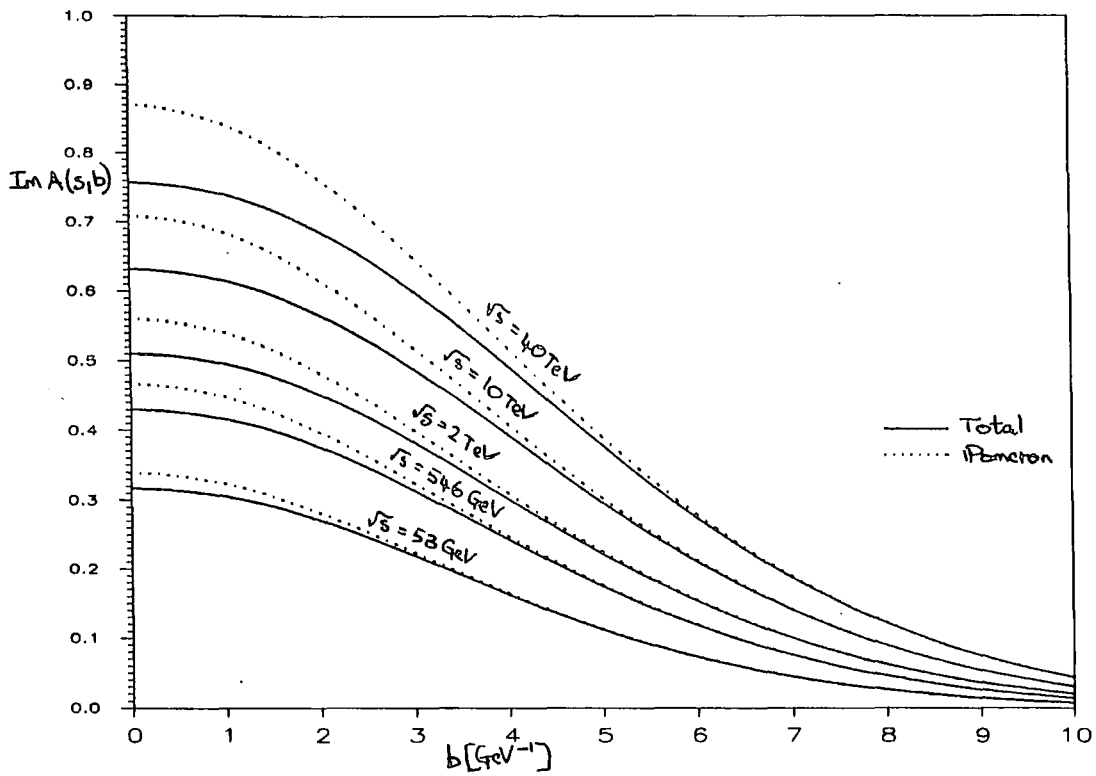


FIG.4.33 High energy behaviour of the profile function $Im A(s, b)$ using fit (4a).

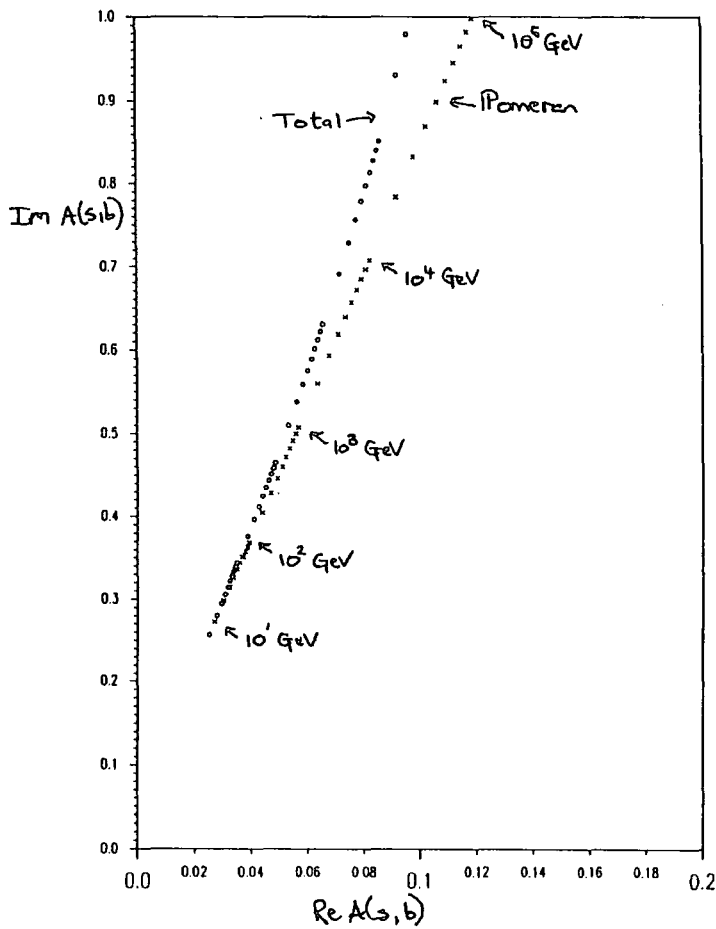


FIG.4.34 Argand plot for $A(s, b = 0)$ using fit (4a) for Pomeron alone and with cut included.

Odderon Models

5.1. Introduction

We saw in the previous chapter that it does not seem possible to explain the ISR and Collider data within the framework of a Pomeron plus weak cut model without invoking an extra contribution. This must be either increasing with energy or perhaps independent of energy and exposed by the shrinkage of the small $|t|$ amplitude. In either case it cannot involve the exchange of quarks (this would produce a cross-section that falls rapidly with energy) and so must be due to gluon exchange. The Pomeron and Pomeron cuts have been identified with even charge conjugate multiple-gluon exchange, so it seems natural to try to interpret this extra term as an odd-charge-conjugation multiple-gluon exchange contribution. To preserve colour this must have a primitive representation as three gluon exchange as in fig.5.1 just as the primitive representation of the Pomeron is two gluon exchange.

In this chapter we shall explore the idea of adding an odd charge conjugate contribution or 'Odderon' and see whether it improves the agreement with the data. The $P + P \otimes P$ model could not reproduce the large change between the ISR pp data and Collider $\bar{p}p$ data in the dip region whilst still keeping large $|t|$ at ISR energies almost energy independent. This would not be such a problem if pp and $\bar{p}p$ were noticeably different due to the presence of an odd charge conjugate contribution. As we discussed in §2.5 the pp and $\bar{p}p$ data at $\sqrt{s} = 53$ GeV are not conclusive but they do place a restriction on how large the difference between $\frac{d\sigma}{dt}(pp)$ and $\frac{d\sigma}{dt}(\bar{p}p)$ can be and limit the possible size of such an odd charge conjugate contribution. We shall look at three models with different approaches to the dynamics of the Odderon. Firstly, a model proposed by Donnachie and Landshoff, which we shall refer to as the DL model, in which the odd charge conjugate contribution is due to multiple scattering of the partons by the exchange of three gluons as in figure 5.1(a) and is energy independent; then a model proposed by Gauron, Leader and Nicolescu (1985), which we shall refer to as the GLN model, in which the odderon contribution increases with energy as fast as asymptotic theorems will allow it; and finally a model in which the odderon contribution is thought of as reggeized three gluon exchange and grows with energy in the same way as the Pomeron (see fig.5.1(b)).

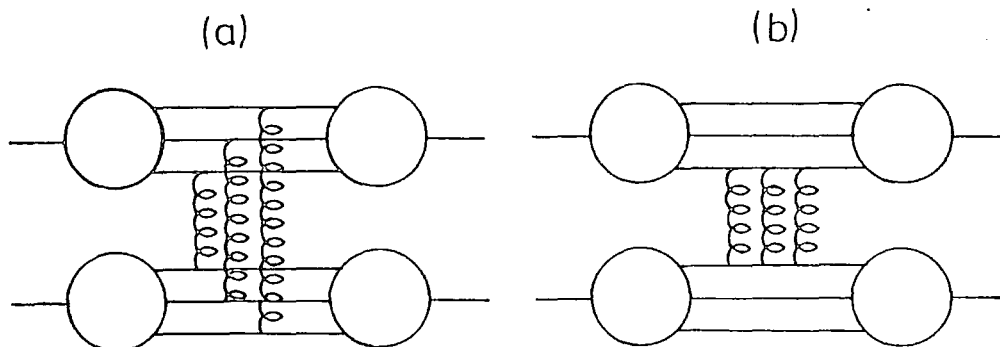


FIG. 5.1 (a) 3 gluon exchange. (b) primitive representation of reggeized 3 gluon exchange.

5.2 The Donnachie-Landshoff Model

In this model the large $|t|$ amplitude is dominated by the triple gluon exchange of fig.5.1(a). This gives a purely real, energy independent contribution with odd charge conjugation and so appears with a +ve sign in the pp amplitude and -ve sign in $\bar{p}p$.

The small $|t|$ region is described by a Pomeron with intercept greater than one as in §4 which gives an almost pure imaginary contribution. Since the 3g amplitude is real and the Pomeron is imaginary, they alone cannot produce the dip in $\frac{d\sigma}{dt}(pp)$. Another contribution is needed and this is provided by the Pomeron cut which is also mainly imaginary but with the opposite sign to the Pomeron (as in §4.4). The relative phase and t -dependence of the pole and cut are such that their interference still leaves a substantial real part and produces a shoulder rather than a dip in $\frac{d\sigma}{dt}$. The dip is produced by cancellation of the remaining real part of the amplitude by the 3g contribution. Since 3g exchange has odd charge conjugation it cancels in pp but adds in $\bar{p}p$ and so produces a dip in pp scattering but a shoulder in $\bar{p}p$. A prediction of the model (Donnachie and Landshoff (1984a)) was therefore that the dip seen at the ISR in pp scattering would not be present at similar energies in $\bar{p}p$ scattering.

The original motivation for this model stemmed from a calculation of a triple scattering mechanism in pp elastic scattering (Landshoff (1974)) in which each of the valence

quarks scattered through the same angle (none of them being far off shell) and then recombined to reform the proton.

If spin-one gluons are exchanged in this triple scattering mechanism then it is found that the differential cross-section behaves like :

$$\frac{d\sigma}{dt} \sim t^{-8} \quad \text{for } R^{-2} \ll |t| \ll s \quad (5.2.1)$$

independent of energy. R is a measure of the radius of the three-quark proton (see Donnachie and Landshoff (1979)). The data for $p_{lab} \geq 400$ GeV from FNAL and the ISR at large $|t|$ are approximately energy independent and seem to obey (5.2.1) rather well for $|t| \geq 3.5$ GeV², as can be seen in fig.5.2 . However, the analysis of the data in §2.6 indicated some energy dependence at large $|t|$ and there is considerable uncertainty about whether the behaviour (5.2.1) will be significantly modified by QCD corrections like that in fig.5.3(a) and thus whether it has any relevance at available energies and $|t|$ ranges. In the leading logarithm approximation these diagrams give the 3g amplitude an energy dependence through a factor like $e^{-b \log^2 s}$ which is incompatible with the large $|t|$ pp data (Landshoff and Pritchard (1980)). Hence the agreement with the large $|t|$ data is not entirely convincing evidence for 3g behaviour.

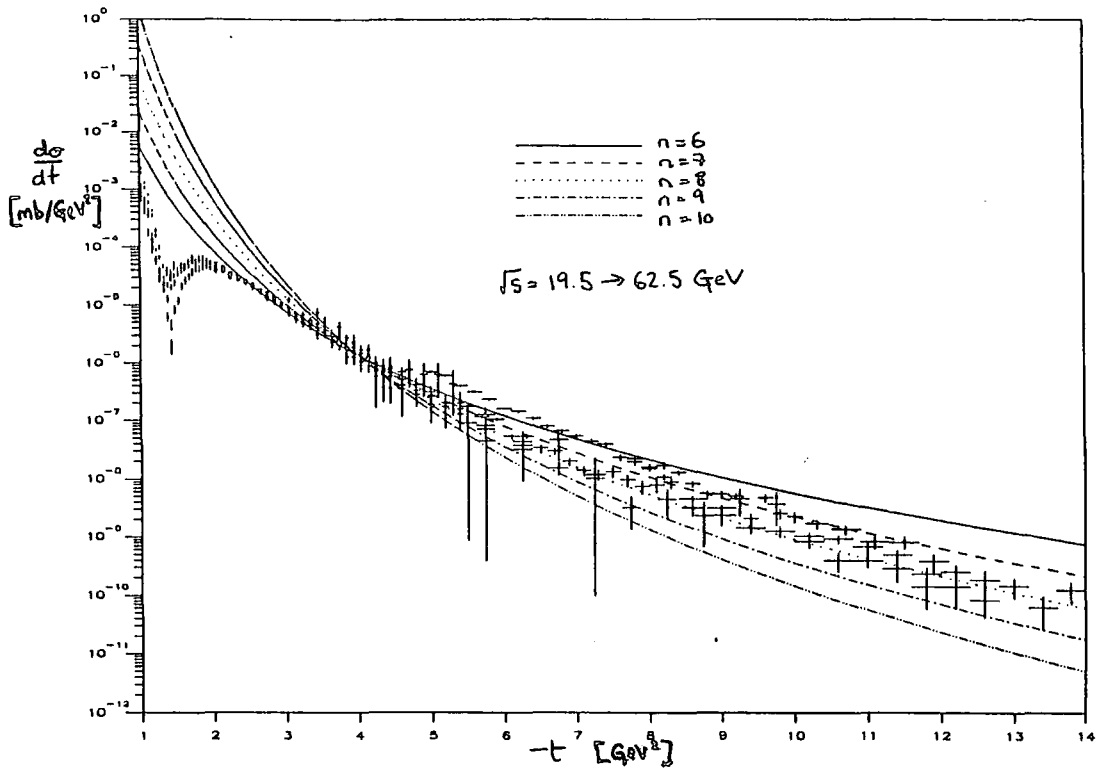


FIG. 5.2 Comparison of ISR and FNAL large $|t|$ data with $\frac{d\sigma}{dt} \simeq 0.09t^{-n}$ mb GeV $^{-2}$ with $n=6, 7, 8, 9, 10$.

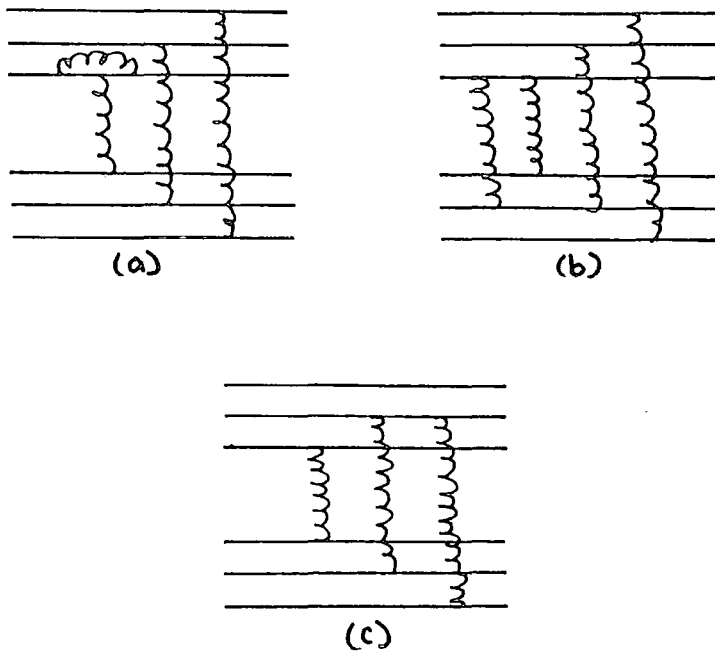


FIG. 5.3 Higher order QCD corrections to the primitive diagram of fig.5.1(a).

The diagrams like that in fig.5.3(b) will cancel the infra-red divergence at $t = 0$ and so the expression (5.2.1) is valid only for large enough $|t|$ where the t -scale is defined by R^{-2} . This is modelled by introducing a cut off at small $|t|$ so that the divergent behaviour is damped for $|t| \leq 2 \text{ GeV}^2$. The cut off is not well determined and can be adjusted appropriately. The mechanism described in Donnachie and Landshoff (1984a) is to modify the gluon propagators at some small value of $|t|$: $t_1 \approx 0.3 \text{ GeV}^2$, and to adjust the magnitude of the term so that at large $|t|$ it has the behaviour $\frac{d\sigma}{dt} \simeq 0.09t^{-8} \text{ mb GeV}^{-2}$. The resulting contribution to $\frac{d\sigma}{dt}$ for different choices of the cut off, t_1 , are shown in figure 5.4. The cut off chosen corresponds to a radius of 0.35 fm. It can be seen that the cut off controls the magnitude of the three gluon term in the dip region and makes a significant difference to the t -dependence of the three gluon contribution for $|t| \geq 2 \text{ GeV}^2$ allowing better agreement with the data around the second maximum. All the curves in the above figure are normalized so that they have the same magnitude at large $|t|$.

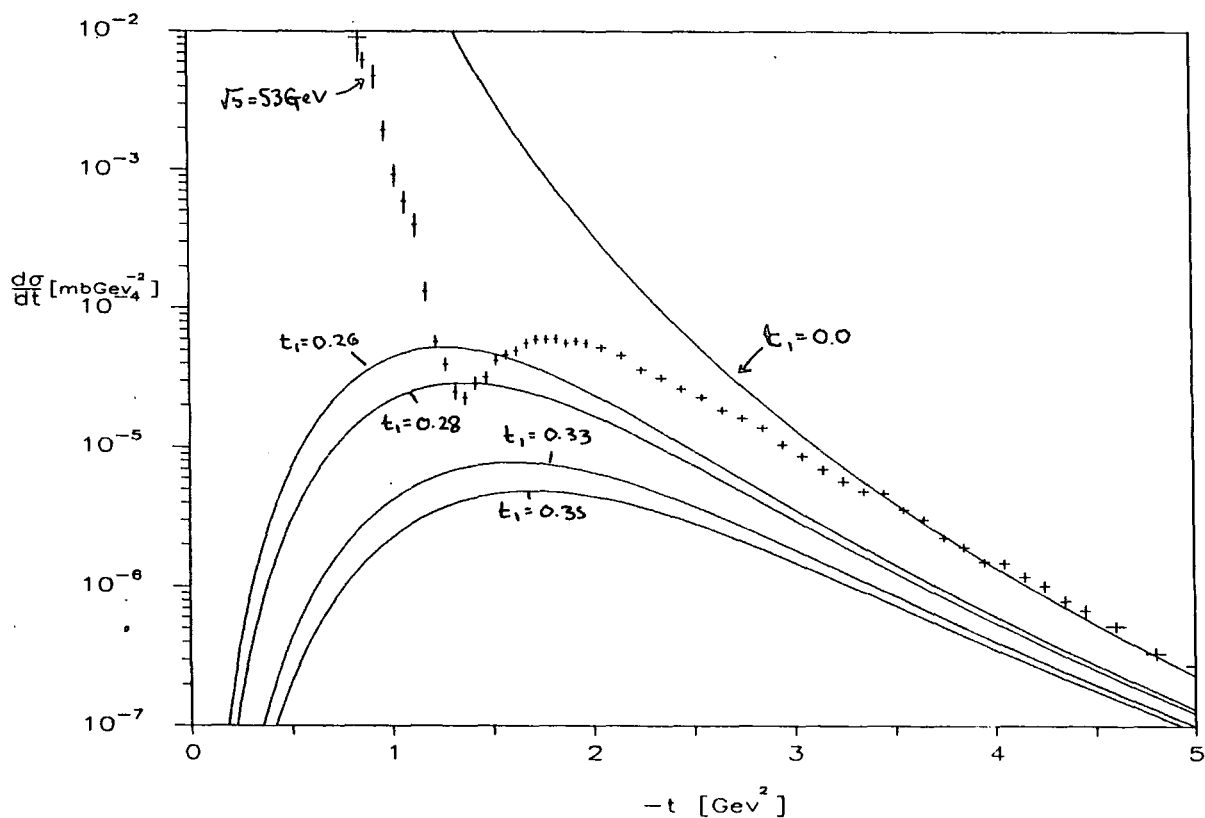


FIG. 5.4 Contribution of the 3 gluon term to $\frac{d\sigma}{dt}$ for different values of the cut off, $t_1 [\text{GeV}^2]$.

The Pomeron parametrization is the same as used in (4.4.1) but with the residue function written as

$$G_P(t) = 3\beta F_1(t) \quad (5.2.2)$$

The Pomeron is assumed to have a γ^μ coupling with the quarks, with coupling strength, β , and $F_1(t)$ is the Dirac form factor of the proton. The amplitude then satisfies quark additivity and s -channel helicity conservation. The form used for $F_1(t)$ is

$$F_1(t) = \frac{4m_p^2 - 2.79t}{4m_p^2 - t} \frac{1}{(1 - t/0.71)^2} \quad (5.2.3)$$

We saw previously that with $s_0 = m^2$ in (4.4.7) this gives a good description of the small $|t|$ data at both ISR and collider. However, the arbitrariness of the scale, s_0 , introduces an exponential factor $e^{\alpha'_P \log s_0 t}$ into the t -dependence of the Pomeron contribution and so the agreement probably mainly reflects the fact that in both ep and pp elastic scattering the scale is the proton radius.

The contribution from the Pomeron cut is calculated with the eikonal form (3.6.10) using the Pomeron amplitude (4.4.1) with residue from (5.2.2) and (5.2.3). The major difference from §4.4 is that the Gribov vertex (4.4.2) is replaced by a constant, less than one, so that the cut is similar to that in the eikonal approximation (§7) below but with a factor λ which suppresses the $P \otimes P$ term. This results in a t -dependence for the Pomeron cut of roughly half the exponential slope of the Pomeron (exactly half for a simple exponential t -dependence of the Pomeron residue) but with the same trajectory as in (4.4.3). The Pomeron cut only gives a large contribution to the amplitude in the t -range $1 \leq |t| \leq 2 \text{ GeV}^2$ since it has a t -dependence approximately midway between the Pomeron and triple gluon contributions. This is in contrast to the model described in §4 where the Pomeron cut had a much shallower slope and dominated the amplitude for $t \geq 2 \text{ GeV}^2$. The cut contribution is adjusted so that it cancels the imaginary part of the Pomeron in the dip region at $|t| \approx 1.4 \text{ GeV}^2$. The 3g contribution then cancels the remaining real part of the amplitude in pp scattering producing a dip, but adds in $\bar{p}p$ producing a shoulder. Interference between the Pomeron cut and 3g contributions continues out to large $|t|$ producing some difference between the magnitudes of pp and $\bar{p}p$ but since the Pomeron cut is dying away with increasing $|t|$ this effect is small for $|t| > 5 \text{ GeV}^2$. Since the triple gluon contribution is purely real it does not contribute to σ_T . The Pomeron cut gives a larger contribution to σ_T than in §4 because of its different t -dependence and this is compensated by increasing the magnitude and

energy dependence of the Pomeron term but otherwise the results of §4.2 are essentially unchanged.

Using this model a good account of the ISR pp data was obtained by Donnachie and Landshoff (1984a). The more recent $\bar{p}p$ data from the ISR and the Collider which show a shoulder rather than a dip seem to support this model (though the difference between the $\frac{d\sigma}{dt}(pp)$ and $\frac{d\sigma}{dt}(\bar{p}p)$ data at $\sqrt{s} = 53$ GeV is not compelling). Straightforward use of this parametrization with this more recent data produces too high a shoulder in $\bar{p}p$ at $\sqrt{s} = 53$ GeV and the shoulder in $\bar{p}p$ predicted at the collider energy lies a factor of $8\times$ below the collider data. In Donnachie and Landshoff (1986) they adjust the parameters to try to cope with the new data.

In order to get agreement with the new $\bar{p}p$ data it is necessary to describe the collider shoulder as an interference effect between the Pomeron and the Pomeron cut in a similar way to fit(4c) in §4.6 rather than as an effect produced by the $3g$ term (weak Odderon). To make this work the Pomeron must be given a flatter t -dependence to make it larger in the shoulder region (since the cut subtracts more off the Pomeron) which is accomplished by exploiting the $e^{\alpha'_P \log s_0 t}$ factor noted above and replacing $s_0 = m_p^2$ by $s_0 = 1/\alpha'_P$, which is given some theoretical motivation through the work of Veneziano (1968). The triple gluon contribution is a relatively small effect at this value of $|t|$ and only produces a small difference between pp and $\bar{p}p$ at $\sqrt{s} = 546$ GeV. This effect also increases the size of the real part in the ISR dip region left by the cancellation of the imaginary parts of the Pomeron and Pomeron cut which was previously cancelled in pp by the $3g$ contribution. However, to reproduce the $\bar{p}p$ data at $\sqrt{s} = 53$ GeV and avoid making pp and $\bar{p}p$ too different in the dip region it is necessary to reduce the part played by the $3g$ contribution in cancelling the real part of the $P + P \otimes P$ amplitude. This limitation on the size of the $3g$ term at the ISR prevents it being responsible for the shoulder at the collider. The cancellation of the real part of the $P + P \otimes P$ amplitude is produced by a large $R \otimes P$ term. The $f \otimes P$ contribution at ISR energies is $1/12^{th}$ the size of P or $P \otimes P$ in the dip region but the phases are such that it reduces the real part of the amplitude substantially. The $\omega \otimes P$ is a small effect because the magnitude of the ω contribution is smaller than that of the f and it is almost purely imaginary in the dip region.

The dip found in the ISR data is deepest at $\sqrt{s} = 31$ GeV and $|t| = 1.43$ GeV². The

amplitude is made to vanish at this point by adjusting the strength of the $P \otimes P$ cut through λ_{2P} in equation (B.5) so that the imaginary part of the amplitude cancels and then adjusting the 3g cut off so that the real part of the amplitude is cancelled. As the energy differs from $\sqrt{s} = 31$ GeV the positions of the zeroes in the real and imaginary parts change differently with energy and the dip fills in as the data indicate. As in the PWC model most of the movement of the dip is produced by the shrinkage of the Pomeron contribution and so the dip moves in to smaller $|t|$ as the energy increases. The shape of the dip depends upon how the 3g contribution is cut off at small $|t|$ which can be adjusted to fit the data.

In their earlier work Donnachie and Landshoff also considered the effects of including triple-Pomeron and Pomeron-two gluon exchange. These are expected to make little difference and were omitted in their latest parametrization. The calculation of the 3-Pomeron term (described in appendix B) follows that of 3g exchange differing from the eikonal prescription for 3-Pomeron exchange but giving approximately the same t -dependence. The strength of the contribution is not very well known and is sensitive to the magnitude of the Pomeron term and perhaps should include the suppression factor present in the two-Pomeron cut calculation. Its phase and energy dependence are determined by the trajectory $\alpha_{3P}(t) = 1 + 3\epsilon_P + \frac{\alpha'_P}{3}t$ and so is an almost pure imaginary term like the Pomeron which grows faster with energy than the Pomeron or 2-Pomeron cut. Its inclusion thus has the effect of lowering the shoulder produced at the collider (though the strength of the 2-Pomeron cut has to be increased by 10% to compensate the 3-Pomeron term at the ISR the energy dependence of the 3-Pomeron term means a net decrease in the height of the shoulder at the collider by a factor of two). Multiple Pomeron exchange is important in that it is expected to prevent violation of the Froissart bound at high energy (see §6). However, since it is uncertain whether it is significant yet we shall omit it also. The Pomeron-two-gluon exchange term has the same shape as 3-gluon exchange but is negligible since a small alteration in the parameters of the other terms will mask its effect.

We attempted to reproduce the parametrization given in Donnachie and Landshoff (1986) which gives an excellent description of the ISR and Collider data but the fit is very sensitive to the exact parameter values and precise details of the parametrization used. The parametrization we have used is given in appendix B. The main problem in getting agreement with the data using this seems to be the slightly high value of

α'_P used ($\alpha'_P = 0.25 \text{ GeV}^{-2}$) which gives too much shrinkage for $|t| \geq 0.5 \text{ GeV}^2$ and too large a real part in the dip region. In order to obtain better agreement with the data we adjusted the parameters of the Pomeron, 2-Pomeron cut, f -Pomeron cut and $3g$ terms.

The calculation of the triple gluon amplitude involves a double integral at each t -value. We evaluated it at a number of t -points and obtained intermediate values by interpolation. The Pomeron cut and Regge-Pomeron cuts were calculated using (3.6.9) and involve double integrals at each s and t point (For a discussion of how we evaluated these numerically see §6 below). We found that the energy dependences of the approximate forms of the full integrals for the $P \otimes P$ and $R \otimes P$ terms given in Donnachie and Landshoff (1984) are not sufficiently accurate to be used as replacements for the full integrals in the fitting procedure. To allow us to fit the data we used an exponential approximation to the form factor (5.2.3), as in (4.4.1), giving an analytic solution for the integrals (equation (4.4.3) with $b_1 = 0$). We first fit to small $|t|$ and the collider shoulder giving reasonable values for the Pomeron and Pomeron cut parameters; then use these in a fit to σ_T to determine the f parameters and fine tune the Pomeron at $t = 0$ and finally vary the t -dependence of the Pomeron, f -Pomeron cut and strength of the Pomeron cut to fit the ISR dip region and collider shoulder.

The parameter values found differ slightly from those in Donnachie and Landshoff (1986). Like them, we have included a $P \otimes P$ term in the calculation of σ_T , but following §4.2 we have allowed the f and ω Regge trajectories to differ and also included the Regge-Pomeron cut terms. The results for σ_T , shown in fig.5.5(a), are comparable to those obtained in §4.2. The parameters found are given in appendix B. The Pomeron cut, which now makes a sizeable contribution to the amplitude at $t = 0$, is compensated by increasing the magnitude of the Pomeron term rather than its intercept, which is the same as that obtained in (4.2.7). We have not changed the parameters of the ω from (4.2.6) although they should be slightly affected by the inclusion of the $\omega \otimes P$ cut. Figure 5.5(b) shows the contributions of the various parts of the amplitude to σ_T . At $\sqrt{s} = 546 \text{ GeV}$ the Pomeron cut gives a contribution 13% that of the total compared with $\approx 2\%$ in the PWC model.

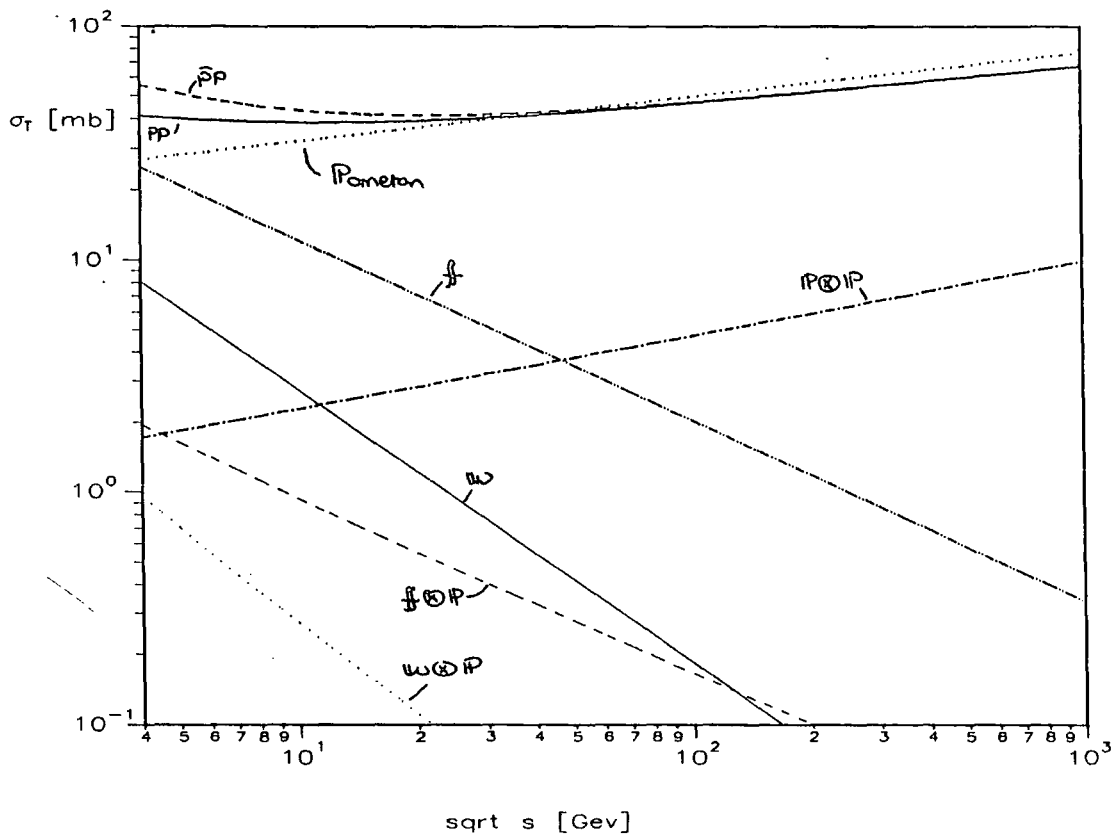
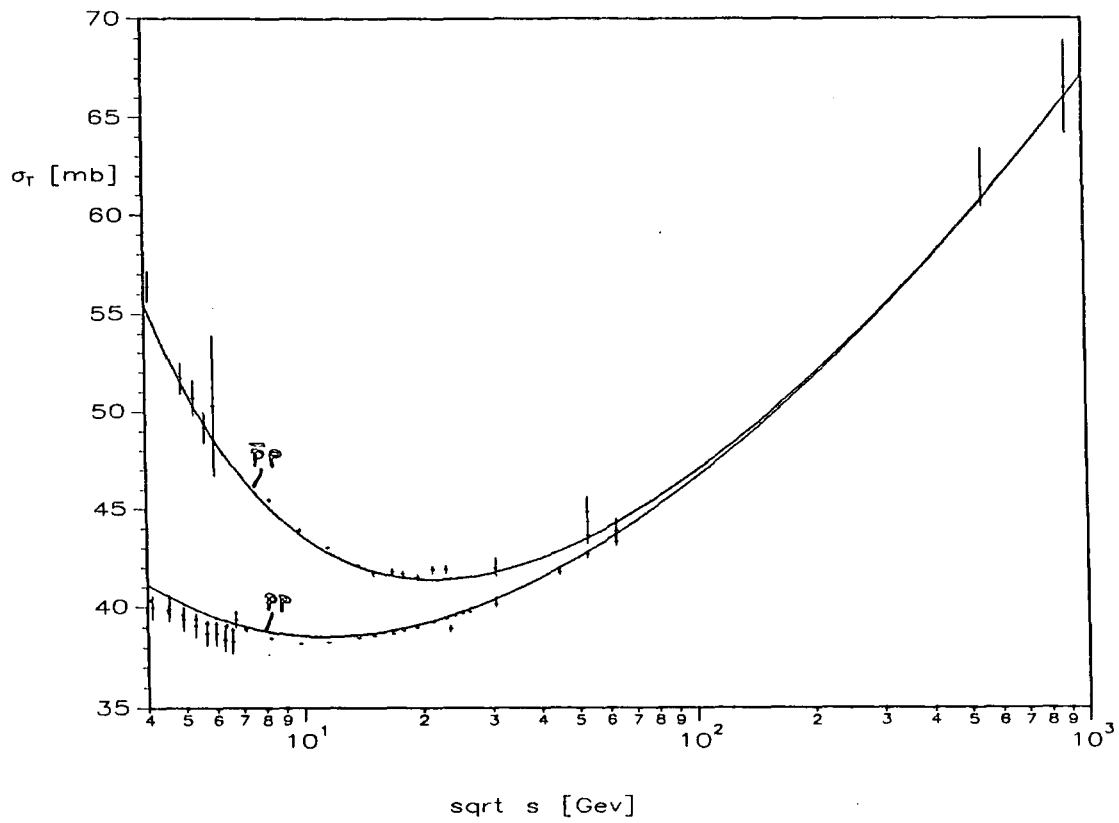


FIG. 5.5 Fit to σ_T using the DL model (a) compared with the pp and $\bar{p}p$ data, (b) individual contributions to σ_T .

Figure 5.6 shows the contributions of the various terms to the differential cross-section

at $\sqrt{s} = 53$ GeV. The only important terms at this energy in the dip region are the Pomeron, Pomeron cut, f -Pomeron cut and 3-gluon terms. The Reggeon terms and the ω -Pomeron cut are negligible. Also shown is the contribution of $P + P \otimes P$ alone which shows the importance of the $f \otimes P$ and $3g$ terms in producing the dip in pp .

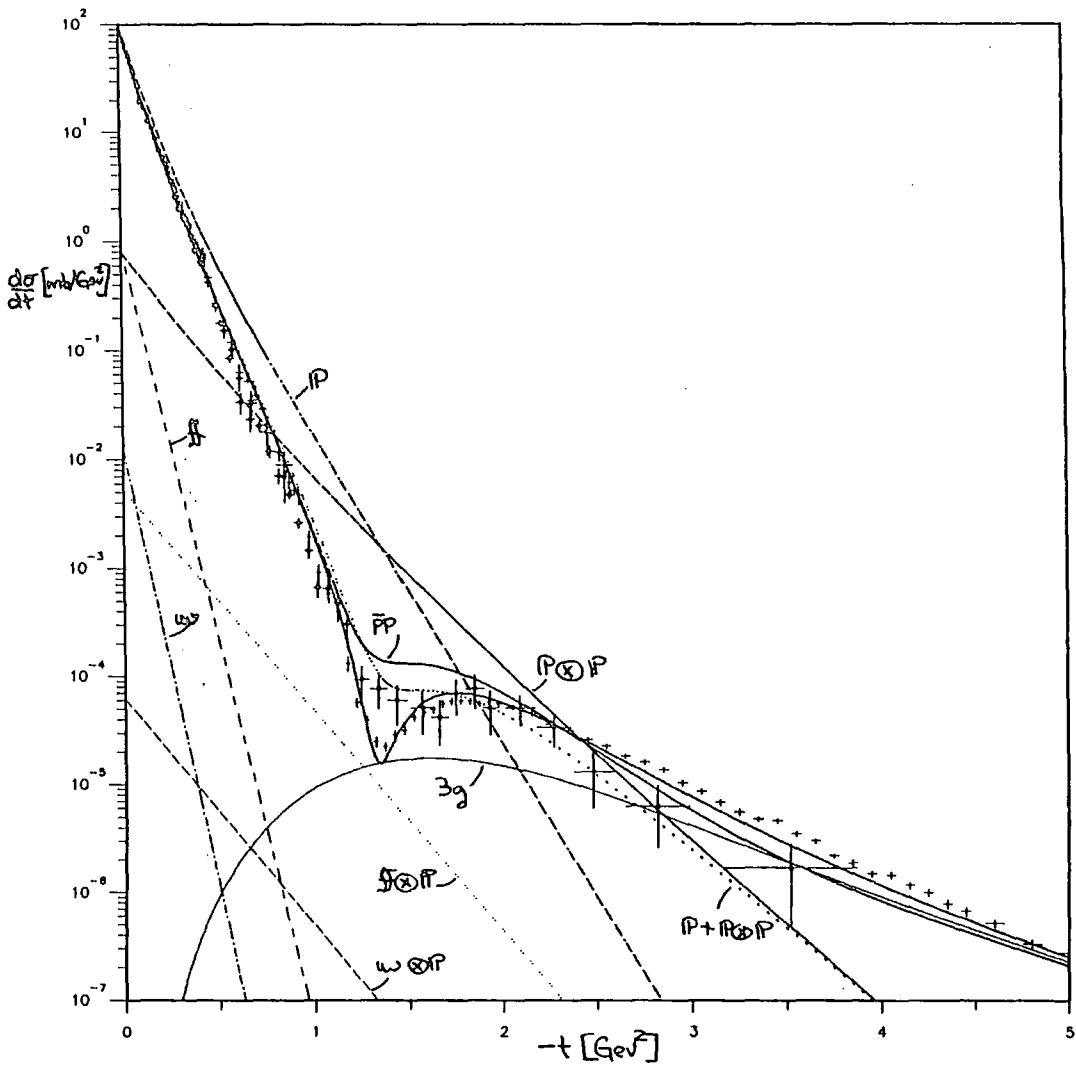


FIG. 5.6 Individual contributions to $\frac{d\sigma}{dt}$ made by the various terms in the DL model.

The comparison with $\frac{d\sigma}{dt}$ at other energies is shown in fig.5.7 . The small $|t|$ fit at the ISR and Collider compares well with that obtained in the PWC model. The description of the ISR dip is not as good as that in Donnachie and Landshoff (1986) but is nonetheless reasonable and in agreement with the data except possibly at $\sqrt{s} = 23.5$ GeV where the dip is a little too far out in $|t|$ and slightly the wrong shape. The shoulder in $\bar{p}p$ at the Collider is very well accounted for whilst that at $\sqrt{s} = 53$ GeV is too high but consistent with Donnachie and Landshoff (1986).

Comparing the model with the data at $\sqrt{s} = 53$ GeV and $|t| = 1.35$ GeV² in table 5.1 we find that the calculated pp and $\bar{p}p$ cross-sections are equally far away from the actual $\bar{p}p$ data. The 30% normalization error quoted in the $\bar{p}p$ data means the calculated cross-section is only slightly too high for $\bar{p}p$ but the agreement is no better than without an odd charge conjugation contribution (though the pp data at the same energy indicate that the normalization error is saturated). This indicates that the 3g contribution is too large (though using $t_1 = 0.35$ GeV² for the cut off as in Donnachie and Landshoff (1986) makes little difference to the quality of the fit).

	Data	Model
$\bar{p}p$	$(7.7 \pm 2.7) \times 10^{-5}$	14.2×10^{-5}
pp	$(2.1 \pm 0.6) \times 10^{-5}$	1.6×10^{-5}

TABLE 5.1

We find we need a smaller value of α'_p to control the shrinkage between the ISR and the Collider and the movement of the dip in pp at the ISR. If we compare the Pomeron t -dependences at $\sqrt{s} = 53$ GeV using the exponential residue (4.4.1) with $\alpha'_p = 0.16$ GeV⁻² and using the dipole form factor residue (5.2.3) with $\alpha'_p = 0.25$ GeV⁻² we find they are very similar so we will get a good description of the data with the dipole form factor residue and $\alpha'_p = 0.16$ GeV⁻² provided we use $s_0 \approx 4$ GeV² rather than $\frac{1}{\alpha'_p}$.

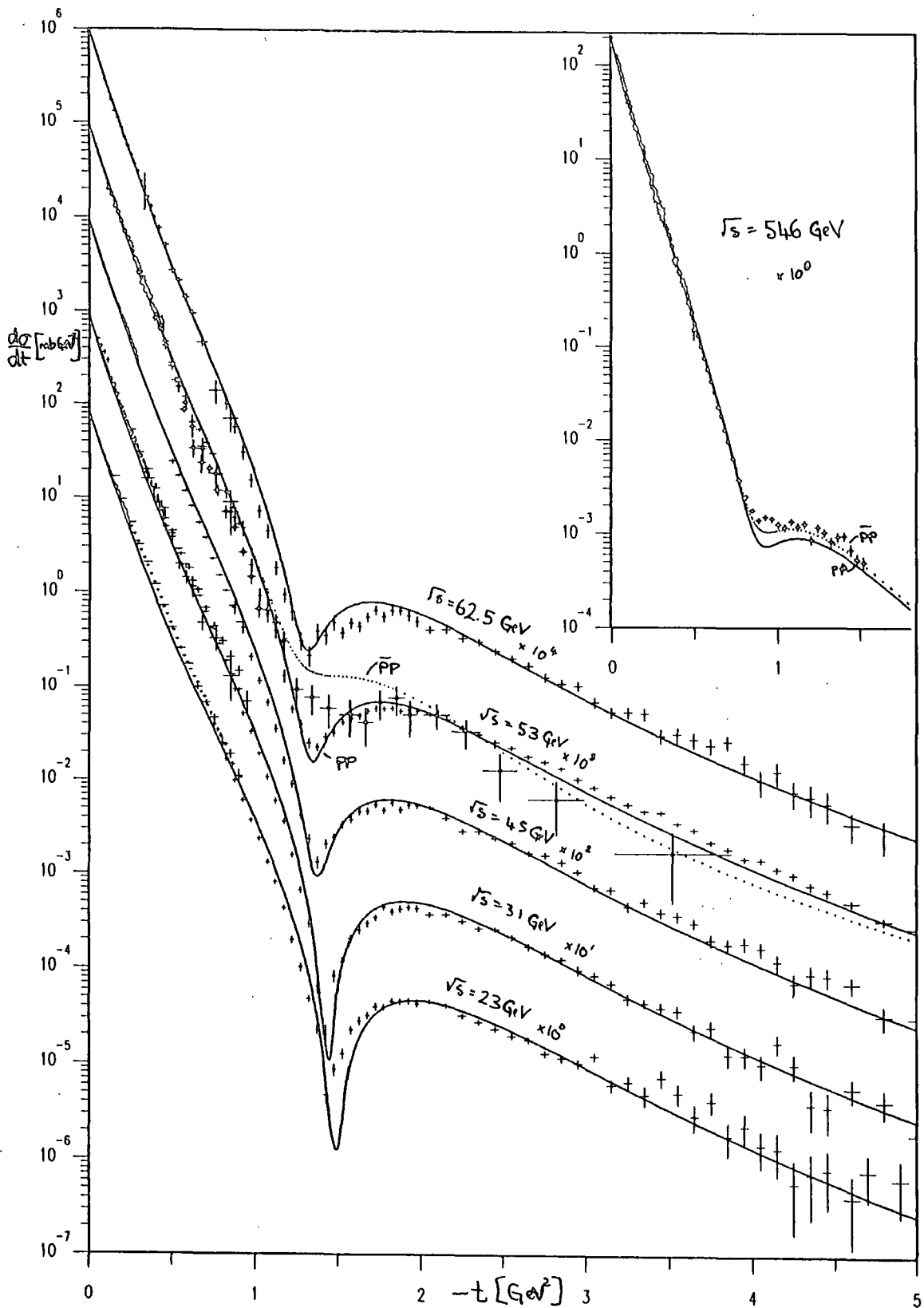


FIG. 5.7 Differential cross-section obtained using DL model.

The smaller value for α'_P produces a better cancellation of the real part of the Pomeron and its cut but a comparatively large $f \otimes P$ is still needed to prevent the dip moving too far out to larger $|t|$ at low energy. We explicitly tried fitting without an $f \otimes P$ term but as expected this gives too much energy dependence to the dip position at

the ISR. The absorption enhancement factors λ_{fP} and $\lambda_{\omega P}$ for the $f \otimes P$ and $\omega \otimes P$ cuts in (B.6) were held fixed in our fits at the same value required for the 2-Pomeron cut ($\lambda_{fP} = \lambda_{\omega P} \approx \lambda_{2P}$) and the strength of the $f \otimes P$ cut in the dip region adjusted by varying the t -dependence of the f Reggeon. The resulting t -dependence of the f is not too different from that used in the PWC model ($a_f^{PWC} = 2.7 \text{ GeV}^{-2}$, compared with $a_f^{DL} = 1.9 \text{ GeV}^{-2}$) giving a similar exponential fall off to the Pomeron over ISR energies. Since the f Reggeon and the Pomeron have the same quantum numbers their contributions cannot be easily separated. The $f \otimes P$ contribution is usually assumed to be negligible at ISR energies since it dies away fairly fast with increasing energy and there are considerable uncertainties in its calculation. In models in which the cuts are generated by an eikonal series a small alteration in the t -dependence of the Born term can make higher terms significant in the dip region (In the PWC model of §4 the small value of λ_{RP} made the $R \otimes P$ cuts negligible at ISR energies). The only theoretical restrictions on the t -dependence of the f Reggeon come from the f dominated Pomeron hypothesis and exchange degeneracy, neither of which usefully constrain the t -dependence of the f Reggeon in this parametrization. The best place to test whether this large an $f \otimes P$ term is acceptable is in low energy pp and $\bar{p}p$ scattering. In fig.5.8 we show the extrapolation of the fit down to low energies.

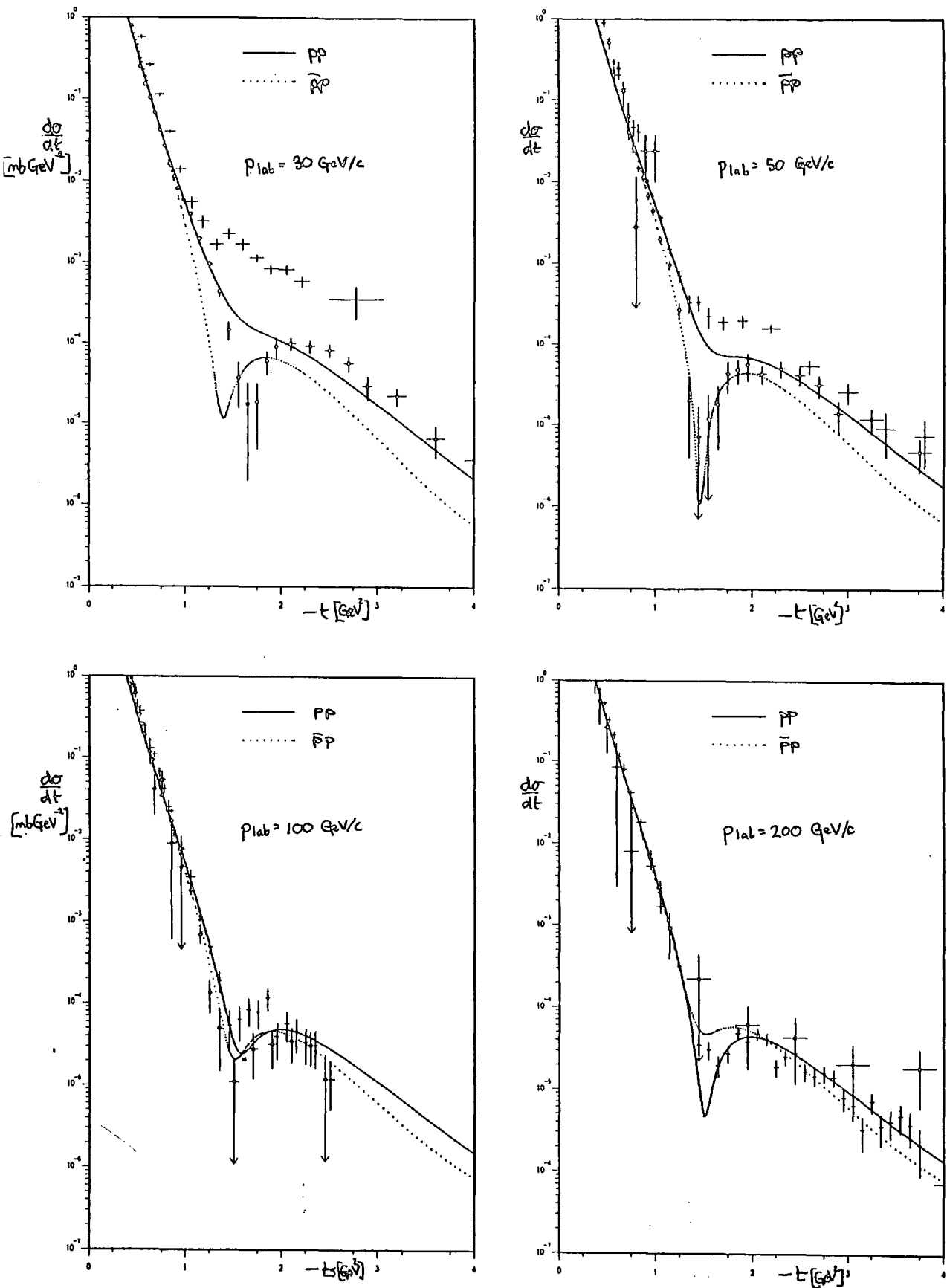


FIG. 5.8 Extrapolation of above fit to $\frac{d\sigma}{dt}$ to low energies.

The model gives qualitative agreement with the dip structure in both pp and $p\bar{p}$ down to $p_{\text{lab}} = 30 \text{ GeV}/c$. At $p_{\text{lab}} = 30 \text{ GeV}/c$ it produces a dip in $\frac{d\sigma}{dt}(p\bar{p})$ and a shoulder in $\frac{d\sigma}{dt}(pp)$ as in the data but the dip occurs at too small a value of t and the shoulder is too low by a factor of three. At $p_{\text{lab}} = 50 \text{ GeV}/c$ the model gives quite good quantitative

agreement in the dip region (though the prediction is not so good in the region beyond the dip). At $p_{lab} = 100$ GeV/c the dip in $\frac{d\sigma}{dt}(\bar{p}p)$ has filled in slightly and a similar dip has formed in $\frac{d\sigma}{dt}(pp)$ and by $p_{lab} = 200$ GeV/c the $\bar{p}p$ dip has turned into a shoulder whilst that in pp has deepened further.

The phase of the $f \otimes P$ term is such that it adds to the $P \otimes P$ contribution and at $p_{lab} = 30$ GeV/c pulls the dip too far in to the forward direction. In the odd charge conjugation part of the amplitude at $p_{lab} = 30$ and 50 GeV/c the $\omega \otimes P$ term is comparable in magnitude to the $3g$ term so that the $pp/\bar{p}p$ difference depends crucially on the $\omega \otimes P$ contribution. The full odd charge conjugation term is certainly not properly accounted for by these terms because the cross-over zero at small $|t|$ is not very well represented. At lower energies where the cross-over is more evident the predictions for pp and $\bar{p}p$ do not cross and have the wrong shape (though other non-leading trajectories and spin effects are important at these low energies).

Using (instead of (B.3)) an effective ω Reggeon with a $(1 + \frac{t}{t_0})$ absorption factor in the residue (pole dominated cut) to describe the small $|t|$, low energy data produces interference with the $\omega \otimes P$ cut at larger $|t|$ and destroys the qualitative agreement with the data at $p_{lab} = 30$ GeV/c though the prediction at $p_{lab} = 50$ GeV/c is still quite reasonable. Leaving out the $\omega \otimes P$ cut and just keeping the effective ω Reggeon term fails to produce the correct dip structure at either $p_{lab} = 30$ or 50 GeV/c.

Thus the low energy predictions of the model agree tolerably well with the $pp/\bar{p}p$ data down to $p_{lab} = 50$ GeV/c but do not give an adequate description of the data at $p_{lab} = 30$ GeV/c for which lower energy effects are important. The $R \otimes P$ cuts generated in this model have little in common with the Regge cuts needed to reproduce the low energy structure in the strong cut absorption model which typically requires enhancement factors of $\lambda_{RP} \approx 2.5$. There is evidence though, that the $R \otimes P$ cuts in the strong cut absorption model are pole-dominated and shrink faster with energy than expected from (B.6) (see for example Collins and Fitton (1975)) and there is enough theoretical uncertainty in the $R \otimes P$ cut calculation to allow contributions with both energy dependences to be present.

The necessity for a large $f \otimes P$ cut seems an unsatisfactory aspect of the model in that the stable position of the dip through FNAL and ISR energies arises as a result of a

quite complicated cancellation of the imaginary parts of the P , $P \otimes P$ and $f \otimes P$ terms. It also lessens the role the $3g$ term plays in cancelling the real part of $P + P \otimes P$. Since the data seem to prefer less of a difference in pp and $\bar{p}p$ than the $3g$ term produces, the two main roles the $3g$ term plays are to free the $P \otimes P$ term so that it can be used to fit the Collider shoulder and to give the large $|t|$ cross-section. The main test of the model is still the existence of a high energy $pp/\bar{p}p$ difference since all the other major features of the data are produced by adding another degree of freedom to the parametrization. It is perhaps arguable that the Collider shoulder provides support for the model in that it shows structure produced by the $P \otimes P$ contribution which was previously a necessary ingredient of the model but had only shown itself in the dip region. However, the change in the t -dependence necessary to account for the shoulder also affects the fit in the dip region at the ISR and the $3g$ term alone is not sufficient to enable the model to get the dip position and the $pp/\bar{p}p$ difference right. The $3g$ term does give the t -dependence observed in the data at large $|t|$ but this is by no means compelling phenomenologically or theoretically.

It might be expected that because the $f \otimes P$ contribution is comparatively large in the dip region at high energies a $pp/\bar{p}p$ difference might be produced by the $\omega \otimes P$ cut. A model which uses this has to contend with the problem that the magnitude and phase of the $\omega \otimes P$ term results in a factor of $30\times$ between the real parts of the two contributions so that it is difficult to make this work.

The behaviour of σ_T at very high energies predicted by the model is similar to that of the PWC model but the larger $P \otimes P$ cut term reduces the rate at which σ_T rises and ameliorates the unitarity problems. The high energy prediction for σ_T is shown in fig.5.9 in which the Pomeron and Pomeron cut contributions are shown individually. It can be seen from the figure that at $\sqrt{s} \approx 10^7$ GeV a cross-over point is reached where the increase in the Pomeron contribution is offset by the increase in the Pomeron cut so that the total cross-section decreases unphysically with energy thereafter. This is expected to be counteracted by higher order Pomeron cuts.

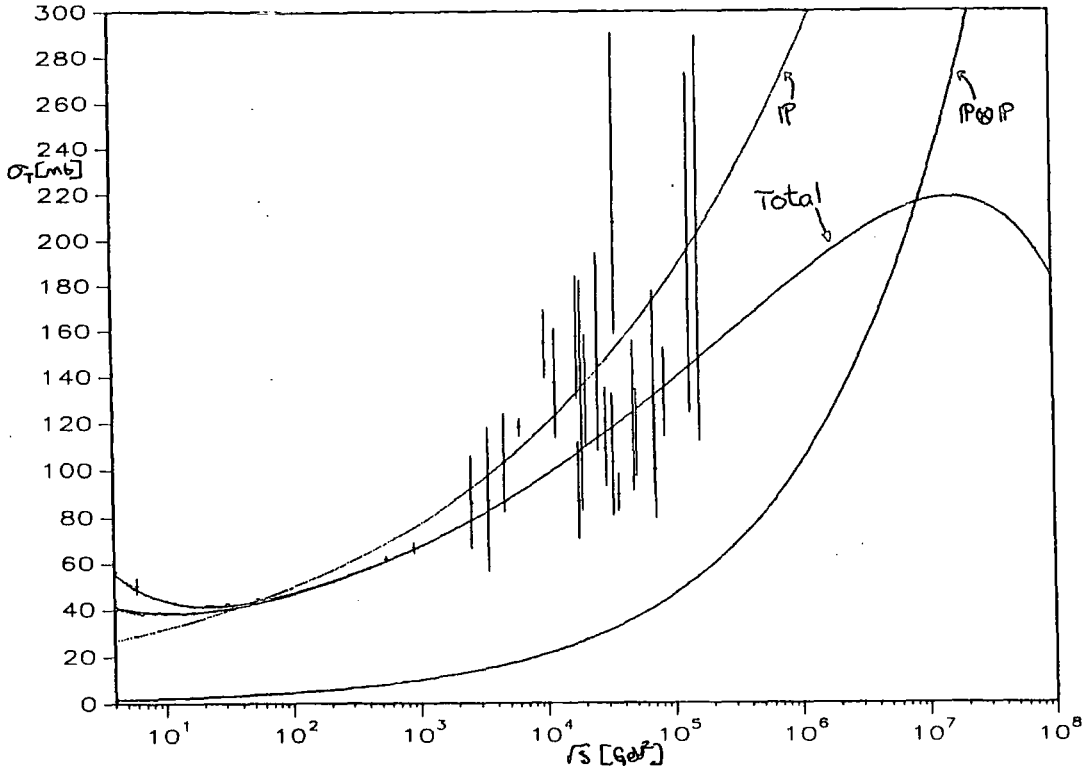


FIG. 5.9 High energy prediction for σ_T in DL model (note the $P \otimes P$ cut gives a negative contribution to the amplitude).

The energy at which the diffractive limit condition, $\text{Im } A(s, b) \leq \frac{1}{2}$, is violated in the model is increased from $\sqrt{s} \approx 200$ GeV for the Pomeron contribution alone, to $\sqrt{s} \approx 4$ TeV with the cut contribution included. The behaviour of the profile function as a function of energy at fixed impact parameter, $b = 0$, is shown on an Argand plot in fig.5.10. The Pomeron cut contribution makes the profile function at small b decrease with energy for $\sqrt{s} \geq 70$ TeV, giving a peripheral shape in b (see figure 5.11). The effect of the 3-gluon term on the Argand plot is to shift the curves along the real axes by a fixed amount (in opposite directions for pp and $\bar{p}p$).

Thus, although unitarity violation is not important in this model at $S\bar{p}pS$ Collider energies, by LHC and SSC energies other contributions must be included to prevent this happening. At these energies higher order Pomeron cuts are expected to be important and will perhaps prevent unitarity violation. However, the form (3.6.10) used to calculate the multiple Pomeron cuts leads to satisfaction of the Froissart bound at asymptotic energies but does not satisfy unitarity requirements at $b = 0$.

The high energy behaviour of the differential cross-section is shown in fig.5.12. It can

be seen that the model predicts a slight dip at $\sqrt{s} = 1$ Tev and $|t| = 0.8 \text{ GeV}^2$ which moves in to smaller $|t|$ and deepens as the energy increases. A second shoulder develops at $|t| = 2.5 \text{ GeV}^2$, due to $P \otimes P + 3g$ interference, which becomes more distinct and shrinks inwards with increasing energy. The small $pp/\bar{p}p$ difference in the dip region vanishes by $\sqrt{s} = 5$ Tev but that in the region of the second shoulder remains up to very high energies. However, the behaviour of $\frac{d\sigma}{dt}$ will be significantly modified at large $|t|$ by the addition of the 3-Pomeron term which must become important for $\sqrt{s} \geq 4$ Tev as seen above.

This model shows one way in which including an odd charge conjugation term can produce a reasonably good fit to all the pp and $\bar{p}p$ data for $p_{lab} \geq 50 \text{ GeV}/c$ (though our fit relaxes some of the constraints of the model). The price payed is the necessity for relatively strong $R \otimes P$ cuts and although this does not produce any inconsistencies the simplicity of the original model is lost and the resulting description somewhat unsatisfying. The unitarity problems encountered in the PWC model are postponed to higher energies but are not irrelevant to the phenomenology of the model.

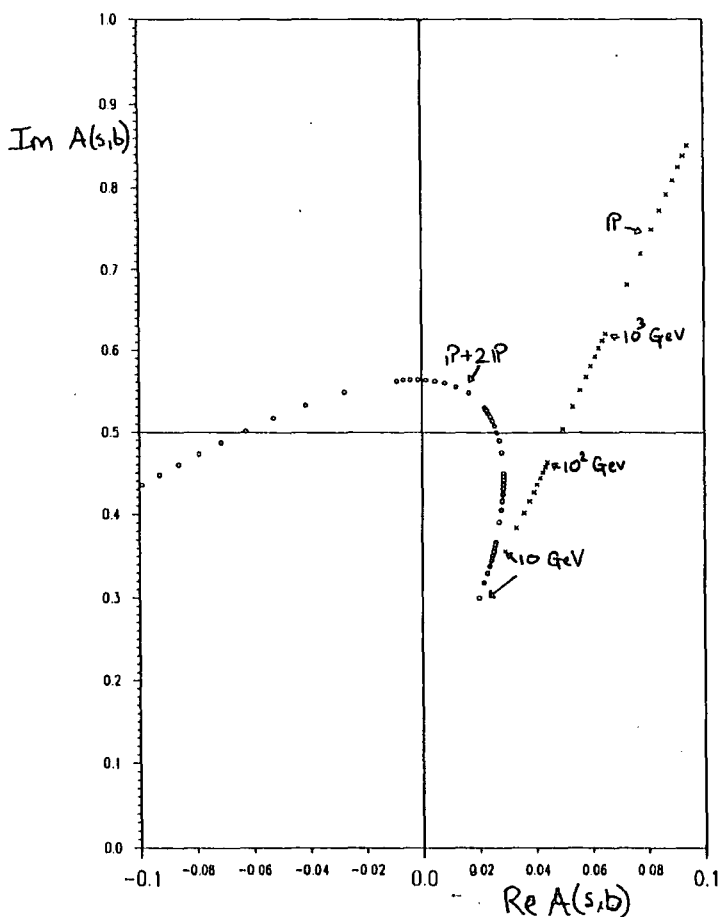


FIG. 5.10 Argand plot of $Re A(s, b)$ against $Im A(s, b)$ for DL model at $b = 0$ for various energies for pp and $\bar{p}p$.

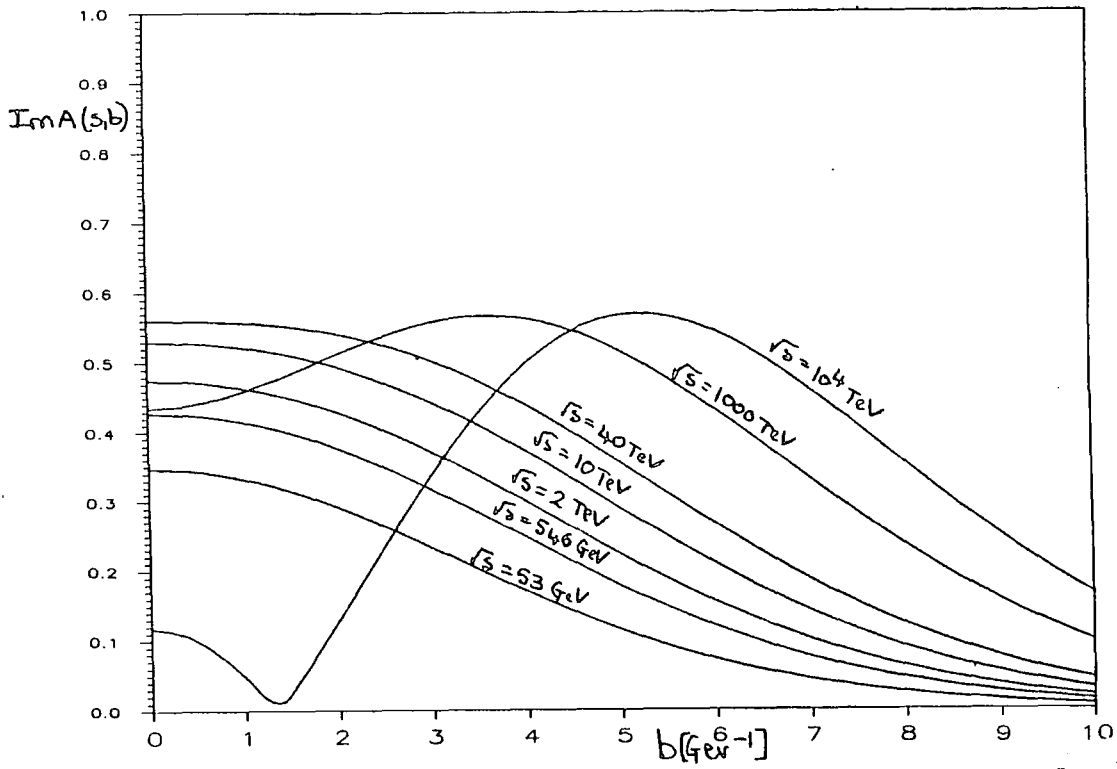


FIG. 5.11 Prediction of $Im A(s, b)$ for DL model at various energies as a function of b .

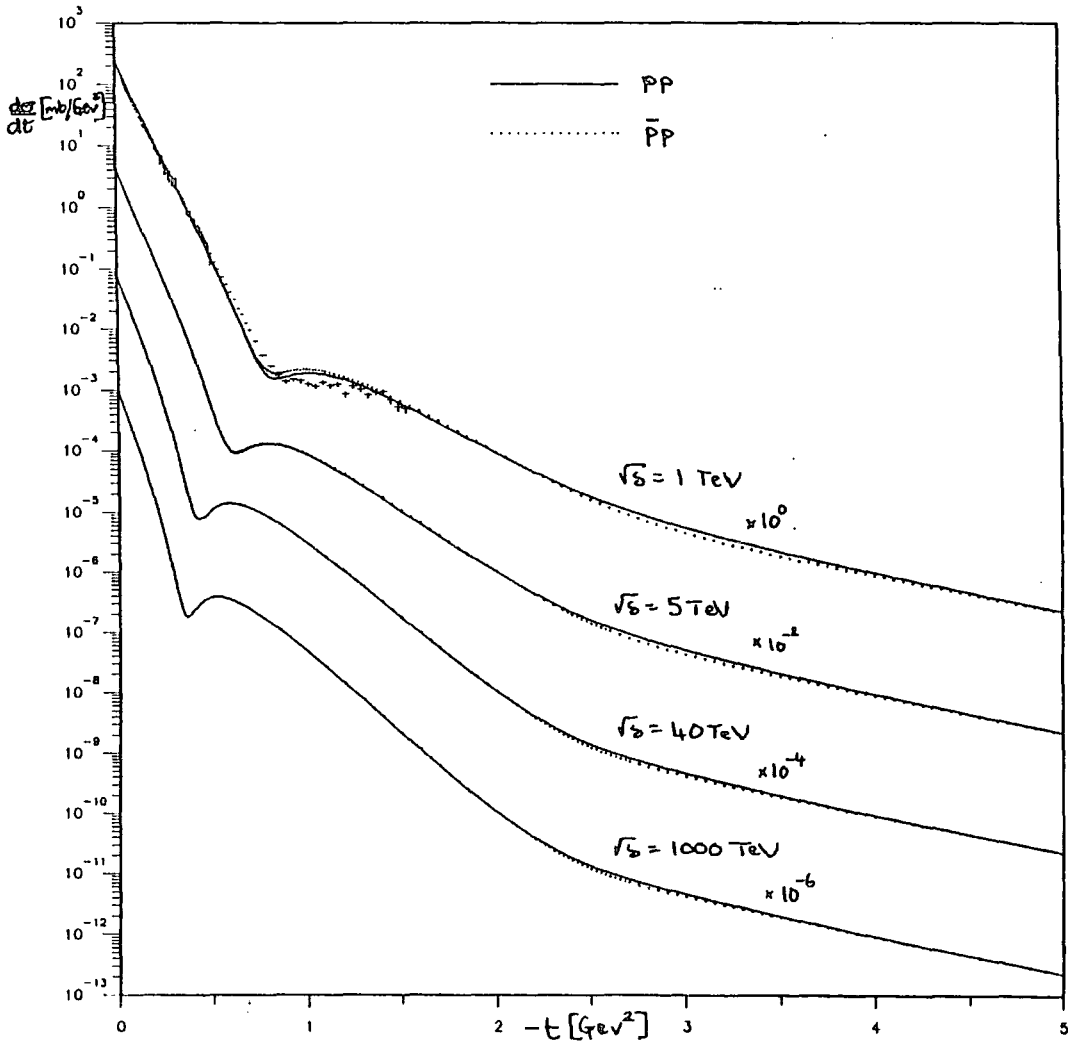


FIG. 5.12 High energy prediction of $\frac{d\sigma}{dt}(pp)$ and $\frac{d\sigma}{dt}(\bar{p}p)$ in DL model.

5.3. The Maximal Odderon Model (GLN Model).

An alternative approach to the Odderon term is that it is the $C = -1$ contribution (strong Odderon), rather than the $C = +1$ contribution as in the DL model (weak Odderon), which is responsible for the rapid rise in $\frac{d\sigma}{dt}$ between the ISR and the Collider in the dip region. In the model proposed by Gauron, Leader and Nicolescu (the GLN model) the rise in the $pp, \bar{p}p$ total cross-sections is attributed to an even signated contribution they term the ‘‘Froissaron’’ which grows as fast as allowed by the Froissart bound producing asymptotically a $\sigma_T \sim \log^2 s$ behaviour. This is maximal growth in a functional rather than quantitative sense since the coefficient of the $\log^2 s$ rise is much smaller than the $\frac{\pi}{m_\pi^2} \approx 60$ mb allowed theoretically (see §3.3). In the absence of any understanding of the dynamics of the $C = +1$ amplitude there is no reason for supposing the $C = -1$ odd charge conjugate amplitude does not obey the same maximum and also increase with energy at the maximum rate allowed by asymptotic theorems. This corresponds to the imaginary part increasing as $s \log s$ (see Roy and Singh (1970)) giving the Odderon behaviour.

The apparent $\log^2 s$ growth of the total cross-sections has a long history. The uncertainty in the value of the hadronic mass scale s_0 is frequently used in $\log^2 \frac{s}{s_0}$ fits to σ_T to introduce a term with $\log s$ energy dependence (see Block and Cahn (1985)) and to reproduce part or all of the fall in $\sigma_T(pp)$ with increasing energy for $\sqrt{s} < 10$ GeV (in §4.2 this fall was produced by exchange degeneracy breaking of the secondary Regge trajectories and residues). This effect is also present in the Odderon $\log \frac{s}{s_0}$ contribution to σ_T and has been used to produce all of the $pp, \bar{p}p$ total cross-section difference, so that no Regge contributions are needed in the σ_T fit and $\Delta\sigma$ changes sign at $\sqrt{s} = \sqrt{s_0} \approx 24$ GeV (see Lukaszuk and Nicolescu (1973)). It is more normal to suppose the Odderon contribution acts in addition to the $C = -1$ secondary Regge contribution (primarily due to ω Reggeon exchange in pp scattering) which is responsible for the low energy $\Delta\sigma$ as in §4.2 and that the Odderon contribution to σ_T is only significant at the upper limit of the ISR energy range where the secondary Regge contribution is small (see Kang and Nicolescu (1975)).

The correct phases of the even and odd amplitudes are given by writing down functions which are real analytic and possess the appropriate crossing symmetry as below.

$$A^+(s, 0) \sim \sqrt{su} \log^2 \sqrt{su} \rightarrow -C_+ s e^{-i\frac{\pi}{2}} \left(\log s - i\frac{\pi}{2} \right)^2 \quad (5.3.1)$$

$$A^-(s, 0) \sim \frac{1}{2} (s - u) \log^2 \sqrt{su} \rightarrow -C_- s \left(\log s - i \frac{\pi}{2} \right)^2 \quad (5.3.2)$$

Thus the real part of the Froissaron has an $s \log s$ dependence and that of the Odderon an $s \log^2 s$ dependence.

Depending on the sign of the Odderon contribution the pp and $\bar{p}p$ cross-sections will either cross over for large enough s ($\geq s_0$) if C_- positive in (5.2.2) or, for C_- negative, attain a minimum difference and then increase with energy (or for suitable $C_- < 0$ and s_0 cross over and back again). The analysis of Block and Cahn (1985), in which the ρ and σ_T , pp and $\bar{p}p$ data were fitted, indicated that any Odderon contribution was small but not ruled out by the data. For an Odderon with an $s \log^2 s$ energy dependence they found that a positive value for the coefficient C_- was favoured so that the pp and $\bar{p}p$ cross-sections crossed over for $\sqrt{s} \approx 80$ GeV. However, the GLN analysis finds $C_- < 0$ so that $\Delta\sigma$ instead approaches a minimum value for $\sqrt{s} \approx 100$ GeV and gives a good fit to the data as shown in figure 5.14 (see Gauron and Nicolescu (1983)). The discrepancy exemplifies the fact that as far as σ_T and ρ are concerned the data do not require an Odderon contribution and if it is present its parameters are not well tied down. It should also be noted that a more recent examination of the $\log^2 s$ dependence of σ_T (Block and Cahn (1987)), incorporating the UA5 data at $\sqrt{s} = 900$ GeV, indicated that an asymptotic $s \log^2 s$ dependence for the $C = +1$ amplitude is not favoured.

It is also believed that the Odderon behaviour should be universal and therefore present in all hadronic reactions. The addition of an Odderon term to the amplitude in $\pi^- p \rightarrow \pi^0 n$ charge exchange scattering (where $I = 1, \mathfrak{F} = -1$) can be used to explain the anomalous polarization data and this is claimed as further support for the Odderon idea (see Gauron and Nicolescu (1984a)). However, it seems preferable to believe that the Odderon contribution, if it exists, is due to gluon exchange and does not involve the exchange of valence quarks since the exchange of massive particles implies a finite range of interaction.

The explicit parametrization of σ_T used in Gauron, Leader and Nicolescu (1986) was

$$\begin{aligned} \sigma_T = & F_1 \left(\log^2 s - \frac{\pi^2}{4} \right) + F_2 \log s + F_3 \\ & \pm O_1 \pi \log s \pm O_2 \frac{\pi}{2} + C_P + \frac{C_{2P} \log s}{\log^2 s - \frac{\pi^2}{4}} \\ & + C_R^+ s^{\alpha_R^+(0)-1} \pm C_R^- s^{\alpha_R^-(0)-1} + (1 \pm 1) C_{\tilde{R}} s^{\alpha_{\tilde{R}}(0)-1} \quad \text{for } \begin{array}{l} \bar{p}p \\ pp \end{array} \end{aligned} \quad (5.3.3a)$$

with

$$\begin{aligned} F_1 &= 0.29 \text{ mb} & O_1 &= 0.031 \text{ mb} \\ F_2 &= -1.70 \text{ mb} & O_2 &= -0.30 \text{ mb} \\ F_3 &= 8.47 \text{ mb} \\ C_P &= 29.4 \text{ mb} & C_{2P} &= -1.69 \text{ mb} \\ C_R^+ &= 48.8 \text{ mb} & \alpha_R^+(0) &= 0.54 \\ C_R^- &= 38.5 \text{ mb} & \alpha_R^-(0) &= 0.41 \\ C_{\tilde{R}} &= 35.8 \text{ mb} & \alpha_{\tilde{R}}(0) &= -0.21 \end{aligned} \quad (5.3.3b)$$

The above equation represents a Froissaron contribution to σ_T with $\log^2 s$, $\log s$ and constant components; an Odderon with a $\log s$ and a constant component; a Pomeron term with intercept one giving a constant contribution; a Pomeron cut term which gives a small contribution that falls as $1/\log s$; secondary Reggeon terms (R) representing mainly f and ω Reggeons and a low energy term (\tilde{R}) representing daughter contributions. With the above parameter values this gives a good description of σ_T which is shown in figure 5.13(a). It can be seen that instead of becoming equal at high energies the cross-sections approach each other to within a millibarn and then slowly diverge again. A breakdown of the various contributions is given in figure 5.13(b). Below $\sqrt{s} \approx 100$ GeV the Pomeron gives the main contribution to σ_T ; at ISR energies the Pomeron gives about $\frac{3}{4}$ of the cross-section, the Froissaron about $\frac{1}{4}$. At the Collider energy the contributions are about equal. In the $C = -1$ amplitude the Odderon gives the dominant contribution for $\sqrt{s} \geq 60$ GeV. At $\sqrt{s} \approx 11$ GeV its contribution to σ_T changes sign due to the non-leading components. The behaviour of $\Delta\sigma$ is shown in figure 5.14. The effect of the Odderon can be seen for $\sqrt{s} \geq 20$ GeV where it produces a deviation from the simple power behaviour predicted by the Regge pole model.

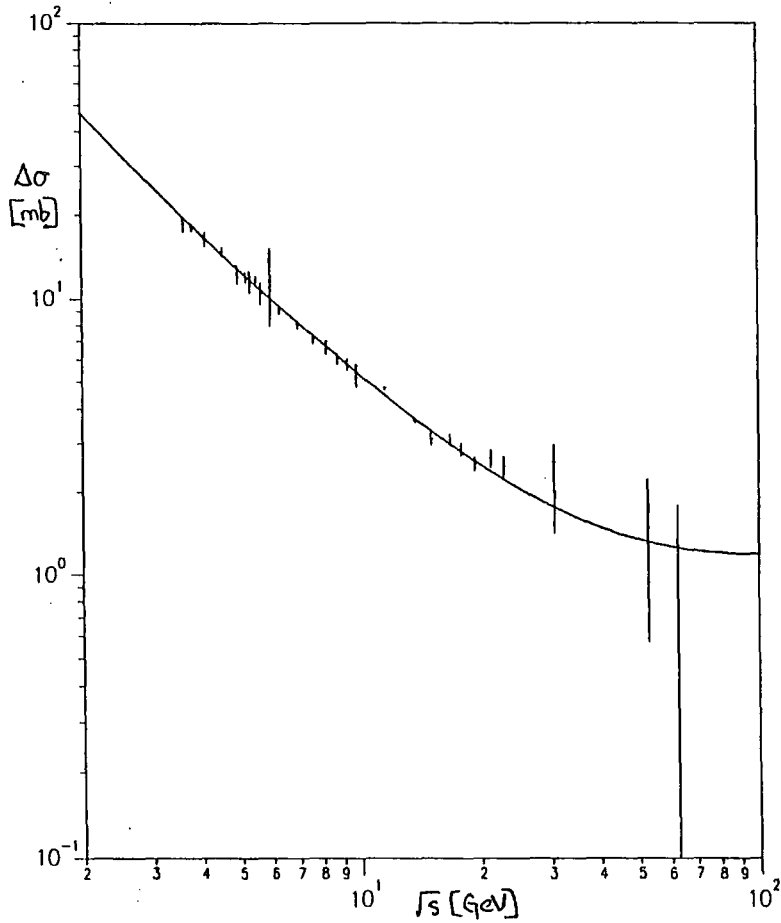


FIG. 5.14 GLN model prediction for $\Delta\sigma$ using the parametrization of (5.3.3).

Asymptotically only the contributions increasing with energy are important so that

$$\sigma_T \sim F_1 \log^2 s + F_2 \log s \pm O_1 \pi \log s \quad (5.3.4)$$

and $\Delta\sigma$ increases with energy as $\log s$ whilst σ_T increases as $\log^2 s$. Figure 5.15 shows the behaviour of σ_T at asymptotic energies with the ratio $\sigma_T(pp)/\sigma_T(\bar{p}p)$ approaching unity and σ_T tending to a $\log^2 s$ behaviour.

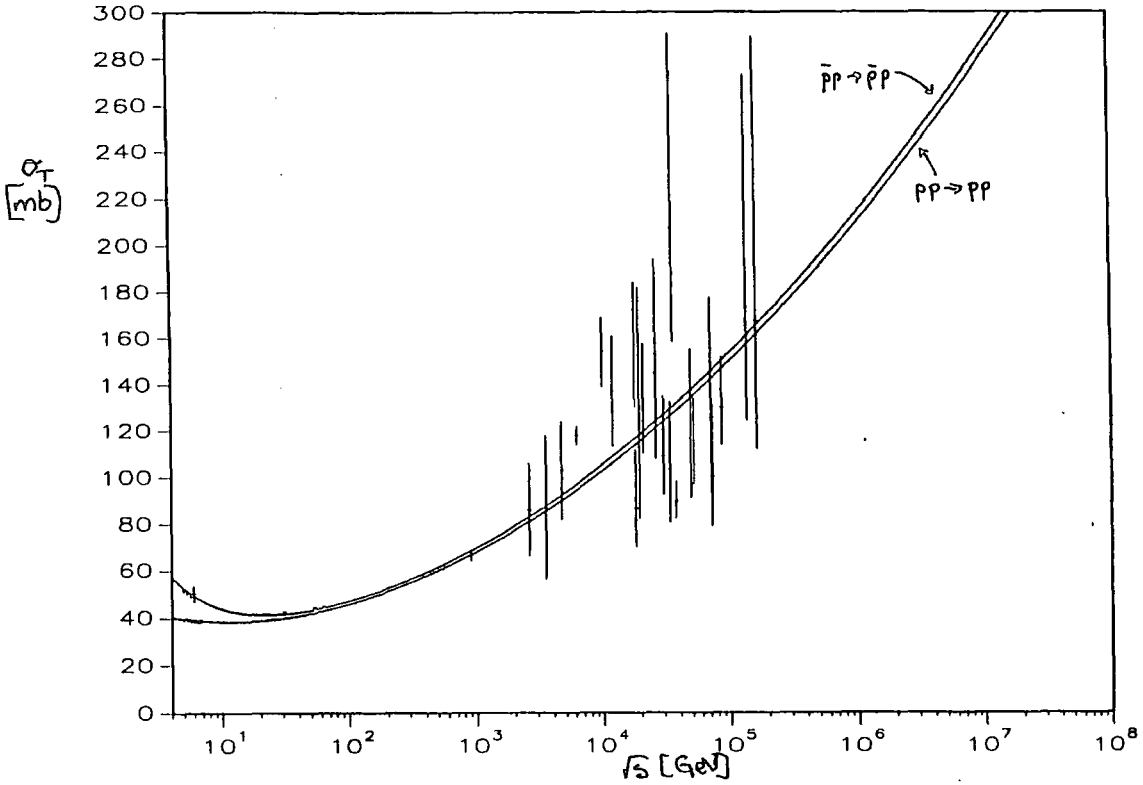


FIG. 5.15 Asymptotic prediction for σ_T in GLN model.

The asymptotic behaviour of ρ , the ratio of the real to imaginary parts at $t = 0$, is given by

$$\rho(pp) \rightarrow \frac{O_1}{F_1} \quad , \quad \rho(\bar{p}p) \rightarrow -\frac{O_1}{F_1} \quad \text{where} \quad \frac{O_1}{F_1} \approx 0.107 \quad (5.3.5)$$

Thus $\rho(pp)$ and $\rho(\bar{p}p)$ tend to opposite \pm constant values since the $s \log^2 s$ component of the imaginary part of the amplitude is given by the Froissaron with $C = +1$ and the $s \log^2 s$ component of the real part is given by the Odderon with $C = -1$. The prediction for ρ compared with the data and its asymptotic behaviour are shown in figure 5.16 . The asymptotic limit where $\rho(pp) \simeq \rho(\bar{p}p)$ occurs only for $\sqrt{s} \geq 10^{20}$ GeV.

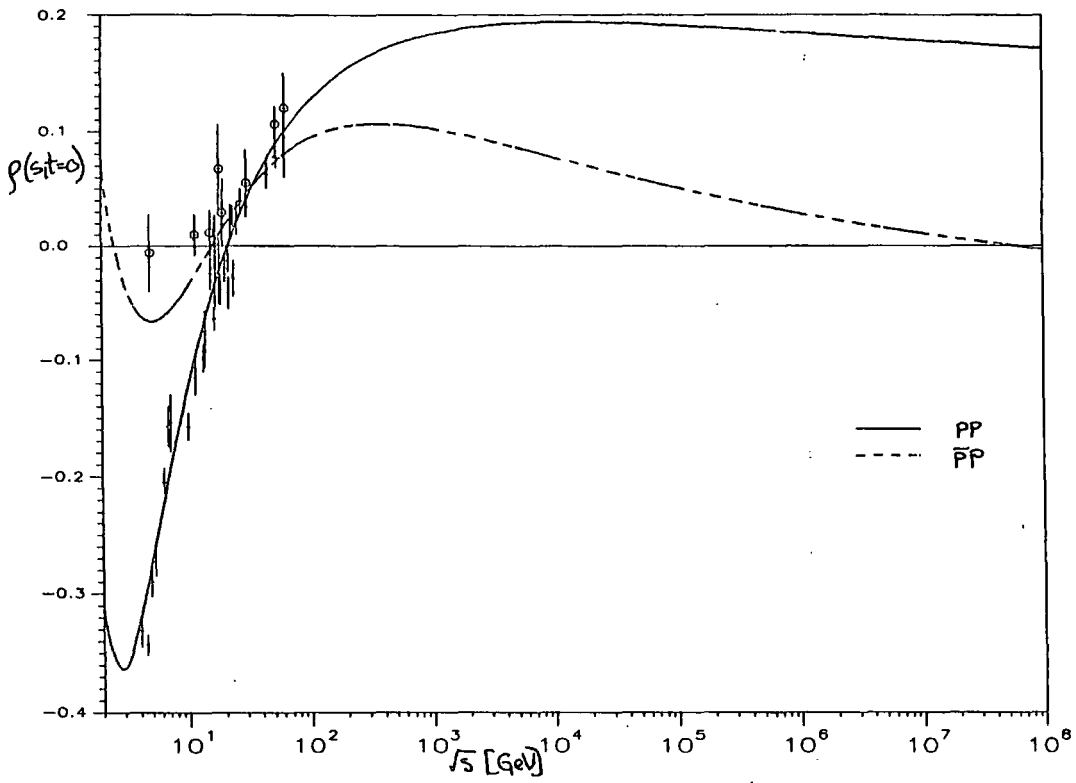


FIG. 5.16 Prediction for $\rho(pp)$ and $\rho(\bar{p}p)$ in GLN model.

The best signature for the presence of an Odderon would be a difference in the $pp, \bar{p}p$ differential cross-sections at high energy where conventionally the odd charge conjugation amplitude is vanishingly small. The ISR and Collider data indicate a possible difference in pp and $\bar{p}p$ $\frac{d\sigma}{dt}$ persisting to high energies. This prompted GLN to parametrize the t -dependence of the Odderon and use it to produce these differences. Since the Odderon is much smaller than the Froissaron at $t = 0$ its effect can be ignored in fitting the small $|t|$ data. Effectively, the only asymptotic constraint on the t -dependence of the amplitude is produced by the MacDowell-Martin bound which relates the forward slope of the absorptive part of the amplitude to the total cross-section through $B_A(s, t = 0) > C\sigma_T$ (see Martin (1985)). Then B_A must increase at least as fast as σ_T . Applied to the Froissaron this means that the slope at $t = 0$ must increase like $\log^2 s$.

The form used by Gauron, Leader and Nicolescu (1985) automatically satisfies asymptotic constraints and corresponds for large $\log s$ to a grey disk with radius growing as $R_+ \log s$. In the j -plane this gives the simple form below which represents a triple pole at $j = 1$

$$A_j^+(t) = \frac{1}{[(j-1)^2 - tR_+^2]^{\frac{3}{2}}} \quad (5.3.6)$$

This is modified at lower energies by including a residue function :

$$\beta_+(j, t) = Ae^{b_1^+ t} + B(j-1)e^{b_2^+ t} + C(j-1)^2 e^{b_3^+ t} \quad (5.3.7)$$

The t -dependences of the exponentials effectively just introduce a constant into the radius which is asymptotically negligible. The powers of $(j-1)$ give non-leading terms with constant and $\log s$ energy dependences in σ_T which were needed in (5.3.3) to fit σ_T , but their effect on the t -dependence of the Froissaron is not important and this can be effectively represented by just the first term which gives

$$\begin{aligned} A^-(s, t) &\sim \frac{J_1(R_+ \sqrt{-t} \log se^{-i\frac{\pi}{2}})}{R_+ \sqrt{-t} \log se^{-i\frac{\pi}{2}}} e^{b_1^+ t} \\ &\simeq e^{\left(b_+ + b_\infty \log \frac{s}{s_+}\right)t} \end{aligned} \quad (5.3.8)$$

where the simple exponential gives a good approximation to the t -dependence of the Bessel function at small $|t|$ and was used by Gauron and Nicolescu (1984b) in a fit to the forward scattering data.

In order to reproduce the small $|t|$ data it is necessary to include a Pomeron term which was given a trajectory $\alpha_P(t) = 1 + 0.25t$. It is this which is mainly responsible for the shrinkage observed at ISR energies and below. The major effects produced by the Froissaron are the rise in $\frac{d\sigma}{dt}$ at small $|t|$ and some of the shrinkage between the ISR and the Collider. In the latter it is not so much the $\log^2 s$ t -dependence of the slope which is important so much as the energy dependence at $t = 0$ (nevertheless a non-zero value for b_∞ was found to be necessary).

In extending the model to larger $|t|$ the Odderon term becomes important and is the dominant contribution to the amplitude beyond the dip region. The Froissaron and Pomeron pole and cut contributions fall rapidly below the data for $|t| \geq 2 \text{ GeV}^2$. A breakdown of the contributions to $\frac{d\sigma}{dt}$ at $\sqrt{s} = 53 \text{ GeV}$ is shown in figure 5.17 .

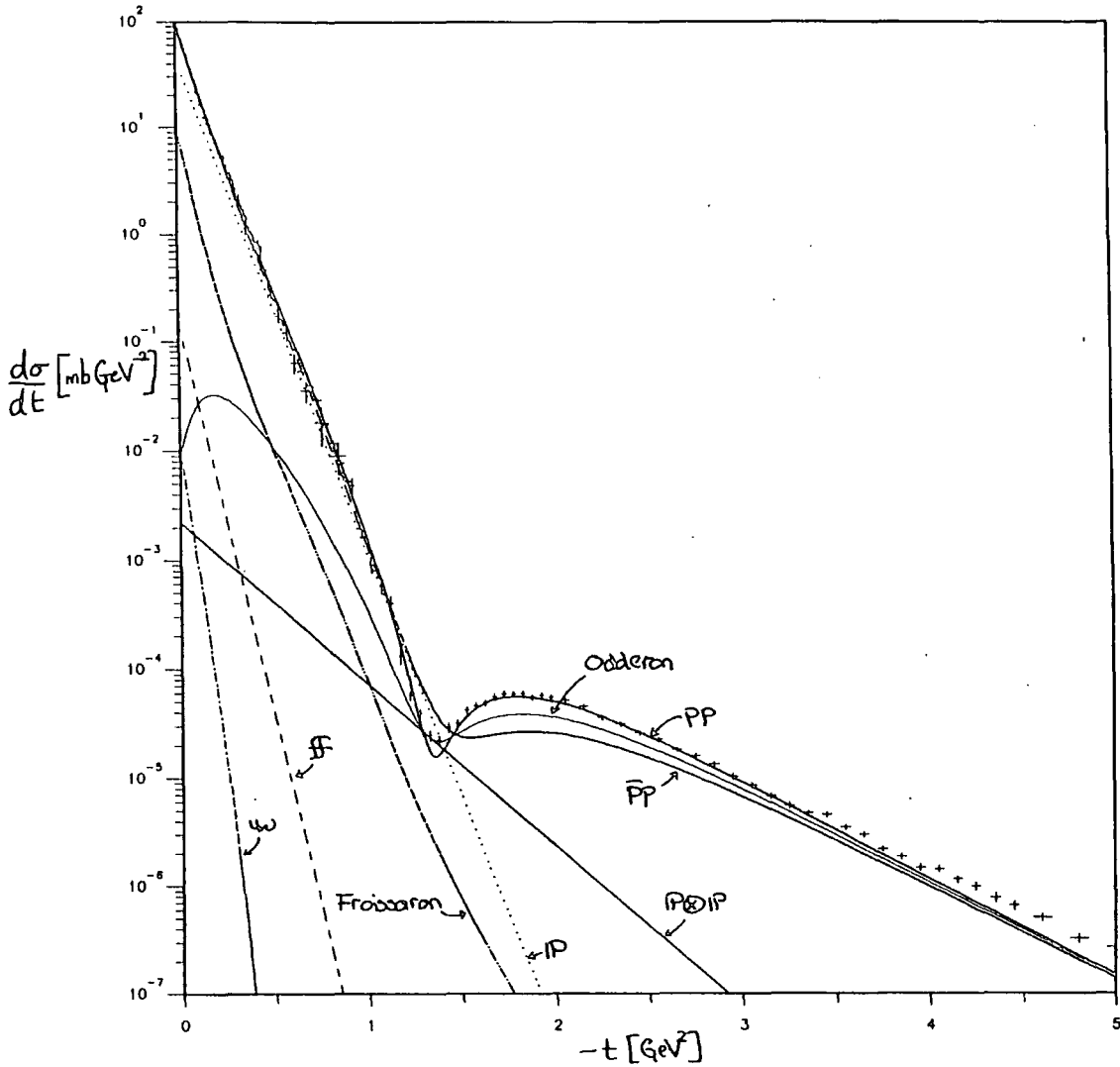


FIG. 5.17 Comparison of the individual contributions to $\frac{d\sigma}{dt}$ in the GLN model at $\sqrt{s} = 53$ GeV.

The t -dependence of the Odderon is constructed in a similar way to that of the Froissaron. Instead of (5.3.6) there is a double pole at $j = 1$:

$$A_j^-(t) = \frac{\beta_-(j, t)}{(j-1)^2 - tR_-^2} \quad (5.3.9)$$

This gives three terms with real parts growing as s , $s \log s$ and $s \log^2 s$.

At ISR energies the way in which the dip is produced is in some ways similar to the DL model. The major difference is that whilst the $3g$ term in the DL model is purely real the Odderon contribution in the GLN model has a substantial imaginary part

in the dip region. The cross-section beyond the dip is dominated by the purely real energy independent component of the Odderon which has a flat t -dependence. This is cancelled in the dip region by the $\log s$ component of the Odderon which has opposite sign and steeper t -dependence and produces a zero crossing in the $C = -1$ amplitude near the dip position which is effectively independent of energy over the ISR energy range. Thus the $C = -1$ contribution mimics the energy independent behaviour, with a zero in the dip region, of the $3g$ term in the DL model. This cancels with the real part of the $C = +1$ contribution producing a zero in the real part of the pp amplitude and because there is a zero crossing in the $C = -1$ amplitude a zero is also produced nearby in the real part of the $\bar{p}p$ amplitude. The imaginary part of the $C = +1$ amplitude, dominated at ISR energies in the forward direction by the Pomeron, is cancelled near the dip region by the Pomeron cut but this is overshadowed by the imaginary part of the Odderon amplitude. In pp , the Odderon moves the zero in the imaginary part slightly closer to the forward direction, but in $\bar{p}p$ prevents a zero from being produced. The zeroes in the real and imaginary parts of the pp amplitude give a dip in $\frac{d\sigma}{dt}(pp)$ whilst in $\bar{p}p$ there is a zero in the real part of the amplitude but not in the imaginary part and this gives a shoulder instead of a dip in $\frac{d\sigma}{dt}(\bar{p}p)$. The real and imaginary parts of the pp and $\bar{p}p$ amplitudes at $\sqrt{s} = 53$ GeV are shown in figure 5.18 .

The effect of the Odderon at the ISR is to lower the height of the second maximum in $\frac{d\sigma}{dt}(\bar{p}p)$ by a factor of two relative to $\frac{d\sigma}{dt}(pp)$ and to fill the dip in slightly. This agrees quite well with the $pp/\bar{p}p$ data.

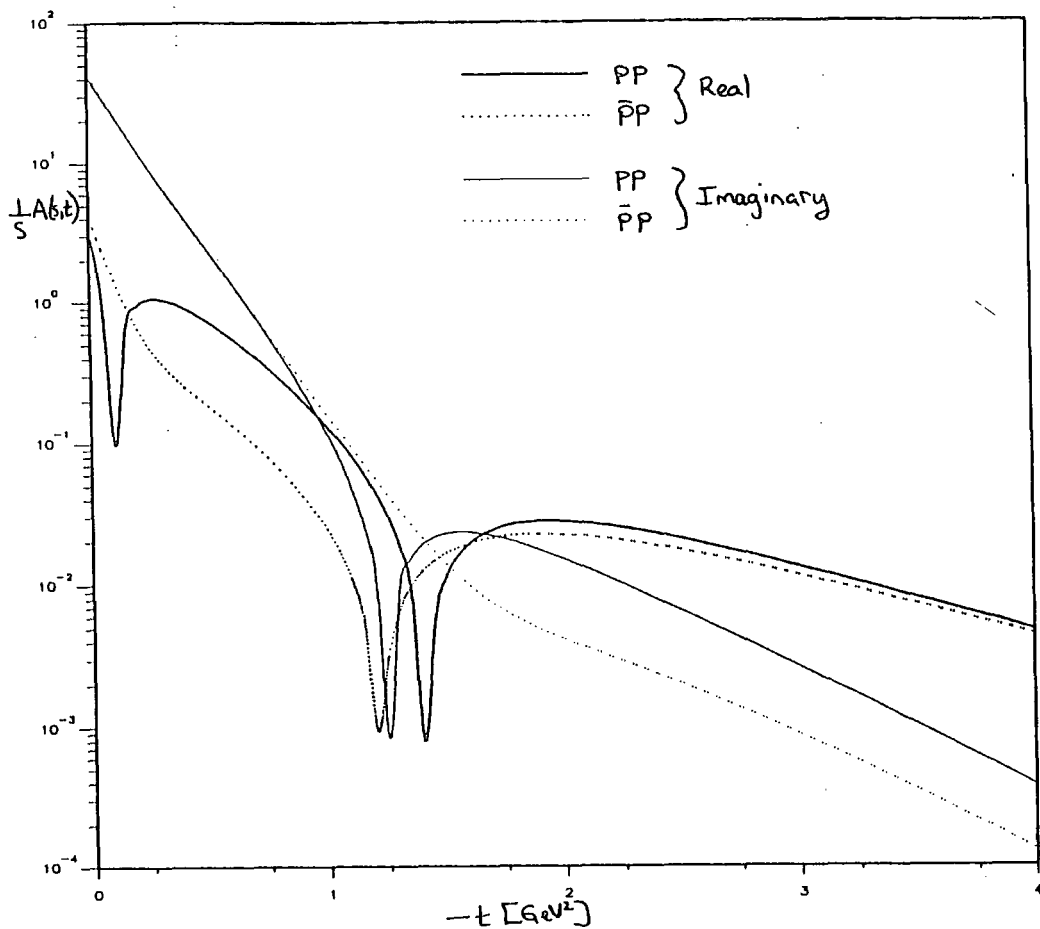


FIG. 5.18 Real and imaginary parts of the pp and $\bar{p}p$ amplitudes in the GLN model at $\sqrt{s} = 53$ GeV.

At the Collider energy the Pomeron cut has decreased slightly and is not important. The large change in the dip region between the ISR and the Collider is mainly produced by the fast increase in the Odderon contribution which results from the movement of the zeroes in the $\log s$ component of the Odderon from a $\cos(R - \sqrt{-t} \log s)$ factor ($|t|_{\text{dip}} \sim 1/\log^2 s$). At ISR energies the zero in the real part occurs for $|t| \geq 2$ GeV² and so is hidden underneath the large $|t|$ component of the Odderon. The imaginary part of the Odderon is hidden under the forward peak and more gets exposed by shrinkage. This parametrization gives a very good fit to the $\bar{p}p$ data at the Collider.

The pp differential cross-section is predicted to still have a dip but the height of the second maximum has increased by a factor of ten.

The leading component of the Odderon has little effect except at $t = 0$. The major effect of neglecting it would be to alter the asymptotic predictions of the model. The next to leading component of the Odderon gives a constant contribution to σ_T so that at high energies the difference between $\sigma_T(pp)$ and $\sigma_T(\bar{p}p)$ becomes negligible. The ratio of the real to imaginary parts of the amplitude would go to zero asymptotically rather than a constant value as in (5.3.5). The asymptotic predictions of (5.3.4) and (5.3.5) are therefore not supported by the behaviour of the differential cross-section (though neither are they contradicted by it).

Using the parametrization given in appendix C (reproduced from GLN (1986)) a good description of the pp and $\bar{p}p$ data for $\sqrt{s} \geq 23$ GeV is obtained and this is displayed in figure 5.19 . The complicated cancellations of energy dependent contributions which occur in the dip region means that it is difficult to maintain the approximate energy independence of the data and the fit to the shape of the dip is not so good at $\sqrt{s} = 23.5$ GeV and lower energies. In order to describe the lower energy data $R \otimes P$ cuts have been included which only give a small effect at ISR energies and produce a good fit to the data at $p_{lab} = 50$ GeV/c. However, the energy dependence does not allow such a good description of the data at neighbouring energies. The low energy behaviour is shown in figure 5.20 .

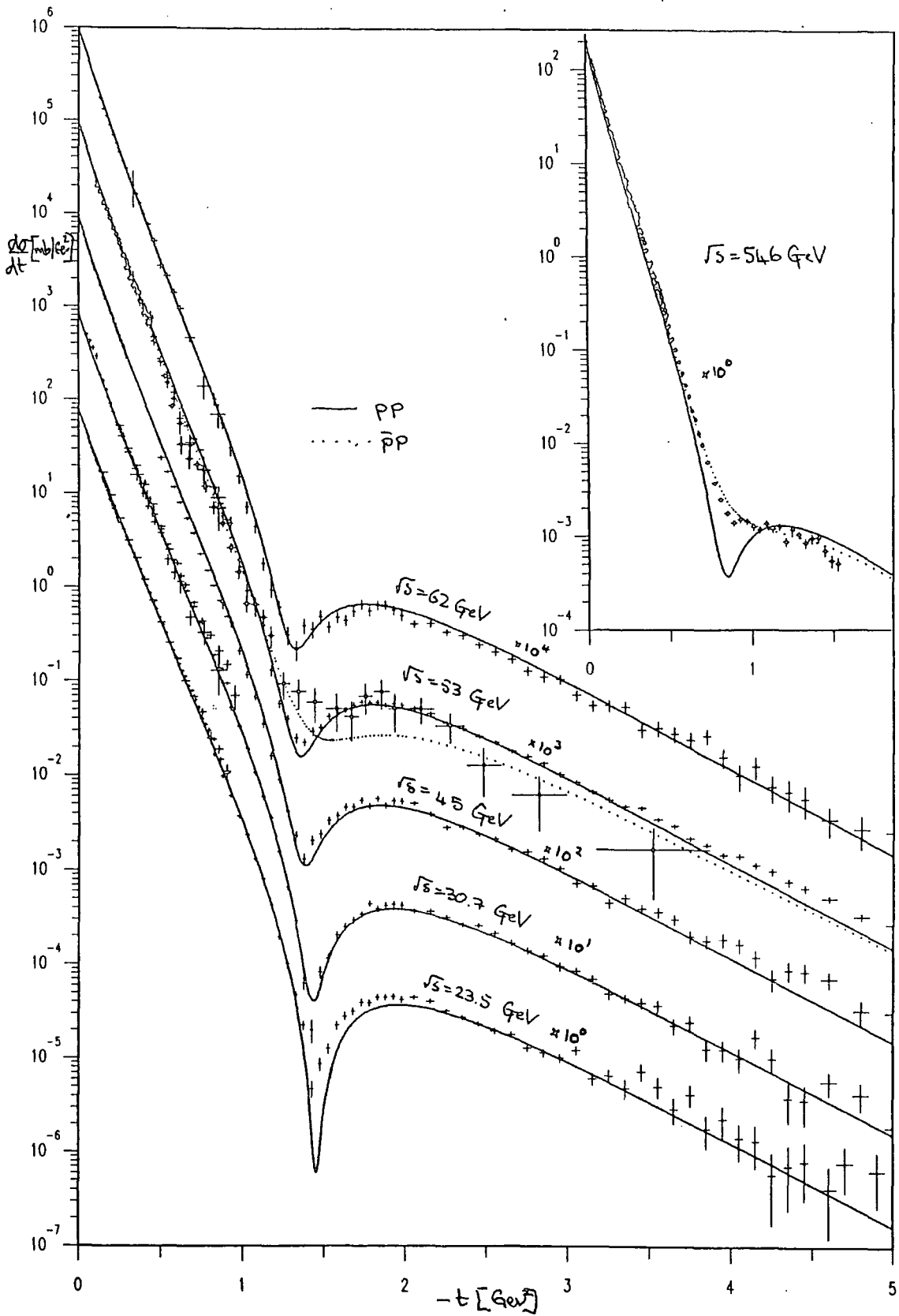


FIG. 5.19 $\frac{d\sigma}{dt}(pp)$ fit in GLN model at ISR and Collider energies.

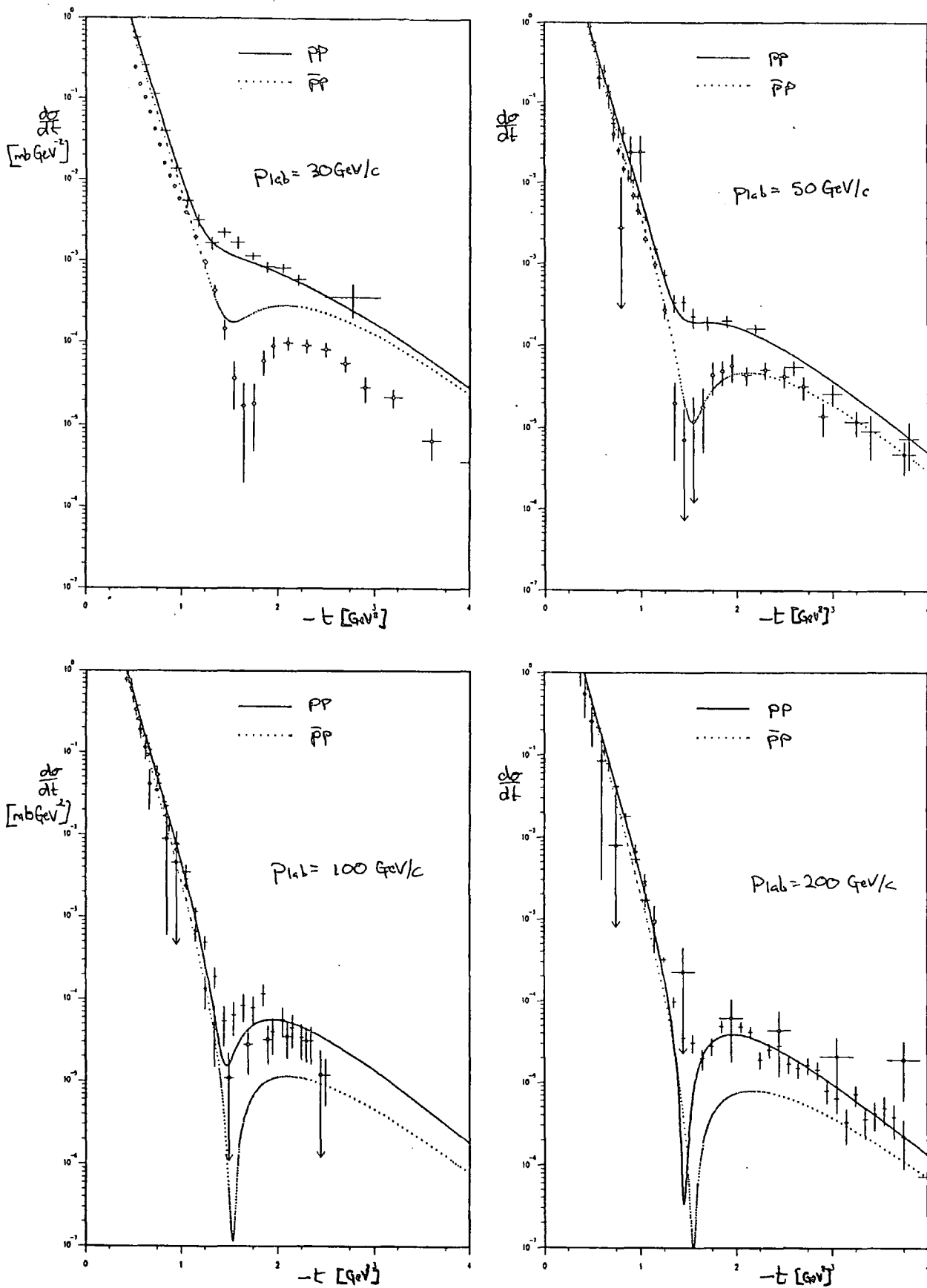


FIG. 5.20 Low energy $\frac{d\sigma}{dt}$ predictions of the GLN model for pp and $\bar{p}p$ at $p_{\text{lab}} = 30, 50, 100$ and $200 \text{ GeV}/c$.

At higher energies the dip/shoulder structure is controlled by zeroes in $J_1(b\sqrt{-t} \log s)$

for the Froissaron and $\cos(b\sqrt{-t}\log s)$ for the Odderon and moves in to smaller $|t|$ as $\frac{1}{\log^2 s}$. The dip/shoulder difference between pp and $\bar{p}p$ persists at higher energies. Figure 5.21 shows the behaviour of $\frac{d\sigma}{dt}$ up to $\sqrt{s} = 40$ Tev.

This model shows how the Collider shoulder can be attributed to an odd charge conjugation contribution growing rapidly with energy and how this growth can be masked at lower energies. However, the complicated Odderon components and their t -dependences are somewhat *ad hoc*. The leading component does not affect the t -dependence at all. It is the arbitrary non-leading terms which produce all the structure of the differential cross-section. The even charge conjugation amplitude is equally arbitrary and since it cannot be distinguished from the Pomeron contribution its effects are difficult to tie down from the data. Also, since the Froissaron represents in some sense the sum of all the Pomeron and Pomeron cut contributions, including a separate Pomeron contribution involves some double counting.

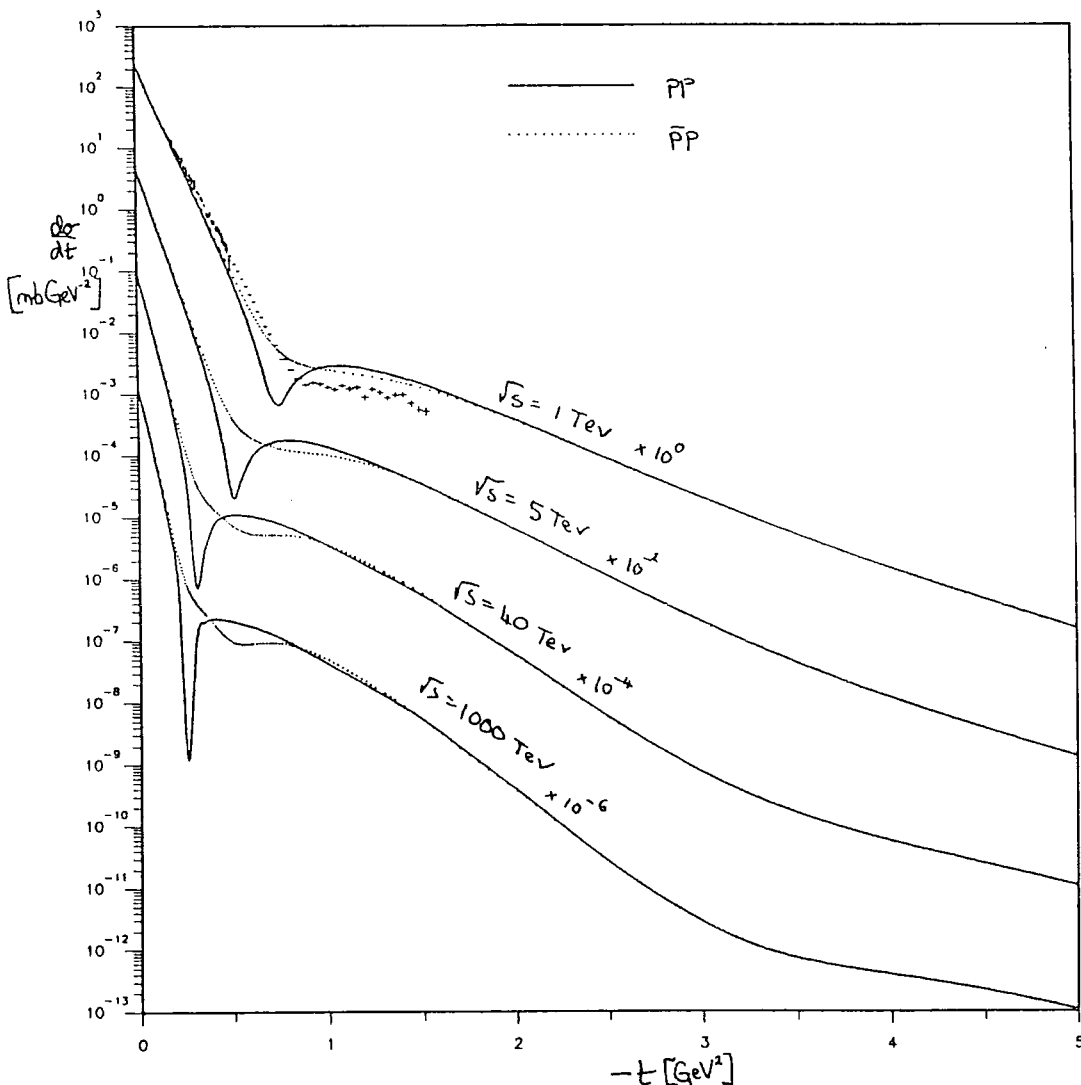


FIG. 5.21 High energy $\frac{d\sigma}{dt}$ predictions of the GLN model for pp and $\bar{p}p$ for $\sqrt{s} = 1 \rightarrow 1000$ Tev.

5.4. Reggeized Odderon Contribution

It seems unlikely that simple perturbative QCD processes are believable over the $|t|$ range of the elastic scattering data. The Pomeron should be a much more complicated object than the two gluon picture of §3.5, with many gluons exchanged. We might then ask why we do not get a similar object to the Pomeron but with odd charge conjugation. At large $|t|$ we might expect such an object to have a representation in terms of 3 gluon exchange and for it to Reggeize accordingly as in figure 5.22 .

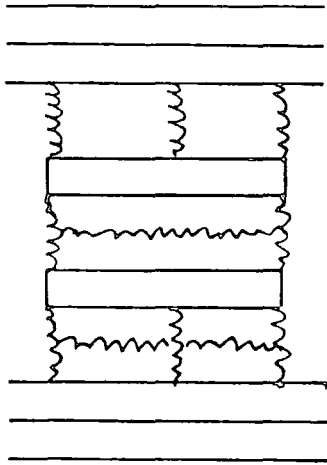


FIG. 5.22 Reggeized 3-gluon exchange.

Since each gluon has odd charge conjugation and gives a factor $\frac{is}{t}$, the 3g contribution to the amplitude is

$$\left(\frac{i}{s}\right)^2 \left(\frac{-s}{t}\right)^3 = \frac{s}{t^3} \quad (5.4.1)$$

which is purely real; +ve in pp , -ve in $\bar{p}p$; has the same s dependence as the Pomeron and is helicity non-flip. It is difficult to see how any simple connection with this idea can survive at small $|t|$ (see White (1985)), nevertheless the Pomeron does behave as expected of two gluon exchange and so we might expect a Reggeized odderon to have a similar trajectory with an intercept close to one and a shallow slope.

The odderon has odd charge conjugation and thus odd signature so that its phase is

given by

$$\left(1 + \Im e^{-i\pi\alpha(t)}\right) = - \left(e^{-i\pi\alpha(t)}\right) \text{ with } \Im = -1 \quad (5.4.2)$$

Thus, as for the 3g contribution in the DL model, the odderon has the right phase to add to the real part in $\bar{p}p$ in the dip region and subtract in pp . Since the primitive diagram for the odderon involves three gluons rather than the two in the primitive diagram for the Pomeron, we might expect that $1 < \alpha_o(0) < \alpha_p(0)$ as an extra coupling constant is given by the extra gluon in the triple odderon vertex renormalizing the odderon pole. We also expect $0 < \alpha_o < \alpha'_p$ since $\alpha' = \frac{1}{\text{string tension}}$ and the string tension of three gluons should be greater than that of two. However, since we are not in a region where perturbative QCD is expected to be valid, these arguments cannot be taken too seriously.

It is difficult to understand why the coupling of the odderon should be much different from that of the Pomeron. The coupling is presumably dominated by coupling to the ω meson with quantum numbers $J^{PC} = 1^{--}$ in the same way as the Pomeron is dominated by the f meson and so the Odderon should couple to hadrons as strongly as does the Pomeron. Since the odderon is almost purely real it does not contribute to the total cross-section. A large odderon contribution would effect ρ and the optical point in $\frac{d\sigma}{dt}$, but at ISR energies the phase is known reasonably accurately and is consistent with dispersion relations and the data show $\rho(pp) \simeq \rho(\bar{p}p)$, so that the odderon contribution at $t = 0$ must be quite small, as was found in the previous two models.

We have examined whether a Reggeized odderon contribution can account for the discrepancy between the data and predictions of the pole and weak cut model of §4 and take over the role of the term (4.7.2) in fit 4(d). From (3.4.7), we have for the odderon amplitude :

$$A_o(s, t) = \pm s G_o \left(e^{-i\frac{\pi}{2} s} \right)^{\epsilon_o} e^{(a_o + \alpha'_o (\ln s - \frac{i\pi}{2})) t} \text{ for } \begin{array}{l} pp \\ \bar{p}p \end{array} \quad (5.4.3)$$

An Odderon of similar form to this was proposed in Joynson, Leader and Nicolescu (1975) to explain the $\pi^\pm p$ scattering differences.

It might be hoped that the energy dependence of the odderon would allow it to be sufficiently small at $\sqrt{s} = 53$ GeV to give agreement with the $pp/\bar{p}p$ difference in the dip region but increase enough with energy to produce the Collider shoulder and so be

effectively negligible at energies other than $\sqrt{s} = 546$ GeV as was the term (4.7.2). The phases of the extra term used to produce the Collider shoulder in the four fits described in §4.7 are given in table 5.2 . We see from this that the Odderon has the wrong phase (see (5.4.2)) to simply replace the term (4.7.2). The extra contribution required to fit the shoulder data in these fits had a large imaginary part which cannot be produced by the odderon phase. The two Odderon parametrizations described above in §5.2 and §5.3 had a very different form from the fits of §4 in that the Odderon dominated large $|t|$ rather than the Pomeron cut.

Fit	φ_{ex}
Fit (4a)	1.28
Re-fitted (4a)	1.35
Fit (4d)	1.90
Re-fitted (4d)	1.35

TABLE 5.2 Phase factors for term (4.72) used in fits (4a) and (4d) from §4.7.

We nevertheless tried fitting the pp and $\bar{p}p$ data at $\sqrt{s} = 23.5, 53$ and 546 GeV² using (5.4.3) and the parametrization used in §4.4 with the parameters of (4.2.7). The results, in which two types of fits arose, reflect the problems discussed above. In the first (fit(5.4a)) the Pomeron cut contribution dominated large $|t|$ and was comparatively large in the shoulder region at the Collider. The Odderon filled in the dip from $P + P \otimes P$ interference in $\bar{p}p$ at the Collider energy and cancelled the real part of $P + P \otimes P$ in the dip region at ISR energies. The major problem with this is the resulting very large $pp/\bar{p}p$ difference produced in the dip region which is incompatible with the data at $\sqrt{s} = 53$ GeV. This also gave a poor fit to the energy dependence of the pp ISR data in the dip region and beyond, shown in figure 5.23 . The Odderon parameters are given in table 5.3(a) which show the its trajectory does at least conform to the above expectations. In the second type of fit (fit(5.4b)) the magnitude of the Odderon and the Pomeron cut were similar at large $|t|$. The Collider shoulder was produced by the Odderon, which had a large intercept, $\alpha_o(0) = 1.201$, (see table 5.3(b)) disagreeing with the above. The shape of the shoulder produced was not in very good agreement with the data. The Odderon was still too large at $\sqrt{s} = 53$ GeV in the dip region to agree with the observed $pp/\bar{p}p$ difference and the fit to the ISR

data not very good, though better than the fit(5.4a). This is shown in figure 5.24 .

In the light of the results of sections §5.2 and §5.3 it is not surprising that the simple parametrization of (5.4.3) does not produce good results. In order to be compatible with the $pp/\bar{p}p$ difference at the ISR it is necessary to somehow cancel the Odderon in the dip region. A parametrization using (5.4.3) in which the Odderon dominates large $|t|$ would produce far too large a difference in the dip region. An approach, consistent with the model of §4, which would give the appropriate result would be to produce the Odderon zero by interference between the Odderon and the Odderon-Pomeron cut. However, we have not attempted to try this since the data on the $pp/\bar{p}p$ difference are not good enough to give a believable parametrization.

The direct effect of the Odderon contribution in these fits on σ_T is very small, however the change produced in the magnitude of the Pomeron cut at $t = 0$ decreases σ_T by approximately a millibarn. At very high energy, only fit (5.4b) shows any noticeable difference between $\sigma_T(pp)$ and $\sigma_T(\bar{p}p)$. This is shown in figure 5.25 .

parameter	fit (5.4a)	fit (5.4b)
α'_P	0.166 GeV ⁻²	0.241 GeV ⁻²
a_P	1.14 GeV ⁻²	1.93 GeV ⁻²
x	0.925	0.712
a_1	3.53 GeV ⁻²	3.63 GeV ⁻²
b_1	-0.64 GeV ⁻²	-1.11 GeV ⁻²
λ_{2P}	0.230	0.060
$\alpha_o(0)$	1.063	1.201
α'_o	0.094 GeV ⁻²	0.000 GeV ⁻²
G_o	0.909	1.047
a_o	1.70 GeV ⁻²	0.97 GeV ⁻²

TABLE 5.3 Parameters of fits (5.4a) and (5.4b).

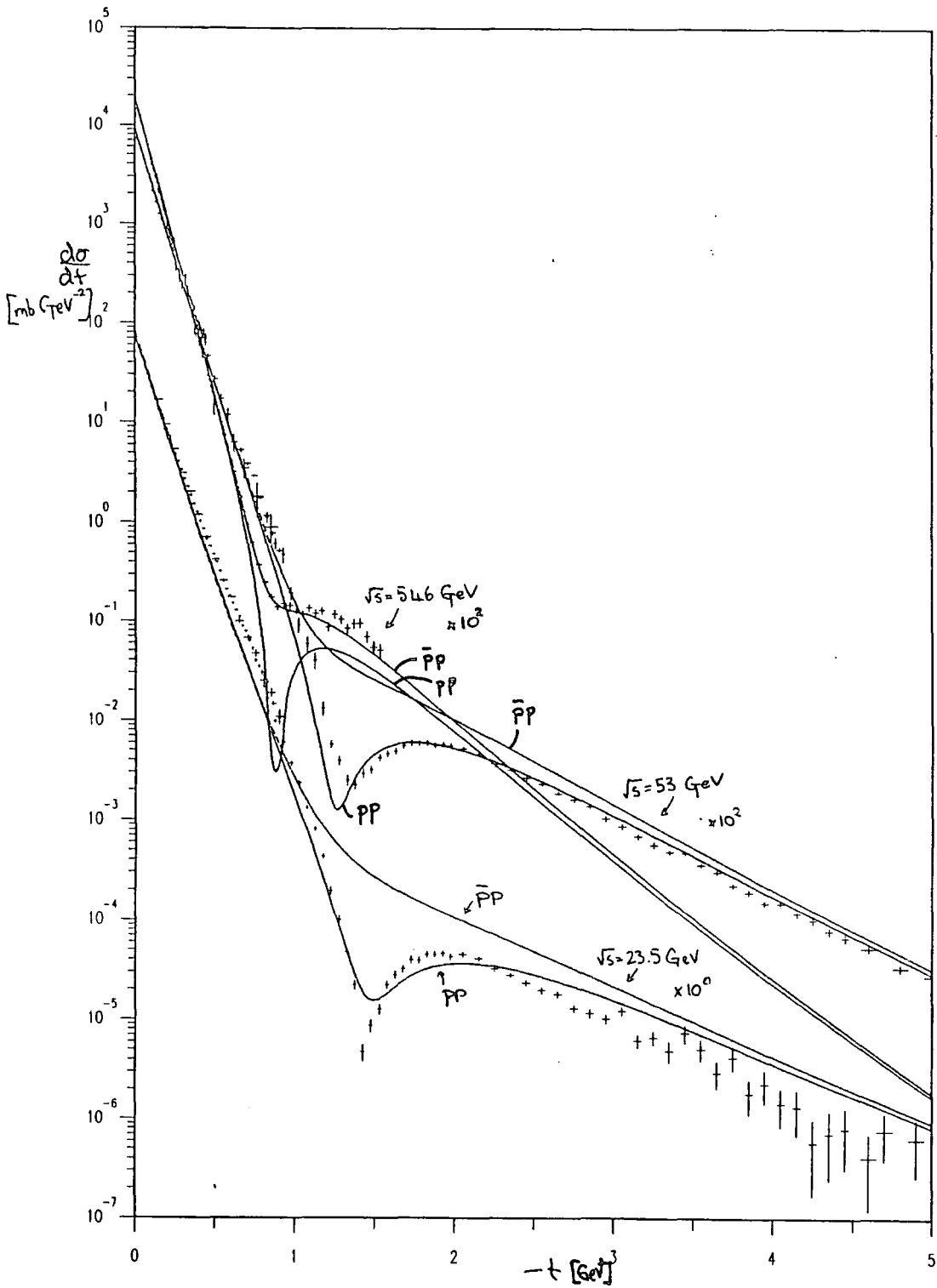


FIG. 5.23 Results of fit (5.4a) at $\sqrt{s} = 23.5, 53$ and 546 GeV .

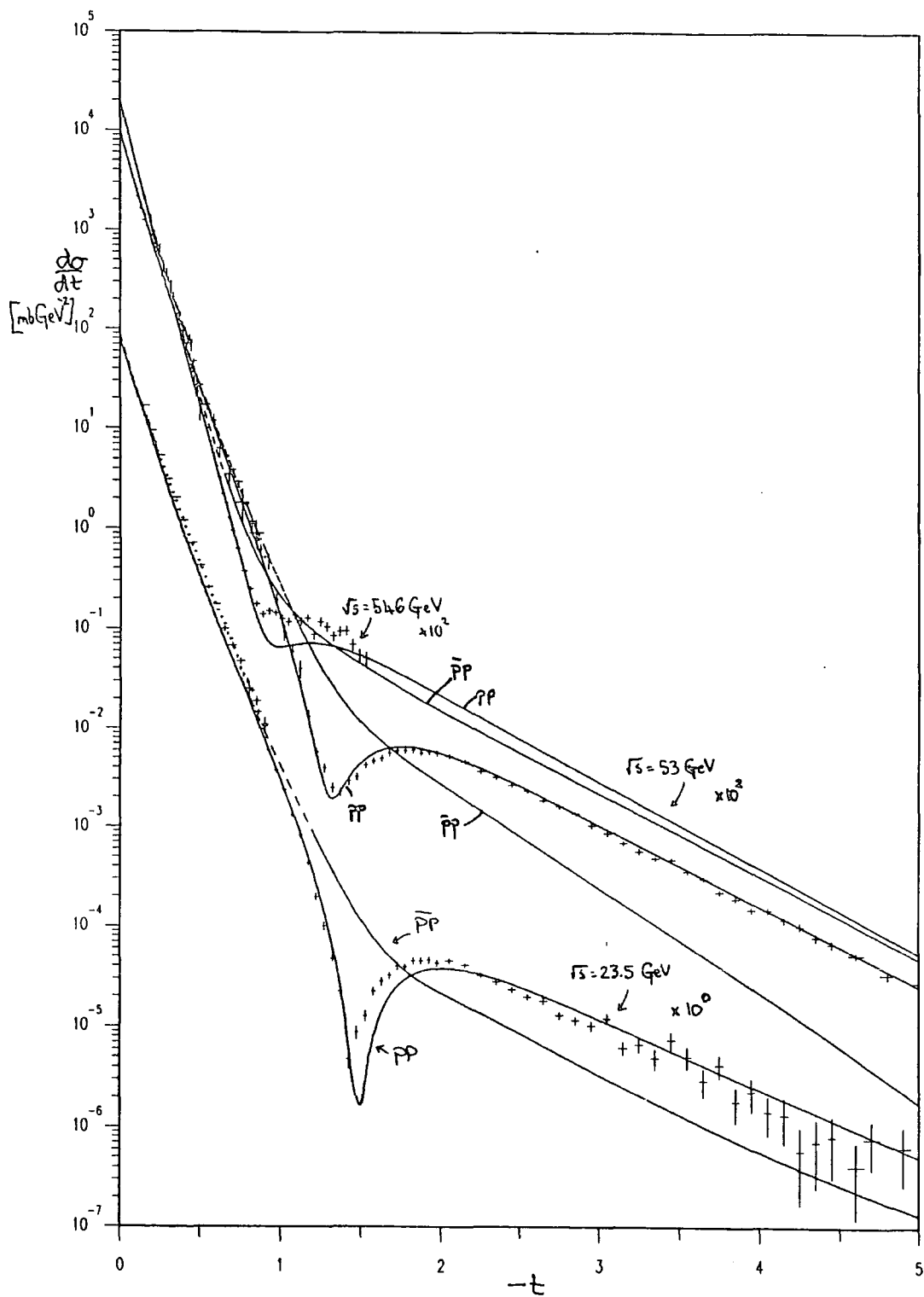


FIG. 5.24 Results of fit (5.4b) at $\sqrt{s} = 23.5, 53$ and 546 GeV .

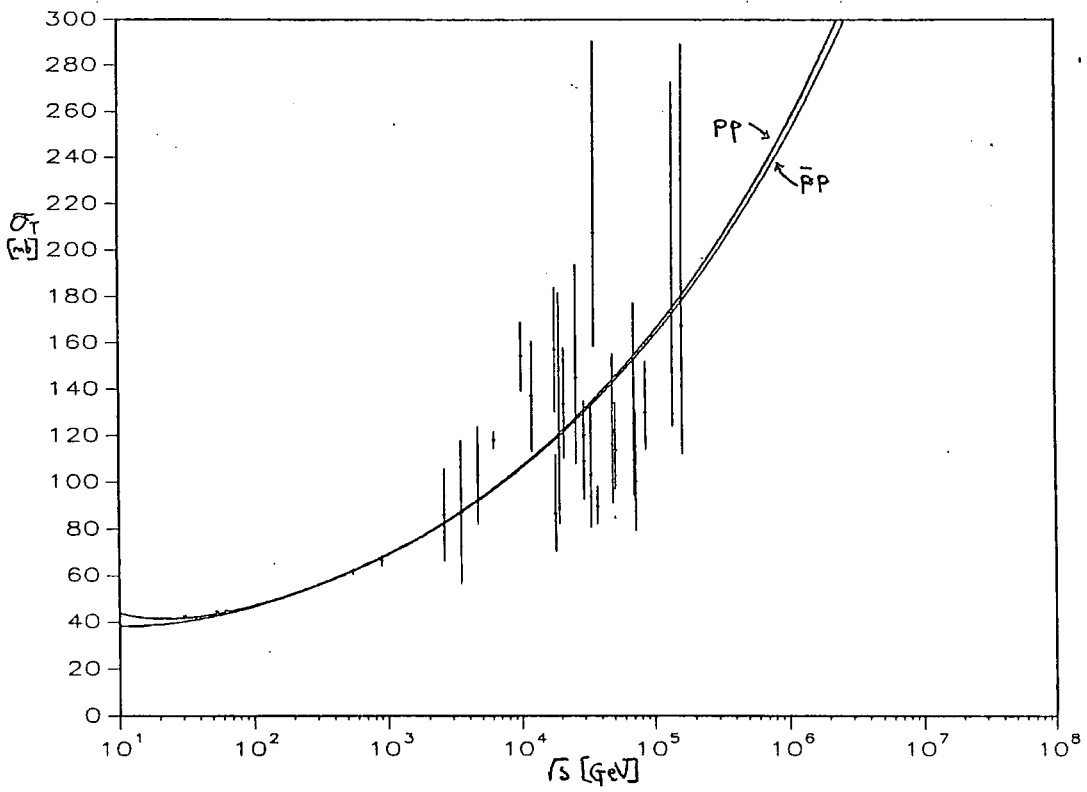


FIG. 5.25 Results of fit (5.4b) at high energy for $\sigma_T(pp)$ (full line) and $\sigma_T(\bar{p}p)$ (dotted line).

The Impact Picture Model of Bounrely, Soffer and Wu.

6.1. Introduction

An eikonal type of model was used some time ago (BSW (1979)) to give a good description of pp elastic scattering at the ISR and lower energies. A prediction of the model was that the height of the second maximum in $\frac{d\sigma}{dt}$ would increase rapidly with energy. Subsequent data has shown the magnitude of the first structure relative to the optical point increase from 10^{-7} at the ISR to 10^{-5} at the $\bar{p}p$ collider. Changing the parameters slightly to fit the new data has given a good account of the high energy behaviour of the differential cross-section (BSW (1984a)). In particular it gives a good description of the change from a dip in $\frac{d\sigma}{dt}$ at the ISR to a shoulder at the $\bar{p}p$ collider. It is therefore worth investigating how the filling in of the dip comes about and so we shall review the details and results of their model.

The relevant formulae giving the full scattering amplitude but not including spin effects are given below.

From equations (3.2.10), (3.2.13) and (3.2.18) we have for the scattering amplitude

$$A(s, t) = 4\pi i s \int_0^{\infty} b db J_0(b\sqrt{-t}) (1 - e^{-\Omega_0}) \quad (6.1.1)$$

The opacity, Ω_0 , has two contributions :

$$\Omega_0(s, b) = S_0(s)F(b^2) + R_0(s, b) \quad (6.1.2)$$

The first part is due to diffractive scattering and gives the asymptotic energy behaviour of the amplitude; while the second is a Reggeon exchange contribution which dies off at high energy but is necessary to describe the low energy data. The diffractive scattering component can be thought of as due to Pomeron exchange, the higher order terms in the eikonal series giving multiple Pomeron exchange. The s - and b -dependences of the Pomeron contribution are given by

$$S_0(s) = \frac{s^c}{(\ln s)^{c'}} + \frac{u^c}{(\ln u)^{c'}} \quad (6.1.3)$$

$$F(b^2) = \frac{1}{2} \int_{-\infty}^0 dt J_0(b\sqrt{-t}) \tilde{F}(t) \quad (6.1.4)$$

where

$$\tilde{F}(t) = f [G(t)]^2 \frac{a^2 + t}{a^2 - t} \quad (6.1.5)$$

$$G(t) = \frac{1}{\left(1 - \frac{t}{m_1^2}\right) \left(1 - \frac{t}{m_2^2}\right)} \quad (6.1.6)$$

The function $S_0(s)$ is motivated by the high energy behaviour of massive QED in which the amplitude for single tower exchange has the form (Cheng and Wu (1970)):

$$A_{tower}(s, t) = \frac{is s^c}{(\ln s)^2} F(t) \quad (6.1.7)$$

The form for $S_0(s)$ used in (6.1.3) has been given a real part by the addition of a crossing symmetric ($s \rightarrow u$) term and the power of the logarithm in the denominator is made a free parameter. This asymptotic behaviour corresponds to a j -plane singularity of the form (provided c' not a +ve integer) :

$$(j - c - 1)^{c' - 1} \quad (6.1.8)$$

so that with $c' < 1$ it corresponds to a hard Regge cut.

As we saw in §3.6, it can be shown from field theory calculations that single tower exchange in massive QED eikonalizes, which gives some reason for hoping that this is the correct form for the Born term in the eikonal series. However, this form for $S_0(s)$ has some theoretical drawbacks: it does not have the Regge phase expected from dispersion relations and it corresponds to a fixed hard singularity in the j -plane. The latter point means that it is incompatible with t -channel unitarity and some mechanism must exist whereby the singularity disappears onto an unphysical sheet for t above threshold, for example a soft cut which passes through $j = 1 + c$ for all values of t between the t -channel elastic and inelastic thresholds.

The t -dependence of the Born term is given by the function $\tilde{F}(t)$ which is proportional to the square of the proton electromagnetic form factor, $G(t)$, up to a slowly varying function of t . The ansatz of proportionality between the matter distribution and the charge distribution was used extensively before large- $|t|$ data became available at the ISR. Direct proportionality is ruled out because it predicts a second dip around $|t| = 4 \text{ GeV}^2$ which is not present in the data (Chou and Yang (1970)) and in fact any simple

form for the t -dependence of the Born term gives the same result (Sukhatme(1977)). The chosen form for the slowly varying function, with a pole at $t = a^2 \approx 4 \text{ GeV}^2$, pushes the next zero in the imaginary part of the amplitude out in $|t|$ so that no more dips are predicted. However, it has the problem that it can no longer be factorized into two real equal functions of t to represent the coupling of a single exchange to each of the colliding particles, as one would expect for the first term of an eikonal series. However, since it does not satisfy t -channel unitarity anyway it does not really have to factorize.

The Reggeon exchange contribution in equation (6.1.2) is given by

$$R_0(s, b) = \frac{1}{is} \int_{-\infty}^0 dt J_0(b\sqrt{-t}) \tilde{R}_0(s, t) \quad (6.1.9)$$

where

$$\tilde{R}_0(s, t) = \begin{cases} (C_+ + C_- e^{-i\pi\alpha_R(t)}) s^{\alpha_R(t)} & \text{for } pp \\ (C_+ e^{-i\pi\alpha_R(t)} + C_-) s^{\alpha_R(t)} & \text{for } \bar{p}p \end{cases} \quad (6.1.10)$$

and $\alpha_R(t) = \alpha_R(0) + \alpha'_R(t)$.

A good fit is obtained using the following parameters[†]:

$$\begin{array}{ll} c = 0.167 & c' = 0.748 \\ m_1 = 0.586 \text{ GeV} & m_2 = 1.704 \text{ GeV} \\ a = 1.953 \text{ GeV} & f = 7.115 \text{ GeV}^{-2} \\ C_+ = -55.6 & \alpha_R(0) = 0.308 \\ C_- = -1.03 & \alpha'_R = 0.694 \text{ GeV}^{-2} \end{array} \quad (6.1.11)$$

Using this parametrization the first term in the eikonal series is just

$$A^{(1)}(s, t) = 4\pi is \int_0^\infty b db J_0(b\sqrt{-t}) \Omega_0(s, b) \quad (6.1.12)$$

and using: $F(t) = \frac{1}{2} \int_0^\infty b db J_0(b\sqrt{-t}) \int_{-\infty}^0 dt' J_0(b\sqrt{-t'}) F(t')$, this gives

$$A^{(1)}(s, t) = 4\pi is S_0(s) \tilde{F}(t) + \tilde{R}_0(s, t) \quad (6.1.13)$$

[†] The Pomeron parameters are taken from (BSW (1984a)); the Reggeon parameters are similar to those used in (BSW (1979)) but have been adjusted by us to fit σ_T with these Pomeron parameters.

It is useful to compare this with the parametrization of the Pomeron and Reggeons we used previously. For the Pomeron we had from equation (4.4.1) :

$$\begin{aligned} A^P(s, t) &= -G_P(t) (e^{-i\frac{\pi}{2}s})^{\alpha_P(t)} = isG_P(t) (e^{-i\frac{\pi}{2}s})^{\epsilon + \alpha'_P t} \\ &= \frac{isG_P(t)}{\cos \frac{\pi}{2}(\epsilon + \alpha'_P t)} \left(s^{\epsilon + \alpha'_P t} + u^{\epsilon + \alpha'_P t} \right) \end{aligned} \quad (6.1.14)$$

Thus, if $\alpha'_P = 0$ and $c' = 0$, then

$$\epsilon \Leftrightarrow c \quad \text{and} \quad \frac{G_P(t)}{\cos \frac{\pi}{2}\epsilon} \Leftrightarrow 4\pi \tilde{F}(t) \quad (6.1.15)$$

corresponding to the fact that the Pomeron contribution in equation (6.1.2) factorizes into a function of s and a function of t and so represents a fixed pole in the j -plane at $j = 1 + c$.

For the Reggeons in equation (4.4.5), we had a sum of even and odd signature contributions due to f and ω Reggeon exchange :

$$A^R(s, t) = -G_f(t) (e^{-i\frac{\pi}{2}s})^{\alpha_f(t)} \mp iG_\omega(t) (e^{-i\frac{\pi}{2}s})^{\alpha_\omega(t)} \quad \text{for } \begin{array}{l} pp \\ \bar{p}p \end{array} \quad (6.1.16)$$

Comparison with $\tilde{R}_0(s, t)$ yields

$$\begin{aligned} A_f(s, t) &= 4\pi(C_+ + C_-) \cos \frac{\pi}{2}\alpha_R(t) (e^{-i\frac{\pi}{2}s})^{\alpha_R(t)} \\ A_\omega(s, t) &= \pm i4\pi(C_+ - C_-) \sin \frac{\pi}{2}\alpha_R(t) (e^{-i\frac{\pi}{2}s})^{\alpha_R(t)} \quad \text{for } \begin{array}{l} pp \\ \bar{p}p \end{array} \end{aligned} \quad (6.1.17)$$

So we have

$$\begin{aligned} G_f(t) &\Leftrightarrow -4\pi(C_+ + C_-) \cos \frac{\pi}{2}\alpha(t) \\ G_\omega(t) &\Leftrightarrow -i4\pi(C_+ - C_-) \sin \frac{\pi}{2}\alpha(t) \end{aligned} \quad (6.1.18)$$

and since from (6.1.11) C_+ is negative, these parametrizations differ only in their t -dependence.

6.2. Details of the Computation

In order to calculate the scattering amplitude at a given value of s and t we need to compute two Bessel transforms numerically. The Bessel transform of the t -dependent part of Pomeron contribution, $F(b^2)$, in equation (6.1.4), is independent of s and t so that it can be performed independently and referenced as a table. That leaves the inverse transformation to be calculated numerically at each (s, t) point. The Reggeon contribution, $\tilde{R}_0(s, t)$, has a simple exponential t -dependence and so its transform has an analytic expression.

We use Simpson's rule to do the integrals since the integrands are highly oscillatory due to the function $J_0(b\sqrt{-t})$. The number of integration points needed to obtain sufficient accuracy was fixed by trial and error. The asymptotic behaviour of the zeroth order Bessel function, $J_0(x)$, is given by

$$J_0(x) \simeq \sqrt{\frac{2}{\pi x}} \cos(x - \frac{\pi}{4}) \quad \text{for large } x. \quad (6.2.1)$$

so has a period $\approx 2\pi$ and dies off only slowly as $1/\sqrt{x}$. The integral for $F(b^2)$ was performed out to $|t| = 20 \text{ GeV}^2$. At large b the function $J_0(b\sqrt{-t})$ oscillates very rapidly as a function of b and so a large number of integration points are necessary. We used 20000 points at 250 values of b out to $b = 25 \text{ GeV}^{-1}$ to set up a table for $F(b^2)$ which takes approximately 4 minutes of cpu time on the IBM 3081. The other integration over b was performed out to $b = 25 \text{ GeV}^{-1}$ using 2700 points and calculates $A(s, t)$ at about 200 (s, t) -points per minute. Thus it was not possible to fit the data allowing $\tilde{F}(t)$ to vary, because it would take too long to calculate the transform numerically, but $S_0(s)$ could be varied. The accuracy obtained in $\frac{d\sigma}{dt}$ is always better than 1 part in a 1000 even at large $|t|$. This was checked by changing the integration ranges and the number of integration points in each of the integrals and by using the expression: $A(s, t) = \frac{1}{2} \int_0^\infty b db J_0(b\sqrt{-t}) \int_{-\infty}^0 dt' J_0(b\sqrt{-t'}) A(s, t')$. Comparing the results with (BSW (1984a)), which uses the above parametrization, shows agreement to about 1%.

6.3. High Energy Behaviour of the Profile Function, $A(s, b)$

The Reggeon contribution dies off fairly rapidly with energy so we shall ignore it for the moment in considering high energies and see how the Pomeron part alone behaves.

As $s \rightarrow \infty$ at fixed b , we have $Re \Omega_0(s, b) \rightarrow \infty$, due to its s^c power behaviour, so that $A(s, b) \rightarrow \frac{i}{2}$. The profile function is then dependent upon many terms in the series, each of which individually would violate unitarity. From fig.6.1 we can see that the profile function starts out at ISR energies looking something like a gaussian in shape. As the energy increases, $Im A(s, b)$ rises less at small b than at large b so becoming flatter than a gaussian. At sufficiently high energy the profile function is essentially equal to $\frac{i}{2}$ out to some radius, r , which increases with energy, and then drops rapidly to zero. Thus it behaves more and more like a black disk as the area around the edge becomes relatively less important. This is true of any reasonable input to the eikonal series (3.2.13) which grows with energy since the effect of summing the series is more or less to chop off the imaginary part of the profile function at the diffractive limit $Im A(s, b) = \frac{1}{2}$.

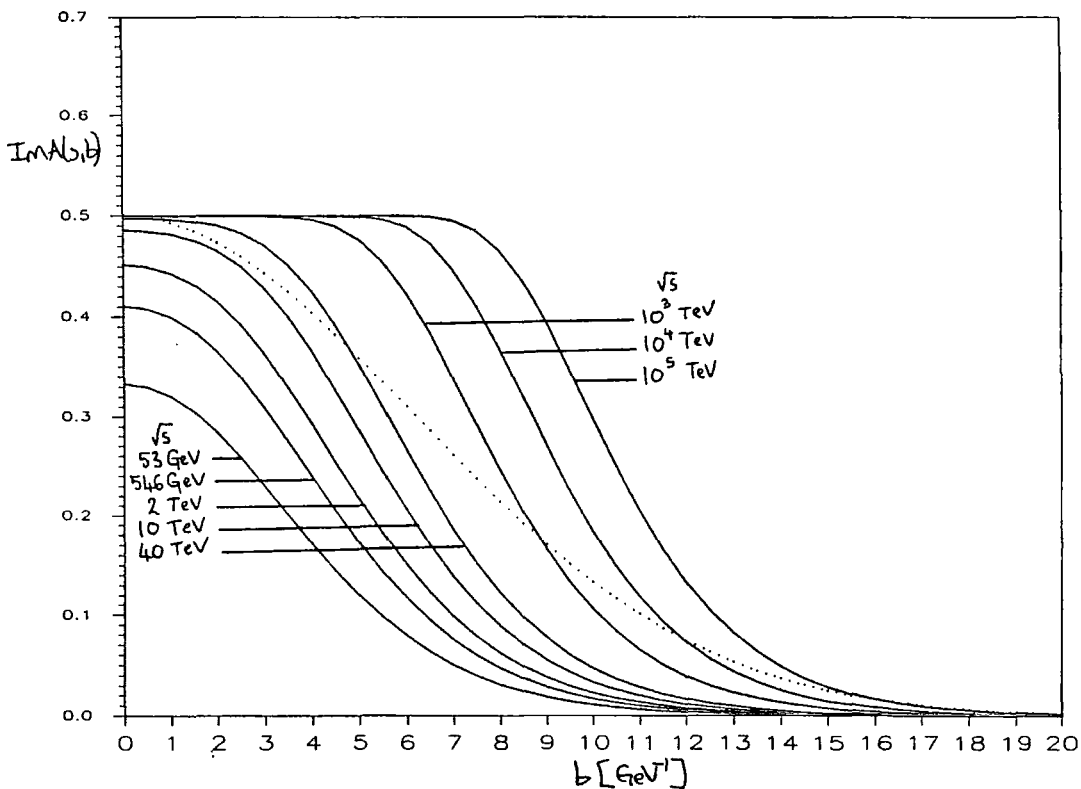


FIG. 6.1 Imaginary part of the profile function in BSW model at $\sqrt{s} = 53, 546, 2 \times 10^3, 10^4, 4 \times 10^4, 10^6, 10^7$ and 10^8 GeV as a function of b (Reggeon contribution not included). Dashed curve is a Gaussian function with the same radius as the curve at $\sqrt{s} = 10^6$ GeV.

Even at $\sqrt{s} = 546$ GeV the first term of the series has an imaginary part bigger than $\frac{i}{2}$ for small values of b so that higher order terms in the series are important. Fig.6.2 shows the effect on $Im A(s, b)$ of adding successively more terms to the series. It can be seen that at large b , where $Im A(s, b)$ is small, the effects of eikonalization are small and the profile function is essentially just due to the first term in the series.

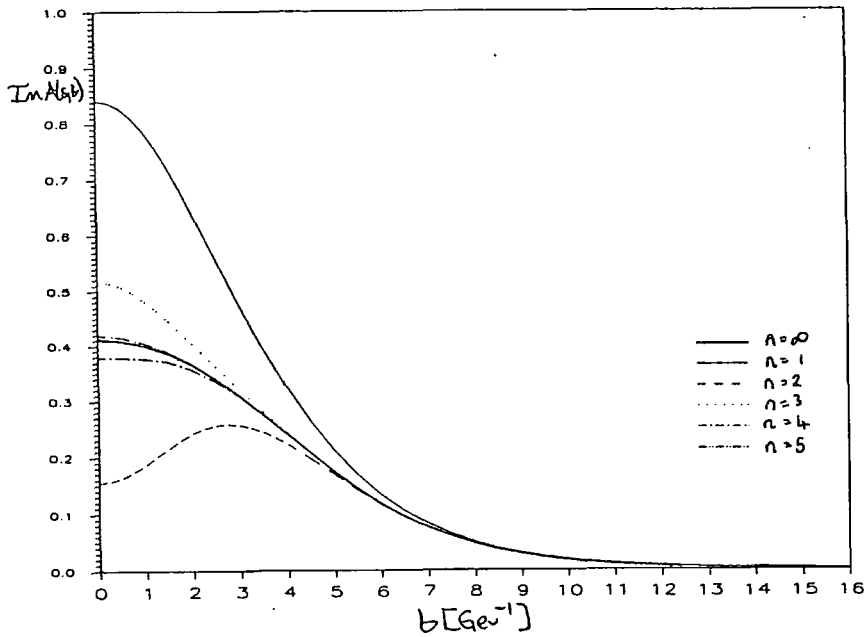


FIG. 6.2 Effect on profile function of adding successively more terms to the eikonal series (3.2.13) at $\sqrt{s} = 546$ GeV.

At high enough energy, $Im A(s, b)$ will not be able to increase any more in the central region and will only increase peripherally. However, at current energies, $Im A(s, b)$ is still rising at small b and the amplitude is not yet peripheral in that sense. This can be seen in fig.6.3 which shows the change in $Im A(s, b)$ as a function of b between $\sqrt{s} = 53$ and 546 GeV, 5 and 40 Tev, 10^3 and 10^4 Tev respectively, the first of which is at currently accessible energies and doesn't show a pronounced peak away from $b = 0$. On the other hand, $\Delta G_{inel}(s, b)$, which loosely speaking gives the value of b at which new inelastic processes are occurring, does show a peak at $b = 5 \text{ GeV}^{-1}$ over the same energy range.

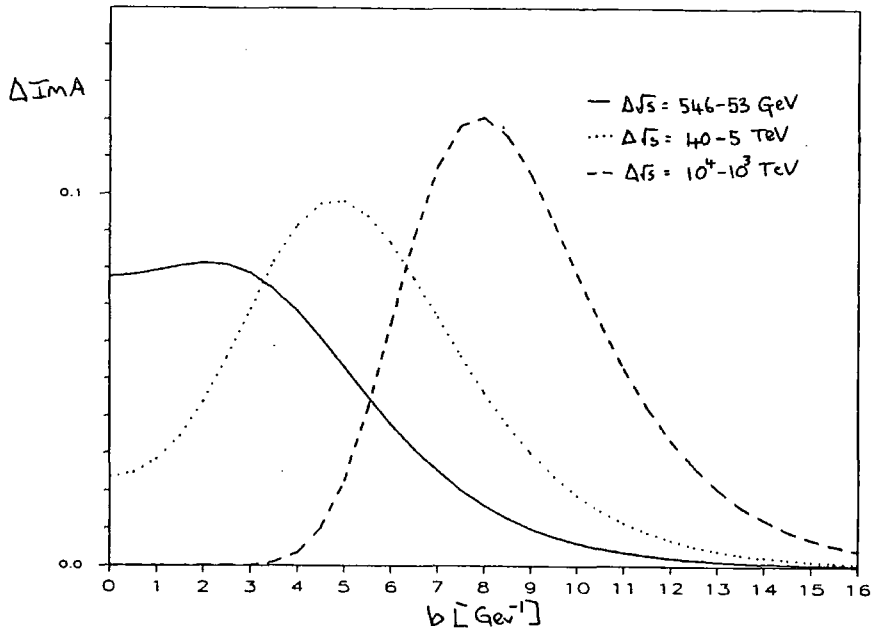


FIG. 6.3 BSW model prediction for $\Delta \text{Im } A(s, b) = \text{Im } A(s_2, b) - \text{Im } A(s_1, b)$ for $(s_1, s_2) = (53, 546), (5 \times 10^3, 40 \times 10^3), (10^6, 10^7)$ GeV.

The Argand plot of $\text{Im } A(s, b)$ against $\text{Re } A(s, b)$ at fixed b and varying s in fig.6.4 shows how the profile function ends up at $\frac{i}{2}$ as $s \rightarrow \infty$ and avoids violating unitarity. The ratio, $\text{Re}/\text{Im } A(s, b) = \rho'(s, b)$, tends to zero as $s \rightarrow \infty$, so that Re/Im for the scattering amplitude, $\rho(s, t)$, also tends to zero.

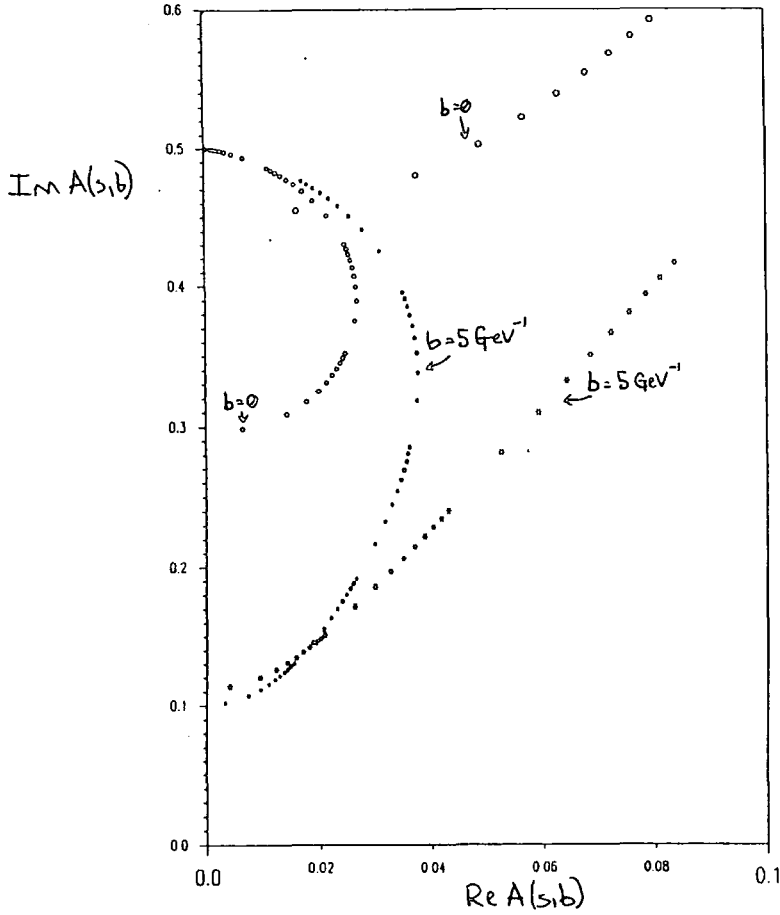


FIG.6.4 Argand plot for profile function for Born term and full eikonal series in BSW model at $b = 0$ and 5 GeV^{-1} for $\sqrt{s} = 10 \rightarrow \infty \text{ GeV}$.

6.4. High Energy Behaviour of σ_T and the Froissart Bound.

In terms of impact parameter amplitudes we have

$$\sigma_T = 4 \int_0^{\infty} d^2 \mathbf{b} \text{Im} A(s, \mathbf{b}) \quad (6.4.1)$$

As we found above, at sufficiently high energy the profile function resembles a black disk of radius, r , and with $\text{Im} A(s, b) = \frac{1}{2}$ then

$$\sigma_T = 2\pi r^2 \quad (6.4.2)$$

If we take the radius of the black disk as the value of b for which $\text{Im} A(s, b) = \frac{1}{2}$ then we have for the radius, $r(s)$, as a function of s :

$$1 - e^{-\text{Re} \Omega(s, r(s))} = \frac{1}{2} \quad \text{or} \quad \text{Re} \Omega = \ln 2 \quad (6.4.3)$$

So that

$$F(r^2) = \frac{\ln 2}{S_0(s)} \quad (6.4.4)$$

At sufficiently high s , where $S_0(s)$ is large, $F(r^2)$ will be small, corresponding to a large value of r . Since b and $\sqrt{-t}$ are conjugate variables, the behaviour of $F(b^2)$ in equation (6.1.4) at large b is dominated by the nearest t -channel singularity of $\tilde{F}(t)$. From (6.1.6) the nearest t -channel singularity is at $t = m_1^2$. So to get the large b behaviour of $f(b^2)$ we approximate $\tilde{F}(t)$ in (6.1.4) by

$$\tilde{F}(t) \simeq \frac{1}{(m_1^2 - t)^2} \frac{f m_1^4 m_2^4}{(m_2^2 - m_1^2)^2} \left(\frac{a^2 + m_1^2}{a^2 - m_1^2} \right) \quad (6.4.5)$$

and using (Gradshteyn, Ryzhik p.686) we get

$$\begin{aligned} \frac{1}{2} \int_{-\infty}^0 J_0(b\sqrt{-t}) \frac{1}{(a^2 - t)^{\mu+1}} dt &= \int_0^{\infty} x dx J_0(bx) \frac{1}{(a^2 + x^2)^{\mu+1}} \\ &= \left(\frac{b}{2a} \right)^\mu \frac{K_{-\mu}(ab)}{\Gamma(\mu + 1)} \end{aligned} \quad (6.4.6)$$

where K is the modified Bessel function of the 2^{nd} kind. Putting $\mu = 1$ and using the above in equation (6.1.4) gives

$$F(b^2) = \frac{f m_1^4 m_2^4}{(m_2^2 - m_1^2)^2} \left(\frac{a^2 + m_1^2}{a^2 - m_1^2} \right) \frac{b}{2m_1} K_1(m_1 b) \quad (6.4.7)$$

The asymptotic behaviour of $K_\nu(x)$ is given by (Gradshteyn, Ryzhik p.963)

$$\begin{aligned} K_\nu(x) &= \sqrt{\frac{\pi}{2x}} e^{-x} \sum_{k=0}^{\infty} \frac{1}{k!(2x)^k} \frac{\Gamma(\nu + k - \frac{1}{2})}{\Gamma(\nu - k + \frac{1}{2})} \\ &\simeq \sqrt{\frac{\pi}{2x}} e^{-x} \quad \text{independent of } \nu \text{ at large } x \end{aligned} \quad (6.4.8)$$

Using this asymptotic expression in (6.4.7) gives us

$$\begin{aligned} F(b^2) &\simeq \frac{f m_1^4 m_2^4}{(m_2^2 - m_1^2)^2} \left(\frac{a^2 + m_1^2}{a^2 - m_1^2} \right) \frac{b}{2m_1} \sqrt{\frac{\pi}{2m_1 b}} e^{-m_1 b} \\ &= 1.81 \sqrt{b} e^{-0.586b} \end{aligned} \quad (6.4.9)$$

with the values from (6.1.11).

In fig.6.5 we compare this asymptotic estimate to our numerical calculation of the Bessel transform in equation (6.1.4). At large b they are similar. At $b = 5 \text{ GeV}^{-1}$ the difference between the asymptotic prediction and the numerical value is about 15%

and decreases slowly as b increases. In fact if we also include the contribution from the simple pole at $t = m_1^2$ using

$$\tilde{F}(t) = \frac{f(t)}{(m_1^2 - t)^2} = \frac{f(m_1^2)}{(m_1^2 - t)^2} - \frac{f'(m_1^2)}{(m_1^2 - t)} + \dots \quad (6.4.10)$$

where

$$f(t) = \frac{f m_1^4 m_2^4}{(m_2^2 - t)^2} \left(\frac{a^2 + t}{a^2 - t} \right) \quad (6.4.11)$$

to give using (6.4.6)

$$F(b^2) = f(m_1^2) \frac{b}{2m_1} K_{-1}(m_1 b) - f'(m_1^2) K_0(m_1 b) \quad (6.4.12)$$

and include 2^{nd} order terms in the expansion of K_{-1} , we get agreement with the numerically calculated value to about 1% at $b = 5 \text{ GeV}^{-1}$. This method could be used to calculate $F(b^2)$ for $b > 1 \text{ GeV}^{-1}$ and so allow the parameters of $F(b^2)$ to be varied, tabulating $K_\nu(x)$ for $x < 1$.

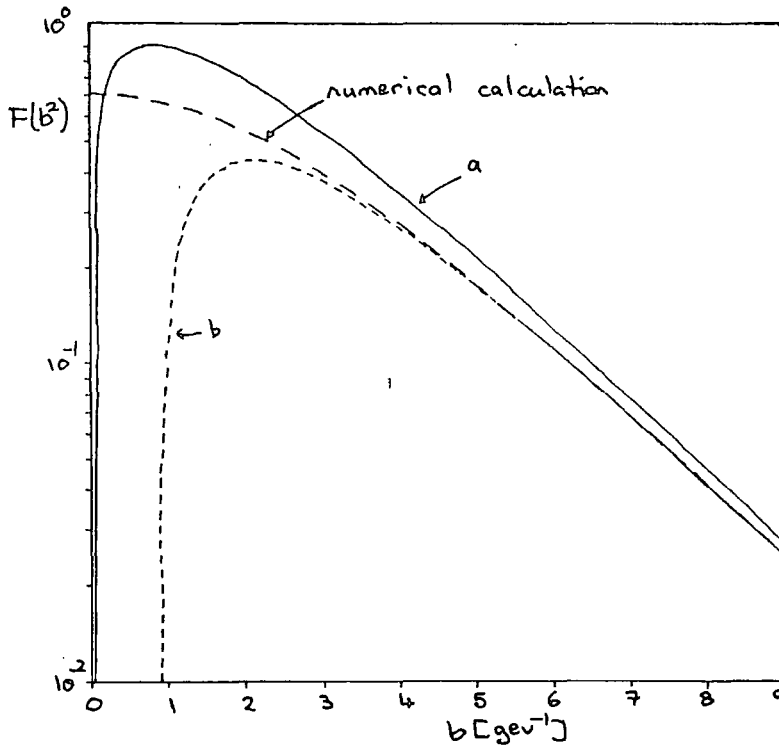


FIG.6.5 Comparison of asymptotic prediction for $\tilde{F}(b^2)$ for (a) (6.4.9), (b) (6.4.12); with numerical calculation.

Combining equations (6.4.4) and (6.4.9) at large b gives us

$$e^{-m_1 r(s)} \sim \frac{1}{S_0(s)} \quad (6.4.13)$$

and so at large s , using (6.1.3),

$$r(s) \sim \frac{1}{m_1} \ln S_0(s) \sim \frac{c}{m_1} \ln s \quad (6.4.14)$$

From (6.4.2) this gives for the asymptotic behaviour of σ_T :

$$\sigma_T \sim \frac{2\pi c^2}{m_1^2} \ln^2 s \quad (6.4.15)$$

and so satisfies the Froissart bound $\sigma_T \leq \frac{\pi}{m_\pi^2} \ln^2 s$ since the coefficient in (6.4.15), $\frac{2\pi c^2}{m_1^2} \ll \frac{\pi}{m_\pi^2}$.

Putting in the values from (6.1.11) we get

$$\sigma_T \sim 0.2 \ln^2 s \text{ mb} \quad (6.4.16)$$

In figure 6.6 we plot the high energy behaviours of σ_T , σ_{el} and the ratio $R \equiv \frac{\sigma_{el}}{\sigma_T}$ and their asymptotic predictions. From the figure we see that at $\sqrt{s} = 10^6$ GeV the calculated value is about 20% above the asymptotic prediction which shows that it is not yet a good approximation to ignore the effects of the grey fringe. However, the cross-section does seem to be growing with a *constant* + $0.2 \ln^2 s$ mb behaviour, where the constant is approximately 32 mb and is negligible at asymptotic energies compared to the $\ln^2 s$ term.

In the black disk limit we expect, $R \rightarrow \frac{1}{2}$ and $\sigma_{el} \rightarrow \pi R^2 \sim \frac{\pi c^2}{m_1^2} \ln^2 s = 0.1 \ln^2 s$. The ratio, R , of the elastic to total cross-sections is a good indicator of the onset of asymptotic black disk behaviour. At $\sqrt{s} = 1$ TeV, R is only 0.17, by 40 TeV it has risen to 0.24, and thereafter it rises slowly towards 0.5. Thus we will not reach the point where the contribution of the edge of the black disk is negligible until very high energies $\gg 10^6$ GeV. The behaviour of σ_{el} and R and their asymptotic predictions are also shown in fig.6.6 .

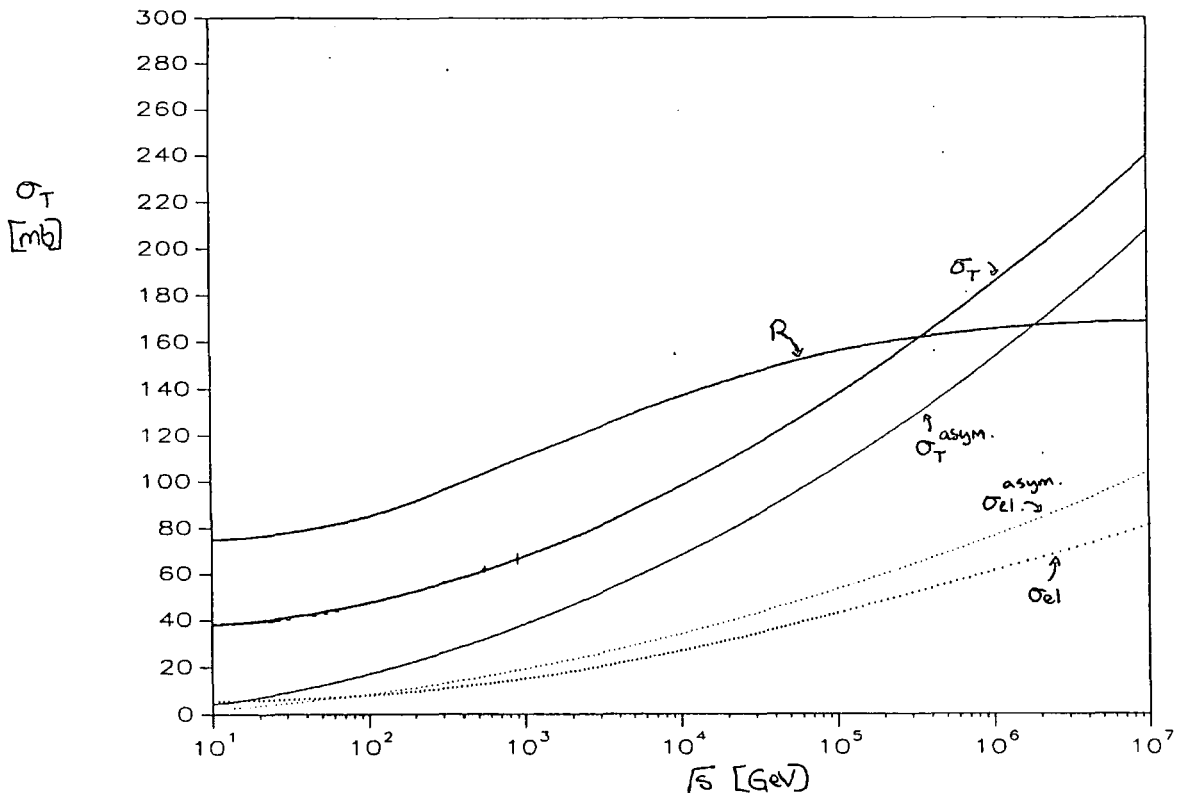


FIG.6.6 High energy behaviours of σ_T , σ_{el} and the ratio $R \equiv \frac{\sigma_{el}}{\sigma_T}$ (normalized to 0.5 at 250 mb) in the BSW model and their asymptotic predictions.

A breakdown of the different contributions to σ_T shows that as the energy increases the relative importance of higher terms increases. At ISR energies, the contributions of the 2nd and 3rd terms of the series relative to the 1st term are about 25% and 10% respectively. The effect of higher terms on σ_T seems less than on the profile function because the contribution to σ_T at a given impact parameter is weighted by b but the higher terms mainly affect $A(s, b)$ at small b .

6.5. High Energy Behaviour of Re/Im.

As noted above, we expect the real part of the amplitude at $t = 0$ to go to zero asymptotically. Derivative analyticity relations (Bronzan, Kane and Sukhatme (1975)) give

$$\rho(s, t = 0) \simeq \frac{\pi}{2} \frac{1}{\sigma_T} \frac{d}{d \ln s} \sigma_T \quad \text{for large } s \quad (6.5.1)$$

and using equation (6.1.15) this gives

$$\rho(s, t = 0) \simeq \frac{\pi}{2} \frac{2}{\ln s} \quad (6.5.2)$$

which describes how Re/Im asymptotically tends to zero but, as fig.6.7 shows, up to $\sqrt{s} = 10^8$ GeV we do not yet see this behaviour.

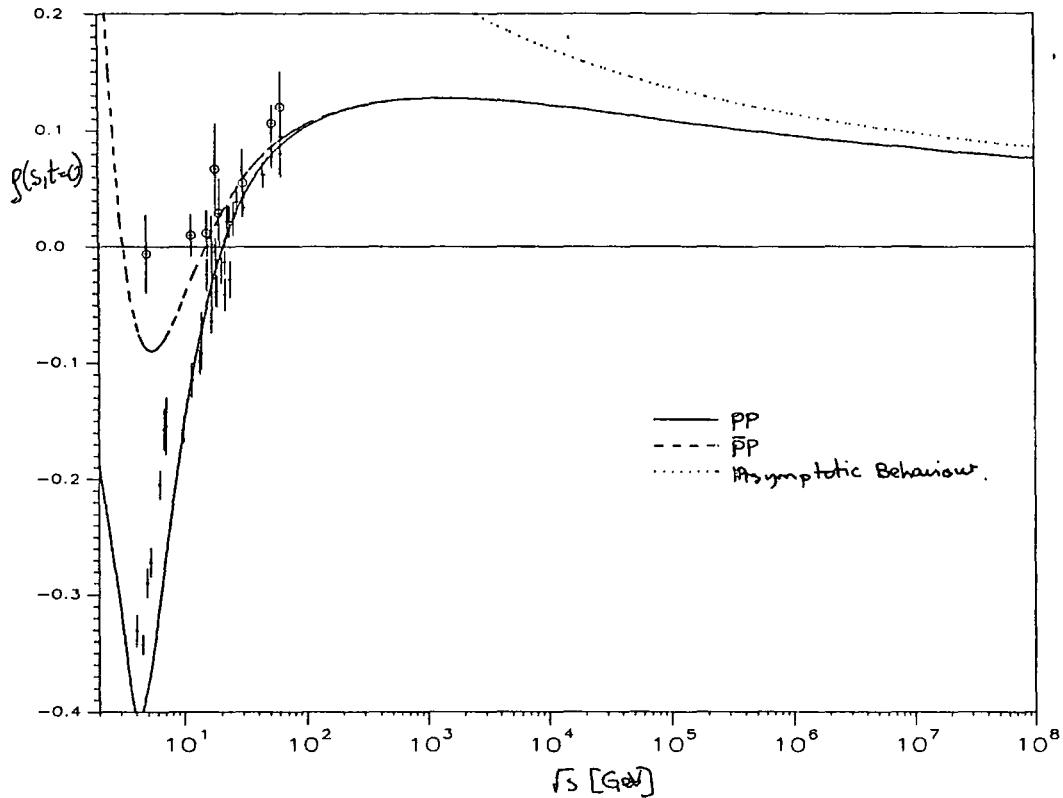


FIG.6.7 High energy behaviour of $\rho(s, t = 0) \equiv \frac{\text{Re}}{\text{Im}} A(s, t = 0)$.

6.6. High Energy Behaviour of $\frac{d\sigma}{dt}$.

The prediction for $\frac{d\sigma}{dt}$ without the Reggeon exchange contribution gives a reasonable account of the data for $|t| < 0.8 \text{ GeV}^2$ at both $\sqrt{s} = 53 \text{ GeV}$ and $\sqrt{s} = 546 \text{ GeV}$ and for the large $|t|$ data at $\sqrt{s} = 53 \text{ GeV}$. However, as we can see in fig.6.8, the dip at $|t| = 1.35 \text{ GeV}^2$ is not deep enough at $\sqrt{s} = 53 \text{ GeV}$ and a little too deep at $\sqrt{s} = 546 \text{ GeV}$ and the 2nd maximum has increased too much to give good agreement with the more accurate new data that has since appeared from the collider. The shape

of the dip in the Pomeron contribution does not alter appreciably between the ISR and the collider. For $|t| \geq 5 \text{ GeV}^2$ the prediction of the model lies well above the ISR and FNAL data. At $|t| = 8 \text{ GeV}^2$ it is a factor of $10 \times$ too large.

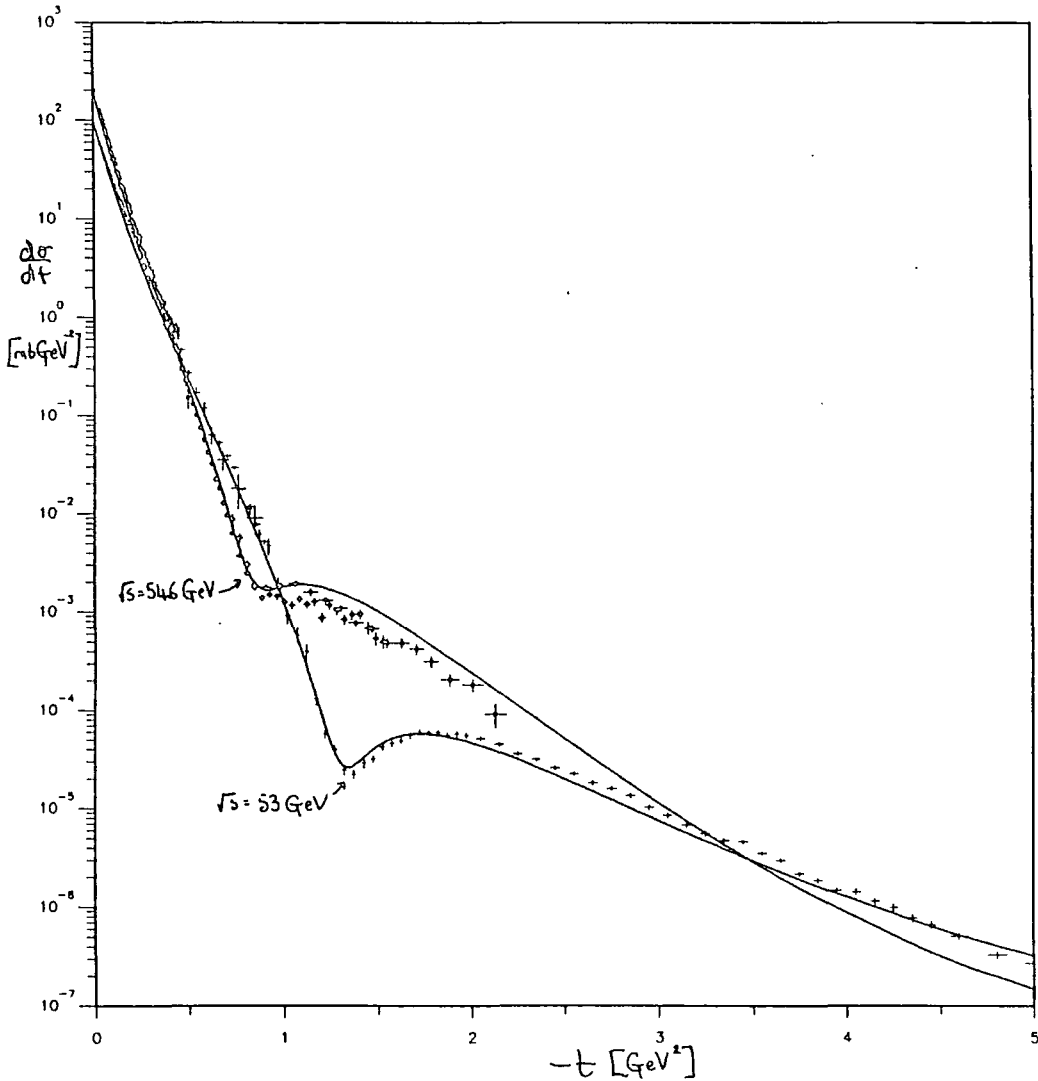


FIG. 6.8 $\frac{d\sigma}{dt}$ for BSW model at $\sqrt{s} = 53$ and 546 GeV (no Reggeon contribution included).

The structure of $\frac{d\sigma}{dt}$ is formed by the superposition of many terms of the eikonal series. Adding successive terms to the sum gives a result which at small $|t|$ converges quite rapidly onto the full exponential result but at large $|t|$ needs something like five terms before starting to approach the final result. This is the same thing we saw in the profile function where small $|t|$ corresponds to large b and at large b the first few terms give a good approximation to the final answer. The differential cross-section resulting from summing successively greater numbers of terms in the eikonal series is displayed in fig.6.9 . The dip in $\frac{d\sigma}{dt}$ of the input of the eikonal series is due to its change of sign at

$|t| = 4 \text{ GeV}^2$ and is not present in the sum of the series, at least not for $|t| < 20 \text{ GeV}^2$. The first term of the series has a fixed phase but this is not true for the sum of the series, which has a t -dependent phase.

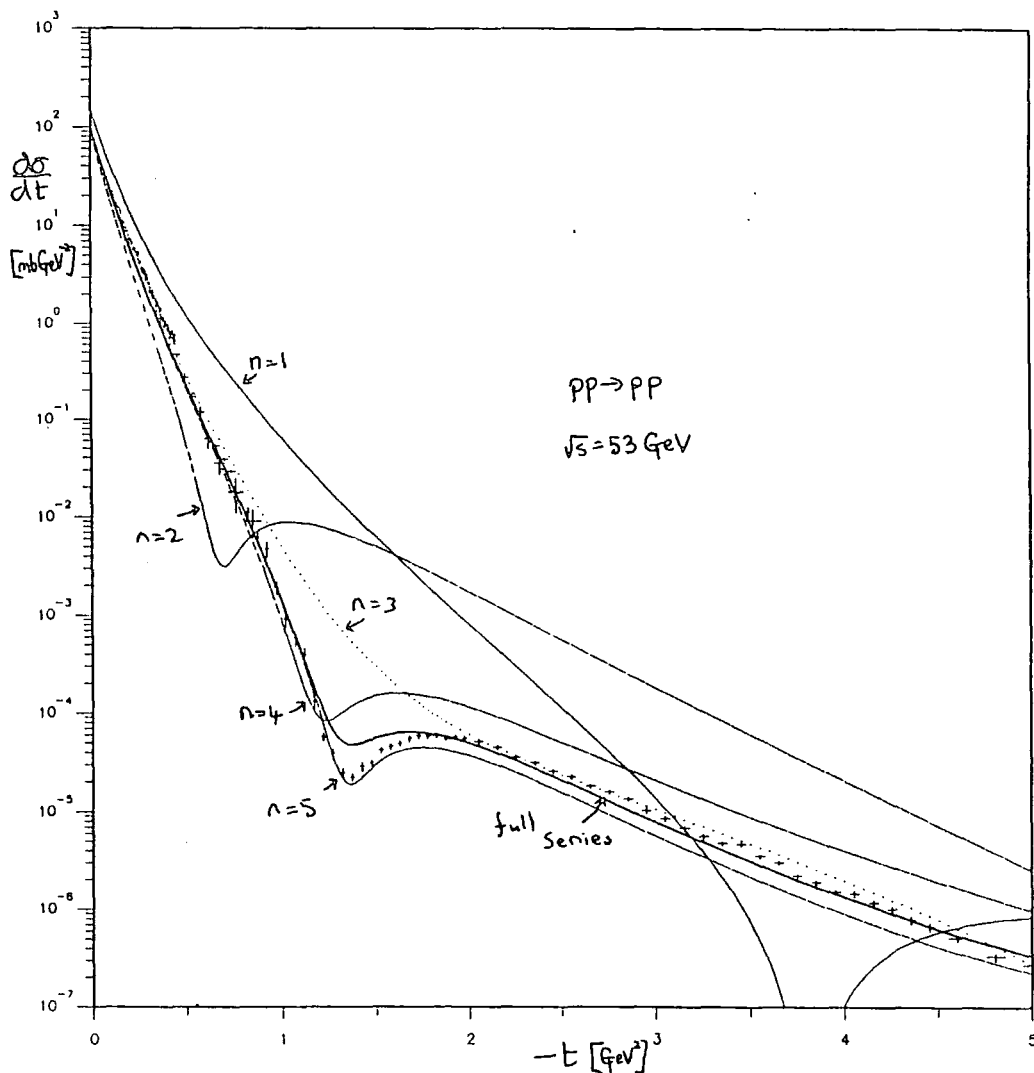


FIG. 6.9 $\frac{d\sigma}{dt}$ for BSW model from summing successively greater numbers of terms in the eikonal series (no Reggeons).

At even higher energies the model predicts that the 2^{nd} maximum continues to increase at a fast rate and the dip deepens again and continues to shrink in towards the forward peak. At $\sqrt{s} = 5 \text{ TeV}$ secondary structure starts to appear in the form of a slight shoulder around $|t| = 2 \text{ GeV}^2$ and moves in as the energy increases. This is due to the re-emergence of the second zero in the imaginary part of the full amplitude. It does not give a dip because the real part washes it out. At 40 TeV the model gives a sharp dip

at $|t| = 0.35$ and the 2nd maximum is only a factor of 10^{-3} down on the magnitude at the optical point. So as energy increase the model predicts that the dip should shrink inwards and become deeper and new dips start to appear. This behaviour agrees with (BSW (1984b)) and is shown in fig.6.10 .

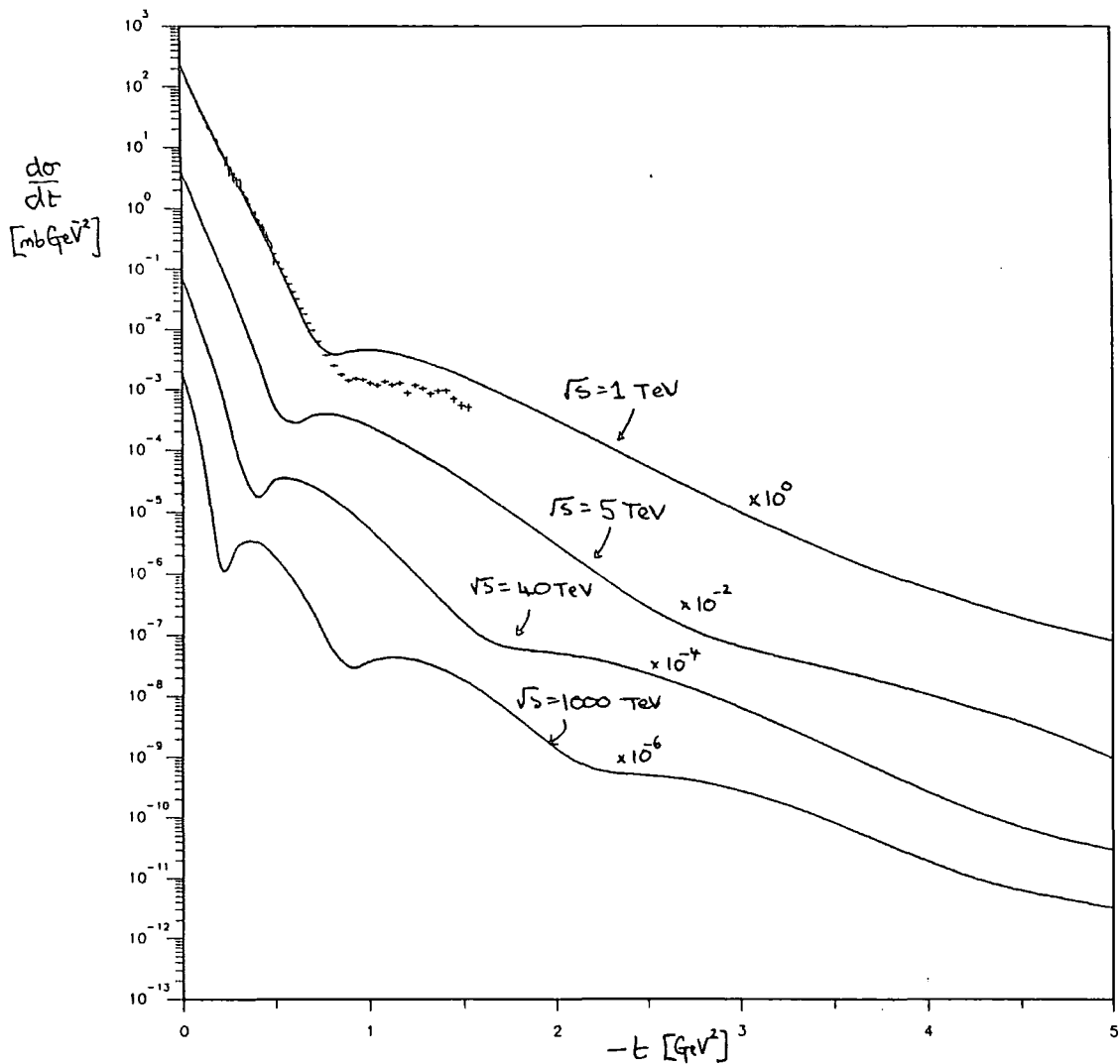


FIG. 6.10 High energy prediction for $\frac{d\sigma}{dt}$ in BSW model at $\sqrt{s} = 1, 5, 40$ and 1000 TeV (with no Reggeon contribution and compared with data at $\sqrt{s} = 546$ GeV).

6.7. The Reggeon Contribution.

To fit the low energy pp and $\bar{p}p$ total cross-sections we need to include the Reggeon exchange contribution to the scattering amplitude. This has both an even and an odd signature part and the odd part gives rise to the difference in the pp and $\bar{p}p$ total cross-sections, $\Delta\sigma = \sigma_T(pp) - \sigma_T(\bar{p}p)$, seen at low energies. As we observed in §4, this difference is well described by ω Reggeon exchange with trajectory intercept $\frac{1}{2}$. Here however, we are adding the Reggeon contribution to the opacity, equation (6.1.2), so that the effects of multiple exchanges involving Reggeons are also included. The total effect of the Reggeons is therefore different from that of the Regge pole we start with, and so to give the right total contribution the input Reggeons must have different trajectories from those used in §4. The additional terms tend to increase the effective shrinkage so that the slope α'_R of our input Regge trajectory must be smaller than normal just as we found for the Pomeron contribution. The effect on the intercept of the Regge trajectory is smaller because for $\sqrt{s} > 10$ GeV the dominant higher term corrections to single Reggeon exchange are those involving multiple Pomeron/single Reggeon exchange i.e $R + R \otimes P + R \otimes P \otimes P + \dots$; and their trajectory has the same intercept as single Reggeon exchange because the effective Pomeron trajectory is close to unity in this energy region, corresponding to a constant contribution to σ_T .

The form used for $S_0(s)$ in equation (6.1.3) means that the total Pomeron contribution to σ_T rises again for $\sqrt{s} < 6$ GeV because of the logarithm in the denominator (see fig.6.11). This is just an artefact of the parametrization which is meant to hold at asymptotic energies and indicates that we are extending the result to a region where it is not valid. However, we can hope that the important features of the model will not be affected by ignoring low energy corrections to the asymptotic form of the Pomeron contribution.

Since the Reggeon parameter values corresponding to the latest Pomeron parameters (6.1.11) in this model have not been given explicitly in BSW (1984a) we have fitted them to the $\sigma_T(pp)$ and $\sigma_T(\bar{p}p)$ data from §2.2 using the parameter values from BSW (1979) as a starting point. We have kept the Reggeon trajectory slope, α'_R , fixed since it is not well determined by fitting σ_T and mainly effects the amount of shrinkage observed. The fit is not much improved by allowing α'_R to vary anyway.

A reasonable fit to σ_T was obtained for $\sqrt{s} > 7$ GeV consistent with BSW (1984a). The values obtained are given in (6.1.11). The low value for the intercept, $\alpha_R(0) = 0.308 \text{ GeV}^{-2}$, is caused by the shape of the Pomeron contribution which determines the form the even part of the Reggeon contribution must have. The very low energy fit is not very good and this seems to be a general feature of eikonalizing the Reggeons. At very low energies the two Reggeon exchange terms become significant and the even and odd signature parts do not cancel as they do for single Reggeon exchange in pp scattering. Their effect can be seen in fig.6.12 showing $\Delta\sigma$ against $\log \sqrt{s}$, where for $\sqrt{s} > 10$ GeV the model gives a straight line corresponding to the $s^{\alpha_R(0)-1}$ power behaviour from the $R+R\otimes P+\dots$ terms but for $\sqrt{s} < 10$ GeV the power behaviour is modified by these $R\otimes R$ terms. The magnitudes of successive multi-Pomeron/Reggeon terms are down on single Reggeon exchange by about a factor of $3\times$ for each Pomeron.

The low value for the Reggeon intercept is reflected in the slightly too steep energy dependence of the predicted value for $\Delta\sigma$ in fig.6.12 compared with the data. The data is consistent with $\alpha_R(0) = \frac{1}{2}$ down to $\sqrt{s} < 4$ GeV indicating that single ω exchange is the dominant odd signature contribution to the amplitude down to very low energies. By allowing the f and ω trajectories different intercepts, a better fit to $\Delta\sigma$ for $\sqrt{s} > 10$ GeV could be obtained but the bad very low energy behaviour is unavoidable.

The prediction for ρ with these parameters is shown in fig.6.13 and both are in fair agreement with the data. The contribution to ρ from just Pomeron exchanges is also shown.

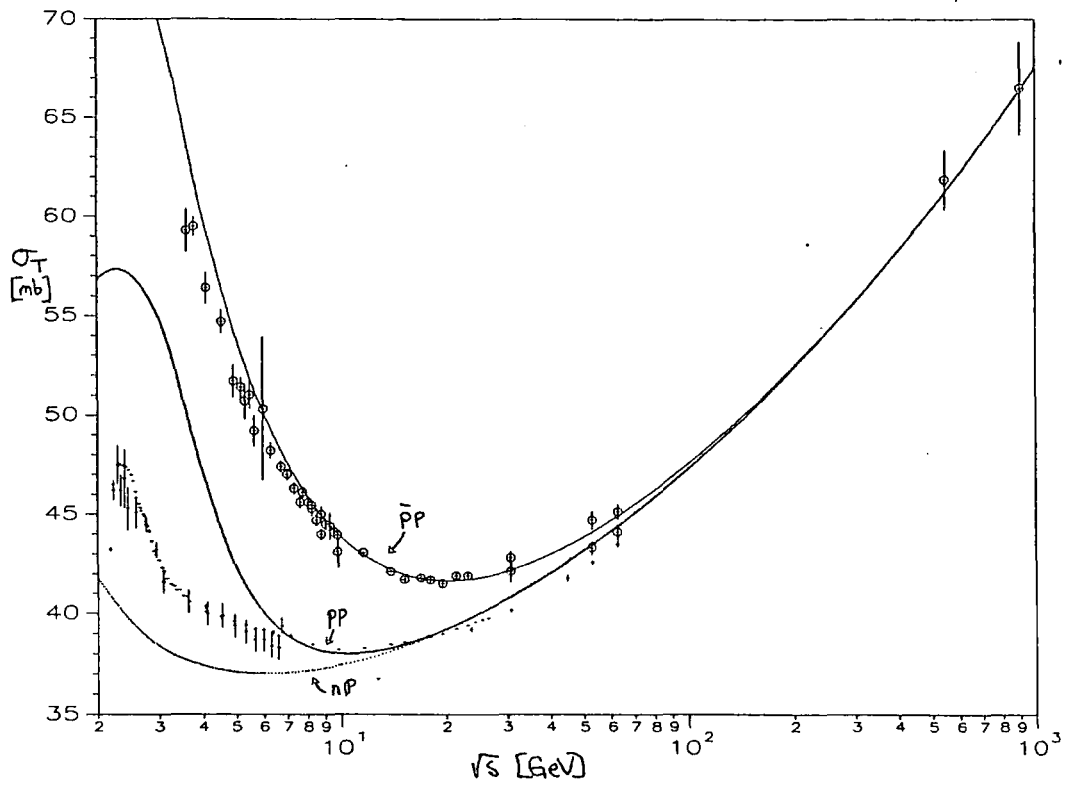


FIG. 6.11 Fit to σ_T in BSW model compared with pp and $\bar{p}p$ data. Dotted line is multiple Pomeron contribution.

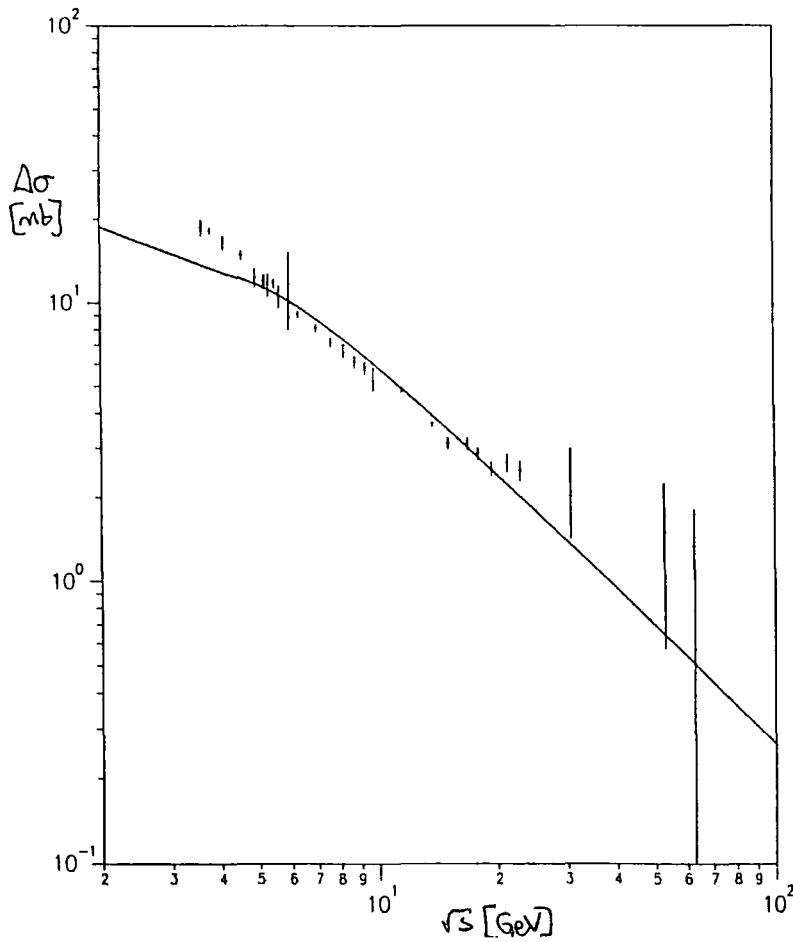


FIG. 6.12 Comparison of BSW model prediction with $\Delta\sigma$ data.

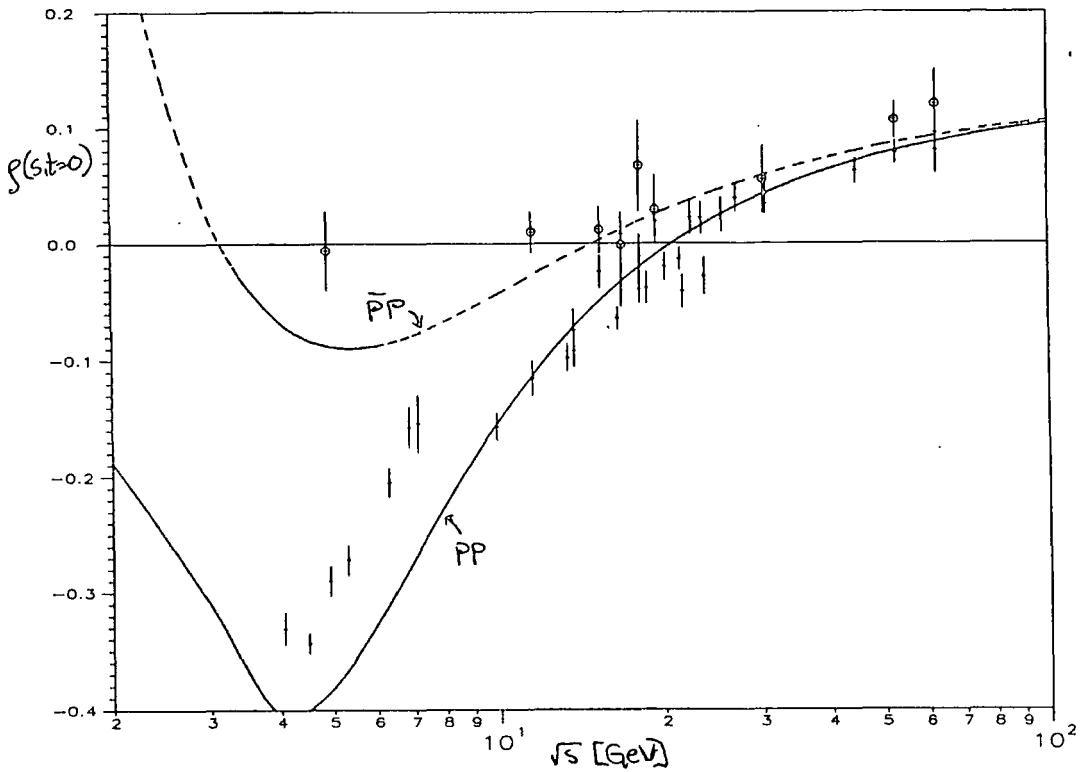


FIG. 6.13 Comparison of BSW model prediction with ρ data.

6.8. $\frac{d\sigma}{dt}$ with Reggeon Contribution Included.

As noted in the previous section, for $\sqrt{s} > 10$ GeV the main Reggeon contribution is given by $R + R \otimes P + \dots$ where the magnitude at $t = 0$ decreases by a factor of about three for each Pomeron exchange included. The successive terms have a flatter and flatter t -dependence and also do not shrink with energy as the pole term does since the $R \otimes P^n$ cuts are fixed (because the Pomeron pole is fixed). So they become relatively more important at large $|t|$ and higher s . In the dip region at $\sqrt{s} = 53$ GeV the single Reggeon exchange term has shrunk out of sight but the $R \otimes P$ term still has an important effect. It is the contribution of the $f \otimes P$ term which deepens the shallow dip given by the Pomeron exchange contributions to give agreement with the dip in the ISR data. The effect of including the Reggeons is to decrease the magnitude of the real part of the amplitude in the dip region sufficiently to give a reasonable dip. It has very little effect on the imaginary part of the amplitude.

At $\sqrt{s} = 546$ GeV the $f \otimes P$ term is too small to have any noticeable affect. So we just get a shallow dip from the Pomeron contribution alone, as in fig.6.8 . Extrapolating the fit through the ISR energy region (see fig.6.14), we see that the dip deepens between $\sqrt{s} = 23.5$ and 30.7 GeV and then fills in again as the energy increases and as the data requires but that the energy dependence of the height of the 2^{nd} maximum makes the fit fall seriously below the data at $\sqrt{s} = 23.5$ GeV. It was this energy dependence that allowed the fit to the collider shoulder. The odd signature Reggeon contribution produces a significant difference between pp and $\bar{p}p$ scattering only at the lowest ISR energy $\sqrt{s} = 23.5$ GeV and no observable difference at $\sqrt{s} = 53$ GeV.

At lower energies, as we saw in §2.5, the dip in the data fills in again in pp scattering but remains in $\bar{p}p$ scattering. This model predicts the filling in of the dip at low energy in pp scattering and allows a good description of the low energy $\frac{d\sigma}{dt}(pp)$ data as was obtained in BSW (1979). However, the odd signature contribution produces dips in the wrong place in $\bar{p}p$ scattering at low energy (fig.6.15). It is not clear whether the parametrization of the residues of the Reggeons can be adjusted to control this problem. Their magnitude at $t = 0$ is more or less fixed by fitting the total cross-section and the effective trajectories of the total Reggeon contributions should have a slope of about unity to agree with the effective shrinkage observed in processes where quantum numbers are exchanged and with the trajectories obtained from the particle masses. The question is whether the t -dependence of the residues of the input Reggeons can be varied to give the total Reggeon contribution the right magnitude and phase to fit $\frac{d\sigma}{dt}(pp)$ and $\frac{d\sigma}{dt}(\bar{p}p)$ whilst satisfying the above constraints. We shall investigate this in a slightly different context in the next chapter. At very low energies, $p_{lab} = 10$ GeV/c, the model does give a cross-over zero effect through cancellation of the ω and $\omega \otimes P$ cut (as in the absorption model), but needs further adjustment to agree with the pp and $\bar{p}p$ data.

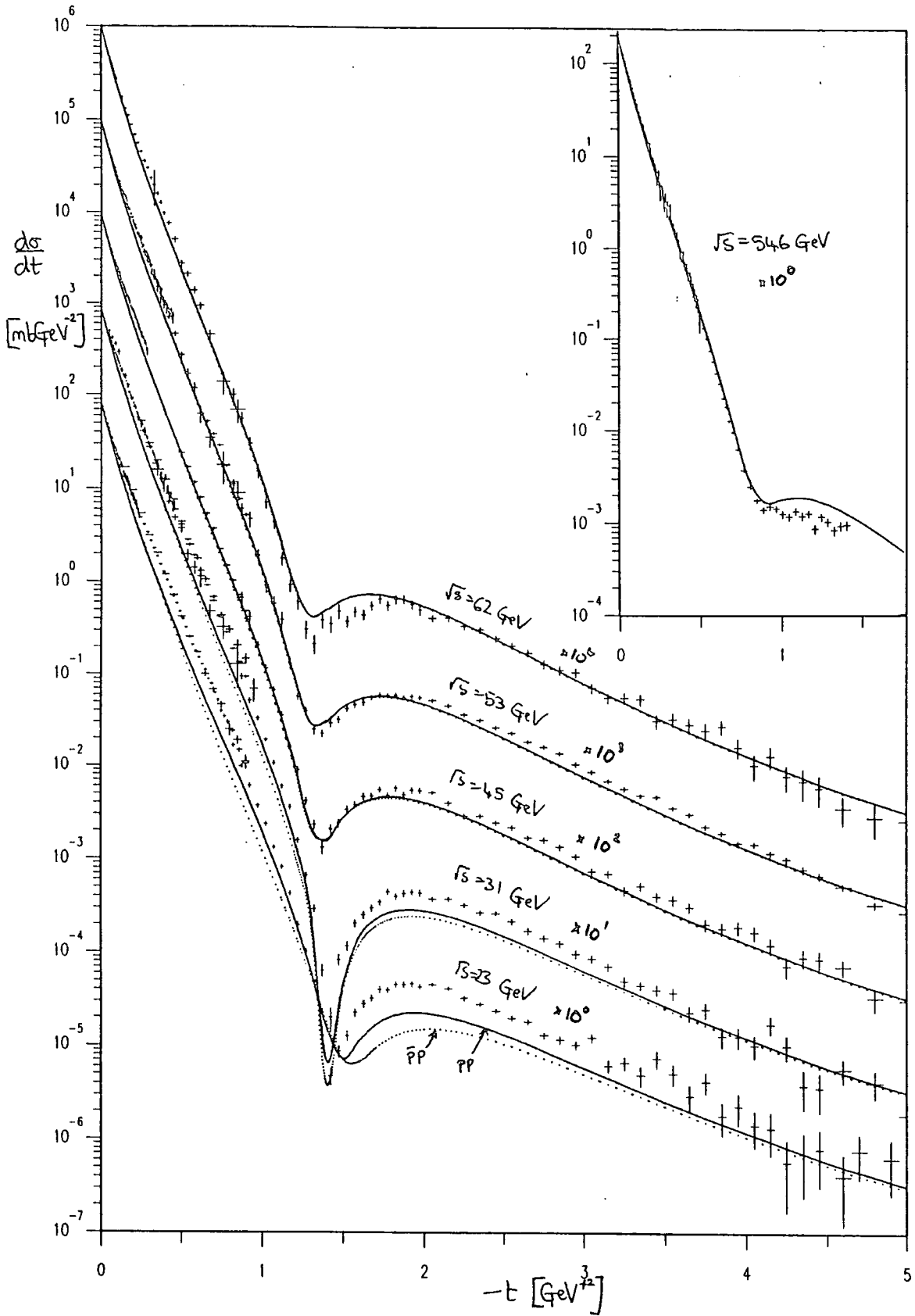


FIG. 6.14 Fit to $\frac{d\sigma}{dt}$ in the BSW model compared with data for $\sqrt{s} = 23.5, 30.7, 44.7, 53, 62.5$ and 546 GeV (dotted line is for $\bar{p}p$).

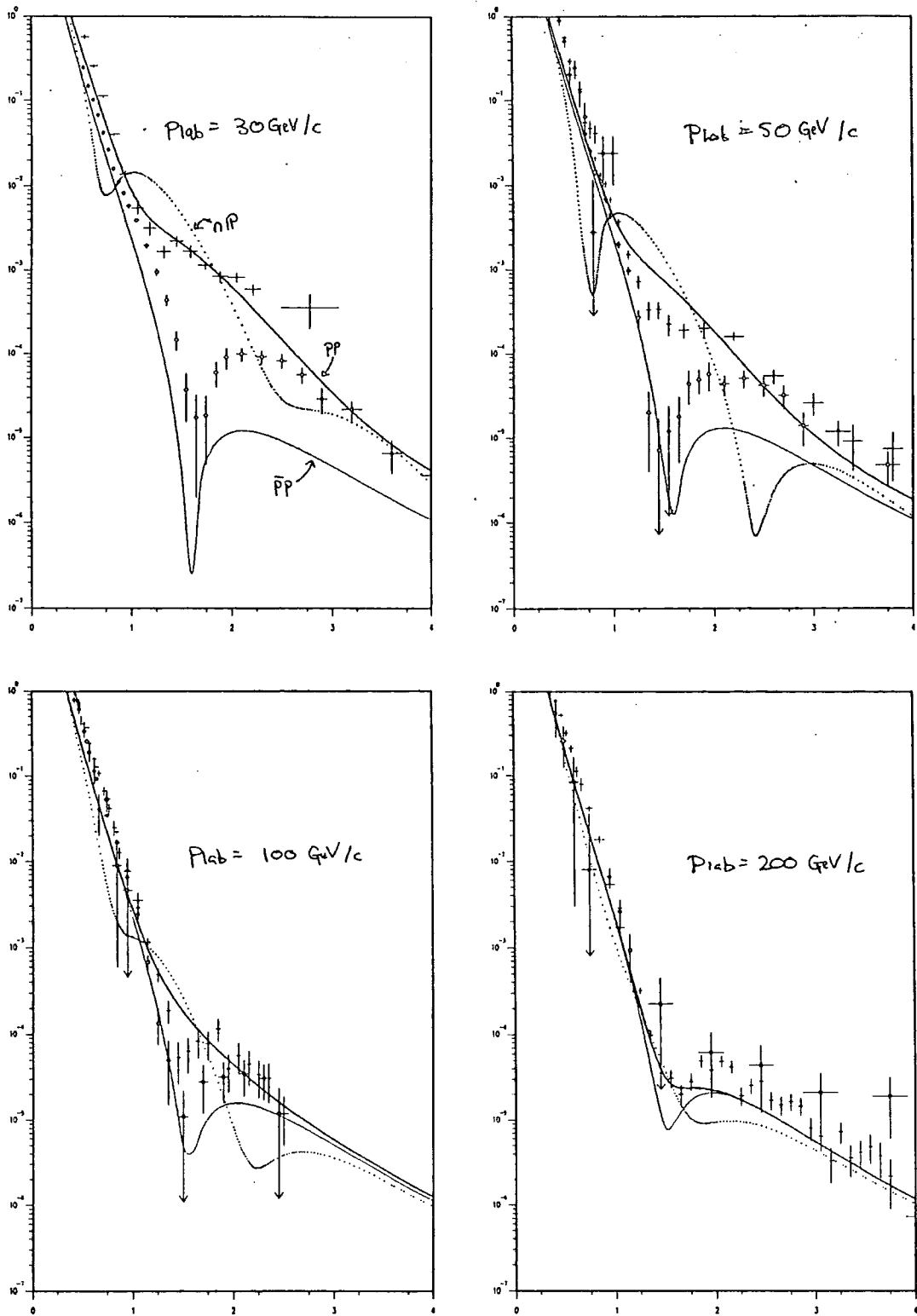


FIG. 6.15 Low energy prediction of the BSW model for $\frac{d\sigma}{dt}$ (thick line is pp prediction, dotted line is for $\bar{p}p$, thin line is without Reggeon contribution).

6.9. Conclusions

We have found that though this model is able to describe reasonably well the rapid growth of the differential cross-section in the dip region from the ISR to the Collider, this energy dependence gives problems at the low energy range of the ISR. The fact

that the model needs $R \otimes P$ cuts to still be significant at the highest ISR energies in order to reproduce the dip in the ISR data means that the cuts will be very important at low energies, even dominating for $|t| > 1 \text{ GeV}^2$, and so it has not been possible to fit the low energy pp and $\bar{p}p$ data. It also means that the input Reggeon trajectory must be flatter than expected from the particle masses. Producing the $R \otimes P$ cuts by adding a Reggeon contribution to the opacity in equation (6.1.2), also produces $R \otimes R$ cuts which disrupt the low energy behaviour of σ_T .

As noted in §3.6, the planar diagrams in the eikonal series corresponding to n -ladder exchanges do not contribute to the leading energy behaviour of the n -Pomeron cut but give non-leading corrections to single Pomeron exchange and other cuts, so that part of the eikonal series gives a re-summation of Pomeron exchange. Only the parts with couplings nested give contributions to the leading behaviour of the n -Pomeron cut. Similarly part of the $R \otimes P^n$ terms in the eikonal series re-sums the Reggeon exchanges and part gives contributions to the Regge-Pomeron cut terms. So perhaps it is acceptable that the input Regge trajectories do not agree with the trajectories from the particle masses, since the physical Reggeons include these corrections, and also that we should not include $R \otimes R$ exchanges in the sum. For similar reasons, perhaps we should not be too concerned that the input Pomeron term does not factorize (6.1.5), since the physical Pomeron exchange also has these corrections.

However, because the Pomeron doesn't factorize we lose the simple physical picture of eikonalization in terms of Glauber scattering, with the proton having some energy independent matter distribution represented by the e-m form factor, and the growth of the total cross-section with energy by the increasing strength and range of the exchanged Pomeron. So that we have no good reason for using the form factor parametrization for the residue of the Pomeron in (6.1.6).

In view of this and the problems we encountered with $S_0(s)$ in (6.1.3) the motivation for using the above form for the Pomeron is not very strong, especially not at current energies. We would prefer a phenomenological description of the input Pomeron as a Regge pole since as we have seen in §4 the forward diffraction peak shows features of Regge behaviour such as shrinkage and is well described by (4.4.1). This is the subject of the next chapter.

The Reggeon-Eikonal Model

7.1. Introduction

In the previous chapter we saw how the BSW model allowed us to satisfy unitarity and the Froissart bound with a Pomeron amplitude which grew with energy like s^{1+c} by using it as the Born term in an eikonal series. This gave a reasonable fit to the high energy data. However, the model did not treat the Pomeron as a Regge pole but as a fixed pole, with a non-factorizable residue and its treatment of the low energy behaviour of $\frac{d\sigma}{dt}(\bar{p}p)$ was unsatisfactory. In this chapter we examine whether a Regge pole input to the eikonal series can make any improvement.

In §4 we used a model in which single Pomeron exchange dominated the amplitude and this gave a good account of the rise of the total cross-section with energy and the shrinkage of the small $|t|$ differential cross-section. Single Pomeron exchange should still dominate the amplitude at small enough $|t|$ at current energies in the Reggeon-Eikonal model and the phenomenological description of the Pomeron used previously, which has the correct Regge phase and small trajectory slope, should give a good fit to the data with some changes to the parameters. The multiple exchange corrections, which ensure that the Froissart bound and unitarity are satisfied at high energies, should dominate at larger $|t|$. Field theory calculations show that multiple exchanges of Reggeons with nested couplings should eikonalize. Since the Regge pole is a moving singularity¹ in the j -plane which obeys the phase-energy relation we can avoid some of the theoretical problems we had with the input to the eikonal series in the BSW model (§6.1).

The idea that we should use a Reggeon as the first term in an eikonal series to generate multiple scattering corrections dates back to Arnold (1965). The model of Chiu and Finkelstein (1968) used this idea with the Pomeron trajectory fixed at $\alpha_P(t) = 1$, whilst Frautschi and Margolis (1968) used a linear t -dependent trajectory passing through one at $t = 0$ and found that the data then available were compatible with $\alpha'_P = 1$. Later, the idea was explored by Collins et al (1974a) with a Pomeron intercept greater than one and they found the ISR data to be reasonably well fitted with $\alpha'_P = 0$ out to $|t| = 3 \text{ GeV}^2$ but that the fit fell below the data for larger $|t|$. The Chou, Yang model,

with $\alpha_P(t) = 1$, also falls below the data beyond the 2^{nd} maximum and gives a 2^{nd} dip around $|t| = 4 \text{ GeV}^2$. The fall off at large $|t|$ predicted by these models is inconsistent with the data from Nagy (1979) which shows that beyond $|t| = 2 \text{ GeV}^2$ the data is to a good approximation given by a simple exponential behaviour with small slope, $\frac{d\sigma}{dt} \simeq \text{constant} \times e^{2t}$, and no further structure. As noted in Sukhatme (1977), the energy independence of the large $|t|$ data shows that for an even signature amplitude the real part of the amplitude must be small (from dispersion relations).

To the extent that the parametrization used in the BSW model gives the impact parameter decomposition of the data we should expect to obtain substantially the same results as in the previous chapter. However, it is not clear what the effect of allowing some t -dependence in the phase of the Pomeron will be and how much freedom there is in obtaining $A(s, b)$ from the differential cross-section data using (3.2.11).

Using the parametrization of the Pomeron in equation (4.4.1) as input to the eikonal series we get

$$A^P(s, t) = -G_P e^{c_P t} (e^{-i\frac{\pi}{2}s})^{\alpha_P(0)} \quad \text{where } c_P = a_P + \alpha'_P \left(\ln s - i\frac{\pi}{2} \right) \quad (7.1.1)$$

which, using equation (3.2.11), gives for the eikonal phase :

$$\chi_P(s, b) = -\frac{G_P}{8\pi s} (e^{-i\frac{\pi}{2}s})^{\alpha_P(0)} \frac{e^{-\frac{b^2}{4c_P}}}{c_P} \quad (7.1.2)$$

This is then used to generate the eikonal series through $A(s, b) = \frac{e^{i\chi_P} - 1}{2i}$, which ensures that unitarity is satisfied. Expanding the exponential and using equation (3.2.10) gives

$$A(s, t) = \frac{16\pi s}{2i} \sum_{n=1}^{\infty} \frac{1}{n!} \left(\frac{G_P (e^{-i\frac{\pi}{2}s})^{\alpha_P(0)}}{8\pi i s c_P} \right)^n \frac{c_P}{n} e^{\frac{c_P}{n} t} \quad (7.1.3)$$

The n^{th} term can be identified with the n -Pomeron exchange contribution and from (3.4.16) it can be seen that in the j -plane this gives a discontinuity of the form $(j - \alpha_n(t))^{n-2}$, thus representing a Regge cut with a branch point at $\alpha_n(t) = 1 + n\epsilon + \frac{\alpha'_P t}{n}$.

As we saw in the previous chapter higher order exchanges give a significant contribution to the amplitude, so that the Born term is not a good approximation. From the above we see that the n -Pomeron exchange term behaves like

$$A^{nP}(s, t) \sim s^{n\epsilon} e^{\frac{c_P}{n} t} \quad (7.1.4)$$

where $\epsilon = \alpha_P(0) - 1$ is small and positive. Thus at fixed t the energy dependence of the n^{th} term is given by $s^{n\epsilon}$ and so higher order terms become more important as the energy increases. At fixed energy, higher terms decrease more slowly with increasing $|t|$ and so become relatively more important at large $|t|$. The phase of the amplitude in (7.1.4) is controlled by ϵ and α'_P . These are both small so the Pomeron term is almost pure imaginary and the eikonal series consists of a sum of imaginary terms with alternating sign and increasingly flat t -dependence. This results in a sequence of dips in the differential cross-section.

The single exponential form for the Pomeron residue in (7.1.1) does not possess enough freedom to give a good fit to the differential cross-section. We choose to parametrize the residue by a sum of exponentials as

$$\begin{aligned} G_P(t) &= G_P e^{a_P t} (1 - x_1(1 - e^{a_1 t}) - x_2(1 - e^{a_2 t}) - \dots) \\ &= G_P \sum_{j=1}^N x_j e^{c_j t} \end{aligned} \quad (7.1.5)$$

where we used up to six exponential terms. The Bessel transforms can then still be calculated analytically using equations (A.4) and (A.5) term by term in the series. As we saw in the previous chapter, calculating these integrals numerically takes too much computer time to allow us to fit data. We did however use numerical integration to compute the high energy behaviour and to check the accuracy of the series expansion. We restrict the a_i to be less than a_P so that the amplitude cannot grow with energy at large $|t|$, and restrict the x_i to be positive so that the Pomeron amplitude cannot change sign.

We separated the s - and t -dependence of the amplitude at $\sqrt{s} = 53$ GeV by writing the parametrization in such a way that at this energy it is not much affected by variation of the Pomeron trajectory. By rewriting the Pomeron amplitude in (7.1.1) as

$$A^P(s, t) = is G_P(t) \left(e^{-i\frac{\pi}{2}} \frac{s}{53^2} \right)^\epsilon e^{\alpha'_P (\ln \frac{s}{53^2} - i\frac{\pi}{2}) t} \quad (7.1.6)$$

we find ϵ only affects the phase, not the magnitude, of A^P at $\sqrt{s} = 53$ GeV and α'_P only affects the imaginary part of the exponential slope.

Then we find

$$A(s, t) = 8\pi s \sum_{n=1}^{\infty} \frac{(-\Gamma)^n}{2in!} \sum_{k=0}^{N-1} \sum_{i_k=1}^{\{n - \sum_{m=1}^{k-1} i_m\}} \frac{2n! e^{\frac{t}{c}}}{c \prod_{m=1}^N i_m!} \quad (7.1.7)$$

where $i_m = n - i_1 - i_2 - \dots - i_{N-1}$ and $c = \frac{\sum_{m=1}^{N-1} \prod_{j \neq m}^N c_j i_m}{\prod_{j=1}^N c_j}$. The free parameters in Pomeron contribution are then : $\alpha_P(0), \alpha'_P, G_P, \{x_i, a_i, i = 1, 6\}$.

7.2. Fitting $\frac{d\sigma}{dt}$ and σ_T .

We wish first of all to see if we can fit the change in the differential cross-section from the ISR to the Collider and then to extrapolate the model to both higher and lower energies. It is not so easy to separate the fits to σ_T and $\frac{d\sigma}{dt}$ as in §4, where the cut contribution at $t = 0$ was small, because in this model the cut contributions are significant even at $t = 0$. All the parameters of (7.1.3) are correlated and have an effect on both σ_T and $\frac{d\sigma}{dt}$. However, it is approximately true that changing the Pomeron term at some value of t will not significantly affect the n-Pomeron exchange terms until larger $|t|$ and so it is possible to alter the large $|t|$ parametrization of the Pomeron residue without affecting the small $|t|$ fit very much.

As noted above, we have written the parametrization in equation (7.1.6) in such a way that α'_P and $\alpha_P(0)$ have little effect on $\frac{d\sigma}{dt}$ at $\sqrt{s} = 53$ GeV (at small $|t|$ at least) and we expect that the Reggeons should make only about a 10% contribution to small $|t|$ $\frac{d\sigma}{dt}$ at this energy (as in §4). Thus we should be able approximately to tie down the parameters of the Pomeron residue in (7.1.5) : G_P, x_i, a_i ; by fitting small $|t|$ $\frac{d\sigma}{dt}$ at $\sqrt{s} = 53$ GeV. We chose to fit at $\sqrt{s} = 53$ GeV because the $\frac{d\sigma}{dt}$ data is most accurate at this energy; the higher order terms in the eikonal series are not too big so the series converges quite rapidly, and the Reggeon contribution is small. Provided the slope of the Pomeron trajectory, α'_P , has only a small effect on σ_T we can then determine the Pomeron intercept, $\alpha_P(0)$, and the Reggeon parameters by fitting σ_T . This leaves α'_P to be determined by fitting small $|t|$ $\frac{d\sigma}{dt}$ at the Collider. The large $|t|$ structure of $\frac{d\sigma}{dt}$ can then be fitted at $\sqrt{s} = 53$ GeV, without affecting the small $|t|$ fit, by varying the Pomeron residue at large $|t|$. The s - and t -dependence of the amplitude are then approximately determined and we can extrapolate the fit to higher and lower energies.

In fitting the small $|t|$ $\frac{d\sigma}{dt}$ data at $\sqrt{s} = 53$ GeV, we initially fixed $\alpha_P(0)$ in the Pomeron amplitude (7.1.6) at the value in obtained in §4: $\alpha_P(0) = 1.094$, and set the slope of the trajectory to zero. The phase of the Pomeron is then independent of t and the parametrization similar to that used in the BSW model and in Collins *et al* (1974a). In these fits to small $|t|$ we used the data at $\sqrt{s} = 53$ GeV from Baksay (1978) and

Breakstone (1984) (see §2.5). It can be seen from fig.6.9 in the previous chapter, that using five terms in the series expansion of (7.1.3) gives sufficient accuracy for $|t| < 1 \text{ GeV}^2$. At $|t| = 1 \text{ GeV}^2$ calculating with five terms gives an accuracy of $\approx 10\%$ in $\frac{d\sigma}{dt}$ (see fig.7.2) and is sufficiently fast to allow us to fit, though it becomes prohibitively expensive in terms of computer time to allow more than four parameters to vary. Varying four parameters and using above data it takes about 8 minutes cpu time on the IBM 3081 for a fit to converge.

Parametrizing the Pomeron residue in equation (7.1.5) by only a single exponential and fitting the forward diffraction peak for $0 < |t| < 0.1 \text{ GeV}^2$, the model produces a dip at $|t| \simeq 0.6 \text{ GeV}^2$ which does not appear in the data until $|t| \simeq 1.35 \text{ GeV}^2$. Including in the fit the data out to $|t| = 0.85 \text{ GeV}^2$ from Breakstone (1984) (see §2.5) still produces a dip too close in at $|t| \simeq 0.9 \text{ GeV}^2$ and fails to get a good fit to very small $|t| < 0.1 \text{ GeV}^2$. Using two terms in the residue we find a good fit out to $|t| = 0.85 \text{ GeV}^2$. Similar results were found in Collins *et al* (1974a). We repeated these fits for a non-zero value of α'_P : $\alpha'_P = 0.28 \text{ GeV}^{-2}$ from table 4.7. We found that it now took four terms in the Pomeron residue to get rid of the premature dip and give a good fit to the data for $|t| \leq 0.85 \text{ GeV}^2$

In order to fit the σ_T data, we must include the Reggeon contribution to the amplitude which we initially choose to add to the multiple Pomeron exchange contribution as in (4.2.1) rather than to eikonalize the Reggeon exchanges along with the Pomeron as in (6.1.2). We use the parametrization of the Reggeons from equation (4.4.5) and the parameter values from table 4.4, but allow the f Reggeon coupling strength, β_f , and its trajectory intercept, $\alpha_f(0)$, to vary in order to fit σ_T with the new Pomeron contribution. We fitted the $\sigma_T(pp)$ data from §2.2 and forced a fit to the collider data as in §4.2, varying the parameters $\alpha_P(0)$, $\alpha_f(0)$ and β_f . This gave a good fit to σ_T and approximately fixed these parameters. We then fitted small $|t| \frac{d\sigma}{dt}$, allowing α'_P to vary and using the data at $\sqrt{s} = 53 \text{ GeV}$ for $|t| \leq 0.85 \text{ GeV}^2$ and at $\sqrt{s} = 546 \text{ GeV}$ for $|t| \leq 0.7 \text{ GeV}^2$ (varying four terms takes 15 minutes cpu time). However, we find that to some extent the parameters are still correlated; the shape of the Pomeron residue and the value of the intercept of the Pomeron trajectory affect how much shrinkage is seen, the trajectory slope and the shape of the residue affect σ_T and the Reggeons affect the small $|t|$ differential cross-section. An iterative approach is needed to obtain a good fit. First fitting σ_T and very small $|t| < 0.3 \text{ GeV}^2$, and then extending this

to larger $|t|$ until we found a reasonable fit to both $\frac{d\sigma}{dt}$ for $|t| \leq 0.7 \text{ GeV}^2$ at the two energies and to σ_T over the whole energy range. The fit (7a) to σ_T obtained with the parameter values of table 7.1 is shown in fig.7.1 below. The fit to small $|t|$ $\frac{d\sigma}{dt}$ is shown in fig.7.2; the dotted lines correspond to the sum of five terms of the eikonal series and the full lines to the complete series.

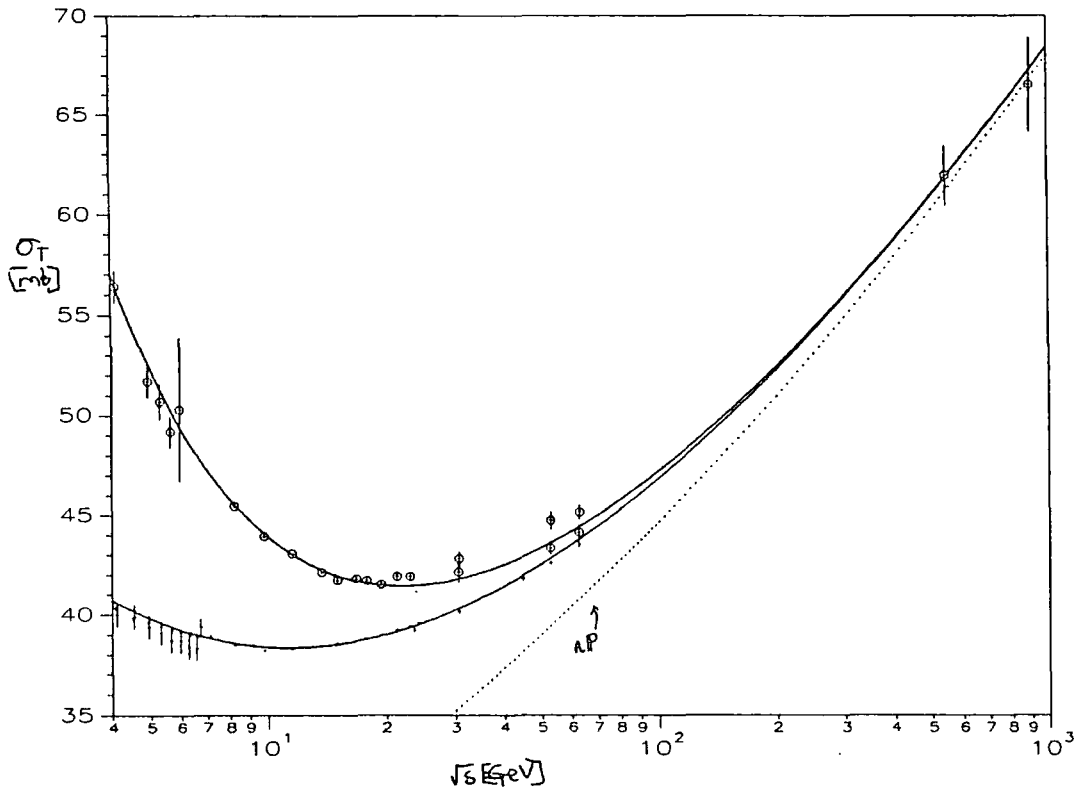


FIG. 7.1 Fit (7a) to σ_T in Reggeon-Eikonal model (dotted line is multiple Pomeron exchange contribution).

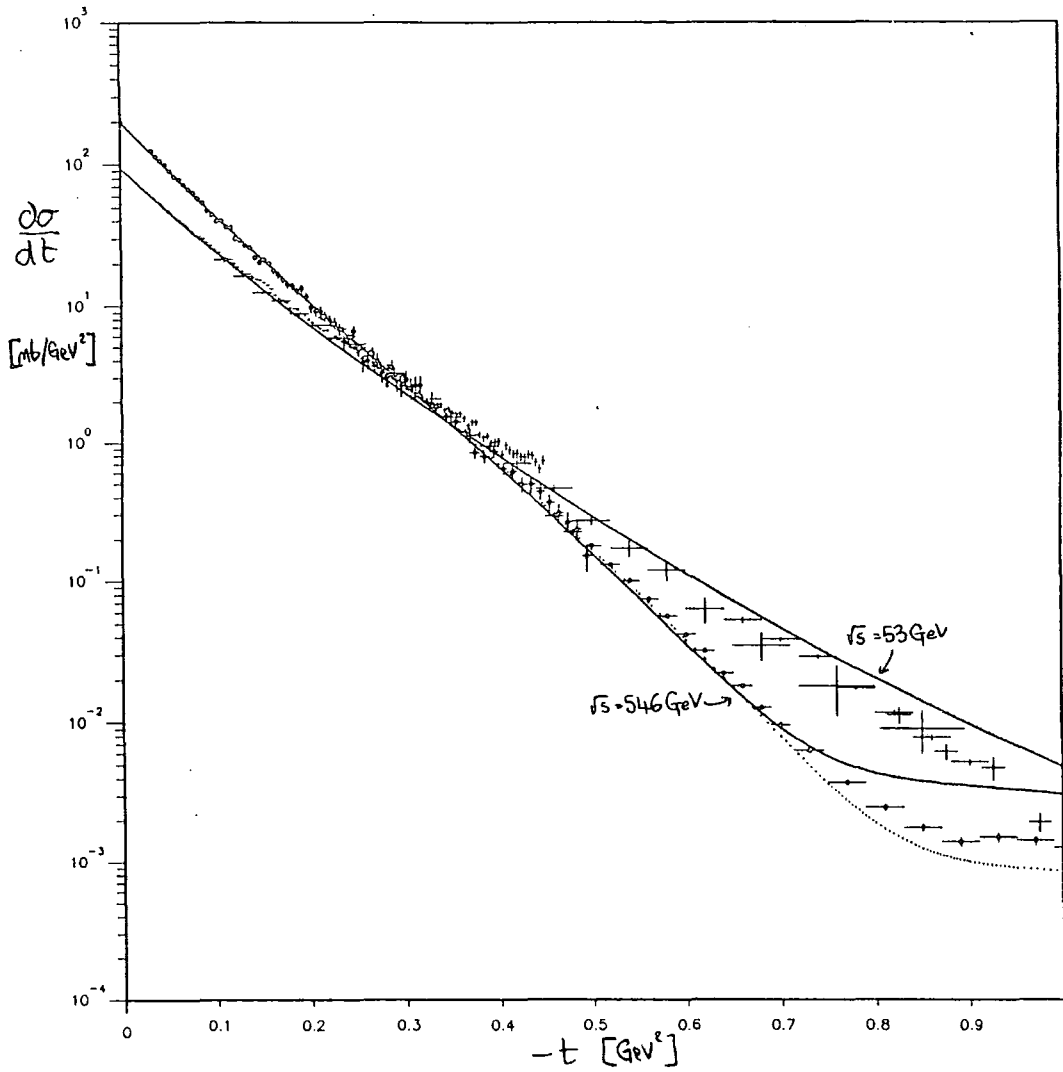


FIG. 7.2 Fit (7a) to $\frac{d\sigma}{dt}$ at $\sqrt{s} = 53$ and 546 GeV in Reggeon-Eikonal model (dotted line is sum of five terms of eikonal series).

$\alpha_P(0)$	1.118	β_f	71.5 mb	x_2	0.0659
α'_P	0.056 GeV^{-2}	$\alpha_f(0)$	0.630	a_2	-3.69 GeV^{-2}
G_P	126.5	x_1	0.236	x_3	0.0780
a_P	5.173 GeV^{-2}	a_1	6.12 GeV^{-2}	a_3	-3.071 GeV^{-2}

TABLE 7.1 Parameter values of fit (7a) used in (7.1.7).

We tested the effect on σ_T of varying α'_P and $\alpha_P(0)$. By construction, α'_P in (7.1.6)

has little effect at $\sqrt{s} = 53$ GeV. Its effect at lower energies is also very small and easily compensated for by small changes in the Reggeon parameters. At the Collider energy, changing α'_p from 0.0 to 0.1 GeV⁻² increases σ_T by 1.6 mb. Changing $\alpha_p(0)$ has a larger effect on σ_T at the Collider. The Pomeron contribution is approximately independent of $\alpha_p(0)$ at $\sqrt{s} = 53$ GeV. Increasing $\alpha_p(0)$ by 0.02 produces a 4 mb rise at $\sqrt{s} = 546$ GeV. Thus, it is still a good approximation that $\alpha_p(0)$ determines how fast the Pomeron contribution to σ_T rises with energy. The effect of α'_p can produce a change of ≤ 0.01 in $\alpha_p(0)$. If the Pomeron were responsible for all the increase in σ_T between the ISR and the Collider then we would have $\alpha_p(0) \approx 1.10$, so that this is the smallest value of $\alpha_p(0)$ which can reproduce the rise in σ_T (this value can be modified slightly by the dependence of σ_T on α'_p and the small $|t|$ fit).

Equation (7.1.6) implies that the differential cross-section should be more or less independent of α'_p and $\alpha_p(0)$ at $\sqrt{s} = 53$ GeV. Changing α'_p from 0.0 to 0.3 GeV⁻² increases $\frac{d\sigma}{dt}$ at $|t| = 0.5$ GeV² by about 3% and at $|t| = 1.0$ GeV² by about 40%. To a good approximation $\frac{d\sigma}{dt}$ at $\sqrt{s} = 53$ GeV is independent of α'_p for $|t| \leq 0.7$ GeV². Similarly, changing $\alpha_p(0)$ does not affect $\frac{d\sigma}{dt}$ appreciably over this t -range.

The effect of the cuts is to increase the amount the forward peak shrinks between the ISR and the Collider, which is given approximately by $\alpha_{\text{eff}} \approx 0.3$ GeV⁻² (see §2.6). Figure 7.3 shows the effect of varying the slope of the Pomeron trajectory from $\alpha'_p = 0.0 \rightarrow 0.3$ GeV⁻² on the fit to the Collider small $|t|$ data. If α'_p is too large there is too much shrinkage at large $|t|$ at the Collider and the fit falls below the data. At $|t| = 0.5$ GeV² we see that $\alpha'_p = 0.10$ GeV⁻² is probably already too large and produces too much shrinkage. On the other hand the data is quite compatible with $\alpha'_p = 0$ as we found in the previous chapter with the BSW model.

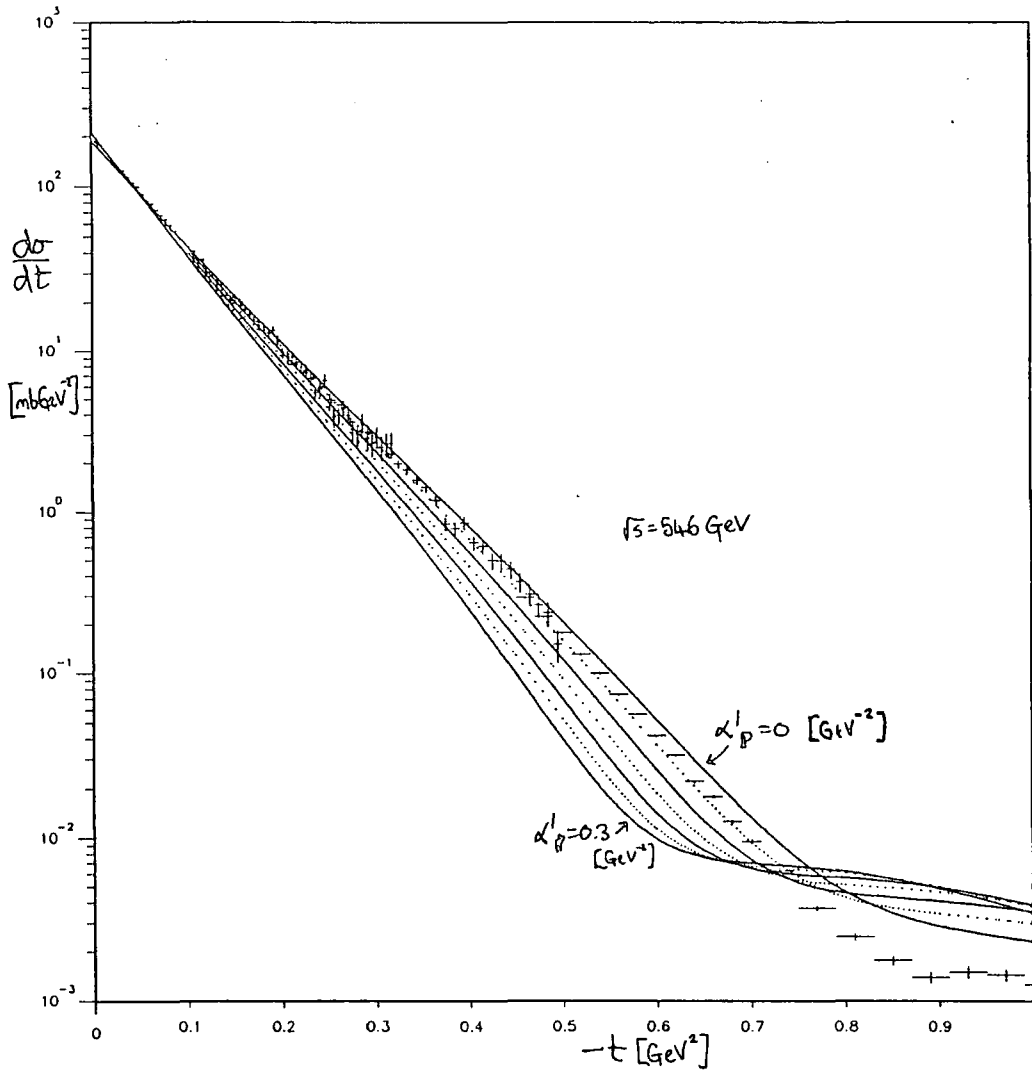


FIG. 7.3 Effect of α'_p on shrinkage of $\frac{d\sigma}{dt}$ at $\sqrt{s} = 546$ GeV for $\alpha'_p = 0.0 \rightarrow 0.3$ GeV $^{-2}$ in steps of 0.05 GeV $^{-2}$.

7

The above argument is dependent on how much the effective shrinkage is affected by $\alpha_p(0)$ and the structure of the residue. Increasing $\alpha_p(0)$ in the above fit produces only a relatively small increase in the observed shrinkage so that results should not be affected much by the change in $\alpha_p(0)$ produced by refitting σ_T for different α'_p . We also expect the structure of the residue to have little effect because it is constrained by the data at $\sqrt{s} = 53$ GeV. However, the only way to evaluate properly these effects is to attempt to fit with different α'_p . Fixing $\alpha'_p = 0.1$ GeV $^{-2}$ and repeating the above fits to small $|t|$ and σ_T we were able to obtain a reasonable fit similar to the above. For $\alpha'_p = 0.15$ GeV $^{-2}$ the fit was below the Collider data for $|t| \geq 0.5$ GeV 2 and gave the maximum value of α'_p compatible with the small $|t|$ data. For $\alpha'_p = 0.2$ GeV 2 the best fit gives a dip at $|t| = 0.6$ GeV 2 and lies below the Collider data for $|t| \geq 0.3$ GeV 2 .

7.3. Fitting the $\frac{d\sigma}{dt}$ data in the dip region and beyond.

Having obtained a good fit to σ_T and to $\frac{d\sigma}{dt}$ for $0 \leq |t| \leq 0.7 \text{ GeV}^2$ we then tried to fit the dip region and large $|t|$ data at $\sqrt{s} = 53 \text{ GeV}$ by varying the parameters which control the large $|t|$ behaviour of the Pomeron residue : x_2, a_2, x_3, a_3 , in equation (7.1.5). With only five terms in the series (7.1.7) leads to quite large inaccuracies for $|t| > 1.1 \text{ GeV}^2$ at $\sqrt{s} = 53 \text{ GeV}$. For $|t| > 2 \text{ GeV}^2$ the result is $\approx 50\%$ lower than that of the complete series and to get good agreement with the full exponential series at large $|t|$ it is necessary to use six terms at $\sqrt{s} = 53 \text{ GeV}$ for $|t| \leq 6 \text{ GeV}^2$ (see fig.7.5) and seven terms at $\sqrt{s} = 546 \text{ GeV}$. Using more terms in the series does mean however that it is not possible to fit so much data as it takes too much computing time (although five terms gives a less accurate result we found it useful to fit with five terms sometimes since the results with the full series are qualitatively the same).

Fitting the data at $\sqrt{s} = 53 \text{ GeV}$ using six terms in the eikonal series we found it impossible to obtain a dip in the differential cross-section. Increasing the number of terms in our parametrization of the Pomeron residue (7.1.5) to six exponential terms gave no improvement (it is necessary then to use only five terms in the series because of the increased computer time involved). The best that can be done is to fit the forward peak as well as possible to as large a value of $|t|$ as possible. This produces a zero crossing in the imaginary part of the full amplitude in the right position at $|t| \approx 1.35 \text{ GeV}^2$, which is filled in by the real part of the amplitude to give a shoulder.

It is not possible to obtain a dip in this model because the real part of the amplitude is too large in the dip region. This results from the large value of $\alpha_P(0)$ necessary to produce the rapid increase of σ_T between the ISR and the Collider. As α'_P increases the height of the shoulder increases so that it is also not possible to obtain a dip by changing α'_P . A smaller value for $\alpha_P(0)$ ($\alpha_P(0) \leq 1.07$) in the above fit can produce a sharp dip rather than a shoulder in the appropriate region.

Previous fits of this type, for example Chou and Yang (1968) with $\alpha_P(0) = 1 \text{ GeV}^{-2}$ and Collins *et al* (1974a) with $\alpha_P(0) = 1.06 \text{ GeV}^{-2}$, were able to obtain a sharp dip because the total cross-section data then available did not indicate so large a value for $\alpha_P(0)$. With $\alpha_P(0) = 1.06 \text{ GeV}^{-2}$ the above fit closely resembles these parametrizations and, as they do, falls below the data for $|t| > 3 \text{ GeV}^2$. It was possible

to obtain a shallow dip in the BSW model (see fig.6.8) because the Pomeron input used did not obey the phase-energy relation. The phase of $S_0(s)$ produced by the $(\ln u)^{c'}$ denominator in equation (6.1.3) corresponds to a Regge pole with intercept $\alpha_P(0) = 1.074 \text{ GeV}^{-2}$, rather than $\alpha_P(0) = 1.146 \text{ GeV}^{-2}$ which is the intercept associated with the s^{1+c} energy dependence used.

Fig.7.4 shows a breakdown of the contributions of the multiple Pomeron exchange terms to the real and imaginary parts of the amplitude. To get a sharp dip the imaginary part of the amplitude must have a zero whilst the real part is small compared to the imaginary part in the immediate vicinity of the zero. In this fit the real part is large and negative in the dip region and so gives a shoulder.

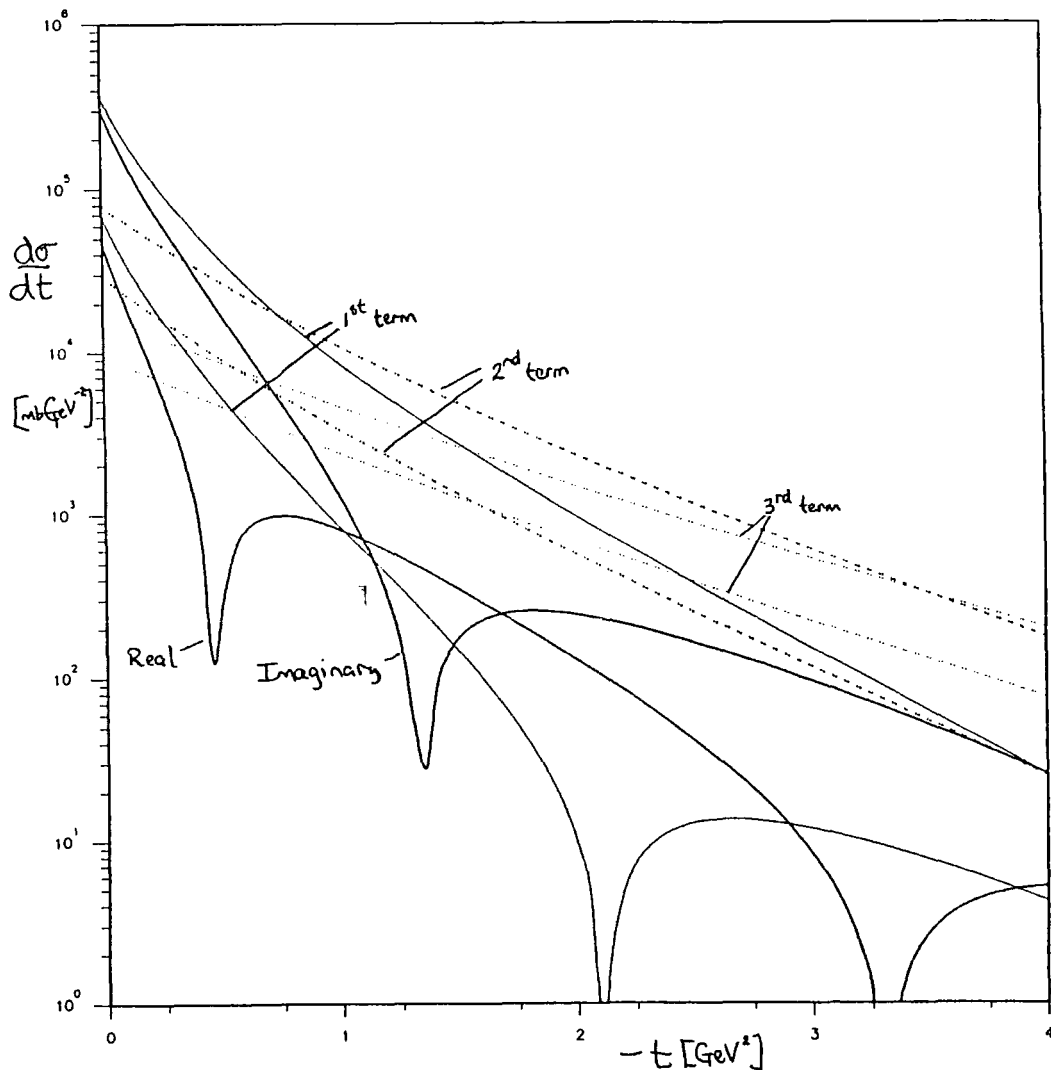


FIG. 7.4 Real and imaginary parts of the full amplitude and the first three terms in the eikonal series.

From equation (7.1.3) we see that Re/Im for the n^{th} term is given approximately by

$$\rho_n(s, t) \simeq \tan \frac{\pi}{2} n \left(\epsilon + \frac{\alpha'_P t}{n^2} \right) \quad (7.3.1)$$

which increases rapidly with increasing ϵ and n , and the importance of α'_P decreases rapidly with increasing n at fixed t . We saw above that as $|t|$ increases the relative importance of higher terms increases so that $\rho(s, t)$ for the full amplitude gets bigger. However, at large s and fixed t , the amplitude becomes pure imaginary so the real parts of the higher terms must cancel at asymptotic energies. If the intercept, $\alpha_P(0)$, in (7.1.1) is close to one the phases of the higher terms are smaller and so the phase of the full amplitude is smaller further out in $|t|$. At small $|t|$ the first term of the eikonal series at $\sqrt{s} = 53$ GeV dominates, whilst the main contribution to the imaginary part of the amplitude for $1 \leq |t| \leq 2$ GeV² comes from the first three terms of the series. At $|t| = 0.8$ GeV² the imaginary parts of the 1st and 2nd terms cancel but the contribution of the 3rd term pushes the zero out to $|t| = 1.35$ GeV². The small $|t|$ dependence of the first term approximately determines the magnitudes of the higher terms in the dip region so that the position of the dip is controlled mainly by the size of the first term. As we noted above, changing the magnitude of the first term does not affect higher terms very much until larger $|t|$. Thus, when first fitting small $|t|$ above, we pushed the dip at $|t| = 0.7$ GeV² out to larger $|t|$ by increasing the pole term at larger $|t|$ by adding flatter terms to the residue.

The main contribution to the real part of the amplitude in the same region comes from the 2nd, 3rd and 4th terms. The real part of the first term has a zero at $|t| \simeq \frac{\epsilon}{\alpha'_P} \approx 2$ GeV². In §4.4, where the model had the diffraction peak dominated by single Pomeron exchange, this energy independent point occurred for $|t| \approx \frac{0.094}{0.28} \approx 0.3$ GeV² and we find in these fits that the real part of the full amplitude has a zero in approximately the same place, as of course it must if it is to account for the energy independence of the data at this point. Fig.7.4 shows that Re/Im for the n^{th} term is increasing with n and that the effect of α'_P is decreasing with n , since the real and imaginary parts of higher n terms are becoming more nearly equal and the phase of terms with $n \geq 2$ changes only slowly with t . The only term that α'_P has a large effect upon is the pole term. Increasing α'_P brings the dip in the real part of the first term in to smaller $|t|$, and since the real part is negative in the dip region this increases the magnitude of the real part and thus the height of the shoulder. So as far as getting a dip is concerned $\alpha'_P = 0$ produces the best results.

So it is not possible to obtain a dip in this model at $\sqrt{s} = 53$ GeV with just multiple Pomeron exchanges. It should be possible to use the same method to produce a dip as the BSW model in §6 i.e adding the Regge-Pomeron cuts generated by including the Reggeon contribution in the eikonal phase, as in (6.1.2). We want the zero in the imaginary part of the amplitude to occur at $|t| = 1.35$ GeV² and expect the real part to be cancelled by the Reggeon contribution, so do not mind producing a large real part from multiple Pomeron exchanges. We want the Reggeon contribution to be as small as possible since, as we saw in §6.7, eikonalizing the Reggeon exchange leads to problems in fitting the low energy differential cross-section data. For this reason we want the magnitude of the Pomeron exchange amplitude to be as small as possible in the dip region, which is produced by making the zero in the imaginary part of the amplitude coincide with the dip position. The Pomeron still controls large $|t|$, so we want to produce a good fit to the large and small $|t|$ data with the Pomeron contribution, and a zero in the imaginary part at the dip position.

Fit (7a) (table 7.1) falls below the data for $|t| > 3$ GeV². We tried to improve this by attaching more weight to the large $|t|$ data and varying the parameters that control the large $|t|$ dependence of the residue : x_2, a_2, x_3, a_3 ; and obtained reasonable fits to the large $|t|$ data for $|t| \leq 5$ GeV² but at the expense of pushing the zero in the imaginary part of the amplitude out to $|t| = 1.6$ GeV² and so increasing the magnitude of the amplitude in the dip region. This fit is shown in figure 7.5 along with the sum of a successively larger number of terms of the eikonal series, which shows that six terms of the series is sufficiently accurate for $|t| \leq 6$ GeV². For $|t| \geq 5$ GeV² the fit still falls below the ISR large $|t|$ data. In these fits we used the complete eikonal series and varied two parameters at a time because of the computer time involved (≈ 20 minutes). Keeping the zero of the imaginary part at $|t| = 1.35$ GeV² by including data at $|t| \approx 1$ GeV² produces a better fit than (7a) for $|t| \leq 1$ GeV² but cannot prevent the predicted cross-section falling below the data for $|t| \geq 3$ GeV² (fit (7b) in table 7.2, curve (b) fig.7.6). Trying to improve the large $|t|$ fit by adding more terms to the residue does not give any better fit. In fact adding a term to the residue with flatter t -dependence at large $|t|$ produces a dip in $\frac{d\sigma}{dt}$ at $|t| = 4.5$ GeV² (see curve (a) fig.7.6).

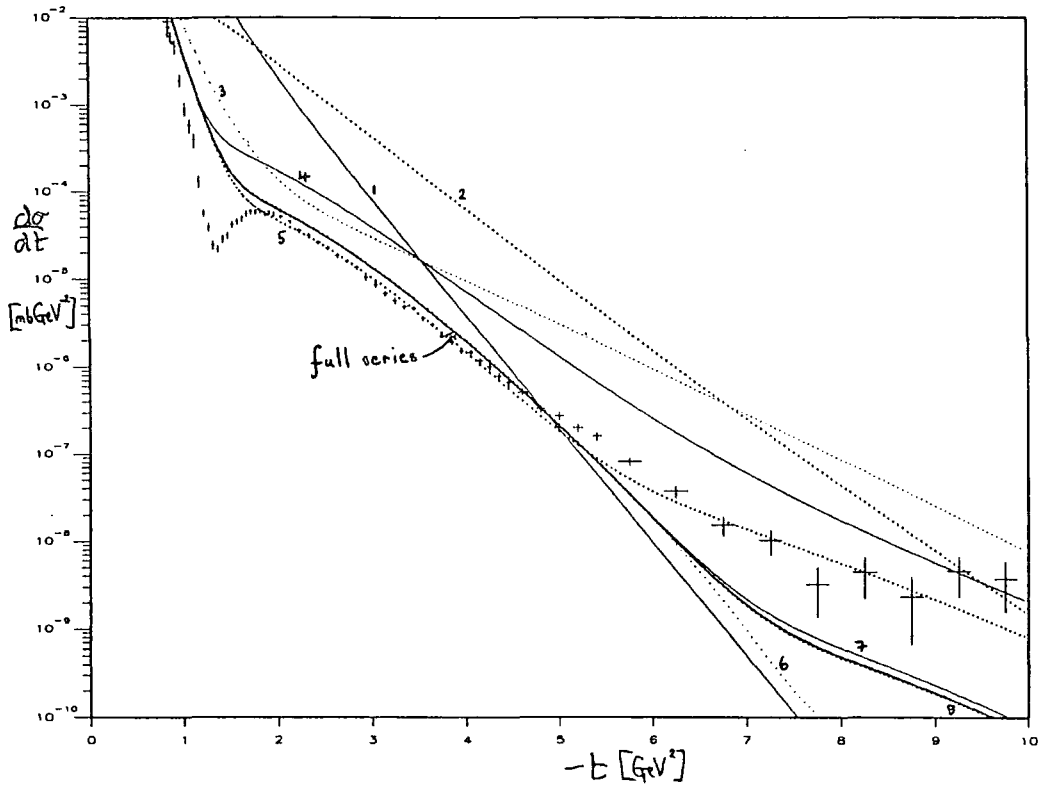


FIG. 7.5 Reggeon-Eikonal model fit. Light curves give predictions using successively more terms in the eikonal series ($n = 1 \rightarrow 8$).

If the first zero crossing in the imaginary part of the amplitude occurs at the dip position at $|t| = 1.35 \text{ GeV}^2$, the second occurs too close in at $|t| = 6 \text{ GeV}^2$ and produces the fall off from the data at large $|t|$ seen above. With the first zero crossing at $|t| = 1.65 \text{ GeV}^2$ the fit to the large $|t|$ data is improved because the second occurs further out. Increasing the pole term at large $|t|$ by giving it a flatter t -dependence has only a small effect on higher terms in the same t -range but, since the imaginary part of the amplitude is negative between the first and second zero crossings, this moves the second zero to smaller $|t|$ making the large $|t|$ fit worse. The energy dependence of the large $|t|$ data at the ISR shows that there is no zero in the imaginary part of the amplitude for $2 \leq |t| \leq 7 \text{ GeV}^2$ over the ISR energy range. To push the second zero crossing further out in $|t|$ in order to fit the large $|t|$ data, the imaginary part of the input pole must be decreased in the region where the output starts to fall below the data, but must be unaffected for smaller $|t|$. To prevent the 2nd dip we find that it

is necessary to make the Pomeron residue in (7.1.5) go negative at large $|t|$ by adding a fifth exponential to the parametrization with a negative coefficient, x_4 , and with small slope, a_4 , so that it dominates at sufficiently large $|t|$. This exactly mirrors the effect of the factor $\frac{a^2+t}{a^2-t}$ in (6.1.5) in the BSW model and gives very similar results. Since the imaginary part of the amplitude dominates at large $|t|$, the trajectory slope, α'_P , has little effect on the large $|t|$ fits to $\sqrt{s} = 53$ GeV except where there is a zero in the imaginary part because the change in the imaginary part it produces can be compensated for by small changes in the residue at large $|t|$. It will however affect the energy dependence of the large $|t|$ fit. To produce a change of sign in the pole term at $|t| = 4$ GeV² would need $\alpha'_P \simeq \frac{\alpha_P(0)}{|t|} \approx 0.25$ GeV⁻², which is incompatible with the small $|t|$ shrinkage. Adjusting the two parameters of the extra term in the residue, using the parameters from fit (7b), gives the fit (7c) in table 7.2 and plotted in fig.7.6 as curve (c). The predicted cross-section for $|t| \geq 6$ GeV² now lies above the data and gives a similar large $|t|$ fit to the BSW model. We have not tried to improve the agreement with the $|t| \geq 6$ GeV² data but this should be possible since as the sign of x_4 in the Pomeron residue (7.1.5) is changed from $+$ \rightarrow 0 \rightarrow $-$ the output goes smoothly from curve $a \rightarrow b \rightarrow c$ in figure 7.6.

Fit (7b)			
G_P	130.7	a_P	5.404 GeV ⁻²
x_1	0.229	a_1	9.66 GeV ⁻²
x_3	0.155	a_3	-2.56 GeV ⁻²
Fit (7c)			
x_4	-2.77×10^{-4}	a_4	-5.181 GeV ⁻²

TABLE 7.2 Parameter values of fits (7b) and (7c). The latter uses the parameters of (7b).

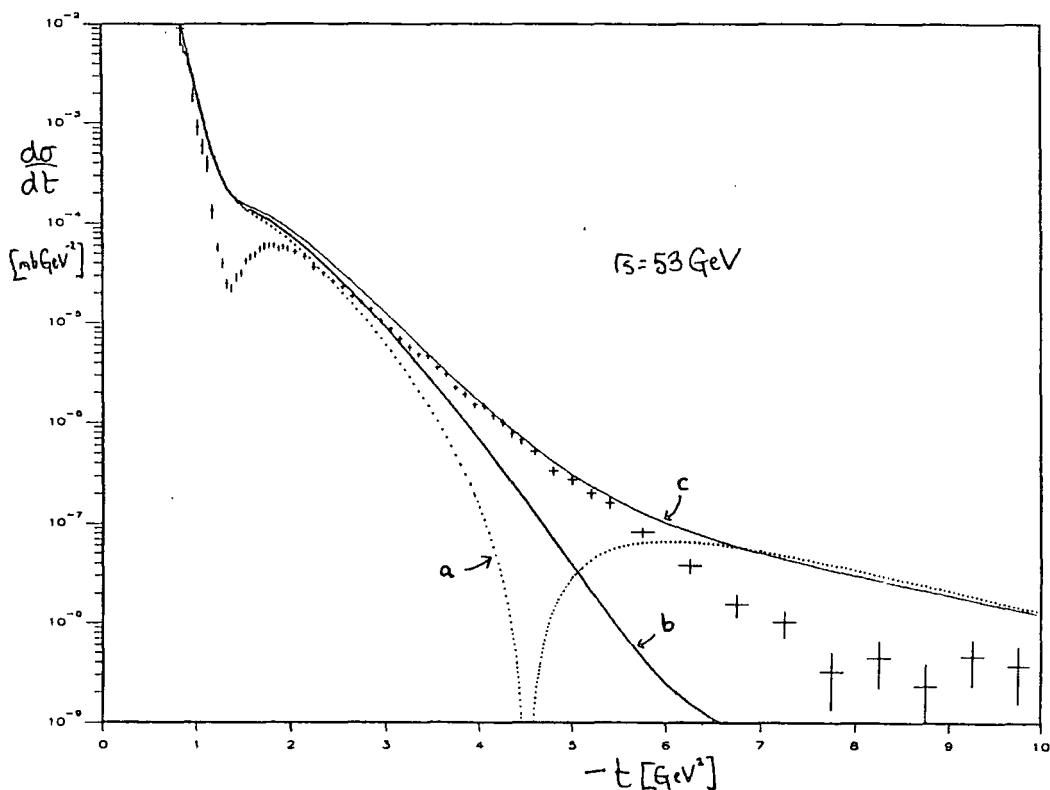


FIG. 7.6 Reggeon-Eikonal model fits to large $|t| \frac{d\sigma}{dt}$ at $\sqrt{s} = 53$ GeV. (a) Fit (7b), (b) extra term added to Pomeron residue, (c) extra term subtracted from Pomeron residue.

We attempted to improve fit (7c) in the region $2 \leq |t| \leq 6$ GeV² at $\sqrt{s} = 53$ GeV by adding another term to the residue, keeping the subtracted term fixed. This gave a good fit in this t -range but affected the fit to small $|t|$ at the Collider for $|t| > 0.5$ GeV². This fit (7d) is shown in fig.7.7 and table 7.3 compared with the BSW model fit from §6. In these fits, (7b \rightarrow d), changing the residue from that of fit (7a) will affect σ_T by ≈ 0.5 mb and so this should also be refitted.

Fit (7d)			
x_2	0.900	a_2	0.90 GeV^{-2}
x_3	0.0792	a_3	-2.66 GeV^{-2}
x_4	-2.77×10^{-4}	a_4	-5.18 GeV^{-2}
x_5	0.07891	a_5	-3.60 GeV^{-2}

TABLE 7.3 Parameter values of fit (7d).

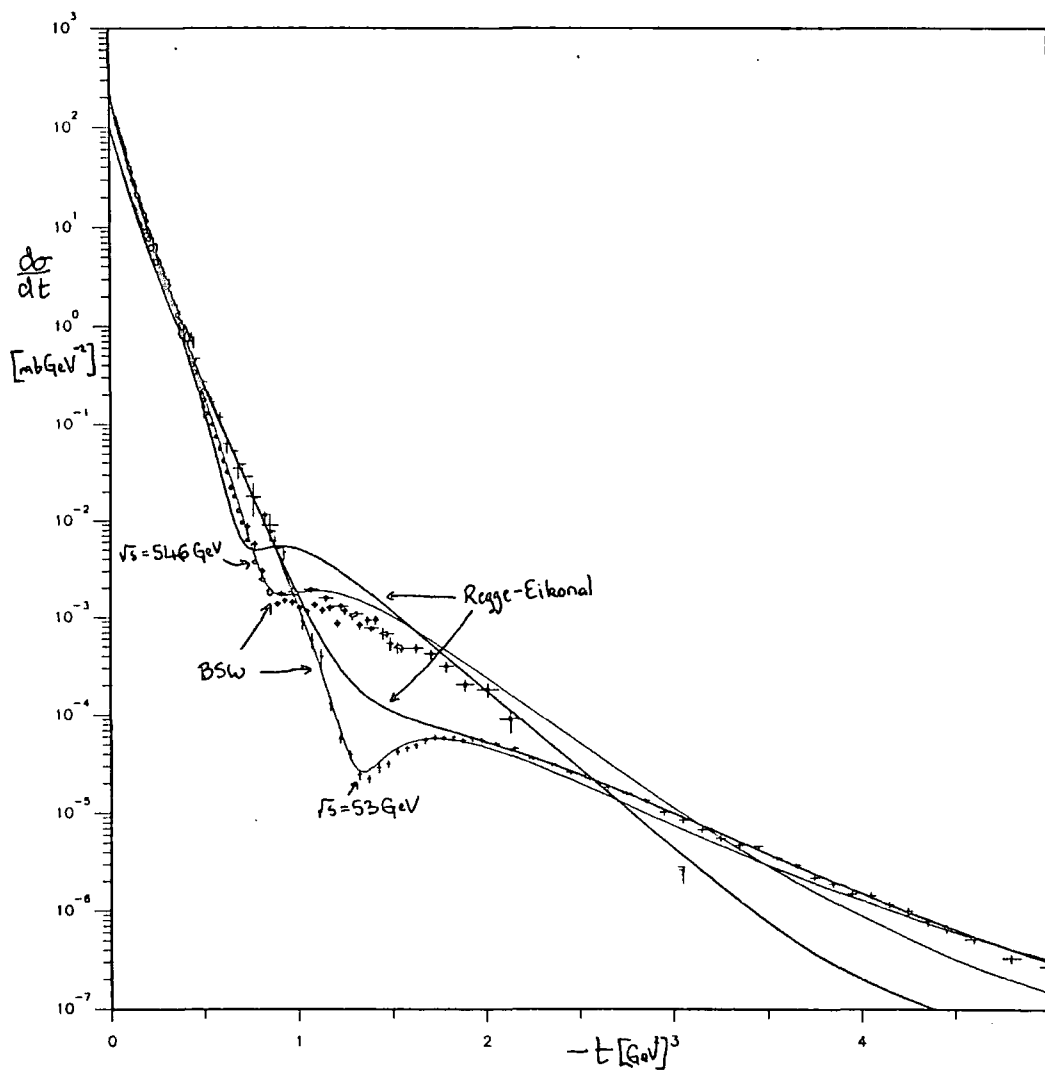


FIG. 7.7 Reggeon-Eikonal model fit (7d) (thick line) at $\sqrt{s} = 53$ and 546 GeV compared with BSW model (thin line).

Extrapolating fits (7c) and (7d) to the Collider energy, we find that they give the shoulder a factor of $4\times$ higher than the data and a slight dip at $|t| = 0.85 \text{ GeV}^2$ (the shallow dip occurs because Re/Im is smaller at lower $|t|$ and the zero in the imaginary part of the amplitude has moved in to $|t| = 0.85 \text{ GeV}^2$). We investigated the reason for the difference between these fits and the BSW model of §6 which gives a shoulder at the Collider only 50% above the data (see fig.6.8). Setting $\alpha'_p = 0$ and repeating the above fits (to σ_T , small $|t|$ and large $|t| \frac{d\sigma}{dt}$) improves the agreement with the Collider shoulder by a factor of two but is still too high (fit (7e)). The difference is now caused by the different shapes of the small $|t|$ fits; the BSW model and this fit (7e) have similar Pomeron contributions at $t = 0$ and similar phases (note that the phase of the Pomeron contribution in the BSW model is energy dependent; at $\sqrt{s} = 53 \text{ GeV}$ it corresponds to $\epsilon_p = 0.074$ and at $\sqrt{s} = 546 \text{ GeV}$ to $\epsilon_p = 0.107$). Comparatively small changes in the small $|t|$ slope can affect the height of the shoulder. This leads us to believe that it should be possible to improve the description of the Collider shoulder, while maintaining similar fits to those above at $\sqrt{s} = 53 \text{ GeV}$, by readjusting the small $|t|$ parametrization (even with non-zero α'_p) but we were unable to do this because of the prohibitive amount of computer time involved. Also, we have not yet taken into account the effect of eikonalizing the Reggeons, which will alter the parameter values anyway. A larger value of α'_p makes it harder to get the magnitude of the shoulder right. This will further limit the value of α'_p but again the maximum value compatible with the data can only be found by explicitly attempting to fit the data. A comparison of the Pomeron contribution from the BSW model, and fits (7c \rightarrow e) at $\sqrt{s} = 546 \text{ GeV}$ is shown in figure 7.8 .

1

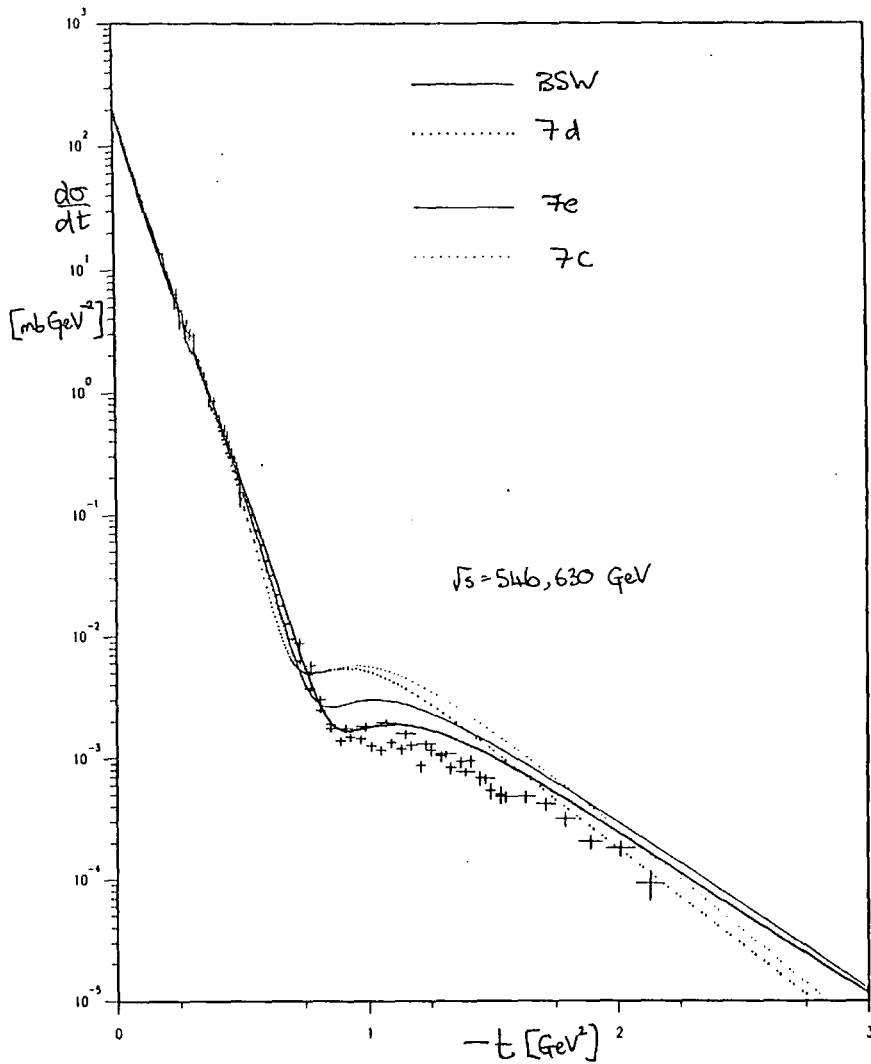


FIG. 7.8 Comparison of Reggeon-Eikonal model fits (7c), (7d) and (7e) with the BSW model at $\sqrt{s} = 546$ GeV.

$\alpha_P(0)$	1.108	β_f	80.8 mb	G_P	131.8
α'_P	0	$\alpha_f(0)$	0.564	a_P	5.468 GeV^{-2}
x_1	0.312	x_2	0.0659	x_3	0.1547
a_1	4.64 GeV^{-2}	a_2	-3.69 GeV^{-2}	a_3	-2.56 GeV^{-2}
x_4	-2.77×10^{-4}	a_4	-5.24 GeV^{-2}		

TABLE 7.4 Parameter values of fit (7e).

7.4. Eikonalized Reggeon Contribution.

We now want to see if it is possible to add a Reggeon contribution to the eikonal phase (7.1.2) which can cancel the real part of the Pomeron contribution at ISR energies and produce a dip as in §6.8. We use the fit (7e) above which gave a good description of the small $|t| \frac{d\sigma}{dt}$ data and σ_T , and a reasonable description of the large $|t|$ data. At $\sqrt{s} = 53$ GeV the imaginary part of the sum of the Pomeron contributions has a zero crossing at $|t| = 1.38$ GeV². Extrapolating fit (7e) to lower energies we find that at $\sqrt{s} = 23.5$ GeV this has moved out to $|t| = 1.6$ GeV² and the cross-section at the second maximum is 40% below the data (see fig.7.10); by $\sqrt{s} = 10$ GeV² the zero has moved out to $|t| = 1.8$ GeV² and the cross-section is a factor 10× below the data. So in order to fit the data, the Reggeon contribution must also offset the energy dependence of the eikonalized Pomeron.

For the Reggeon contribution to the Born term of the eikonal series we use a form similar to (4.4.5) and (6.1.17) but use simple exponentials for the t -dependence of the f and ω residues and, as in (7.1.6), scale the shrinkage of the Reggeons about $\sqrt{s} = 53$ GeV. This gives

$$\chi_R(s, b) = \frac{1}{8\pi s} \left[-G_f (e^{-i\frac{\pi}{2}} s)^{\alpha_f(0)} \frac{e^{-\frac{b^2}{4c_f}}}{c_f} \mp iG_\omega (e^{-i\frac{\pi}{2}} s)^{\alpha_\omega(0)} \frac{e^{-\frac{b^2}{4c_\omega}}}{c_\omega} \right] \quad \text{for} \quad \begin{array}{l} pp \\ \bar{p}p \end{array} \quad (7.4.1)$$

where $c_R = a_R + \alpha'_R (\log \frac{s}{53^2} - i\frac{\pi}{2})$.

We then fit σ_T and $\frac{d\sigma}{dt}$ at $\sqrt{s} = 53$ GeV by varying G_f , $\alpha_f(0)$, a_f , α'_f , G_ω and $\alpha_\omega(0)$. In σ_T the effects of the parameters a_f and α'_f are approximately interchangeable, we fix these in the σ_T fit at $a_f = 3.95$ GeV⁻², $\alpha'_f = 1$ GeV⁻². Since we are using a fixed Pomeron pole ($\alpha'_p = 0$), the Reggeon-Pomeron cuts are also fixed. In the dip region at $\sqrt{s} = 53$ GeV the dominant Reggeon term is the $f \otimes P$ cut, the real part of which is positive, so has the right sign to cancel the real part of the multiple Pomeron exchange. Higher terms are far from small and even $R \otimes R$ cuts are not negligible. The magnitude of the eikonalized Reggeon terms can be altered by adjusting a_f , the phase can be altered by adjusting α'_f which affects the $R \otimes R$ terms. For $\alpha'_f = 1$ GeV⁻² the eikonalized f Reggeon is approximately real in the dip region as required and so we adjust a_f to give the right magnitude to cancel the eikonalized Pomeron term. The

rest of the parameters are fixed by σ_T . The parameters of this fit are given in table 7.5. The low value of $\alpha_\omega(0)$ means that the $\omega \otimes P$ cut is predominantly imaginary in the dip region and so only moves the position of the dip, rather than filling it in. For this reason we keep the odd charge conjugation contribution small in the dip region. The fit to σ_T is shown in figure 7.9.

$\alpha_f(0)$	0.492	G_f	500 mb
α'_f	1.0 GeV^{-2}	a_f	5.5 GeV^{-2}
$\alpha_\omega(0)$	0.141	G_ω	596 mb
α'_ω	0.8 GeV^{-2}	a_ω	6.6 GeV^{-2}

TABLE 7.5 Parameter values of eikonized Reggeon fit.

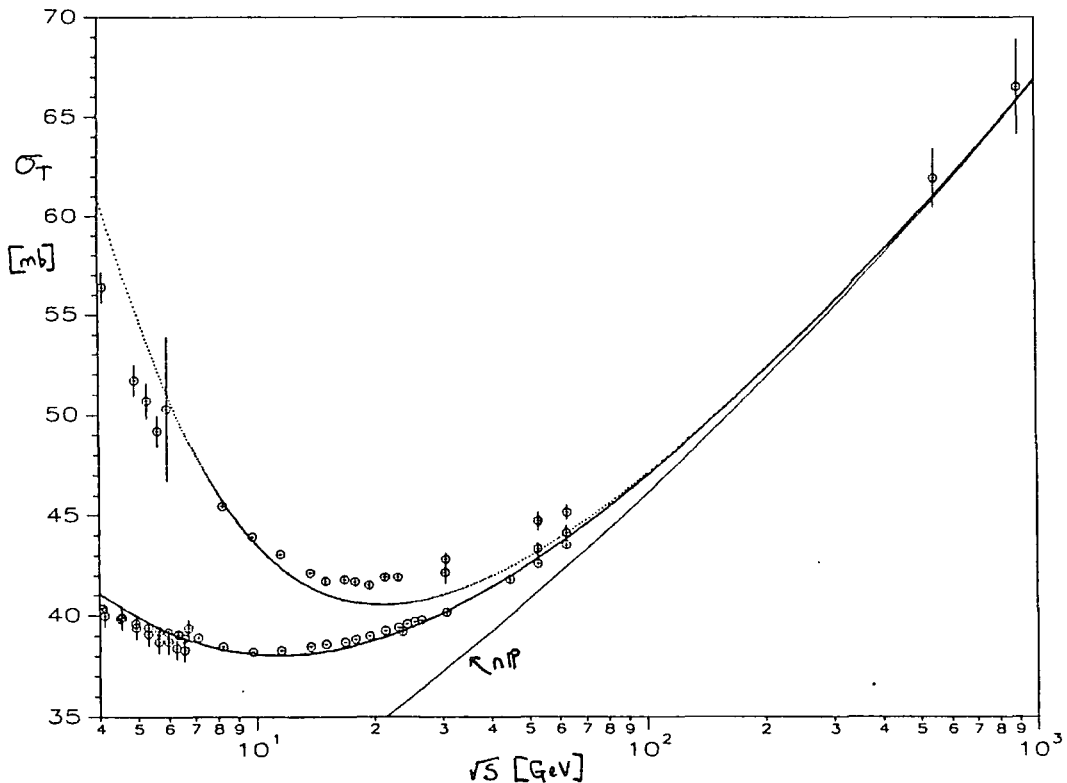


FIG. 7.9 Fit to σ_T using parameters of table 7.5 .

The fit could probably be improved by further adjustment. Unlike the BSW model we have allowed separate intercepts for the f and ω trajectories. This has resulted in a very small value for $\alpha_\omega(0)$ (compare with (6.1.11)). In order that there be some hope of the eikonized Reggeon contributions being compatible with the low energy $\frac{d\sigma}{dt}$ data, their effect at small $|t|$ should be similar to the conventional Reggeons of (4.4.5). We examined the effective trajectories of the even and odd charge conjugation Reggeon contributions. The effective trajectories at $t = 0$ are shown in table 7.6 for the above fit.

\sqrt{s}	Pomeron	Even Reggeon	Odd Reggeon	Total
10 GeV	$1.093 + 0.062t$	$0.501 + 1.162t$	$0.161 + 0.859t$	$0.974 - 0.394t$
53 GeV	$1.088 + 0.086t$	$0.486 + 1.333t$	$0.134 + 1.097t$	$1.068 - 0.097t$
546 GeV	$1.078 + 0.131t$	$0.481 + 1.518t$	$0.128 + 1.290t$	$1.077 + 0.112t$

TABLE 7.6 Effective trajectories at $t = 0$ for above fit.

The behaviour of the f trajectory is reasonable; the ω trajectory is not high enough at $t = 0$ which is reflected in the poor fit to the high energy $\Delta\sigma$. Since the Pomeron intercept is close to one the $R \otimes P$ cuts have approximately the same intercepts as the pole terms and so the intercepts of the Reggeons are not changed by much. The slopes of the effective trajectories are increased by interference with cut terms.

Using fit (7e) for the Pomeron gives the best chance of fitting the $\frac{d\sigma}{dt}$ data because the real part in the dip region is as small as possible in these fits, and so the Reggeon terms are as small as possible. The resulting prediction for $\frac{d\sigma}{dt}(pp)$ at ISR energies is shown in figure 7.10 along with the eikonized Pomeron contribution alone. Whilst the fit at $\sqrt{s} = 53$ GeV is reasonable, the large contribution of the $f \otimes P$ cuts and the energy dependence of the eikonized Pomeron give nothing like the behaviour observed in the data. At $\sqrt{s} = 10$ GeV the eikonized f Reggeon gives a cross-section a factor of $10\times$ too high for $|t| \geq 0.8$ GeV².

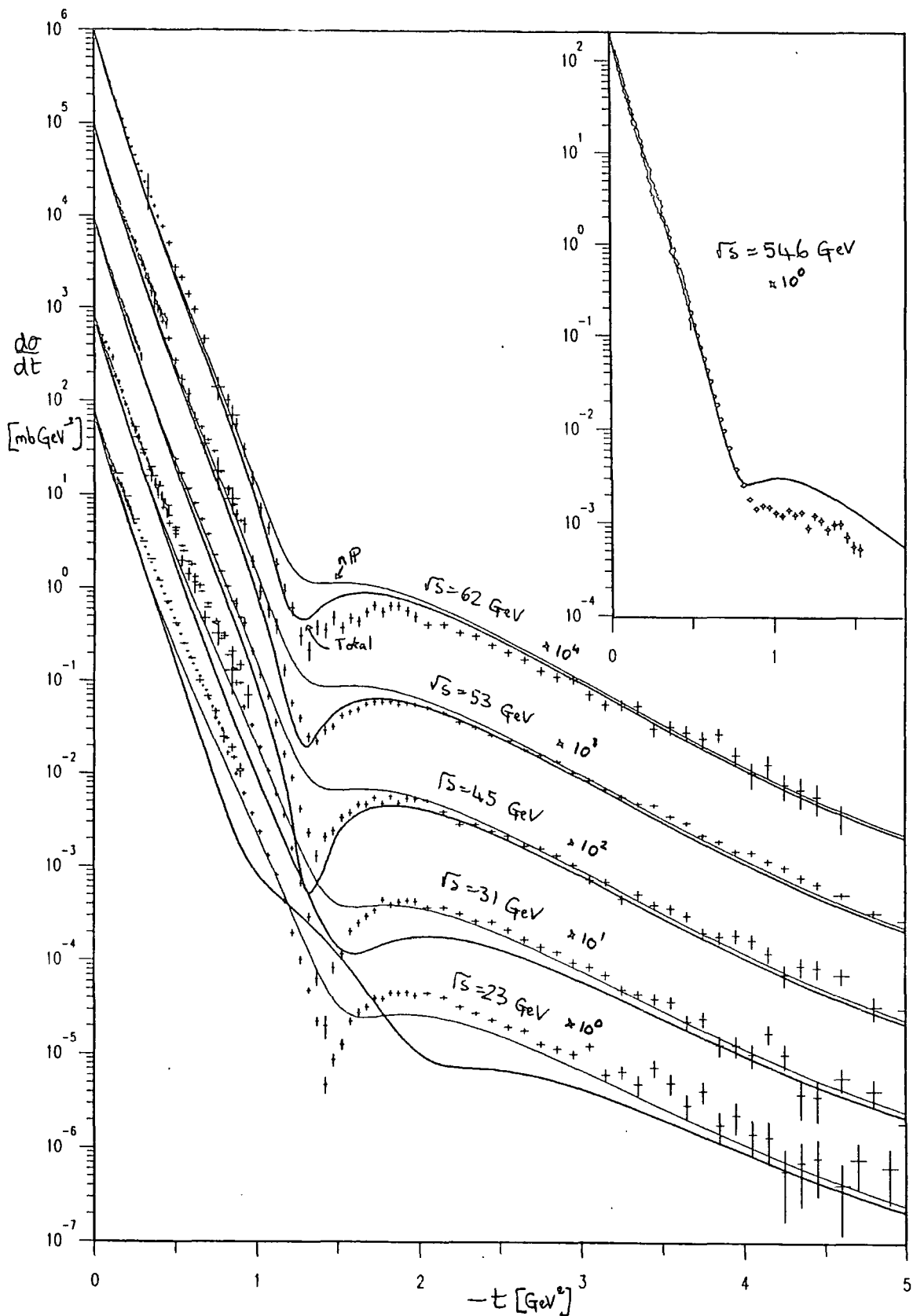


FIG. 7.10 Prediction of $\frac{d\sigma}{dt}$ using parameters of table 7.5 (thin line is eikonalized Pomeron contribution).

7.5. Conclusions.

In the above we found that it was impossible to reproduce the dip in the ISR data with just a Pomeron contribution so that large Reggeon cut terms were needed. In order to avoid further dip structure at large $|t|$ it was necessary to use a non-factorizable Born term in the eikonal series (residue changes sign for $|t| \approx 4 \text{ GeV}^2$). The resulting parametrization gave a very poor description of the σ_T and $\frac{d\sigma}{dt}$ data. One of the major difference between these fits and those of the BSW model is that the Reggeon terms do not need to be so large in the latter in order to produce a dip because the Pomeron contribution does not have the Regge phase.

If the real part of the eikonalized f contribution is positive so that it cancels the real part of the eikonalized Pomeron in the dip region, the imaginary part destructively interferes at large $|t|$, producing greater energy dependence and making it more difficult to get agreement with the data.. It is possible that using a different calculation for the Reggeon cut terms the model can be improved (just using $f + f \otimes P$ will avoid this effect).

In figure 7.11 we show the high energy behaviour of σ_T from fit (7a), which gave a good description of small $|t|$ and σ_T . The contributions from individual terms in the eikonal series (for $n = 1 \rightarrow 8$) are also shown. The total cross-section asymptotically satisfies the Froissart bound as in §6.4 (see Collins (1977) p.278). The behaviour of the profile function is very similar to that of the BSW model in §6.3 and is shown in figure 7.12 (dotted line is Born term).

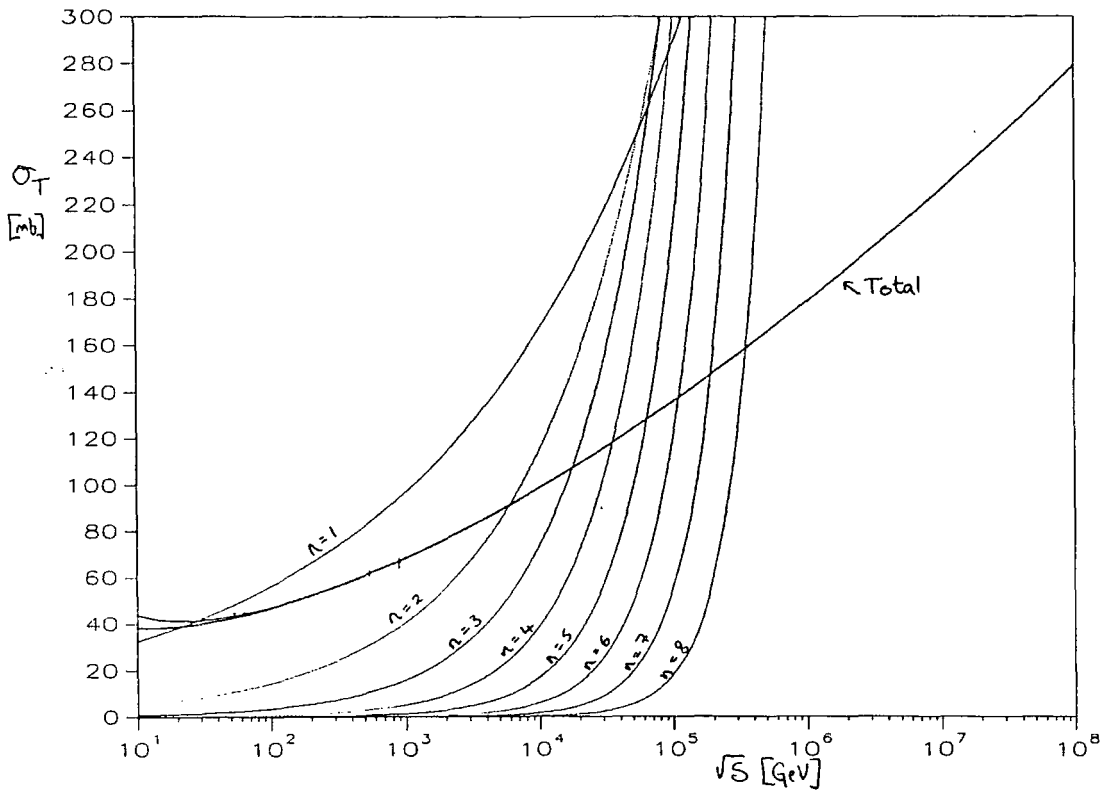


FIG. 7.11 Prediction of σ_T using parameters of fit (7a) (thin lines are individual terms in eikonal series).

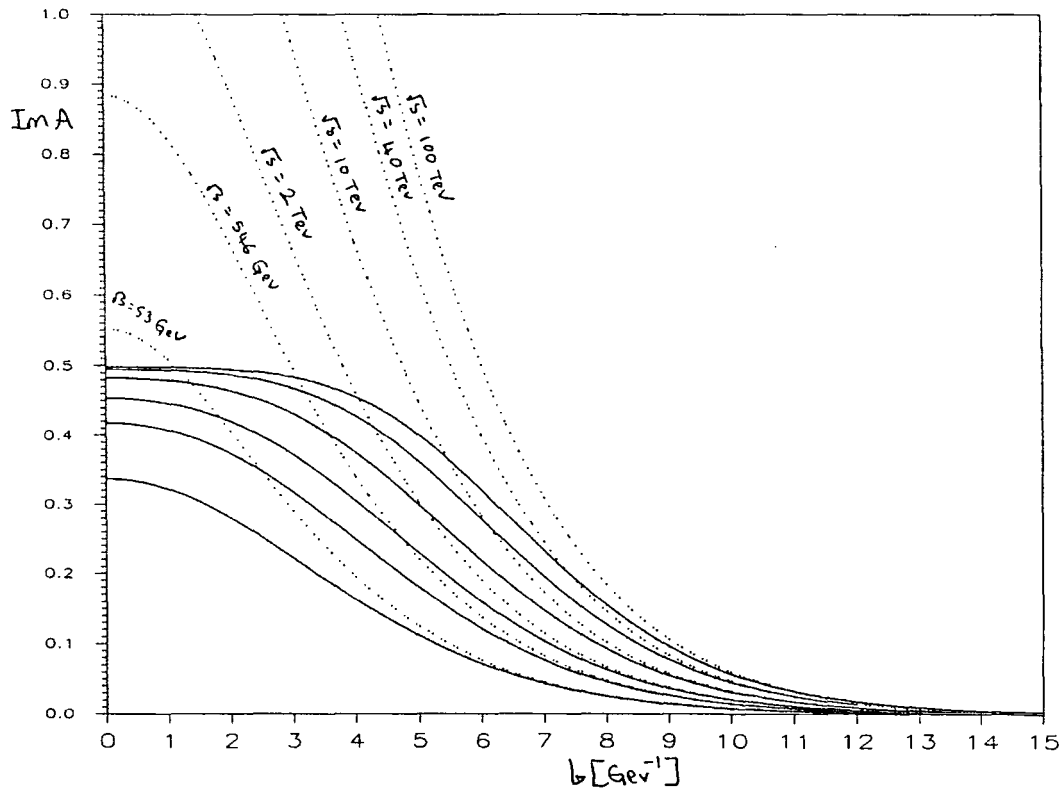


FIG. 7.12 Prediction of imaginary part of the profile function using parameters of fit (7a) at $\sqrt{s} = 53, 546, 2 \times 10^3, 10^4, 4 \times 10^4$ and 10^5 GeV (dotted lines are Born terms in eikonal series).

Reggeon Field Theory Phenomenology

8.1. Introduction

The problem of summing the infinite number of Regge cuts generated by multiple Reggeon exchanges can be tackled by introducing an effective field theory in the complex angular momentum plane. This is developed as a calculus for summing the hybrid Regge-Feynmann graphs like that of figure 3.6 or as a solution to the Reggeon unitarity relations derived from fundamental S-matrix principles. The Reggeons are treated as non-relativistic quasi-particles in 2+1 dimensions with an “energy” given by $E = 1 - j$ (where j is the position of the moving Regge pole in the j -plane) and with two-dimensional momentum \mathbf{k} . The variables conjugate to these are the “time”, $\tau = -i \log s$, and impact parameter, \mathbf{b} , respectively. The mass of the particle is given by $\frac{1}{2\alpha'}$ and $\Delta_0 = 1 - \alpha_0$ is the mass gap. These can interact with each other via a triple-Regge (or higher order) coupling giving rise to diagrams like figure 8.1 .

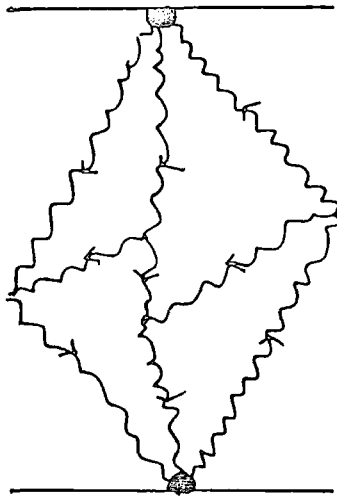


FIG. 8.1 Example graph with 3-Pomeron interactions in RFT.

The satisfaction of the Reggeon unitarity relations ensures that t -channel unitarity is satisfied. RFT also appears to satisfy s -channel unitarity though this is not explicitly built in. Other interaction terms are also possible and in principle they will result

in an infinite number of free parameters but most of these will be unimportant at high enough energy. If no Reggeon-Reggeon interaction terms are present RFT just reproduces graphs similar to those of the eikonal model in which s -channel unitarity was explicitly satisfied but t -channel unitarity was violated.

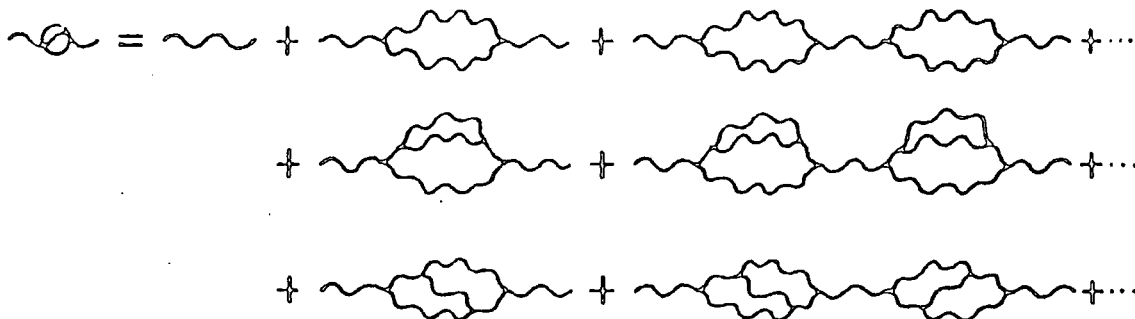


FIG. 8.2 Perturbation expansion for renormalized Pomeron propagator in RFT.

The picture that emerges from RFT is that the bare Pomeron with trajectory $\alpha_0(t)$ will be modified by Pomeron interactions giving a renormalized trajectory $\alpha(t)$. The expansion parameter in the perturbation expansion for the Pomeron propagator (fig.8.2) is $\frac{r_0^2}{\alpha_0'} \log s$, where r_0 is the bare triple-Pomeron coupling and α_0' the bare trajectory slope. If this quantity is small then the perturbation approach will be valid and the series can be approximated by its first few terms. The 3-P coupling can be estimated from the inclusive cross-section data from the ISR and FNAL for $pp \rightarrow pX$ and it is found that $\frac{r_0^2}{\alpha_0'} \log s \simeq 0.01 \log s$. The renormalized triple-Pomeron coupling is then essentially just given by the bare quantity and the only diagrams which contribute appreciably to the elastic scattering amplitude are those shown in figure 8.3 and their s -channel iterations.

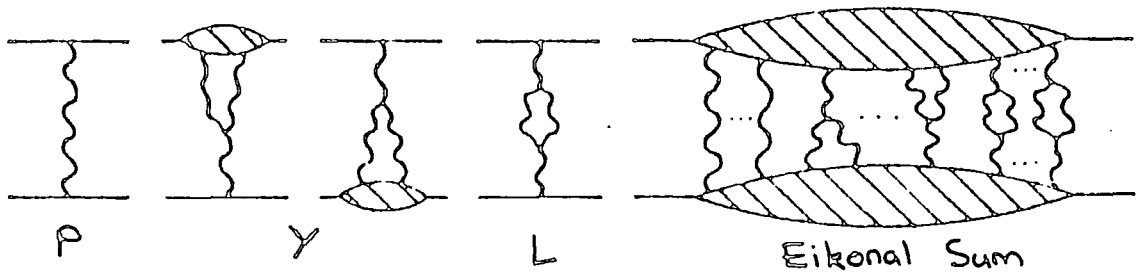


FIG. 8.3 Dominant graphs in perturbative RFT at ISR energies.

As the energy increases the expansion parameter increases logarithmically so that higher order terms become important. If the expansion parameter is large enough the perturbation approach will be invalid and the series must be summed by other means. In the case where the renormalized Reggeon intercept is unity, so that the mass gap $\Delta_0 = 1 - \alpha_0$ vanishes, the infrared behaviour of the theory ($E \rightarrow 0, k \rightarrow 0$) corresponds to a field theory with massless particles and all the multi-Reggeon trajectories collide. This can be studied using the renormalization group equations, and provided an infrared stable fixed point exists the Reggeon Green's functions satisfy scaling laws whose form does not depend on the underlying parameters of the theory. The limit $E \rightarrow 0$ corresponds to $\log s \rightarrow \infty$ and so the infrared behaviour corresponds to asymptotic energies. Both the critical indices governing the scaling law and the functional form of the scaling law can be calculated from a perturbation series in $\frac{\epsilon}{12}$ (where $\epsilon = 4 - D$ and $D = 2$ for RFT).

The energy, s_T , below which the corrections to the scaling law become too large for it to provide a pertinent description of the scattering amplitude is given by

$$\log \frac{s_T}{s_0} \simeq \frac{8\pi\alpha'_0}{3r_0^2} \quad (8.8.1)$$

and the energy above which the perturbation expansion factor exceeds one half so that higher terms are not negligible is given by

$$\log \frac{s_T}{s_0} \simeq \frac{4\pi\alpha'_0}{r_0^2} \quad (8.1.2)$$

so both transition energies are governed by the quantity $\frac{\alpha'_0}{r_0^2}$. The experimental value of the bare triple-Pomeron coupling, r_0 , is not very well determined because of large absorptive corrections which need to be taken into account when extracting its value from inclusive cross-sections. This results in an uncertainty of a factor of three in r_0 which gives a factor of ten variation in $\log s_T$ so that it can range from $\log s_T \approx 7$ where the scaling solution would be applicable at current energies to $\log s_T \approx 100$ for which the perturbation expansion gives the correct description at all attainable energies.

8.2. Behaviour of σ_T .

The asymptotic scaling law prediction for σ_T is given by equation (8.2.1) where successive terms represent the leading contributions of the renormalized Green's functions $G_R^{(1,1)}$, $G_R^{(1,2)}$, $G_R^{(2,2)}$, respectively.

$$\lim_{s \rightarrow \infty} \sigma_T = \beta_0 (\log s)^\eta [1 + \beta_1 (\log s)^{-\lambda} + \beta_2 (\log s)^{-1-\eta}] \quad (8.2.1)$$

The critical exponents, η and λ , can be calculated in perturbation theory (or on a lattice) and have the values shown below (Cardy (1977)).

$$\begin{aligned} \eta &= 0.26 \pm 0.02 \\ \lambda &= 0.49 \pm 0.01 \end{aligned} \quad (8.2.2)$$

Some account should probably also be taken of non-leading terms in $G_R^{(n,m)}$ since the non-leading term in $G_R^{(1,1)}$ may well be more important than the leading term in $G_R^{(1,2)}$ for example.

Using this prediction together with a parametrization of lower Reggeon trajectories by

$$\sigma_T^R = \beta_0 \beta_3 s^{-\frac{1}{2}} \quad (8.2.3)$$

a fit to the $\sigma_T(pp)$ data for $\sqrt{s} \geq 5$ GeV was obtained in Baig (1985). The parameters he found are given in (8.2.4).

$$\begin{aligned}\beta_0 &= 61.49 \pm 2.30 \text{ mb} \\ \beta_1 &= -1.73 \pm 0.03 \\ \beta_2 &= 0.073 \pm 0.09 \\ \beta_3 &= 3.305 \pm 0.21\end{aligned}\tag{8.2.4}$$

The large corrections to the leading behaviour of (8.2.1) given by the term, β_1 , indicate that the asymptotic form is not yet applicable. This sets a lower bound for approximate scaling behaviour at $\sqrt{s} = 546$ GeV. The results of the fit using the above parameters together with a breakdown of the contributions of the individual terms is shown in figures 8.4a and 8.4b . The description of the data for $\sqrt{s} \leq 10^2$ GeV is very poor and at high energies the predicted cross-section is too small to agree with the cosmic ray data.

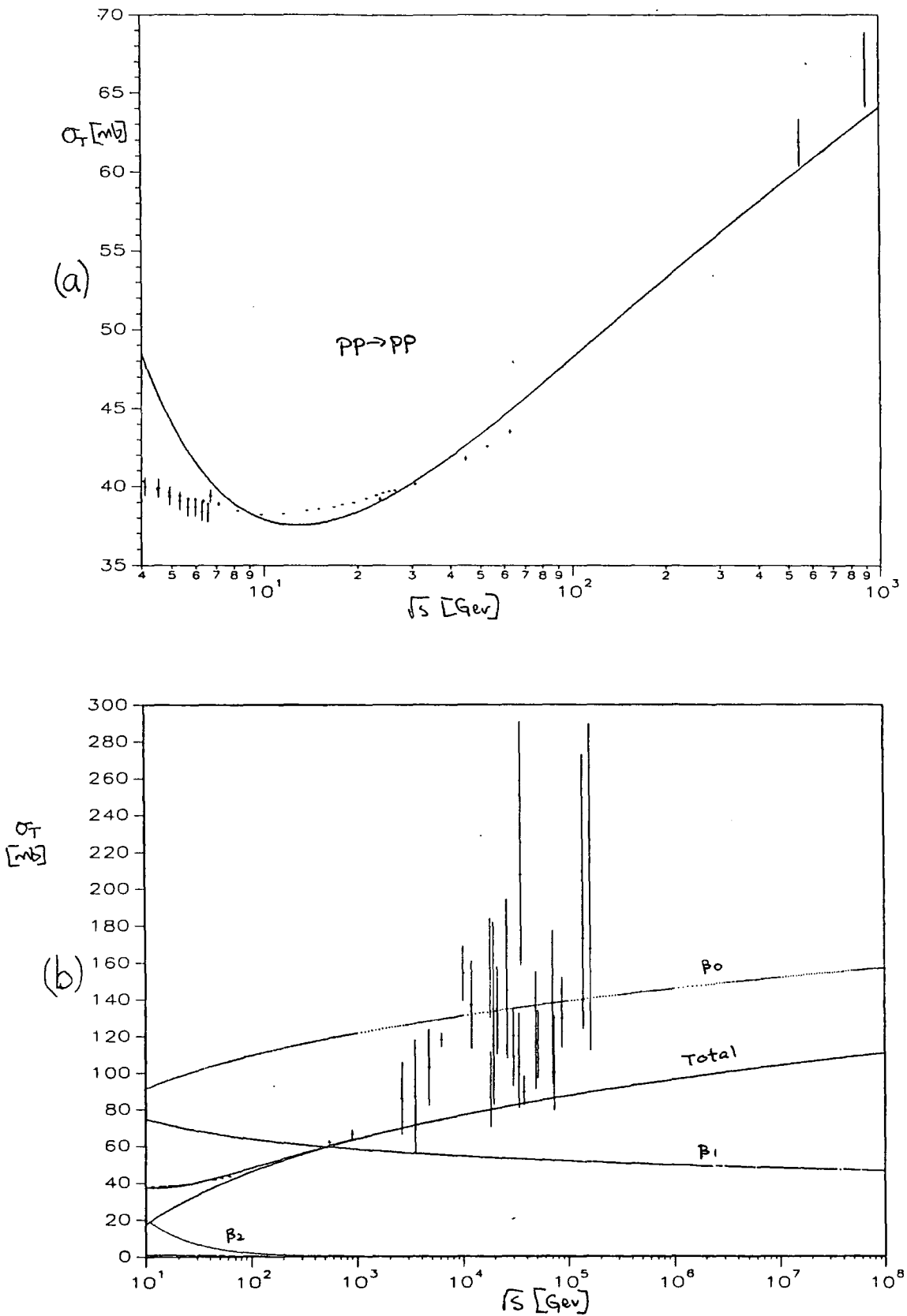


FIG. 8.4 Predicted cross-section for (a) $\sqrt{s} \leq 1$ Tev, (b) $\sqrt{s} \leq 10^5$ Tev (shows contributions of the dominant terms), in the asymptotic RFT scaling law prediction.

In the perturbative Reggeon calculus the energy dependence of the cross-section depends upon the bare mass gap, Δ_0 , and the bare 3-P coupling, r_0 . In the critical Pomeron model the value of Δ_0 is adjusted to give a renormalized Pomeron intercept of one ($\Delta = 0$). This implies a relationship between the bare parameters Δ_0 , α'_0 and r_0 which has no physical motivation, which is somewhat unsatisfactory. The value of the bare Pomeron intercept, α_{0C} , which will result in the critical behaviour, can be calculated in perturbation theory and it is found that a value greater than one is obtained with $\alpha_{0C} - 1 \leq 0.01$. This is too small to produce the observed increase in σ_T (though there is some indication from non-perturbative calculations that the value may be higher). A value some ten times bigger than the critical value, $\alpha_0 - 1 = 0.11$, gives reasonable agreement with the σ_T data. This "supercritical" solution gives a renormalized intercept above one and the renormalization group equation is no longer useful in determining the asymptotic behaviour. However, model calculations in which the infinite number of cuts are summed, indicate that the asymptotic energy dependence goes like $\log^2 s$ so that the Froissart bound seems to still be satisfied. The scattering amplitude which results from the eikonalization of the diagrams in figure 8.3, together with the parameter values used, is given in Pajares et al (1983). This fit is displayed in figure 8.5 with a breakdown of the contributions from the bare Pomeron pole, the triple-Pomeron Y-diagram, the Loop diagram and the higher order Eikonal sum of these. It can be seen that at current energies the bare Pomeron graph gives a contribution about $20\times$ bigger than the loop graph and that the Y-graph is negligible. To a good approximation the Y- and L-graphs can be neglected, which amounts to setting the triple-P coupling, r_0 , to zero. The model then corresponds to the Regge-Eikonal model of §7 with enhancement of higher terms in the series due to diffractively produced resonances. The sum of the series satisfies the Froissart bound and σ_T has an asymptotic $\log^2 s$ dependence. However, at higher energies the contributions of the Y, L and higher order graphs will become more important. In fact, the L-graph has approximately an $s^{2\Delta}$ energy dependence for $\sqrt{s} \geq 100$ GeV and dominates the P term for $\sqrt{s} > 400$ TeV. The asymptotic prediction using just these three terms is therefore invalid for $\sqrt{s} \geq 10$ TeV. The sum of the higher terms in the eikonal series give approximately a 10% contribution at the collider energy but will eventually dominate the pole terms. As in the Regge-Eikonal model, higher terms in the eikonal series :-

$P \otimes P, P \otimes P \otimes P, \dots$ are comparable in magnitude to the Born term (see fig. 7.11).

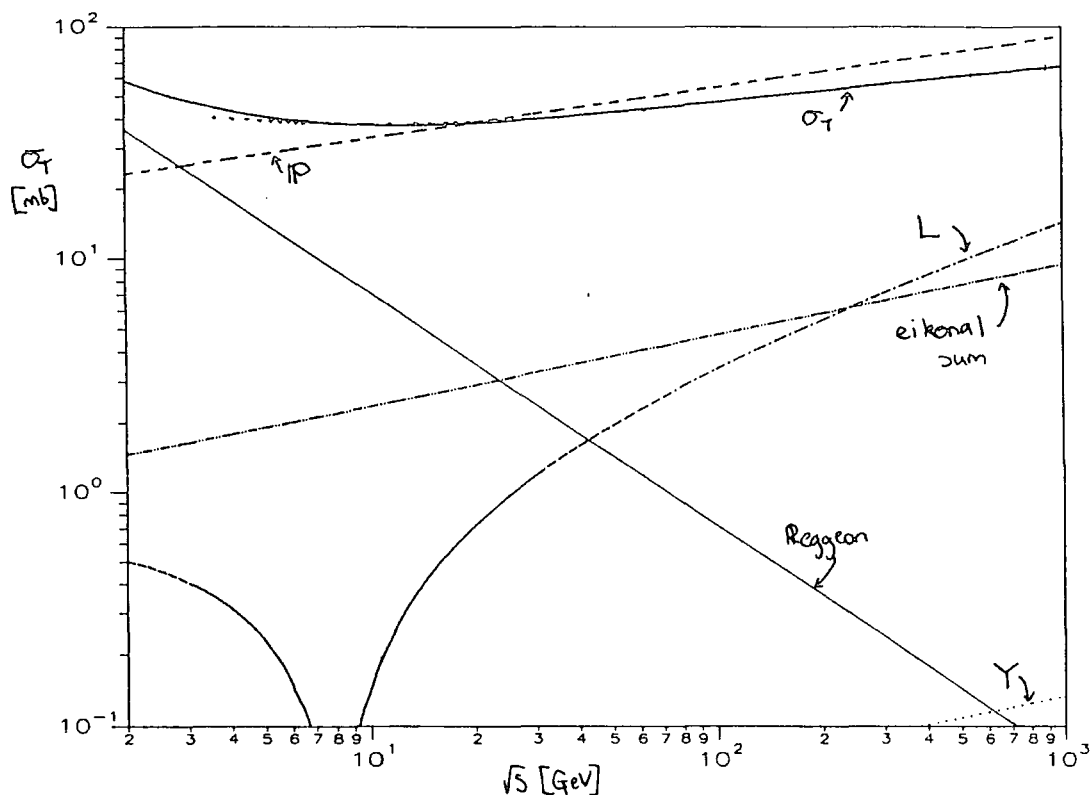


FIG. 8.5 Contributions of the various terms in the perturbative Reggeon calculus prediction for σ_T .

8.3. The Differential Cross-section.

The differential cross-section obtained from the perturbative Reggeon calculus at current energies is governed by the eikonalized Pomeron exchange term. The t -dependence of the bare Pomeron term is approximated by a simple exponential with shrinkage given by α'_0 . This is only a good approximation near $t = 0$ and gives the wrong curvature to $\frac{d\sigma}{dt}$ at larger $|t|$. To reproduce the larger $|t|$ differential cross-section the Pomeron residue must be parametrized by a dipole function as in the Eikonal models. The Y and L graphs in figure 8.3 have a steeper exponential slope than the P graph because of the decrease of the triple-Pomeron coupling with increasing momenta parametrized in the above fits by

$$r(q_1^2, q_2^2, q_3^2) = r_0 e^{-\frac{R}{2}(q_1^2 + q_2^2 + q_3^2)} \quad (8.3.1)$$

Each triple-P coupling gives an extra factor e^{Bt} to the t -dependence. Thus the t -dependence predicted by the perturbative Reggeon calculus is little different to that of the Regge-Eikonal model (at least at current energies).

The t -dependence of the asymptotic critical RFT is governed by a scaling law. The renormalized Pomeron propagator, which gives the leading term in σ_T in (8.2.1) satisfies

$$T_j(t) = (j-1)^{-1+\gamma} T^{(1,1)} \left[-\frac{\alpha'_0 t}{k_2} (j-1)^{-1+\frac{\zeta}{\alpha'}} \right] \quad (8.3.2)$$

This leads, via the Sommerfeld-Watson transformation, to the scaling law

$$\text{Im } A(s, t) = \beta^2(t) s (\log s)^{-\gamma} \tilde{T}^{(1,1)} \left[-\frac{\alpha'_0 t}{k_2} (\log s)^{1-\frac{\zeta}{\alpha'}} \right] \quad (8.3.3)$$

The critical exponents, γ and $\frac{\zeta}{\alpha'}$, and the universal function $\tilde{T}^{(1,1)}$, can be calculated in the $\frac{\zeta}{\alpha'}$ expansion. The unknown constant, k_2 , determines the t -scale and the function $\beta(t)$ is an unknown external particle vertex taken arbitrarily as $\beta(t) = 1$. The only unspecified parameters in the scaling law are thus the t -scale and the normalization.

Equation (8.3.3) predicts that $\sigma_{el}(s)$ should fall with increasing energy. It was also clear from fits to σ_T that this leading term cannot be a good approximation to the full amplitude at current energies. Using (8.3.3) and an $O(\epsilon^2)$ calculation for the critical exponents and $\tilde{T}^{(1,1)}$ gives a two dip structure for $\frac{d\sigma}{dt}$ (Baig *et al* (1984a)). Setting the t -scale by adjusting position of the first dip to coincide with that in $\frac{d\sigma}{dt}(pp)$ at the ISR results in the prediction shown in figure 8.6 for $\sqrt{s} = 53$ and 546 GeV. The small $|t|$ ISR data lie well below the predicted cross-section whilst at large $|t|$ the prediction falls off much too quickly with increasing $|t|$ and has a spurious second dip at $|t| \approx 2.6 \text{ GeV}^2$. At Collider energies the small $|t|$ prediction does reasonably well but for $|t| \geq 0.4 \text{ GeV}^2$ it drops below the data, and although it gets the dip position right the second maximum is too low to agree with the shoulder in the data. In the calculation of Baig (1985) the second maximum lies a factor of $100\times$ below the Collider shoulder. Our recomputation of this quite involved calculation is in close agreement with that of Baig *et al* (1984a, 1985) for $|t| < |t|_{\text{dip}}$ at $\sqrt{s} = 53, 546 \text{ GeV}$ but disagrees as to the height of the 2nd maximum at both energies by a factor of $10\times$. The reason for this disagreement is not understood but still the predicted t -dependence does not agree very well with the data. The details of the computation are described in Baig and Bourrely (1984b). Since the t -scale is controlled by an arbitrary parameter the

agreement with the small $|t|$ data at one energy is not significant though the prediction for larger $|t|$ at the Collider can be improved by including finite energy effects such as the real part of the amplitude, which is asymptotically zero, and a modified form for the external particle coupling, $\beta(t)$.

The conclusion from these analyses is that we are not yet in an energy region where the asymptotic behaviour of the critical RFT is applicable. The perturbative analysis indicates that the critical Pomeron does not reproduce the energy dependence of the σ_T data and that a supercritical Pomeron with $\alpha_0 > \alpha_{0C} > 1$ is needed. The terms that make the perturbative supercritical Pomeron model different from the Regge-Eikonal model discussed in §7 are small at current energies.

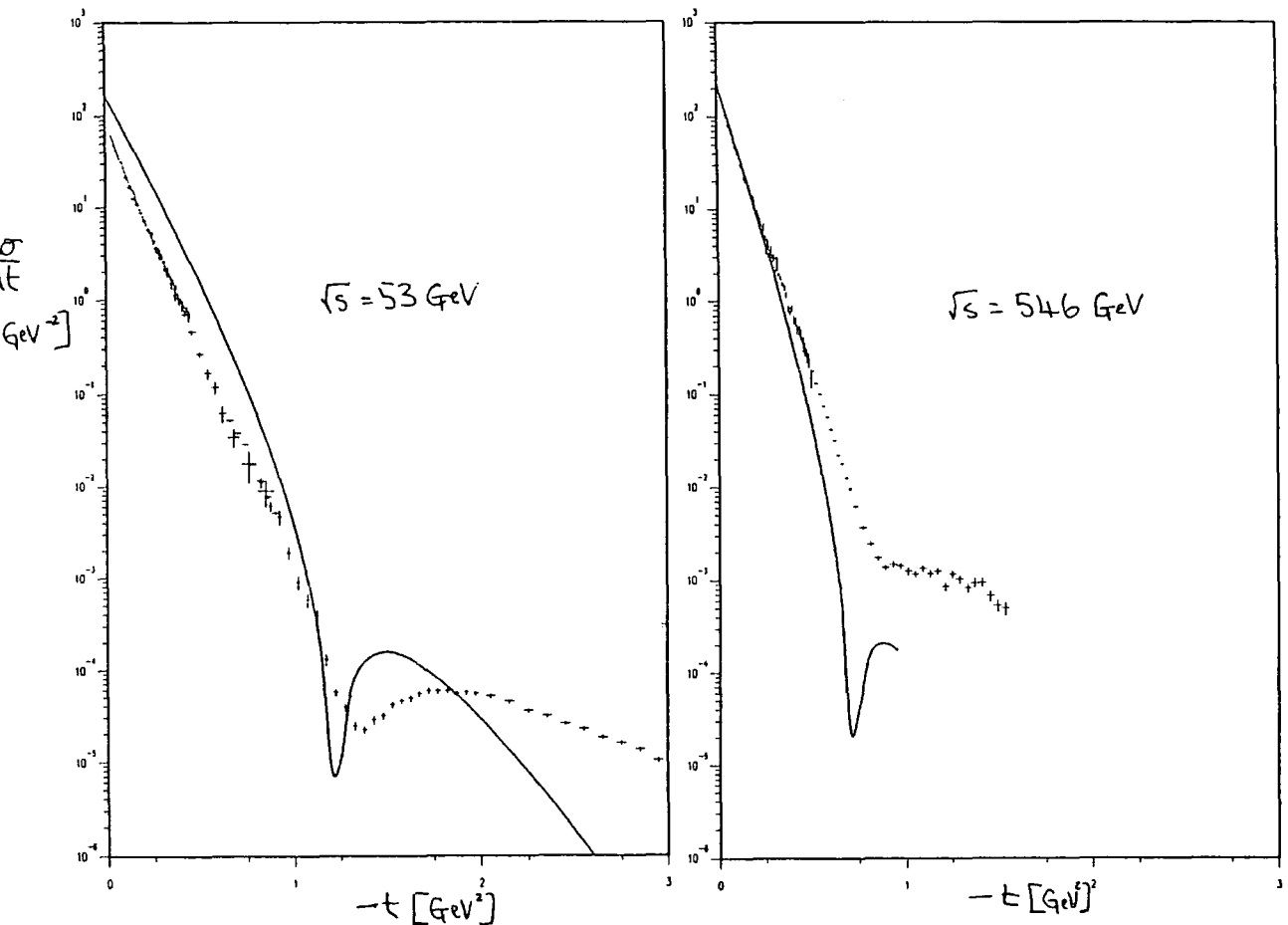


FIG. 8.6 Results of asymptotic RFT calculation for $\frac{d\sigma}{dt}$ at $\sqrt{s} = 53, 546 \text{ GeV}$.

Unitarization Model.

9.1. Introduction

We saw in §4.9 that a Pomeron with trajectory intercept greater than one exceeds the diffractive limit: $A(s, b) \rightarrow \frac{i}{2}$, as $s \rightarrow \infty$. The single Pomeron exchange amplitude first reaches this limit at $b = 0$ for $\sqrt{s} \approx 1$ TeV as shown in the impact parameter plot of fig.4.33. The amplitude will also eventually violate the unitarity bound $Im A(s, b) \leq 1$ at $\sqrt{s} \approx 300$ TeV. Adding terms which counteract the divergent behaviour of the Pomeron so that the full amplitude satisfies the diffractive limit will alter the $\sigma_T \sim s^\epsilon$ behaviour of the Pomeron term to a form consistent with the Froissart bound (3.3.7).

This problem is most acute for the Pomeron and weak cut model of §4 since the weak cut has little effect on the impact parameter amplitude. The different values of the Pomeron intercept, $\alpha_P(0)$, allowed in the fits of table 4.3(a) give the energy at which $Im A(s, b = 0) = \frac{1}{2}$ somewhere between 800 GeV and 2 TeV (see table 4.11). In the Donnachie-Landshoff model of §5.2, the Pomeron contribution similarly exceeds the diffractive limit for $\sqrt{s} = 1$ TeV, but the Pomeron cut term is larger than in the Pomeron and weak cut model and the combined amplitude does not reach the limit until $\sqrt{s} = 10$ TeV. In the eikonal models of chapters 6 and 7 the unitarity corrections prevent the amplitude from violating the diffractive limit, but we found that their effect at the lower ISR energies was inconsistent with the data. In this chapter we examine briefly an alternative model for how unitarity might be restored.

9.2. A Simple Model

The simplest way in which the amplitude can be constrained to stay within the diffractive limit is to truncate $Im A(s, b)$ for $Im A(s, b) > \frac{1}{2}$ as in fig.9.1. There are then no unitarity corrections for energies below approximately 1 TeV, for which $Im A(s, b) \leq \frac{1}{2}$; and above $\sqrt{s} = 1$ TeV, the unitarity correction simply cancels the imaginary part of the profile function above a half.

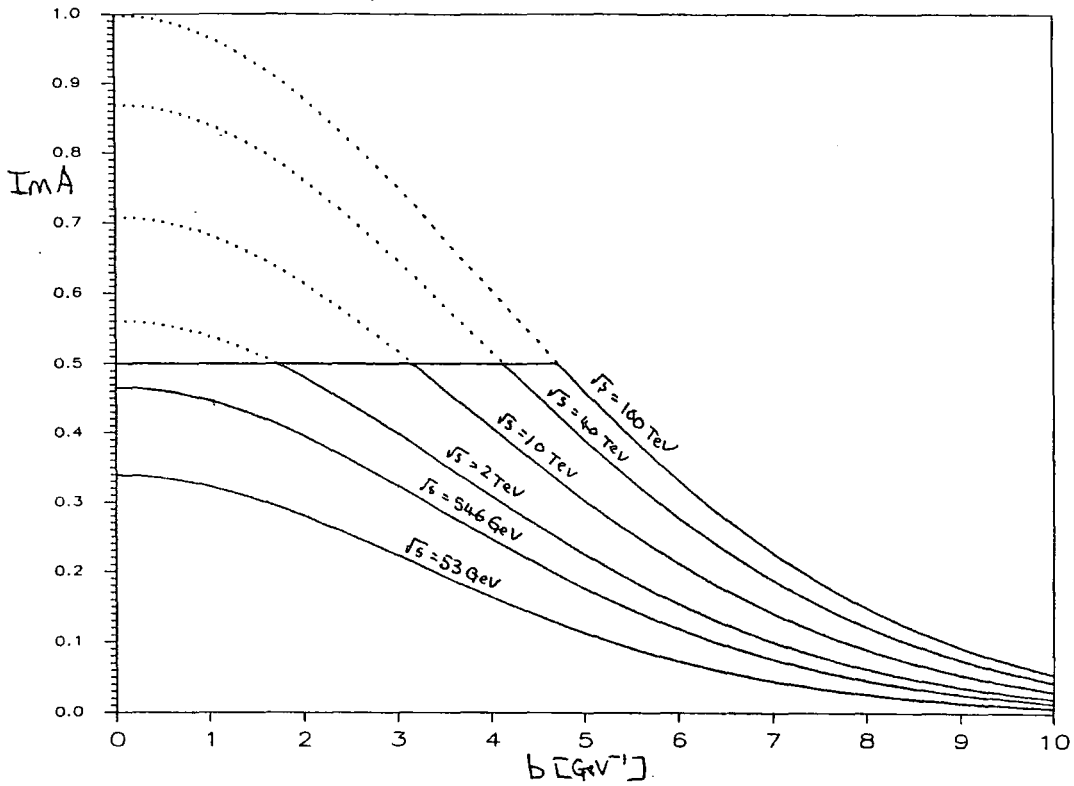


FIG. 9.1 In this simple model $Im A(s, b)$ is truncated for $Im A(s, b) > \frac{1}{2}$; resulting profile function for $\sqrt{s} = 53, 546 \text{ GeV}, 2, 10, 40$ and 100 TeV .

This prescription gives slightly different results to the eikonal model. Since the profile function has a maximum value at $b = 0$, the unitarity correction occurs first at small b and its radius in impact parameter space increases as the energy increases. In eikonal models the unitarity corrections appear gradually with energy rather than occurring suddenly at about 1 TeV as in the above and act over a larger range of b . In a first approximation they have radius $\frac{1}{\sqrt{2}} \times$ that of the Pomeron corresponding to $P \otimes P$ exchange. However, at high energies in eikonal models the profile function approaches a black disk limit (see §6.3) and since the tail of the profile function is dominated by single Pomeron exchange the models should be similar (though requiring different parameters for the Pomeron). In particular they should have the same asymptotic behaviours for σ_T and both satisfy the Froissart bound. This model gives the least effect upon $Im A(s, b)$ that will make the amplitude consistent with the diffractive limit and thus shows the minimum effect unitarity must have on the contribution to σ_T from the Pomeron. The effect on σ_T is shown in figure 9.2 using the Pomeron parameters from fit (4a) of §4.4. At $\sqrt{s} = 2$ and 40 TeV this produces a correction of

0.4 and 14 mb respectively. This is to be compared with a spread of about 10 and 30 mb at the two energies given by the different values of $\alpha_P(0)$ in the fits of table 4.3a (see table 4.11), and so is a comparatively small effect in σ_T at these energies.

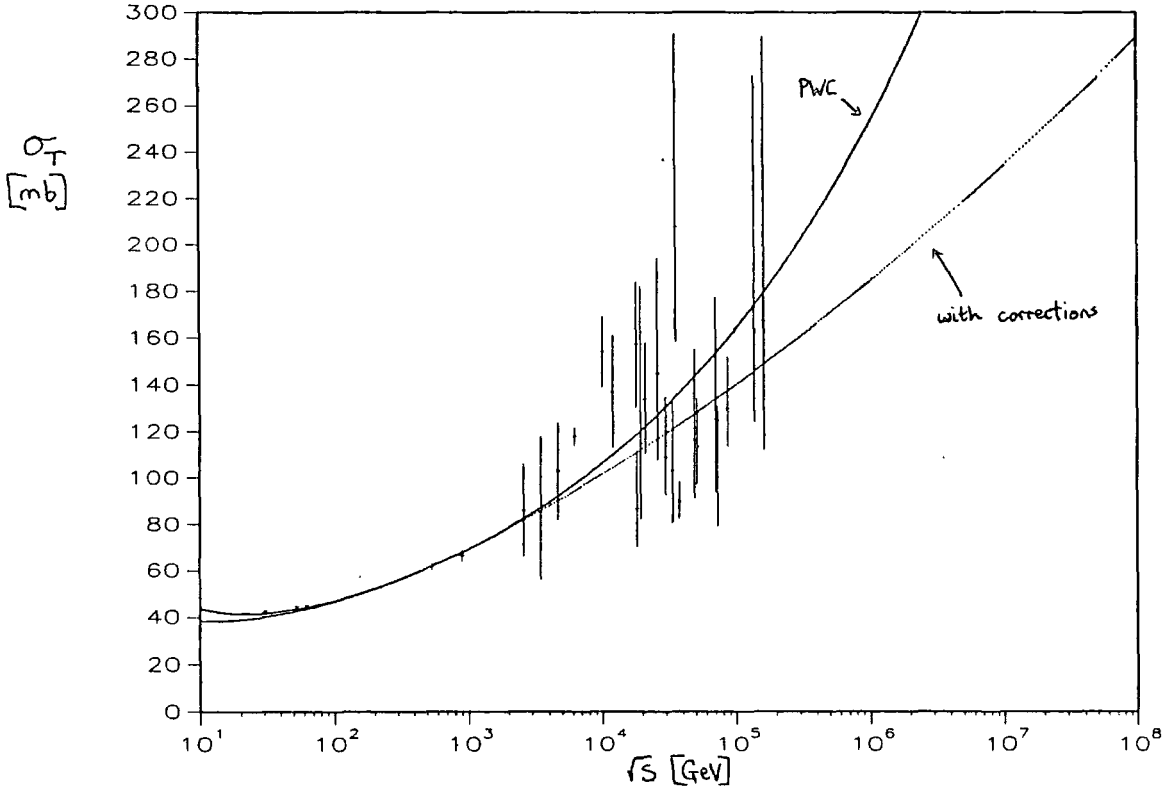


FIG. 9.2 Total cross-section using parameters of fit (4a) (full line) and unitarity correction in this simple model (dotted line).

The effect of the truncation of the profile function on the amplitude $A(s, t)$ is to produce a pure imaginary term with a flat t -dependence which first appears for $\sqrt{s} \geq 1$ TeV. The exponential t -dependence of the correction term and its magnitude at $t = 0$ increase with energy as the radius in impact parameter space increases. At very high energies the slope and magnitude of the Pomeron and correction become more nearly equal so they almost entirely cancel. This behaviour is shown in figure 9.3 at $\sqrt{s} = 1, 2, 10$ and 40 TeV.

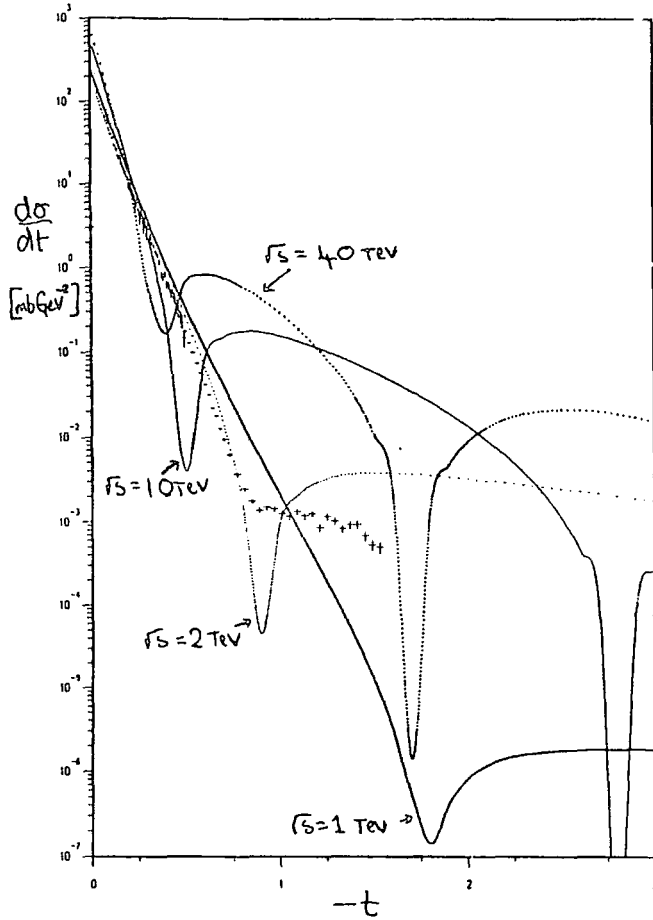


FIG. 9.3 Effect on $\frac{d\sigma}{dt}$ of minimum unitarity correction at $\sqrt{s} = 1, 2, 10$ and 40 TeV.

Thus, this simple model gives a contribution, which occurs suddenly for $\sqrt{s} \geq 1$ TeV, with a very flat t -dependence and increases rapidly with energy. At higher energies the range in impact parameter space increases and so the t -dependence of the correction term increases. Since the term is pure imaginary, interference with the Pomeron produces a sharp dip structure. It is tempting to try to associate this with the problem of the height of the Collider shoulder. However, by allowing the correction an arbitrary range in impact parameter space rather than just the minimum necessary to restore $Im A(s, b) < \frac{1}{2}$, the exponential slope of the correction term can be made arbitrarily steep (though this increases the magnitude at $t = 0$ and thus the effect of the correction on σ_T). If it is given the same range in impact parameter space as the Pomeron it will have the same t -dependence as the Pomeron and so be hidden by the Pomeron contribution. At collider energies the profile function has not reached $Im A(s, b) = \frac{1}{2}$ so that in this simple model there are no unitarity corrections.

9.3. An Extension of the Simple Model

The unitarity correction in the above model occurs suddenly for $\sqrt{s} \geq 1$ TeV. However, we would expect that, as in the eikonal model, the correction occurs as an analytic function of the energy and so has an effect at lower energies also. As in the model above we want the correction to act at smaller b than in the eikonal model. We also want to take account of the real part of the amplitude and the effect of the correction on the real part.

We want an analytic form for the profile function

$$A(s, b) = A(\chi(s, b)) \quad (9.3.1)$$

which satisfies the diffractive limit and in which the corrections appear smoothly as functions of energy and are negligible at ISR energies. This will then have qualitatively the same behaviour as the simple model above but the corrections will have some effect at lower energy and perhaps produce something which looks like the Collider shoulder.

So we want a function which has the behaviour :

$$A(\chi) \rightarrow \frac{i}{2} \quad \text{as } \text{Im } \chi \rightarrow \infty \quad (9.3.2)$$

$$A(\chi) \rightarrow \frac{\chi}{2} \quad \text{as } \text{Im } \chi \rightarrow 0 \quad (9.3.3)$$

The eikonal function (3.2.13) has these properties but at ISR energies $\text{Im } \chi(s, b = 0) \approx 0.6$ and so (9.3.3) is not a good approximation (see fig.6.2). We want a function for which (9.3.3) holds at ISR energies but in which modifications are produced at $\sqrt{s} = 546$ GeV where $\text{Im } \chi(s, b = 0) \approx 0.8$. So we generalize the eikonal function to the form

$$A(s, b) = \frac{i}{2} \left(1 - e^{-\Omega_N(x)} \right) \quad (9.3.4)$$

where

$$\begin{aligned} -\Omega_N(x) &= \sum_{n=1}^N \frac{-x^n}{n} \\ &\rightarrow \begin{cases} \log(1-x) & \text{for } |x| \rightarrow 0 \text{ or } N \rightarrow \infty, |x| < 1. \\ -\frac{x^N}{N} & \text{for } |x| \rightarrow \infty. \end{cases} \end{aligned} \quad (9.3.5)$$

so that

$$A(s, b) \simeq \begin{cases} \frac{i\chi}{2}, & \text{for small } \chi; \\ \frac{\chi}{2}, & \text{for } \chi \text{ large and +ve.} \end{cases} \quad (9.3.6)$$

and if we put $x \rightarrow -i\chi$ then

$$A(s, b) = \frac{i}{2} \left(1 - e^{-\Omega_N(-i\chi)} \right) \quad (9.3.7)$$

will have the behaviour we wanted *. For $N = 1$ we just have the eikonal model of §7 and for $N = \infty$ we have the simple model of §9.2. Increasing N interpolates between the two extremes. This behaviour is shown in figure 9.4(a) using $\chi = \chi_P(s, b)$ and the Pomeron parameters of fit (4a) for $N = 1, 2, 5, 10$ and ∞ . The effect of this on $\frac{d\sigma}{dt}$ at $\sqrt{s} = 546$ GeV is shown in figure 9.4(b).

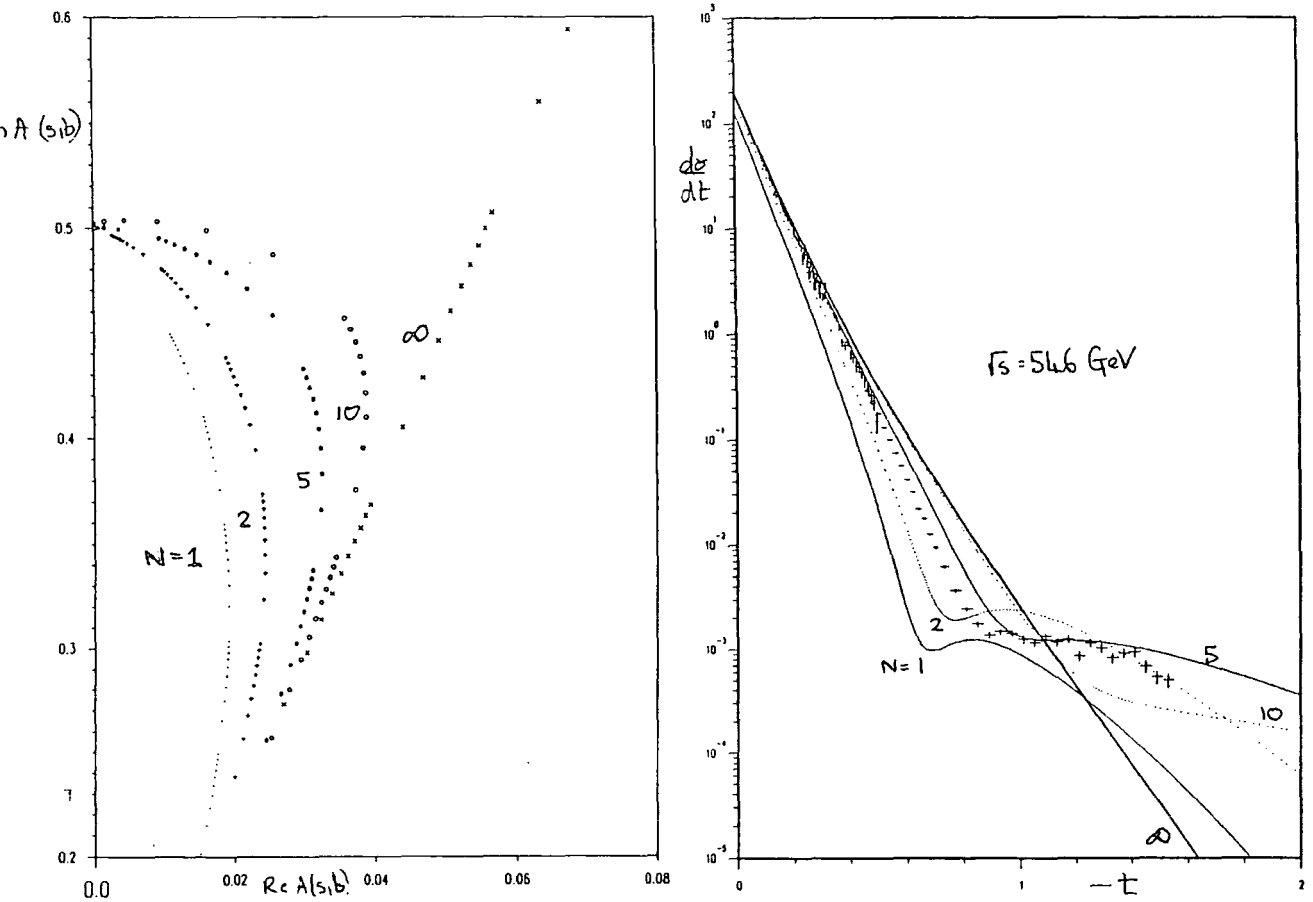
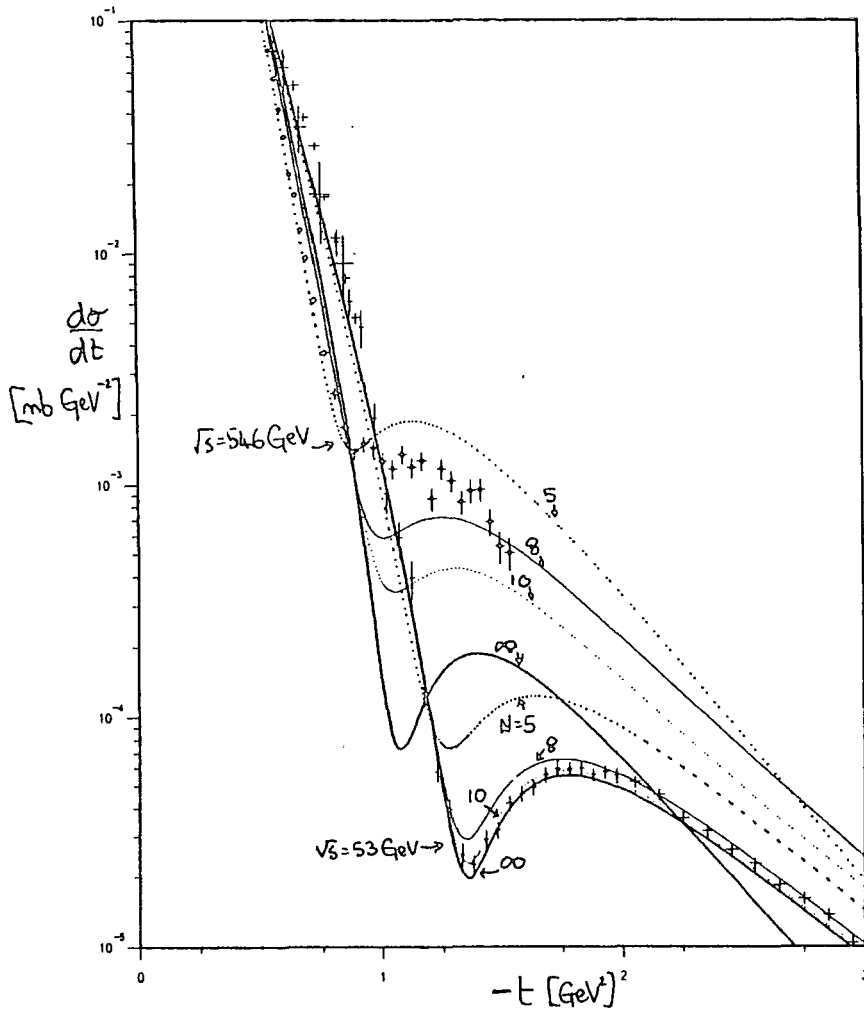


FIG. 9.4 Results using equation (9.3.7) and Pomeron term from fit (4a) for $N = 1, 2, 5, 10$ and ∞ ; (a) Argand plot for profile function at $b = 0$ as a function of energy, (b) $\frac{d\sigma}{dt}$ at $\sqrt{s} = 546$ GeV.

* For x complex we should also have $Re \{x\}^N \rightarrow +\infty$ as $Re x \rightarrow +\infty$ which is satisfied for the values of N we have used but is not true in general. This could be side-stepped by using the function $y = 1 - f(x)e^{-(x^*x)^{\frac{N}{2}}}$ where $f(x) = 1 - x - \dots$ is a polynomial of degree less than N .

As N increases the small $|t|$ differential cross-section approaches that from just the pole. For $N = 5$ this produces a reasonable description of the collider shoulder. It will not of course reproduce the large $|t|$ data at ISR energies without considerable manipulation, but for a suitable choice of Pomeron and N this could probably be accomplished also. This is precisely what the eikonal model of §7 did using $N = 1$ and should have the same problems. We reproduce the large $|t|$ cross-section by a more simple construction. If instead of using $x = -i\chi_P$ in (9.3.4) we use $x = -i(\chi_P + \chi_{\text{cut}})$, where χ_{cut} is the double Pomeron exchange contribution used in §4.4, then (9.3.7) with a suitable value of N gives an amplitude which is essentially just fit (4a) in the ISR energy region, but which has unitarity corrections at the collider energy that may allow a better account of the shoulder.

Using this form for x and varying N has the effect on $\frac{d\sigma}{dt}$ at $\sqrt{s} = 53$ and 546 GeV shown in figure 9.5 (for $n = 5, 8, 10$ and ∞). It can be seen that at $\sqrt{s} = 53$ GeV the dip is moved by the unitarity corrections and fills in slightly. As N increases the corrections become smaller and the amplitude approaches that due to just the pole and cut. At $\sqrt{s} = 546$ GeV the unitarity corrections are larger and move the dip more. Using $N = 8$ gives a correction that does not much effect the ISR data but goes some way to producing a shoulder at the collider. The prediction at the collider is still not very good but indicates that with a suitable parametrization of the Pomeron and cut at the ISR and a suitable choice for x in (9.3.4) a reasonable fit might be obtained.



1
 FIG. 9.5 Results for $\frac{d\sigma}{dt}$ at $\sqrt{s} = 53$ and 546 GeV using equation (9.3.7) and Pomeron and cut terms from fit (4a) for $N = 5, 8, 10$ and ∞ .

The function (9.3.7) produces less effect than the eikonal series at large b where χ is small, so that the unitarity corrections act at smaller b than in the eikonal series and thus have flatter t -dependence. The correction is imaginary and negative (at small $|t|$) and so has the effect of pulling the dip in to smaller $|t|$. Since the correction is larger at higher energies this increases the shrinkage seen. In fit (4a) the zero in the imaginary part of the amplitude is at too large a value of $|t|$ but the unitarity correction pulls it in to smaller $|t|$. One of the major problems we have encountered in the previous chapters in obtaining a satisfactory description of the data is reconciling the energy

independence of the ISR data with the growth of the differential cross-section between the ISR and the Collider. Effectively this model allows a small α_{eff} for the Pomeron at low energy, consistent with the energy dependence at large $|t|$, and an increased α_{eff} between the ISR and the collider. In this case the unitarity correction mimics quite closely the behaviour of the extra term (4.7.2) in fit(4d) which reproduces the collider shoulder. The effect on the real part of the amplitude is to reduce the real part at small b ; this gives the correction term a negative real part in the dip region and so increases the magnitude of the real part of the full amplitude (since the real part of $P + P \otimes P$ was negative in fit (4a)).

If we repeat this for fit (4d) (which has a Pomeron with larger α'_P , and a cut term with energy dependence given by α_{eff} and arbitrary phase), we find the unitarity correction produces a deeper dip at ISR and Collider energies. This is because in fit(4d) allowing an arbitrary phase for the cut resulted in the real part being positive in the dip region so that the unitarity correction reduces this and produces a deeper dip.

We can use the fits of §4.7 (which use an extra, arbitrary term to give the Collider shoulder) to estimate the effect of these unitarity corrections at ISR energies since the energy dependence of the profile function in (9.3.4) is determined by that of $\chi(s, b)$. If we assume the extra term (4.7.2) gives the unitarity correction at $\sqrt{s} = 546$ GeV then the unitarity correction at lower energies is determined. Figure 9.6 shows the same correction that the extra term makes to the profile function at $\sqrt{s} = 546$ GeV applied to the profile function at $\sqrt{s} = 53$ GeV. At $\sqrt{s} = 53$ GeV fits (4a) and (4d) give the results shown in figure 9.7(a) and 9.7(b), which indicate that if the unitarity corrections are generated as above their effects on $\frac{d\sigma}{dt}$ are of order 40% for $|t| \geq 2$ GeV². The validity of this argument depends on the extent to which the extra term is determined by the data, but together with fig.9.5 this provides an indication of the magnitude of the unitarity corrections at ISR energies.

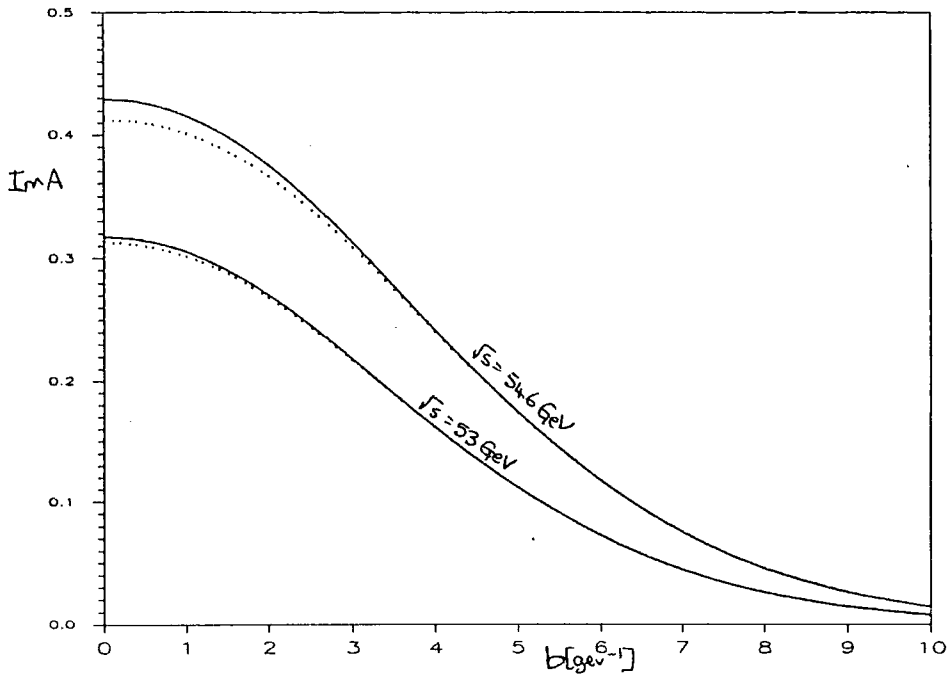


FIG. 9.6 Effect of extra term (4.7.2) on profile function from fit (4a) at $\sqrt{s} = 53$ and 546 GeV (solid line is $P + P \otimes P$, dotted line has extra term included).

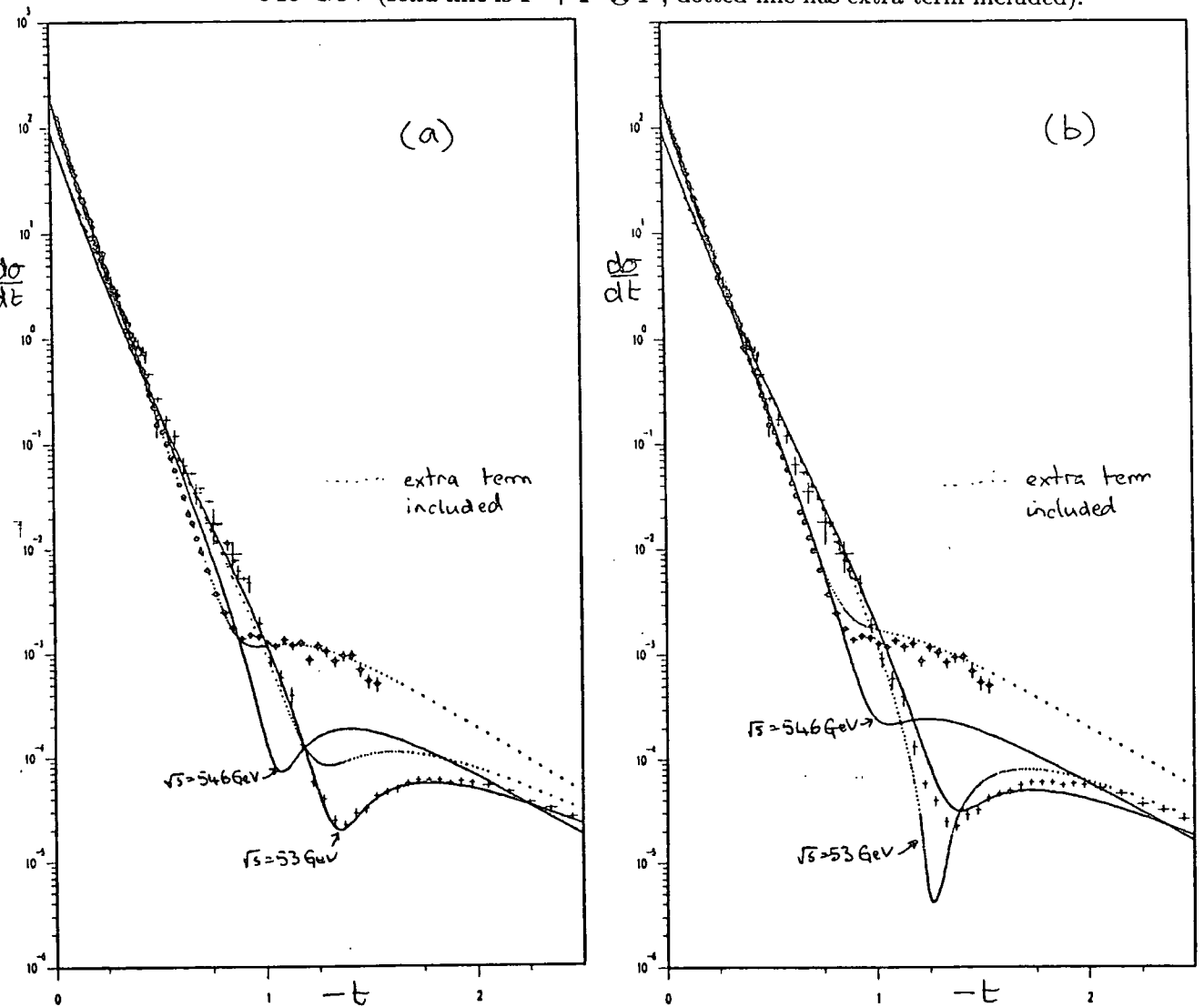


FIG. 9.7 Effect of extra term (4.7.2) on $\frac{d\sigma}{dt}$ at $\sqrt{s} = 53$ and 546 GeV for (a) fit (4a), (b) fit (4d).

In figure 9.8 we show the differential cross-section resulting from extrapolating equation (9.3.7), with the Pomeron and Pomeron cut of fit (4a) and $N = 8$, to $\sqrt{s} = 1, 5, 10$ and 40 TeV (the data at $\sqrt{s} = 546$ GeV are shown for comparison). This produces a shoulder at $\sqrt{s} = 1$ TeV, which deepens into a dip and moves inwards with increasing energy. At $\sqrt{s} = 1000$ TeV the second maximum is only a factor of $300\times$ less than the optical point which shows the rapid increase in the height of the second maximum from these unitarity corrections. The differential cross-section at large $|t|$ is rather more flat and a lot larger compared with other models (see figures 5.12 (DL model), 5.21 (GLN model), 6.10 (BSW model)). The impact parameter picture arising in this model and the eikonal models of §6 and §7 is similar to the BEL (blackier, edgier and larger) description of the data of Henzi and Valin (1979,1983,1985).

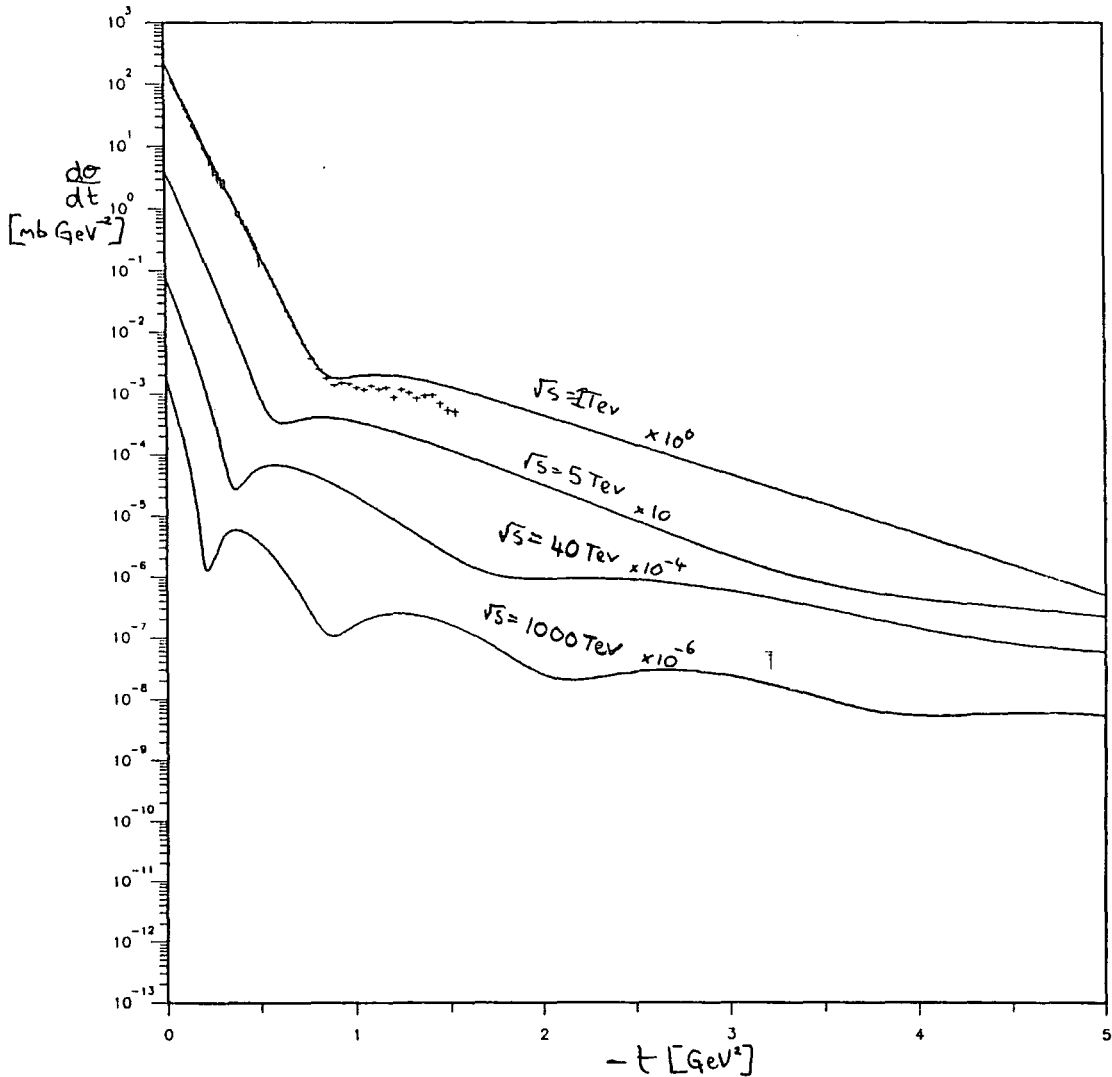


FIG. 9.8 Differential cross-section from (9.3.7) with $N = 8$ at $\sqrt{s} = 1, 5, 10$ and 40 TeV.

General Discussion and Summary

10.1. Summary of results.

In the above we have sought a description of the high energy total and elastic differential cross-sections. We have reviewed the existing models which theoretical and phenomenological prejudice present as likely candidates for the correct approach. No attempt has been made to make this review complete and numerous models have not been discussed. The data present us with certain characteristics which seem to result from the underlying dynamics involved and which we expect the model to describe in a natural manner, rather than as a complicated effect of different dynamical mechanisms. These are :

- the shrinkage of the forward peak with energy;
- approximate constancy of the pp total cross-section for $4 \leq \sqrt{s} \leq 30$ GeV and its subsequent rise up to $\sqrt{s} = 900$ GeV and beyond;
- the energy independence of the large $|t|$ data and dip position for $10 \leq \sqrt{s} \leq 63$ GeV;
- the rise of the differential cross-section from the ISR to the Collider;
- the behaviour of the $pp/\bar{p}p$ difference at low energies and at $\sqrt{s} = 53$ GeV.

How naturally these effects are described by a given model determines how believable the model is. We note that the status of the pp and $\bar{p}p$ difference in $\frac{d\sigma}{dt}$ at $\sqrt{s} = 53$ GeV discussed in §2.5 is enhanced by the inability of any model with an even charge conjugation amplitude to give a natural description of the rest of the data.

We have examined how well these various models explain the above characteristics, using as a basis the PWC model discussed in chapter 4. Prior to the Collider this gave good agreement with the elastic scattering data. The energy independence of the large $|t|$ cross-section at the ISR and the evolution of the dip structure arose in a simple, economical fashion from the interference of the Pomeron and the Pomeron cut. The low energy differential cross-section was reasonably well described by small perturbations which were negligible at higher energies. This model is therefore in conflict with the difference observed in the dip region at $\sqrt{s} = 53$ GeV between pp and $\bar{p}p$, but given the uncertainties in the $\bar{p}p$ data (see §2.5) this did not seem an untenable position. However, it was clear that, confronted with the σ_T and $\frac{d\sigma}{dt}$ Collider data, the model needed some modification.

In its original form the PWC model is incapable of reproducing either the shrinkage at small $|t|$ or the change in dip structure between the ISR and Collider energies whilst retaining the description of a Pomeron cut term dominating the large $|t|$ amplitude. The modifications we made to the model in §4.5 and §4.6, in which we looked at the effects of a non-linear Regge trajectory for the Pomeron and of more t -dependence in the Gribov vertex, did improve the agreement with some aspects of the data, but neither gave a good overall description. Bending the Pomeron trajectory allowed us to produce a sharp dip at ISR energies which developed into a shoulder by the Collider energy, but the magnitude of the shoulder and the energy dependence of the dip were in disagreement with the data. Altering the Gribov vertex in the parametrization of the Pomeron cut allowed us to fit the data at $\sqrt{s} = 53$ and 546 GeV but could not then reproduce the energy independence at large $|t|$. These problems appear to some extent in all the models we looked at. Agreement with the Collider shoulder makes it difficult to maintain the energy independence at ISR energies of $\frac{d\sigma}{dt}$ at large $|t|$ and in the dip region.

In §4.8 we fitted the Pomeron parameters with an arbitrary parametrization of the terms producing the Collider shoulder and ISR large $|t|$. This again demonstrated that the phase necessary to produce the dip at ISR energies is not that of the Pomeron cut alone. We looked at a very simple parametrization of low energy effects which suggested that, at the lower ISR energies at least, these were not necessarily negligible. The conclusion from this analysis of the PWC model is that though it might still be possible to fit the available data by incorporating suitable low energy effects this approach is not supported by the data. If a new mechanism is responsible for the Collider shoulder the situation is improved and, though the model still has some difficulty reproducing the shrinkage at small $|t|$, an arbitrary parametrization of this extra term allows a reasonable description of the data. We also noted that the increased energy dependence of the Pomeron, which was necessary to describe the rising total cross-section, brings it into conflict with unitarity for energies of order 1 Tev.

There seem to be two candidates for necessary modifications of the PWC model: a term with odd charge conjugation to produce the $pp/\bar{p}p$ difference at $\sqrt{s} = 53$ GeV; or correction terms to prevent the Pomeron amplitude violating unitarity. We reviewed the DL and GLN models which are examples of the former and the BSW model which is an example of the latter.

The DL model gave a good overall description of the pp and $\bar{p}p$ data from the ISR and the Collider and, though it does not attempt to account properly for the low energy cross-section, is not unreasonable at low energy. However, on the minus side, the model also requires the existence of residual low energy effects to help produce the ISR dip and the theoretical and phenomenological evidence for the 3-gluon description of the large $|t|$ amplitude is not compelling. The unitarity problem is delayed to energies of order 10 Tev but still needs to be addressed. The GLN model also gave good agreement with the data but lacked any physical motivation for the form of the amplitude. The odd charge conjugation term was responsible for the Collider shoulder which required some mechanism to make it vanish in the ISR dip region in order to be compatible with the relatively small $pp/\bar{p}p$ difference. As in the DL model, the large $|t|$ amplitude is dominated by an energy independent, odd charge conjugation contribution.

We attempted to describe the extra contribution necessary in the PWC model by an odd charge conjugation contribution akin to the Pomeron. However, the phase of the arbitrary term added to the PWC model to produce the shoulder in §4.7 does not look like such an Odderon contribution. The small $pp/\bar{p}p$ difference at $\sqrt{s} = 53$ GeV constrained the size of the simple Odderon contribution we used so that it could not have much effect at the Collider energy and the fits did not reproduce very well the energy independence at large $|t|$. If an Odderon contribution is to be made to work within the PWC model it must be more complicated than the simple form we considered.

We then looked at the BSW model which explicitly satisfies s -channel unitarity and the Froissart bound through eikonalization of the basic exchange. This produced a shoulder at the Collider 50% above the data and again had difficulty reproducing the energy independence of the dip region and large $|t|$. The dip in $\frac{d\sigma}{dt}$ at the ISR was again a result of low energy effects. These were calculated by including a Reggeon contribution in the eikonal phase, which resulted in the parameters of the Regge trajectories being lower and flatter than the corresponding particle masses indicate and gave bad fits to the low energy σ_T and $\frac{d\sigma}{dt}$ data. In order to prevent further, spurious dips in the differential cross-section at large $|t|$ it was necessary to include zero-crossings in the t -dependence of the Born term at large $|t|$. The non-Regge phase of the Born term resulted in better cancellation of the diffractive contribution in the dip region than otherwise and therefore a smaller residual Reggeon contribution. The model gave a

poor fit to the $|t| \geq 6 \text{ GeV}^2$ data from FNAL and the ISR.

In §7 we attempted to construct a similar description but using a Born term with a proper Regge phase and which avoids conflict with t -channel unitarity since it results from a moving j -plane pole. This exaggerated the problems encountered in the BSW model. The large Reggeon contributions required to produce a deep enough dip at the higher ISR energies did not allow a reasonable fit to the lower energy ISR data. It was still necessary to include a non-factorizable zero-crossing in the t -dependence of the Born term and the behaviour of the cross-section in the dip region favoured a small value for α'_p . The magnitude of the shoulder predicted at the Collider was too large to give good agreement with the data.

We also briefly reviewed the predictions of critical and perturbative Reggeon field theory. Though critical Reggeon field theory provides an interesting theoretical framework for doing calculations it does not give a viable phenomenology (at least not at present energies). As with most models it does produce dip/bump structures but their magnitudes are not in agreement with the data. The predicted asymptotic behaviour of the total cross-section, $\sigma_T \sim \log^{0.26} s$, and of the total elastic cross-section, $\sigma_{el} \sim \log^{-\frac{5}{6}} s$ (see Moshe (1978)), are also contrary to the trend of the data. The perturbative Regge calculus seems to be very similar to the Regge-Eikonal description we tested in §7 and seems likely to produce different results only at larger $|t|$ or higher energies, but a description of the differential cross-section has not yet been attempted.

Finally, in §9 we considered an admittedly rather *ad hoc* model for preventing the amplitude violating unitarity in which the ISR energy amplitude is “protected” from unitarity corrections, so that we can have the original PWC model at these and lower energies but which has substantial corrections at the Collider energy and beyond. This disassociates the cut contribution of (3.6.9) from any unitarizing role and properly separates the requirements of s -channel unitarity and the prediction of Mandelstam cuts. We estimated the effect that the unitarity corrections would have at ISR energies to be of order 40% if they were to reproduce the Collider shoulder, but have not attempted detailed fits to the parametrization of the Born term with this general unitarizing form.

It is clear from the above that low energy effects though relatively small at ISR ener-

gies still play an important role in the phenomenology and so a much more detailed description of the low energy dynamics needs to be undertaken for each model that claims to describe the high energy behaviour of the cross-section in order to check the consistency of the model. Further measurement of $\frac{d\sigma}{dt}$ for pp and $\bar{p}p$ at similar energies is essential to confirm the existence of an odd charge conjugation contribution remaining at high energy. The effects of unitarity corrections and Pomeron cuts are important at current energies and will determine the behaviour of the amplitude at the higher energies of the UNK, LHC and SSC.

10.2. Comparison of High Energy Predictions.

In figure 10.1 we compare the asymptotic predictions for σ_T of the various models we have discussed. Also included for comparison is a simple $\log^2 s$ fit to the data as in §4.2 given by equation (10.2.1).

$$\sigma_T = \frac{1}{s}(30s + 0.2s \log^2 s + 66.6s^{0.533} \pm 41.6s^{0.412}) \text{ mb} \quad (10.2.1)$$

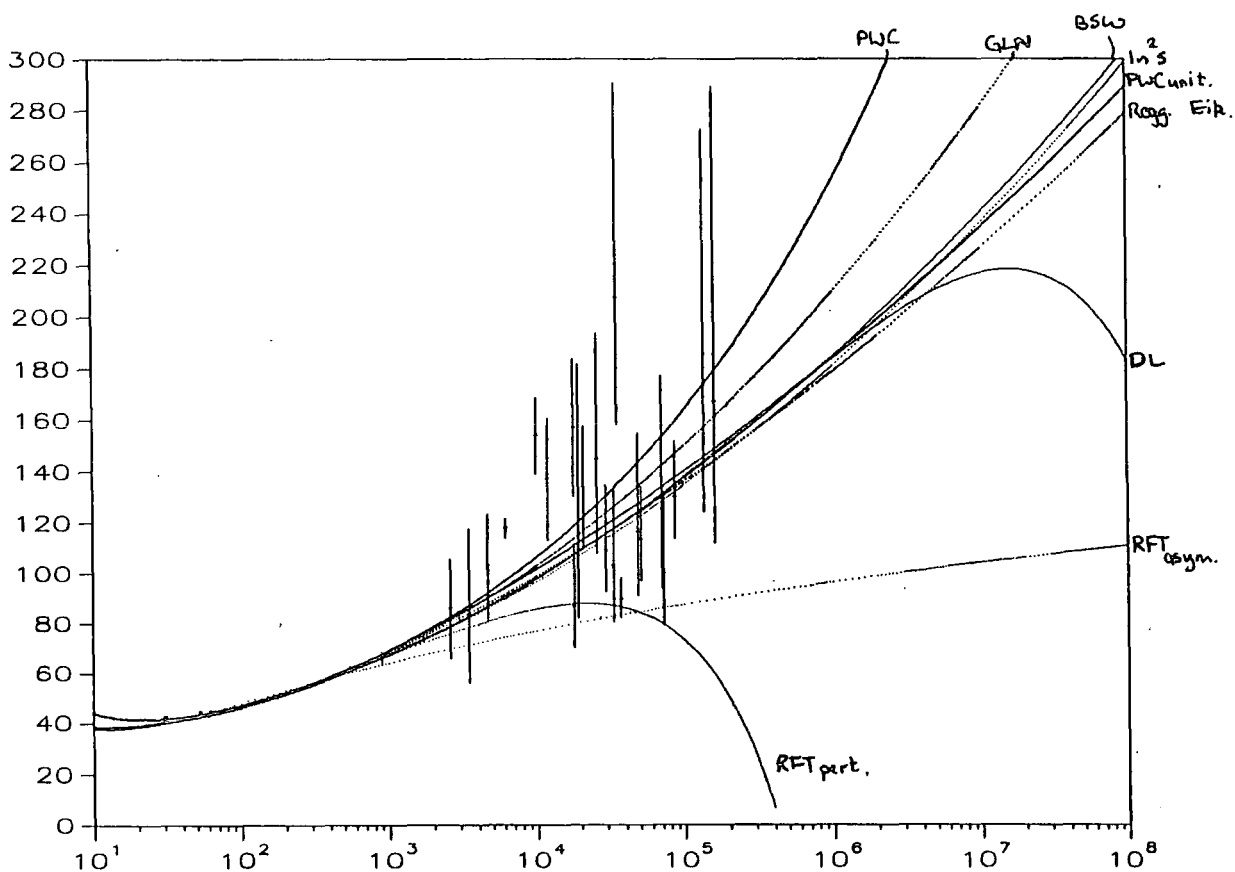


FIG.10.1 High energy σ_T predictions for PWC, DL, GLN, BSW, Regge-Eikonal, critical RFT, unitarized PWC and $\log^2 s$ models.

We see that the DL, BSW, Regge-Eikonal and unitarized PWC model all give very similar predictions for the high energy behaviour of the total cross-section, within 10 mb of each other for $\sqrt{s} \leq 10^6$ GeV. Only the critical RFT model significantly disagrees with the cosmic ray data. The perturbative RFT model and the DL model have unphysical behaviour at high energy because higher order terms have been omitted. The predictions of the various models for $\sigma_T(pp)$ at $\sqrt{s} = 2$ and 40 Tev are given in table 10.1 . Typical values at these two energies are 76 and 120 mb respectively.

Model	$\sqrt{s} = 2$ Tev	$\sqrt{s} = 40$ Tev
PWC §4.2	78.7 mb	137.9 mb
PWC _{unit.} §9.2	78.3 mb	123.9 mb
GLN §5.3	77.3 mb	129.7 mb
BSW §6.4	75.6 mb	120.4 mb
RE §7.2	76.7 mb	120.3 mb
DL §5.2	75.3 mb	120.8 mb
RFT _{asym.} §8.2	68.3 mb	83.5 mb
RFT _{pert.} §8.2	73.6 mb	86.1 mb
$\log^2 s$ §10.1	75.0 mb	118.3 mb

TABLE 10.1 Predictions of $\sigma_T(pp)$ for various models at $\sqrt{s} = 2$ and 40 Tev.

10.3. Future Prospects.

If the recent value of $\rho(\bar{p}p)$ found at $\sqrt{s} = 546$ GeV mentioned in §2.4 turns out to be correct this holds strong implications as to the nature of the high energy amplitude. The first point to mention is that with this new value of ρ the total cross-section at the Collider is reduced by 3% to 59.8 mb. Clearly the phase associated with this value of Re/Im is incompatible with purely an even charge conjugation contribution dominating the small $|t|$ amplitude and hints again at the possibility of a fairly large Odderon contribution at high energies. We note that the Odderon used in the GLN model has the opposite effect to that required by this new data. It reduces the value of $\rho(\bar{p}p)$ to 0.106 and increases $\rho(pp)$ to 0.176 and the value of σ_T at the Collider. If the Odderon is to cancel the real part of the even signatured amplitude in the dip

region it must have positive real part in pp , and so if it is to add to the real part in $\bar{p}p$ at $t = 0$ it must change sign in between. An Odderon similar to that in the GLN model with opposite sign and with a zero crossing at smaller $|t|$ would have the right effect. The Odderon amplitude in the GLN model at $\sqrt{s} = 53$ and 546 GeV is shown in figure 10.2 .

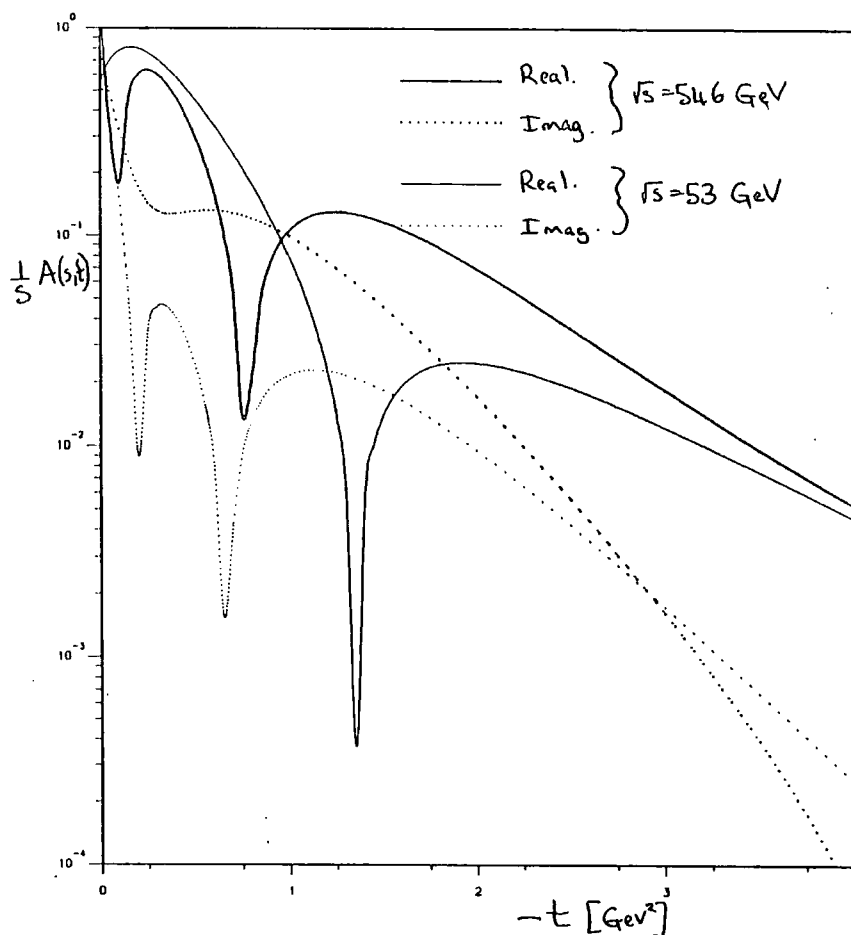


FIG.10.2 Real and imaginary parts of the Odderon contribution at $\sqrt{s} = 53$ and 546 GeV in the GLN model.

Testing this idea in the model of §5.4 would seem a reasonable next step. As noted there, a zero crossing in the real part of the Odderon amplitude in the dip region appears to be necessary if the Odderon is to have any effect on the differential cross-section at the Collider energy.

The situation may be cleared up by data at higher energies from the new machines. It is unlikely that a measurement of σ_T at these energies will help to differentiate much between the various models. A measurement for both ρ or $\frac{d\sigma}{dt}$ in the dip region at

similar energies would help most in defining the Odderon contribution. A measurement of the shrinkage and height of the second maximum would be most useful in fixing the unitarity corrections.

We note, in connection with the above comments, that in response to the measurement of Re/Im at the Collider a new version of the GLN model has recently been published (Gauron (1987)) in which the sign of the Odderon contribution is reversed. This allows the new value of Re/Im to be reproduced by the model at $t = 0$ but a description of the t -dependence has not yet been obtained. This affirms the problem of obtaining a detailed description of the odd C component of the high energy amplitude noted in §5.

10.4. Conclusions.

Of the models we have examined the Odderon models of DL and GLN do best in reproducing the data, though these do not yet give a satisfactory description of the low energy data. If we disregard the recent measurement of ρ at the $S\bar{p}pS$ Collider, then it seems preferable to describe the Collider shoulder as an even charge conjugation effect since this can be attributed to unitarity corrections which must be present if the Pomeron is not to violate unitarity at higher energies. The available data do not allow an odd charge conjugate term to be pinned down very well but indicate that such a term must have complicated structure and energy dependence. Though clearly such a parametrization is possible, it is very speculative. We do not then expect to see any further $pp/\bar{p}p$ differences at higher energies. If this is the case it will be disappointing from a phenomenological viewpoint since the new machines will not reveal more of the tantalizing glimpse of an odd charge conjugation contribution seen at the subsequently decommissioned ISR.

Measurements of cross-sections at higher energies should improve our understanding of the behaviour of the unitarity corrections and perhaps throw more light on the phenomenology at the ISR energies. As it stands, if it is believed an odd charge conjugation contribution survives up to $\sqrt{s} = 53$ GeV as the data suggests, then the choice is between the DL (or similar model with a reggeized $C = -1$ exchange at large $|t|$) or a $C = +1$ dominated model with a small $C = -1$ contribution which surfaces

only in the dip region (and perhaps slightly affects the small $|t|$ slope), though it does not seem to be possible to describe the latter contribution as a Regge pole effect.

Conventional eikonal type models with even signed components only do not reproduce the Collider shoulder and the ISR data very well. It is not too surprising however that the behaviour of the unitarity corrections is more complicated than the simple eikonal model predicts. The description afforded by the unitarized model of chapter 9 seems likely to give a more reasonable account of the data.

So the situation cannot as yet be resolved. The surprising value for the recent measurement for ρ hints that there may be more surprises in store at higher energies. If the value is confirmed it should help to understand the phenomenology of the Odderon.

Appendix A

Normalization and useful formulae.

In the above the elastic scattering amplitude, $A(s, t)$, is dimensionless and the total and differential cross-sections are given by

$$\sigma_T = \frac{0.3893}{s} \text{Im } A(s, t) \text{ mb} \quad (\text{A.1})$$

and

$$\frac{d\sigma}{dt} = \frac{0.3893}{16\pi s^2} |A(s, t)|^2 \text{ mb GeV}^{-2} \quad (\text{A.2})$$

For $f(z)$ analytic in C , Cauchy's integral formula gives

$$\oint_C \frac{f(z)}{z - a} dz = \frac{1}{2\pi i} f(a) \quad (\text{A.3})$$

Integrals involving zeroth order Bessel functions :

$$\int_0^\infty b db J_0(b\sqrt{-t}) e^{-\frac{b^2}{4c}} = 2ce^{ct} \quad (\text{A.4})$$

$$\int_{-\infty}^0 dt J_0(b\sqrt{-t}) e^{ct} = \frac{e^{-\frac{b^2}{4c}}}{c} \quad (\text{A.5})$$

$$\int_0^R b db J_0(b\sqrt{-t}) = \frac{R}{\sqrt{-t}} J_1(R\sqrt{-t}) \quad (\text{A.6})$$

Similarly for the modified Bessel function of the first kind, $I_n(x)$, where

$$I_n(x) = (-i)^n J_n(ix) \quad (\text{A.7})$$

we have

$$\int_0^R b db I_0(b\sqrt{t}) = \frac{R}{\sqrt{t}} I_1(R\sqrt{t}) \quad (\text{A.8})$$

The series expansion of the Bessel function, $J_n(z)$, is given by

$$J_n(z) = \sum_{k=0}^{\infty} (-1)^k \frac{\left(\frac{z}{2}\right)^{n+2k}}{k!(n+k)!} \quad \text{for } |z| < \infty \quad (\text{A.9})$$

and

$$J_1(z) = -J'_0(z) \quad (A.10)$$

The asymptotic behaviour of the Bessel functions are :

$$J_{\pm\nu} \rightarrow \sqrt{\frac{2}{\pi z}} \left\{ \cos\left(z \mp \frac{\pi}{2}\nu - \frac{\pi}{4}\right) + \frac{1}{8z} \sin\left(z \mp \frac{\pi}{2}\nu - \frac{\pi}{4}\right) \right\} \quad \text{for } z \rightarrow \infty \quad (A.11)$$

and

$$I_{\pm\nu} \rightarrow \frac{e^z}{\sqrt{2\pi z}} + \frac{e^{(-z \pm (\nu + \frac{1}{2})\pi i)}}{\sqrt{2\pi z}} \quad \text{for } z \rightarrow \infty \quad (A.12)$$

Appendix B

Details of the DL model parametrization and parameter values.

The following parametrization was used in the fits of §5.2.

Pomeron :

$$A^P(s, t) = -G_P (e^{-i\frac{\pi}{2}} s)^{\alpha_P(0)} e^{c_P t} [(1-x) + x e^{a_1 t}] \quad (B.1)$$

Reggeons :

$$A^f(s, t) = -G_f (e^{-i\frac{\pi}{2}} s)^{\alpha_f(0)} e^{c_f t} \quad (B.2)$$

$$A^\omega(s, t) = \mp i G_\omega (e^{-i\frac{\pi}{2}} s)^{\alpha_\omega(0)} e^{c_\omega t} \quad \text{for } \begin{array}{l} pp \\ \bar{p}p \end{array} \quad (B.3)$$

where $c_R = a_R + \alpha'_R (\log s - i\frac{\pi}{2})$ and

$$\begin{aligned} \beta_P &= G_P \sin \frac{\pi}{2} \alpha_P(0) \\ \beta_f &= \frac{1}{0.3893} G_f \sin \frac{\pi}{2} \alpha_f(0) \\ \beta_\omega &= \frac{1}{0.3893} G_\omega \cos \frac{\pi}{2} \alpha_\omega(0) \end{aligned} \quad (B.4)$$

Pomeron cut :

$$\begin{aligned} A^{2P}(s, t) &= + \frac{\lambda_{2P} G_P^2}{32\pi} (e^{-i\frac{\pi}{2}} s)^{2\alpha_P(0)-1} \left[\frac{(1-x)^2}{c_P} \exp \left\{ \frac{1}{2} c_P t \right\} \right. \\ &\quad + \frac{4x(1-x)}{(a_1 + 2c_P)} \exp \left\{ \frac{c_P(a_1 + c_P)}{(a_1 + 2c_P)} t \right\} \\ &\quad \left. + \frac{x^2}{(a_1 + c_P)} \exp \left\{ \frac{1}{2} (a_1 + c_P) t \right\} \right] \end{aligned} \quad (B.5)$$

Reggeon-Pomeron cuts :

$$A_{RP}(s, t) = \frac{\lambda_{RP} x_R G_R G_P}{16\pi} (e^{-i\frac{\pi}{2}} s)^{\alpha_{RP}(0)} \frac{e^{\frac{c_R c_P}{c_R + c_P} t}}{c_R + c_P} \quad (B.6)$$

where $x_R = \frac{1}{-i}$ for $R = \begin{array}{l} f \\ \omega \end{array}$.

The 3-gluon term (notation corresponds to Donnachie and Landshoff (1979)) :

$$\begin{aligned} A_{3g}(s, t) &= 2s D_{3g} \\ &= \mp \frac{2s K_{3g} \alpha_s^3 A^4}{t_0 - t} \int_0^1 dx_1 dx_2 dx_3 \delta(1 - x_1 - x_2 - x_3) (x_1 x_2 x_3)^6 D(x_1, t) D(x_2, t) D(x_3, t) \\ &= \mp 2s \frac{f_{3g}}{1.586 \times 10^{-7}} \sqrt{\frac{4\pi C}{0.3893}} \times \frac{\text{Integral}}{t_0 - t} \quad \text{for } \begin{array}{l} pp \\ \bar{p}p \end{array} \end{aligned} \quad (B.7)$$

where

$$D(x_i, t) = \begin{cases} \frac{1}{tx_i^2} & \text{if } x_i^2 \geq \frac{t_1}{t}; \\ \frac{2}{t_1^3} x_i^2 t (x_i^2 t + \frac{3}{2} t_1) & \text{otherwise.} \end{cases} \quad (B.8)$$

For large $|t|$ this gives

$$\frac{d\sigma}{dt} \sim f_{3g}^2 C t^{-8} \quad (B.9)$$

In the calculation of §5.2 we calculated the above integral numerically and stored the result (independent of energy) in a look-up table.

$\alpha_P(0)$	1.095	$\alpha_f(0)$	0.610	$\alpha_\omega(0)$	0.412
α'_P	0.161 GeV ⁻²	α'_f	0.805 GeV ⁻²	α'_ω	0.922 GeV ⁻²
β_P	20.7 mb	β_f	73.9 mb	β_ω	41.6 mb
a_P	1.99 GeV ⁻²	a_f	1.89 GeV ⁻²	a_ω	1.99 GeV ⁻²
a_1	4.28 GeV ⁻²	λ_{fP}	0.4	$\lambda_{\omega P}$	0.4
x	0.667	t_0	0.33 GeV ²	C	0.09 mb GeV ⁻²
λ_{2P}	0.450	t_1	0.33 GeV ²	f_{3g}	1.5

TABLE B.1 Parameter values for DL model used in §5.2.

We have also used the form from Donnachie and Landshoff (1986):

$$A_P(s, t) = 2is[3\beta F_1(t)]^2 \left(e^{-i\frac{\pi}{2}} \frac{s}{s_0} \right)^{\alpha_P(t)-1} \quad (B.10)$$

$$A_R(s, t) = 2is[3\beta F_1(t)]^2 [A \pm iB] \left(e^{-i\frac{\pi}{2}} \frac{s}{s_0} \right)^{\alpha_R(t)-1} \quad (B.11)$$

$$A_{2P}(s, t) = -2is \frac{81\lambda_{2P}}{16\pi} \beta^4 \left[\int_0^\infty b db J_0(b\sqrt{-t}) \times \left\{ \int_{-\infty}^0 dt' [F_1(t')]^2 e^{\alpha'_P(\log \frac{s}{s_0} - i\frac{\pi}{2})t'} \right\}^2 \right] \quad (B.12)$$

$$\begin{aligned}
A_{RP}(s, t) = & -2is \frac{2\lambda_{RP}}{16\pi} (3\beta)^4 \left(e^{-i\frac{\pi}{2}} \frac{s}{s_0} \right)^{\alpha_R(0)-1} (A \pm iB) \left[\int_0^\infty b db J_0(b\sqrt{-t}) \right. \\
& \times \left\{ \int_{-\infty}^0 dt' \left[F_1(t') \right]^2 e^{\alpha'_P(\log \frac{s}{s_0} - i\frac{\pi}{2})t'} \right\} \\
& \times \left. \left\{ \int_{-\infty}^0 dt' \left[F_1(t') \right]^2 e^{\alpha'_P(\log \frac{s}{s_0} - i\frac{\pi}{2})t'} \right\} \right]
\end{aligned} \tag{B.13}$$

where $F_1(t)$ is given by (5.2.3)

By analogy with the 3-gluon calculation we also have for the triple-Pomeron exchange term :

$$A_{3P}(s, t) = \frac{iK_{3P}A^4}{t_0 - t} \left(\frac{\beta^2}{4\pi} \right)^3 \int_0^1 \delta(1 - x_1 - x_2 - x_3) \prod_i^3 dx_i (x_i)^6 \left(e^{-i\frac{\pi}{2}} \frac{x_i^2 s}{s_0} \right)^{\epsilon_P + \alpha'_P x_i^2 t} \tag{B.14}$$

and a similar form for Pomeron-two-gluon exchange. These can be calculated for $\alpha_s \approx 0.3$, but unlike the 3-gluon term must be separately evaluated at each energy.

Appendix C

Details of the GLN model parametrization and parameter values.

This parametrization is described in Gauron and Nicolescu (1986). The two terms important at asymptotic energies, the Froissaron and Odderon, are given by

$$A_{\text{Fr}}(s, t) = \frac{is}{0.3893} \left\{ F_1 \log^2 \tilde{s} \frac{2J_1(R_+ \tilde{\tau})}{R_+ \tilde{\tau}} e^{b_1^+ t} + F_2 \log \tilde{s} J_0(R_+ \tilde{\tau}) e^{b_2^+ t} + F_3 [J_0(R_+ \tilde{\tau}) - R_+ \tilde{\tau} J_1(R_+ \tilde{\tau})] e^{b_3^+ t} \right\} \quad (\text{C.1})$$

$$A_{\text{Od}}(s, t) = \frac{s}{0.3893} \left\{ O_1 \log^2 \tilde{s} \frac{\sin(R_- \tilde{\tau})}{R_- \tilde{\tau}} e^{b_1^- t} + O_2 \log \tilde{s} \cos(R_- \tilde{\tau}) e^{b_2^- t} + O_3 e^{b_3^- t} \right\} \quad (\text{C.2})$$

where $\tilde{s} = s e^{-i\frac{\pi}{2}}$ and $\tilde{\tau} = \sqrt{-t} \log \tilde{s}$. We evaluated the complex Bessel functions to an accuracy of one part in 10^{-6} using the series expansion (A.9).

The Pomeron and Pomeron cut contributions are given by

$$A_P(s, t) = -\frac{\beta_P}{0.3893} \frac{e^{a_P t}}{\sin \frac{\pi}{2} \alpha_P(t)} (e^{-i\frac{\pi}{2}} s)^{\alpha_P(t)} \quad (\text{C.3})$$

$$A^{2P}(s, t) = \frac{\beta_{2P}}{0.3893} e^{b_{2P} t} \frac{(e^{-i\frac{\pi}{2}} s)^{\alpha_{2P}(t)}}{\log \tilde{s}} \quad (\text{C.4})$$

where $\alpha_P(t) = 1 + \alpha'_P t$ and $\alpha_{2P}(t) = 1 + \frac{\alpha'_{2P}}{2} t$.

The Reggeon contributions are given by

$$A_f(s, t) = \frac{\beta_f \gamma_f(t)}{0.3893} e^{a_f t} \frac{(e^{-i\frac{\pi}{2}} s)^{\alpha_f(t)}}{\sin \frac{\pi}{2} \alpha_f(t)} \quad (\text{C.5})$$

and

$$A^\omega(s, t) = \mp i \frac{\beta_\omega \gamma_\omega(t)}{0.3893} e^{a_\omega t} \frac{(e^{-i\frac{\pi}{2}} s)^{\alpha_\omega(t)}}{\cos \frac{\pi}{2} \alpha_\omega(t)} \quad \text{for} \quad \begin{array}{l} pp \\ \bar{p}p \end{array} \quad (\text{C.6})$$

where $\alpha_R(t) = \alpha_R(0) + \alpha'_R t$ with $\alpha'_f = \alpha'_\omega = \alpha'_R$ and $\gamma_R(t) = \frac{\alpha_R(t)(\alpha_R(t)+1)(\alpha_R(t)+2)}{\alpha_R(0)(\alpha_R(0)+1)(\alpha_R(0)+2)}$.

The Reggeon-Pomeron cut terms are given by

$$A_{RP}(s, t) = \frac{t^2 \beta_{RP} x_R}{0.3893} e^{a_{RP} t} \frac{(e^{-i\frac{\pi}{2}} s)^{\alpha_{RP}(t)}}{\log \tilde{s}} \quad (\text{C.7})$$

where $x_R = \frac{1}{-i}$ for $R = f$ and $\alpha_{RP}(t) = \alpha_{RP}(0) + \frac{\alpha'_R \alpha'_P}{\alpha'_R + \alpha'_P}$. These Regge-Pomeron cuts are treated as effectively describing the low energy cut effects, their intercepts are treated as free parameters.

A low energy, exchange degenerate, secondary Regge term is also included with the form (C.5) and (C.6) and

$$\gamma_{\bar{R}} = \frac{(\alpha_{\bar{R}}(t) + 1)(\alpha_{\bar{R}}(t) + 2)(\alpha_{\bar{R}}(t) + 3)}{(\alpha_{\bar{R}}(0) + 1)(\alpha_{\bar{R}}(0) + 2)(\alpha_{\bar{R}}(0) + 3)} \quad (C.8)$$

The parameter values used in the above fits are given in table C.1 .

F_1	0.29 mb	O_1	0.031 mb	β_P	29.4 mb
F_2	-1.70 mb	O_2	-0.30 mb	a_P	3.37 GeV ⁻²
F_3	8.47 mb	O_3	0.22 mb	β_{2P}	1.69 mb
b_1^+	4.25 GeV ⁻²	b_1^-	7.02 GeV ⁻²	a_{2P}	0.72 GeV ⁻²
b_2^+	5.40 GeV ⁻²	b_2^-	2.10 GeV ⁻²	$\alpha_{\bar{R}}(0)$	-0.21
b_3^+	6.01 GeV ⁻²	b_3^-	0.98 GeV ⁻²	$\beta_{\bar{R}}$	35.8 mb
R_+	0.43 GeV ⁻¹	R_-	0.13 GeV ⁻¹	$a_{\bar{R}}$	0.38 GeV ²
$\alpha_f(0)$	0.54	β_f	48.8 mb	a_f	0.011 GeV ⁻²
$\alpha_\omega(0)$	0.41	β_ω	38.5 mb	a_ω	1.84 GeV ⁻²
$\alpha_{fP}(0)$	-0.19	β_{fP}	4252.5 mb	a_{fP}	2.93 GeV ⁻²
$\alpha_{\omega P}(0)$	-0.60	$\beta_{\omega P}$	937.4 mb	$a_{\omega P}$	0.60 GeV ⁻²
α'_P	0.25 GeV ⁻²	α'_R	0.88 GeV ⁻²	α_{RP}	0.19 GeV ⁻²

TABLE C.1 Parameter values for GLN model used in §5.3.

References

- C.W.Akerlof *et al*, *Phys. Rev.*, 2864 (1976)
- M.G.Albrow *et al*, *Nucl. Phys.*, B108, 1 (1976)
- U.Amaldi *et al*, *Phys. Letters*, 43B, 231 (1973a)
- U.Amaldi *et al*, *Phys. Letters*, 44B, 112 (1973b)
- U.Amaldi *et al*, *Phys. Letters*, 66B, 390 (1977)
- U.Amaldi *et al*, *Nucl. Phys.*, B145, 367 (1978)
- U.Amaldi, K.Schubert, *Nucl. Phys.*, B166, 301 (1980)
- I.Ambats *et al*, *Phys. Rev.*, D9, 1179 (1974)
- M.Ambrosio *et al*, *Phys. Letters*, 115B, 495 (1982)
- S.Amendolia *et al*, *Phys. Letters*, 44B, 119 (1973)
- N.Amos *et al*, *Nucl. Phys.* B262, 689 (1985)
- R.C.Arnold, *Phys. Rev.*, 140B, 1022 (1965)
- S.H.Aronson, G.H.Bock, *Phys. Rev.*, D28, 476 (1983)
- Z.Asa'd *et al*, *Nucl. Phys.*, B255, 273 (1985)
- D.S.Ayres *et al*, *Phys. Rev.*, D15, 3105 (1977)
- M.Baig, *Z. Physik*, C28, 563 (1985)
- M.Baig, J.Bartels, J.W.Dash, *Nucl. Phys.*, B237, 502 (1984a)
- M.Baig, C.Bourrely, *Comp. Phys. Comm.*, 32, 281 (1984b)
- L.Baksay *et al*, *Nucl. Phys.*, B141, 1 (1978)
- R.Baltrusaitis *et al*, *Phys. Rev. Letters*, 52, 1380 (1984)
- G.Barbiellini *et al*, *Phys. Letters*, 39B, 363 (1972)
- D.Bernard *et al*, *Phys. Letters*, B179, 142 (1986)
- D.Bernard *et al*, *CERN EP/87-147* (1987)
- D.Bernard, P.Gauron, B.Niculescu, *IPNO/TH,87-59* (1987)
- M.M.Block, R.N.Cahn, *Rev. Mod. Phys.*, 57, 563 (1985)
- M.M.Block, R.N.Cahn, , (1987)
- A.Böhm *et al*, *Phys. Letters*, 49B, 491 (1974)
- M.Bozzo *et al*, *Phys. Letters*, 147B, 385 (1984)
- M.Bozzo *et al*, *Phys. Letters*, 155B, 197 (1985)
- C.Bourrely, J.Soffer, T.T.Wu, *Phys. Rev.*, D19, 3249 (1979)
- C.Bourrely, J.Soffer, T.T.Wu, *Nucl. Phys.*, B247, 15 (1984)
- A.Breakstone *et al*, *Nucl. Phys.*, B248, 223 (1984)

A.Breakstone *et al*, *Phys. Rev. Letters*, 54, 2180 (1985)
 S.J.Brodsky, G.Farrar, *Phys. Rev. Letters*, 31, 1153 (1973)
 J.Bronzan, G.Kane, U.Sukhatme, *Phys. Letters*, 49B, 272 (1974)
 G.Carboni *et al*, *Nucl. Phys.*, B254, 697 (1985)
 J.L.Cardy, *Phys. Letters*, 67B, 97 (1977)
 A.S.Carroll *et al*, *Phys. Letters*, 61B, 303 (1976)
 A.S.Carroll *et al*, *Phys. Letters*, 80B, 423 (1979)
 M.K.Carter, P.D.B.Collins, M.R.Walley, *RAL preprint*, (1985)
 H.Cheng, T.T.Wu, *Phys. Rev. Letters*, 24, 1456 (1970)
 C.B.Chiu, J.Finkelstein, *Phys. Letters*, 27B, 510 (1968)
 T.Chou, C.N.Yang, *Phys. Rev. Letters*, 20, 1213 (1968)
 T.Chou, C.N.Yang, *Phys. Rev.*, 170, 1591 (1970)
 P.D.B.Collins, *Introduction to Regge theory and high energy physics*, (1977)
 P.D.B.Collins, *Proc. of the Blois workshop on Elastic and Diffractive Scattering*, (1985)
 P.D.B.Collins, A.Fitton, *Nucl. Phys.*, B91, 332 (1975)
 P.D.B.Collins, F.Gault, *Nucl. Phys.*, B113, 34 (1976)
 P.D.B.Collins, F.Gault, *Phys. Letters*, 73B, 330 (1978)
 P.D.B.Collins, F.Gault, A.Martin, *Nucl. Phys.*, B80, 135 (1974a)
 P.D.B.Collins, F.Gault, A.Martin, *Nucl. Phys.*, B83, 241 (1974b)
 P.D.B.Collins, F.Gault, A.Martin, *Nucl. Phys.*, B85, 141 (1975)
 P.D.B.Collins, F.Gault, A.Wright, *J. Phys.G: Nucl. Phys.*, 4, 471 (1978)
 P.D.B.Collins, P.Kearney, *Z. Physik*, C22, 277 (1984)
 P.D.B.Collins, A.D.Martin, *Hadron Interactions*, (1984)
 P.D.B.Collins, A.Wright, *J. Phys.G: Nucl. Phys.*, 4, 1223 (1978)
 S.Denisov *et al*, *Nucl. Phys.*, B65, 1 (1973)
 A.Donnachie, *Proc. of the Blois workshop on Elastic and Diffractive Scattering*, (1985)
 A.Donnachie, P.V.Landshoff, *Z. Physik*, C2, 55 (1979)
 A.Donnachie, P.V.Landshoff, *Phys. Letters*, B123, 345 (1983)
 A.Donnachie, P.V.Landshoff, *Nucl. Phys.*, B231, 189 (1984a)
 A.Donnachie, P.V.Landshoff, *Nucl. Phys.*, B267, 690 (1986)
 S.Erhan *et al*, *Phys. Letters*, 152B, 131 (1985)
 W.Faissler *et al*, *Phys. Rev.*, D23, 33 (1981)
 G.R.Farrar, C.C.Wu, *Nucl. Phys.*, B85, 50 (1975)
 T.Fearnley, *CERN EP/85-137* (1985)

G.Fidecaro *et al*, *Phys. Letters*, 76B, 369 (1978)

K.J.Foley *et al*, *Phys. Rev. Letters*, 19, 857 (1967)

K.J.Foley, *BNL* 37466 (1985)

S.Frautschi, B.Margolis, *Nuovo Cimento*, 56A, 1155 (1968)

W.Galbraith *et al*, *Phys. Rev.*, 138, B193 (1965)

P.Gauron, B.Nicolescu, *Phys. Letters*, 124B, 429 (1983)

P.Gauron, B.Nicolescu, *Phys. Rev. Letters*, 52, 1952 (1984a)

P.Gauron, B.Nicolescu, *Phys. Letters*, 143B, 253 (1984b)

P.Gauron, E.Leader, B.Nicolescu, *Phys. Rev. Letters*, 54, 2656, (1985a)

P.Gauron, E.Leader, B.Nicolescu, *Phys. Rev. Letters*, 55, 639 (1985b)

P.Gauron, E.Leader, B.Nicolescu, *IPNO/TH*, 86-55 (1986)

I.S.Gradshteyn, I.M.Ryzhik, *Table of Integrals, Series and Products*, (1980)

T.Hara *et al*, *Phys. Rev. Letters*, 50, 2058 (1983)

D.J.Harrison, A.C.Irving, A.D.Martin, *Comp. Phys. Comm.*, 5, 153 (1973)

R.Hendrick *et al*, *Phys. Rev.*, D11, 536 (1975)

R.Henzi, *Proc. of the Blois workshop on Elastic and Diffractive Scattering*, (1985)

R.Henzi, P.Valin, *Nucl. Phys.*, B148, 513 (1979)

R.Henzi, P.Valin, *Phys. Letters*, 132B, 443 (1983)

R.Henzi, P.Valin, *Phys. Letters*, 160B, 167 (1985)

D.Joynson, E.Leader, B.Nicolescu, *Il Nuovo Cimento*, 30A, 345 (1975)

K.Kang, B.Nicolescu, *Phys. Rev.*, D11, 2461 (1975)

B.Kopeliovich, N.Nikolaev, I.Potashnikova, *JINR E2-86-125* (1986)

N.Kwak *et al*, *Phys. Letters*, 58B, 233 (1975)

P.V.Landshoff, *Phys. Rev.*, D10, 1024 (1974)

P.V.Landshoff, *Proc. of the Blois workshop on Elastic and Diffractive Scattering*, (1985)

P.V.Landshoff, D.J.Pritchard, *Z. Physik*, C6, 69 (1980)

J.Linsley, *Lettere al Nuovo Cimento*, 42, 403 (1985)

L.Lukaszuk, B.Nicolescu, *Lettere al Nuovo Cimento*, 8, 405 (1973)

A.Martin, *Proc. of the Blois workshop on Elastic and Diffractive Scattering*, (1985)

M.Moshe, *Phys. Rep.*, 37C, 255 (1978)

E.Nagy *et al*, *Nucl. Phys.*, B150, 221 (1979)

C.Pajares, A.Varas, P.Yepes, *Z. Physik*, C19, 89 (1983)

S.Roy, V.Singh, *Phys. Letters*, 32B, 50 (1970)

R.Rubinstein *et al*, *Phys. Rev.*, D30, 1413 (1984)

J.G.Rushbrooke, *CERN EP/85-124* (1985)

K.R.Schubert, *Landolt-Börnstein, New Series*, Vol.1/9a, (1979)

U.Sukhatme, *Phys. Rev. Letters*, 38, 124 (1977)

G.Veneziano, *Nuovo Cimento*, 57A, 190 (1968)

A.White, *Proc. of the Blois workshop on Elastic and Diffractive Scattering*, (1985)

